Title
Monometallic and Bimetallic Catalyst Systems for the Upgrading of Biomass Products to Diesel Fuel Precursors

Author
Goulas, Konstantinos Antonios

Publication Date
2015

Peer reviewed|Thesis/dissertation

Monometallic and Bimetallic Catalyst Systems for the Upgrading of Biomass Products to Diesel Fuel Precursors

By

Konstantinos Antonios Goulas

A dissertation submitted in partial satisfaction

of the requirements

for the degree of

Doctor of Philosophy

in

Chemical Engineering

in the

Graduate Division

of the

University of California, Berkeley

Committee in charge:

Prof. F. Dean Toste, Co-Chair

Prof. Alexis T. Bell, Co-Chair

Prof. Nitash P. Balsara

Prof. Gabor A. Somorjai

Spring 2015

Monometallic and Bimetallic Catalyst Systems for the Upgrading of Biomass Products to Diesel Fuel Precursors

By

Konstantinos Antonios Goulas

Abstract

Monometallic and Bimetallic Catalyst Systems for the Upgrading of Biomass Products to Diesel Fuel Precursors

by

Konstantinos Antonios Goulas

Doctor of Philosophy in Chemical Engineering

University of California, Berkeley

Professor F. Dean Toste, Co-Chair

Professor Alexis T. Bell, Co-Chair

The condensation of mixtures of acetone, butanol and ethanol (ABE), derived from fermentation processes has recently been reported as a viable pathway to diesel fuel precursor molecules. This process is catalyzed by bifunctional catalysts that include a metal functionality to dehydrogenate the alcohols and a basic functionality to catalyze the aldol condensation between the aldehydes and the acetone. However, the currently used catalysts are poorly understood, in terms of the driving forces of their selectivity, reactivity and stability.

Based on screening reactions, we show that monometallic Pd and Cu catalysts supported on mixed metal oxides derived from hydrotalcites are the most active catalysts for this reaction. Kinetic analysis of these catalysts reveals that the dehydrogenation over the metal catalysts proceeds via a rate-determining C-H bond scission. On the other hand, the aldol condensation over the mixed oxide support takes place via an equilibrated enolate formation and its subsequent abstraction from the surface by an aldehyde. However, the decarbonylation of aldehydes over Pd and the formation of esters over Cu via the Tishchenko reaction limits the usability of monometallic catalysts.

Supporting Pd and Cu on hydrotalcite-derived supports results in the elimination of the Tishchenko side reaction and a reduction of the decarbonylation rates. Complete elimination of decarbonylation was not possible with these supports, due to the incorporation of Cu^{2+} ions in the Mg-Al oxide structure. For this reason, TiO_2 was used as a support; this resulted in complete alloying of Cu and Pd and, in turn, in significant selectivity improvements, combined with enhanced stability in the liquid phase.

The liquid phase stability is due to the absence of any transformation from the anatase to the rutile phase. Kinetic analysis of the C-C bond formation reactions over TiO_2 reveals anatase to be the active phase for these reactions over TiO_2. In contrast to the C-C bond formation reactions over the mixed Mg-Al oxide, the aldol condensation reaction over TiO_2 proceeds via a rate-determining alpha-hydrogen abstraction and enolate formation over an acid-base

pair on the TiO_2 surface. Similar analysis for a ZrO_2 catalyst shows that the enolate formation is also rate-determining over ZrO_2.

Apart from the ABE mixture, fuel precursors can also be derived by condensation of furfural and alcohols. These reactions proceed over transition-metal-free basic oxides via a rate-determining hydride transfer from a butoxide to an adsorbed furfural molecule, as shown by kinetic experiments in the gas and the liquid phase, as well as kinetic isotope effect experiments.

To my family and friends, for their support in this journey.

ACKNOWLEDGEMENTS

This dissertation is the culmination of six years of effort. It would not have been possible without the help of a great number of individuals and organizations that supported me throughout. All of them deserve a great thank you!

First of all, my advisor, Dean Toste, who gave me the chance to work on an intriguing project. He took me in his group at a very difficult point in time and had the patience to guide me through my PhD. He supported me all the way and gave me the freedom to pursue facets of the project that drew my interest, giving me sound advice at every step of the way.

Alex Bell, my co-advisor, was also instrumental in the success of this work. He provided me with guidance and helped me realize what is novel and interesting in the field. He supported me with his words and actions throughout my time here in Berkeley and allowed me to enrich myself through collaborations with his group.

I have had the pleasure of interacting with multiple other faculty at Berkeley, all of whom have been a source of inspiration and to whom I am grateful: Jeff Reimer, for his support in difficult moments and his advice on academic life and NMR; Roya Maboudian, for her advice and for teaching me to be a good GSI; Professors Balsara, Tullman-Ercek and Somorjai for their help in formulating my argument through their comments; Prof. Enrique Iglesia, for teaching me the basics of catalysis and for showing me the importance of rigor in our field.

I am also grateful to great coworkers that helped me through my project: Justin Chen and Adam Grippo for their assistance in reactions and syntheses; Dave Flaherty, Greg Johnson and Eric Sacia, for many great scientific discussions; Lin Louie, Alice Yeh, Gorkem Gunbas, Balki Madhesan, Julie Rorrer, George Arab, Lipeng Wu, Suresh Pindi, Alex Wang, Nikos Petzetakis and Chaeyoung Shin for the collaborative and creative working environment at EBI; Zach Baer and Sanil Sreekumar for getting me started at EBI; last, but definitely not least, I have to thank Dr. Amit Gokhale for his advice and for keeping us all grounded.

In addition to this, I have to acknowledge Greg Johnson for a multitude of TEM samples, Paul Dietrich, for running X-ray absorption spectroscopy on our samples and helping us understand the structure of our catalysts, and Y C Wang for TEM of the first PdCuHT catalyst. Also, I would like to thank Prof. Jeff Long for his kind permission to use his X-ray diffractometer and Prof. Alex Katz for allowing us to use his chemisorption unit.

I would also like to thank the graduate student affairs officers through the years, Rocio Sanchez, Fred Deakin and Carlet Altamirano, for helping us navigate the UC system requirements.

Outside the lab, I have been privileged to have friends, whose support made a huge difference in surviving and thriving throughout the trials and tribulations of graduate school. My first two roommates, Miguel Modestino and Peter Soler, together with the rest of the 2008 Class of Chemical Engineering, welcomed me to the US and to Berkeley and made my transition much smoother. The rest of the 2009 Class provided an invaluable support network. The

camaraderie built in working long hours and tackling hard scientific problems (and the occasional weekend trip) is one that I will forever cherish.

My family has also had a pivotal role in helping me see this project through. My father, whose high standards I aspire to meet has been a source of inspiration, advice and helpful commentary in all matters academic. My mother has helped me keep things in perspective, without sacrificing any of my aspirations and dreams. Finally, my life partner Katy, for her love and patience in the moments of hardship during this journey and the joy that she and our beagle, Elektra, bring to my life.

TABLE OF CONTENTS

Introduction

Emissions of CO_2 from fossil fuel combustion have been a driving force behind the increase in global temperatures over the last 50 years. Because of this, worldwide efforts have been made to reduce CO_2 emissions, culminating in the Kyoto protocol. As part of its commitments under the Kyoto protocol, the EU has mandated a minimum bio-derived content in its diesel supply.

Current methods for biodiesel production use vegetable oils. In these, triglycerides extracted from oleiferous seeds undergo transesterification [1] to fatty acid methyl esters (FAME) or hydrodeoxygenation [1, 2] at high temperature and pressure to produce a hydrocarbon mixture. However, both of these methods are hampered by problems with the vegetable oil supply. In addition to the competition with food supplies, biofuel yields per acre are low in the cases of rapeseed and soybean oil [3] and sustainability issues related to land use change have yet to be addressed in the case of palm oil [4, 5] .

Lignocellulosic biomass, on the other hand, is an inexpensive and widely available biomass source, that also does not compete with food sources [6]. One approach that has been taken towards its utilization, not only for diesel, but also for multiple fuels and chemicals, is to break down the lignocellulosic biomass to its constituents, producing biomass monomers, such as xylose and glucose [7, 8]. These can be chemically converted to biomass platform molecules, furfural and hydroxymethylfurfural, respectively [9, 10]. Pathways for the utilization of these molecules for the production of diesel fuel replacements have been reported by Corma and coworkers [11, 12], as well as Bell and coworkers [13].

Thermal processing of biomass for the production of syngas [14, 15] or bio-oil [8, 16] is another approach that has been taken. However, this approach tends to be associated with high capital expenses, due to the extensive pretreatment and/or reactor equipment required to produce a finished product [8].

Alternatively, the monomers obtained from chemical pretreatment of lignocellulosic biomass, or the sugars obtained from the mechanical pretreatment of sugary biomass can be fermented to produce ethanol or mixtures of short-chain oxygenates, such as acetone, ethanol and butanol [17]. Ethanol can be used directly as gasoline replacement or it can be oligomerized to form heavier products that can be used as fuel [18].

The catalytic upgrading of acetone, ethanol and butanol (ABE) produced by fermentation to diesel fuel precursors was recently reported in the literature [19]. However, the recyclability, reaction rates and process parameters were unsuited to industrial exploitation.

The present dissertation shows the steps taken to develop and design an active, selective and stable catalyst for the ABE condensation, as well as the application of related catalysts to similar processes, such as the oligomerization of short-chained alcohols and the condensation of alcohols with furfural.

Chapter 1 presents the liquid-phase catalyst screening and the gas-phase kinetics for monometallic catalysts. It follows with a section on bimetallic PdCu catalyst design for the elimination of decarbonylation. Chapter 2 presents the pathways of deactivation of the hydrotalcite, carbon and TiO_2-based catalysts. Chapter 3 presents the effects of heat treatment on the stability, activity and selectivity of hydrotalcite-based catalysts in monofunctional and bifunctional reactions. Chapter 4 presents an application of the hydrotalcite catalysts in the metal-free aldol condensation between furfural and butanol, as well as the kinetics of these reactions in the liquid and the gas phase. Chapter 5 presents the kinetics and site requirements for C-C bond formation reactions over the optimal catalyst, TiO_2. Finally, Chapter 6 presents the kinetics of aldol condensation and esterification over ZrO_2 catalysts, as an alternative to the hydrotalcite and TiO_2-based catalysts.

Appendix A presents supporting information, such as X-ray diffractograms, thermogravimetric analyses, X-ray absorption spectra and surface area measurements for the catalysts used in Chapter 1. Appendix B presents supporting information for Chapter 2, including deactivation information for catalysts during liquid and gas phase flow reactions.

REFERENCES

[1] D. Y. Murzin, P. Maki-Arvela and S. I. L, "Triglycerides and Oils for Biofuels," in *Kirk-Othmer Encyclopedia of Chemical Technology*, Wiley VCH, 2012, pp. 1-14.

[2] P. Maki-Arvela, I. Kubickova, M. Snaare, K. Eranen and D. Y. Murzin, "Catalytic Deoxygenation of Fatty Acids and Their Derivatives," *Energy and Fuels,* vol. 21, no. 1, pp. 30-41, 2007.

[3] C. Somerville, "Biofuels," *Current Biology,* vol. 17, no. 4, pp. R115-R119, 2007.

[4] B. Wicke, V. Dornburg, M. Junginger and A. Faaij, "Different palm oil production systems for energy purposes and their greenhouse gas implications," *Biomass and Bioenergy,* vol. 32, no. 12, pp. 1322-1337, 2008.

[5] L. P. Koh and D. S. Wilcove, "Cashing in palm oil for conservation," *Nature,* vol. 448, pp. 993-994, 2007.

[6] D. M. Alonso, J. Q. Bond and J. A. Dumesic, "Catalytic conversion of biomass to biofuels," *Green Chemistry,* vol. 12, p. 1493–1513, 2010.

[7] N. Mosier, C. Wyman, B. Dale, R. Elanderd, Y. Y. Lee, M. Holtzapple and M. Ladisch, "Features of promising technologies for pretreatment of lignocellulosic biomass," *Bioresource Technology,* vol. 96, no. 6, p. 673–686, 2005.

[8] G. W. Huber, S. Iborra and A. Corma, "Synthesis of Transportation Fuels from Biomass: Chemistry, Catalysts, and Engineering," *Chemical Reviews,* vol. 106, no. 9, p. 4044–4098, 2006.

[9] R. Xing, W. Qi and G. W. Huber, "Production of furfural and carboxylic acids from waste aqueous hemicellulose solutions from the pulp and paper and cellulosic ethanol industries," *Energy and Environmental Science,* vol. 4, pp. 2193-2205, 2011.

[10] J. N. Chheda, Y. Roman-Leshkov and J. A. Dumesic, "Production of 5-hydroxymethylfurfural and furfural by dehydration of biomass-derived mono- and poly-saccharides," *Green Chemistry,* vol. 9, pp. 342-350, 2007.

[11] A. Corma, O. de la Torre and M. Renz, "Production of high quality diesel from cellulose and hemicellulose by the Sylvan process: catalysts and process variables," *Energy and Environmental Science,* vol. 5, pp. 6328-6344, 2012.

[12] A. Corma, O. de la Torre, M. Renz and N. Villandier, "Production of High-Quality Diesel from Biomass Waste Products," *Angewandte Chemie,* vol. 123, no. 10, p. 2423–2426, 2011.

[13] M. Balakrishnan, E. R. Sacia and A. T. Bell, "Selective Hydrogenation of Furan-Containing Condensation Products as a Source of Biomass-Derived Diesel Additives," *ChemSusChem,* vol. 7, no. 10, p. 2796–2800, 2014.

[14] F. L. P. Resende, S. A. Fraley, M. J. Berger and P. E. Savage, "Noncatalytic Gasification of Lignin in Supercritical Water," *Energy and Fuels,* vol. 22, p. 1328–1334, 2008.

[15] F. L. P. Resende, M. E. Neff and P. E. Savage, "Noncatalytic gasification of cellulose in supercritical water," *Energy and Fuels,* vol. 21, no. 6, pp. 3637-3643, 2007.

[16] A. V. Bridgewater, "Review of fast pyrolysis of biomass and product upgrading," *Biomass and Bioenergy,* vol. 38, pp. 68-94, 2012.

[17] N. Qureshi and H. P. Blaschek, "Recent advances in ABE fermentation: hyper-butanol producing Clostridium beijerinckii BA101.," *Journal of Industrial Microbiology and Biotechnology,* vol. 27, no. 5, pp. 287-291, 2001.

[18] T. Tsuchida, J. Kuboa, T. Yoshioka, S. Sakuma, T. Takeguchi and W. Ueda, "Reaction of ethanol over hydroxyapatite affected by Ca/P ratio of catalyst," *Journal of Catalysis,* vol. 259, no. 2, pp. 183-189, 2008.

[19] P. Anbarasan, Z. C. Baer, S. Sreekumar, E. Gross, J. B. Binder, H. W. Blanch, D. S. Clark and F. D. Toste, "Integration of chemical catalysis with extractive fermentation to produce fuels," *Nature,* vol. 491, pp. 235-239, 2012.

CHAPTER 1: Catalyst development and kinetics of the ABE condensation over monometallic and bimetallic catalysts

INTRODUCTION

In our earlier work, we proposed using a strategy combining fermentation and chemical upgrading to yield biodiesel precursor molecules [1]. In this sequence, sugars can be fermented to a mixture of acetone, butanol, and ethanol that can be upgraded to heavier ketones in a dehydrogenation-aldol condensation-hydrogenation reaction pathway. We also showed that the ABE condensation reaction can be efficiently catalyzed by physical mixtures of Pd/C and K_3PO_4. However, the disadvantage of this catalyst system was the fact that the water produced during the reaction tended to hydrolyze the potassium phosphate to potassium hydrogen phosphates, which do not catalyze the reaction. Also, reaction rates were relatively low (24 h required for complete conversion of the starting material, corresponding to a turnover frequency of about 0.03 h^{-1}) and the use of toluene as a solvent hampered the applicability of this system in an industrial setting.

We also demonstrated that Cu- and Pd-substituted hydrotalcite materials are efficient catalysts for the ABE condensation. They also showed markedly improved recyclability compared to the original Pd/C-K_3PO_4 system [2]. However, the long reaction times, on the order of 20 h (corresponding to a TOF of 0.06 h^{-1}), make this system impractical as an industrial catalyst.

In this work, we show the steps taken to improve on these catalysts, using batch reactor screening, instrumental characterization techniques, and liquid and gas-phase reaction monitoring. We then proceed to design a bimetallic catalyst based on X-ray absorption data and to show how alloying and surface segregation impact the selectivity and reactivity of ABE process catalysts.

MATERIALS AND METHODS

Pd-modified Y zeolite [3] and Na/Ca/SiO_2-supported Pd [4] were prepared based on methods described in detail elsewhere in the literature.

Preparation of mixed $M_xMg_{1-x}O$ oxides, where M is Ca or Sr was achieved by a variation of the method proposed by Putanov et al., whereby magnesium oxalate is precipitated from a magnesium acetate solution upon addition of oxalic acid [5]. In our experiments, we added a 0.83 M solution of oxalic acid (1.2 equivalents) to a 25 wt% magnesium acetate solution, spiked with calcium or strontium acetate. The resulting milky suspension was aged for 16 h and subsequently the solids filtered and dried *in vacuo* at 343 K. Calcination of the mixed oxalates at 773 K (5 K min^{-1}, 4 h) afforded mixed oxides.

Coprecipitated Cu catalysts were prepared by modifying the procedure outlined by Climent et al. [6]. In this procedure, a solution of magnesium and aluminum nitrates (1.5 M total metal concentration, 3:1 mol Mg:Al) was mixed with a copper and aluminum nitrate solution (1.5 M total metal concentration, 3:1 mol Cu:Al). The resulting solution was heated to 333 K and an equal volume of a solution of ammonium hydroxide (3.375 M) and ammonium carbonate (1 M) was added to it dropwise. The resulting slurry was stirred overnight and the solids filtered and washed with a volume of distilled water equal to five times the volume of the solution. After drying at ambient air at 373 K, the solids were treated in ambient air at 823 K for 4 h (ramp rate 1 K min^{-1}). NiHT and CoHT catalysts were prepared in a similar way, using $Ni(NO_3)_2.6H_2O$ and $Co(NO_3)_2.6H_2O$, respectively, in the place of copper nitrate hemipentahydrate.

Hydrotalcite-supported Cu catalysts were also prepared by incipient wetness impregnation of a solution of copper nitrate hemipentahydrate into a mixed magnesium-aluminum oxide. This oxide was prepared by calcination of synthetic hydrotalcite (Sigma-Aldrich) at 823 K for 4 h (ramp rate 1 K min^{-1}). Following impregnation, the catalyst precursor was dried in ambient air at 373 K and subsequently calcined at 823 K for 4 h (ramp rate 1 K min^{-1}). For the preparation of PdCu/HT and Pd/HT catalysts, a similar procedure was followed, using palladium nitrate hydrate and copper nitrate hemipentahydrate. For RuHT, the calcined hydrotalcite was impregnated with an aqueous solution of $RuCl_3$ and calcined, whereas for PtHT, the calcined hydrotalcite was impregnated with an aqueous solution of H_2PtCl_6 and reduced at 723 K in H_2 for 2 h (ramp 2 K min^{-1}) after drying at 373 K overnight. Titanium dioxide was prepared following a procedure reported by Wang and Ying [7]. A mixture of ethanol and water was added dropwise to a titanium isopropoxide solution in ethanol. The ratio of titanium isopropoxide to water was 1:100. After hydrolysis, the resulting suspension was aged for 16 h at ambient temperature. The solids were separated by filtration and dried in stagnant ambient air at 373 K for 16 h.

Hydroxyapatite was prepared according to Wang, et al. [8]. In this process, a stoichiometric quantity of an ammonium hydrogen phosphate solution was added dropwise at ambient temperature to a calcium nitrate solution, whose pH was adjusted to 11 with aqueous ammonium hydroxide solution. The slurry was aged at 363 K for 1 h and the solids were subsequently filtered and washed with copious amounts of water. After that, they were treated in ambient air at 373 K for at least 16 h and subsequently treated for 4 h at 573 K (ramp rate 5 K min^{-1}).

Surface areas of the catalysts were measured by means of nitrogen physisorption using a Micromeritics Tristar 3000 analyzer. The data were analyzed using the BET and BJH methods for surface area and pore size, respectively.

The structure of the catalysts was investigated by X-ray diffraction (XRD) and X-ray absorption spectroscopy (XAS). XRD experiments were performed using a Bruker D8 instrument using a 2θ-θ geometry, scanning from $2\theta = 20^o$ to 60^o, at a rate of $0.02\,^o/s$.

Thermogravimetric analysis of the catalysts was performed using a TA8020 TGA instrument, using a 5 K min^{-1} ramp to 1123 K. Alumina crucibles were used to hold 20-40 mg of sample.

X-ray absorption spectroscopy experiments were performed on the Sector 10, Materials Research Collaborative Access Team, Insertion Device (ID) and bending magnet (BM) beamlines at the Advanced Photon Source, Argonne National Lab. Experiments were conducted at the Pd K (24350 eV) and Cu K (8979 eV) edges. Experiments were performed in either transmission (Pd and Cu) or fluorescence (Cu) detection modes. A series of 3 ion chambers were used, with the third detector simultaneously measuring a reference foil with all experiments for energy calibration. A Lytle detector was used as the fluorescence detector.

For transmission experiments, samples were packed into self-supporting wafers, in a 6-well sample holder. Sample loading was calculated to give an absorbance (μ_x) of <2.5 to avoid self-absorption effects, and an edge step ($\Delta\mu_x$) between 0.2 and 1.5. Fluorescence samples were packed into self-supporting wafers in a custom fluorescence holder that held the sample at a 45° angle incident to the beam path. The detector was placed at a 90° angle incident to the beam path.

Samples were contained in 1" OD quartz tubes connected to Ultra-Torr fittings with welded ball valves at the end to control the gas atmosphere. For fluorescence experiments, a similar 1" OD quartz tube with a cone attached to the side was used. The samples were then reduced in situ using a 50% H_2/He gas mixture at the prescribed temperature. Samples were held for 0.5 – 1 h (reducing time was determined not to have an effect on the final state) at 523 K, after which the gas flow was switched to He (Ultra High Purity grade) for 15 min. The samples were then cooled to room temperature and scanned under a static He atmosphere.

In all reaction experiments, we used an 1:2.3:3.7 ratio for ethanol:acetone:butanol, since this is the ratio produced by *C. acetobutylicum* during fermentation.

Batch reactions were conducted in pressure tubes (Q-Tubes), using a procedure described in detail elsewhere [1, 2].

Gas-phase reactions were conducted in a tubular fused silica reactor with plug-flow hydrodynamics. In this reactor, the catalyst was supported on a quartz frit. Before reaction, the catalyst was sieved down to a size under 0.18 μm to avoid mass transfer effects during reaction. The reactor was enclosed in a furnace (ATS Pennsylvania) with aluminum inserts, whose temperature was controlled by a PID controller (Watlow).

Gas flow through the catalyst was regulated via mass flow controllers (Parker). Liquid reactants were vaporized into the gas stream through a syringe port in the heated transfer lines. Their flow was regulated by a syringe pump (Legato 100).

The effluent of the reactor was analyzed online using a gas chromatograph (Shimadzu GC 2014) equipped with a flame ionization detector and an HP-1 capillary column.

RESULTS AND DISCUSSION

SCREENING

Rode et al. showed that alkali-substituted zeolites can be efficient catalysts for aldol condensation reactions of butyraldehyde [3]. We therefore examined Pd-modified CsY and NaY zeolites, as a potential catalysts for ABE upgrading. The target products (A-F) of the dehydrogenation/aldol condensation sequence are shown in scheme 1.

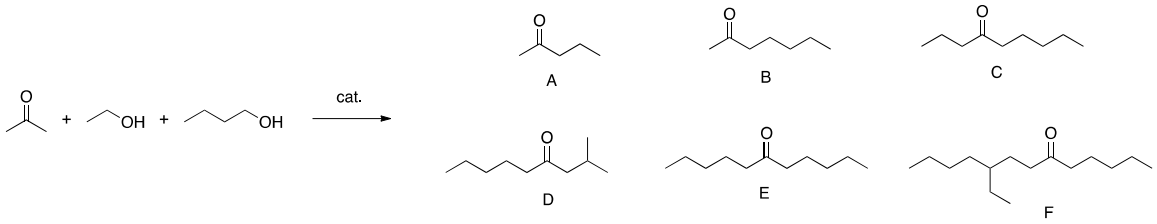

Scheme 1: ABE condensation products

The yield to diesel-range precursors was consistently lower (maximum of 56%) than that of the hydrotalcite-type materials, which took the reaction to full conversion. We also note that higher temperatures gave higher yields of etherification products. Ether formation from alcohols is a well-known acid-catalyzed reaction, suggesting that there are residual acid sites on the zeolites. This is undesirable, since, in a commercial process, the oxygenates would be subjected to hydrodeoxygenation to form alkanes. In this process, ethers, such as dibutyl ether would undergo C-O bond cleavage to form butanes, which are very low added-value products and unsuitable for blending with diesel fuel.

Table 1: Percent yield of ABE condensation products for the series of Pd-modified, alkali-substituted zeolites.

[a]Reaction condition: 2.3 mmol acetone, 3.7 mmol butanol, 1 mmol ethanol, 350 mg catalyst in 1 mL BuOH.

[b]19 mg butylether formed

[c]156 mg butylether formed

Entry[a]	A	B	C	D	E	F	Total Alcohols	Overall
1Pd/NaY, 200 °C	6.4	14.6	-	-	-	-	-	21.0
2Pd/CsY, 200 °C	4.9	23.3	-	-	-	-	-	28.2
5Pd/CsY, 200 °C	7.6	33.5	-	-	-	-	-	41.1
5Pd/CsY, 215 °C[b]	7.3	47	0.8	0.6	1.1	-	-	56.8
5Pd/CsY, 240 °C[c]	4.9	43.4	1.6	1.2	2.8	-	1.3	55.2

We also investigated the possibility of using silica-based catalysts for the ABE reaction. NaOH and CaO supported on silica have been reported as active catalysts for aldol condensation reactions [4]. Excellent yields were achieved when supporting Pd on the basified silica catalysts, as can be seen in table 2. However, the recyclability of these catalysts was rather poor (last three entries on table 2) compared to the hydrotalcite-based materials reported in the past; the yield of ABE products in the third cycle was less than half of that in the first cycle, compared to a modest 10% loss of ABE yield in the case of hydrotalcite-based catalysts [2]. It is possible that the water formed in the reaction leaches away the easily-soluble NaOH and $Ca(OH)_2$, and thereby deactivates the catalyst. We also noted the formation of alcohols in the product stream. This indicates that there is excess hydrogen in the system, since the formation of the C_7 and C_{11} ketones does not require extra hydrogen. The dehydrogenation of the alcohols in the feed produces one mole of hydrogen, which is consumed again in the hydrogenation of the α,β-unsaturated ketone product of the aldol condensation. Possible pathways for the formation of hydrogen include the Tishchenko reaction and decarbonylation reactions. In the former the dehydrogenation of the hemiacetal produced by the reaction of an aldehyde and an alcohol yields an ester. This pathway has been utilized for the single-step production of ethyl acetate from ethanol [9, 10, 11]. In the case of decarbonylation reactions, C-C bond scission is a necessary step in the production of hydrogen from organic oxygenates during reforming over Pt and Pd-based catalysts, [12, 13].

Table 2: Yields of ABE reaction over Na- and Ca-basified SiO_2 catalysts. Reaction conditions: 2.3 mmol acetone, 3.7 mmol butanol, 1 mmol ethanol, 350 mg catalyst in 1 mL BuOH

Entry[a]	A	B (2C7+4C7)	C	D	E	F	Total Alcohols	Overall Yield
$1Pd/10Na/SiO_2$	1.8	26.8	3.2	0.3	22	-	6.0	60.1
$0.75Pd/15Na/15Ca/SiO_2$	4.8	34.8	5.1	0.6	39.8	1.4	4.7	91.2
$0.5Pd/15Na/15Ca/SiO_2$	2.5	32.3	6.6	0.5	42.1	2.2	5.0	91.2
$0.85Pd/17Na/17Ca/SiO_2$	4.1	41.0	4.0	0.9	22.0	0.2	4.7	76.9
$1Pd/10Na/10Ca/SiO_2$	2.9	34.2	1.7	0.5	10.7	-	4.2	54.2
$1Cu/10Na/10Ca/SiO_2$	-	20.8	0.4	-	7.1	-	2.9	31.2
$0.5Pd/15Na/15Ca/SiO_2$, 1st	2.2	31.7	5.4	0.5	38.9	2.0	5.4	86.1
$0.5Pd/15Na/15Ca/SiO_2$, 2nd	2.9	31.5	1.0	0.4	5.6	-	1.6	43.0
$0.5Pd/15Na/15Ca/SiO_2$, 3rd	1.9	29.6	0.6	0.3	5.9	-	1.3	39.6

The hydrotalcite-supported metal catalysts studied previously were made on low surface area supports, ranging from 6 to 26 m^2/g, so it was hypothesized that activity could be increased by increasing the surface area. In order to improve the reactivity, we calcined the hydrotalcite catalyst at 823 K prior to the ion exchange. Consistent with previous studies [14], this increased the surface area of the raw

material up to 200 m^2/g, indicating the formation of the higher surface area periclase structure. However, reaction studies did not show appreciable improvements in the yield of the reaction (83% vs. 80% for the pre-calcined HT and the control respectively), or increased selectivity to the C_{11}+ fraction of the products. This is explained by the measured surface area of the finished metal-hydrotalcite material (26 m^2/g), which was identical to the uncalcined material, as the metal oxide reverts to the lamellar structure upon exposure to water [14] during the metal impregnation.

It is therefore clear that, in order to increase the surface area of the catalyst, it is necessary to retain the cubic structure of the periclase material. This was achieved by co-precipitating the Cu, Mg and Al hydroxycarbonates from a solution of the nitrates, forming a Cu-doped hydrotalcite, and calcining it to form the high-surface-area periclase structure. Our results (Table S 1) indicate that Cu-doped HT materials can be synthesized with surfaces areas between 140 and 200 m^2/g after calcination at 823 K, in agreement with literature reports [15] .

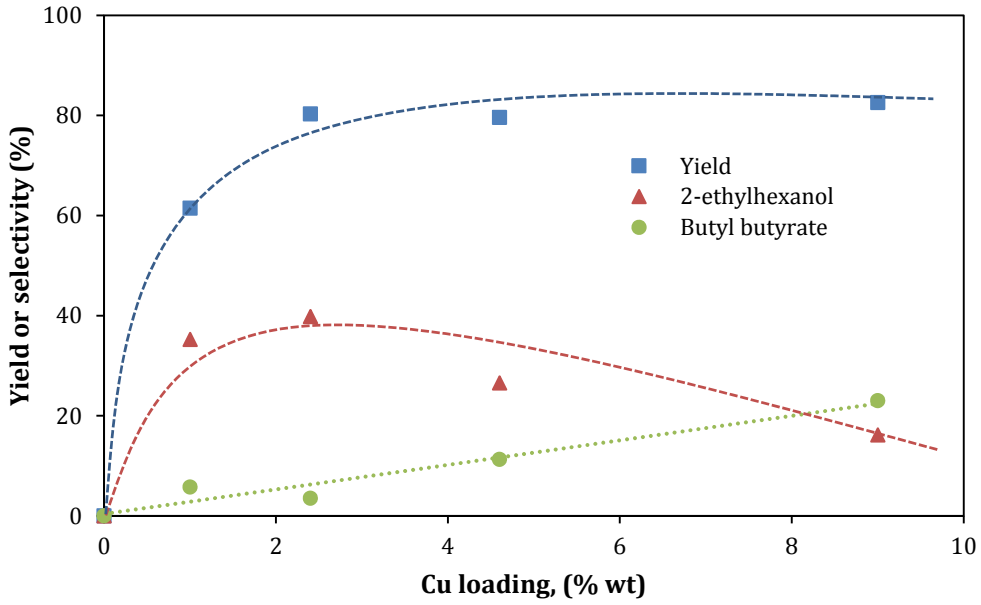

Figure 1: Effects of Cu loading on reaction yield and selectivity. Batch reactor, 513 K, 18 h, : 2.3 mmol acetone, 3.7 mmol butanol, 1 mmol ethanol, 350 mg catalyst in 1 mL BuOH. Dashed lines indicate qualitative trends.

The yields of the ABE condensation reaction using catalysts prepared by coprecipitation are shown in Figure 1. We observed an increase in the yields of ketones A-F with increasing Cu content up to about a 2.5% Cu loading. Furthermore, the selectivity to 2-ethylhexanol and its condensation product with acetone, 4-methyl-2-undecanone, also increase. Increasing Cu content beyond 2.5% did not result in higher yields, but resulted in increased production of butyl butyrate and decreased formation of 2-ethylhexanol and heavier condensation products. This undesirable effect can be attributed to the formation of a hemiacetal over the basic

sites of the HT and its subsequent dehydrogenation by the Cu, as shown in scheme 2. Cu catalysts are known to catalyze hemiacetal dehydrogenation, formed over basic or amphoteric supports, to form esters, a property utilized for the single-step formation of ethyl acetate from ethanol[9, 10, 11].

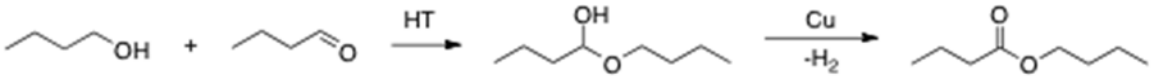

Scheme 2: Formation of butyl butyrate from butanol and butyraldehyde.

Another technique employed for high-surface-area HT-supported catalysts is incipient wetness impregnation of metal nitrates on HT [16] We therefore prepared a 2.5% CuHT catalyst using an incipient wetness impregnation method; the surface area of the sample was 198 m^2 g^{-1}. When tested against the 2.5% CuHT catalyst prepared by coprecipitation, the sample prepared by incipient wetness impregnation showed higher yields (Table 3). A possible reason for this is that coprecipitating the copper nitrate with the magnesium and aluminum nitrates puts copper in random positions throughout the structure and not on the surface, where it can be reduced by H_2 and be active for dehydrogenation reactions. In order to test this hypothesis, we studied the catalyst using X-ray absorption spectroscopy.

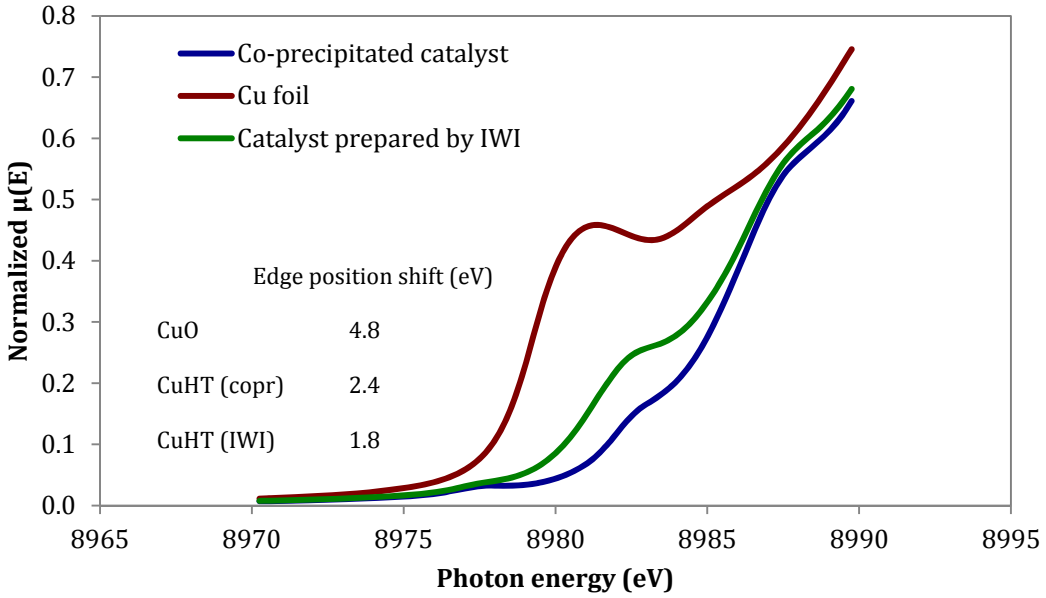

Figure 2: X-ray absorption spectra for 2.5% Cu/HT catalysts. Spectra recorded at room temperature in transmission mode after reduction at 523 K under a flowing 50% H_2/He mixture. Inset represents the edge position shifts from Cu(0), defined as the zero crossing of the second derivative of the extinction coefficient with respect to the energy.

The X-ray absorption near edge structure (XANES) results (Figure 2) are consistent with this hypothesis. After treatment in a hydrogen/helium mixture at 523 K, we expect all accessible Cu to be reduced to a Cu(0) species, in accordance with literature TPR data [17]. However, in the case of these catalysts, a significant portion

of Cu remains oxidized, in a 2+ oxidation state, and in a coordination environment reminiscent of $Cu(H_2O)_6^{2+}$, as evidenced by the shape of the white line. This suggests that Cu is surrounded by the Mg-Al oxide structure and is inaccessible to hydrogen or the alcohols for reduction.

Based on the fact that close to completion, the yield and conversion of the reactions are not very sensitive to the reaction rates, we opted to conduct further experimentation at short reaction times (2 h), with a weight ratio of catalyst-to-substrate equal to about 0.5. Also, we decided to discontinue the use of excess butanol, as this would not be realistic in an industrial setting, wherein one would need to utilize the entire product slate of the fermentation. These conditions resulted in lower conversions (table 3), but at the same time, the conversion values are much more indicative of the suitability of a given catalyst for eventual industrial use.

Table 3: Effects of the solvent and the ratio of substrate to catalyst on the conversion and the yield of 6-undecanone at 513 K, batch reaction. Substrate is ABE mixture.

	Total yield (%)	**Yield E (%)**	**Solvent**	**Mass ratio substrate/catalyst**	**Reaction time**
CuHT (IWI)	89.6	60.4	Butanol	1.25	20
CuHT (Co-Pr)	73.0	35.5	Butanol	1.25	20
CuHT (IWI)	47.5	13.8	None	2	2
CuHT (Co-Pr)	37.8	12.8	None	2	2

In order to further increase the aldol condensation rates, we investigated the possibility of using higher alkaline earth element oxides, since these oxides are known to be more basic than MgO and Al_2O_3 [18] However, achieving high surface areas for these elements in their pure form is challenging [18]. For this reason, we elected to support the catalysts on SiO_2, using an incipient wetness impregnation of the nitrates, followed by calcination at 773 K. This way, we intended to form small metal oxide clusters on SiO_2. These materials were physically mixed with a commercial $Cu/ZnO/Al_2O_3$ catalyst prior to reaction, in order to dehydrogenate the alcohol. The results of these experiments are shown in

Table 4. It is clear that MO/SiO_2 materials behaved poorly, since the product yield was about a third of that of a HT catalyst tested under the same conditions. A possible reason for the poor performance of these materials is that they did not form the cubic MO structure, as evidenced by their X-ray diffractograms (Figure S 1). Instead, there is only a broad peak, attributable to the amorphous SiO_2. A possible reason for this behavior is that the metal nitrates or oxides react with the SiO_2 surface to form surface silicates, which are unreactive for the aldol condensation reactions. The detrimental effects of the formation of silicates for C-C

bond formation reactions were reported in the past for butadiene formation reactions [19].

Table 4: Alternative base screening for ABE condensation. 523 K: 4.6 mmol acetone, 7.4 mmol butanol, 2 mmol ethanol, 350 mg base in physical mixture with 50 mg Cu/ZnO/Al_2O_3. Reaction time 2 hours.

Entry[a]	A	B	C	D	E	F	Total Alcohols	Overall
BaO/SiO_2	-	-	-	-	-	-	-	~0
MgO/SiO_2	-	-	-	-	-	-	-	~0
SrO/SiO_2	0.8	6.7	0.2	0.2	-	0.1	-	8.0
CaO/SiO	1.9	15.9	0.3	-	0.6	-	0.6	19.3
SrO/MgO (1 %)	2.7	17.8	2.6	0.7	11.9	-	1.8	37.5
SrO/MgO (2 %)	1.9	13.4	1.6	0.4	7.8	-	1.1	26.2
CaO/MgO (10 %)	2.0	12.2	6.3	1.1	28.1	-	3.1	52.8
CaO/MgO (5 %)	2.5	15.5	4.2	0.7	19.5	-	2.4	44.8
CaO/MgO (1 %)	2.2	10.7	7.1	1.0	27.0	-	5.1	53.1
Hydroxyapatite	2.4	21.3	0.5	0.3	1.3	-	0.2	26
Perovskite	0.5	22.7	0.6	-	5.1	-	4.0	32.9
HT	0.5	6.0	1.6	0.5	20.0	1.8	28.3	58.7

Doping more basic elements into an MgO structure has been previously proposed as a strategy to improve the basicity of the catalyst and consequently, the aldol condensation reaction rate [20, 21]. As can be seen from Figures S2 and S4, mixed oxides are the dominant phase in low heteroatom substitution percentages. However, increasing the doping gave rise to another phase, possibly the mixed $(M,Mg)CO_3$ carbonate. It is known that oxalates decompose into carbonates upon heating, with the carbonates decomposing to the oxides upon further heating. TGA experiments (Fig. S 3 and S 5) demonstrated an increase in decomposition temperature with an increase in the atomic number of the substituted group IIA element, suggesting an increase in the fraction of carbonates. Since the carbonates are less basic than the oxides, we believe that the increasing proportion of carbonates in the samples result in the observed reduction of the reaction rate upon increasing the doping over 1%.

Perovskite and hydroxyapatite are known basic catalysts that have demonstrated effectiveness for other base-catalyzed reactions, such as ethanol oligomerization [22]. For this reason, we tested them for the ABE reaction, in a physical mixture with Cu-containing catalysts to ensure the dehydrogenation of the alcohols. However, the yields were not high enough (<40%) to warrant further investigations. This is consistent with the observations of Sacia et al. [23], who showed low activity of these catalysts in the trimerization of methyl ketones at similarly low temperatures.

Table 5: Alternative metal catalysts for the ABE condensation reaction. Reaction condition: 4.6 mmol acetone, 7.4 mmol butanol, 2 mmol ethanol, 350 mg 2% M/HT catalyst. Reaction time 2 hours, 523 K. *Pt catalyst was tested with BuOH as solvent.

Entry[a]	A	B	C	D	E	F	Total Alcohols	Overall Yield
RuHT	3.4	20.1	2.9	0.2	10.7	-	5.4	42.7
NiHT	0	5.7	-	-	-	-	-	5.7
CoHT	-	-	-	-	-	-	-	<0.5
PdHT	1.1	7.1	5.6	0.5	18.6	-	25.7	58.6
PtHT*	1.3	7.3	4.9	0.5	13.8	-	26.4	54.2
PdCuHT	5.2	25.9	9.7	1.1	24.7	-	2.5	69.1

Furthermore, we examined a range of different metals for the dehydrogenation part of the chemistry; Pd, Co, Ni, Ru, and Pt were examined as possible catalysts. The results of this investigation are shown in

Table 5. Ni and Co catalysts were inactive, possibly because they cannot be reduced by the alcohols at the reaction temperature. Even after treatment of the Ni and Co catalysts under a hydrogen atmosphere, they were not active for the reaction; this indicates that the alcohols are not able to remove the passivation oxide layer formed over the catalyst, in the case of Ni. On the other hand, Co catalysts were either not reduced, or possibly reoxidized upon exposure to air. On the contrary, Pd followed by Pt, seemed to give the best results. Pt also showed high selectivity to alcohols. Since the reduction of the ketones to the alcohols requires an extra equivalent of hydrogen, the increased selectivity to alcohols suggests the presence of a side reaction. Given the fact that no esters were detected in the products of the reaction, this observation suggests extensive decarbonylation of the alcohol, in order for the hydrogen balance to close. This is consistent with the fact that Pd, and especially Pt, are known C-C bond scission catalysts, used for oxygenate reforming [13] and the decarbonylation of furfural [24]. For this reason, we did not pursue the investigation of PtHT catalysts any further.

OPTIMIZATION

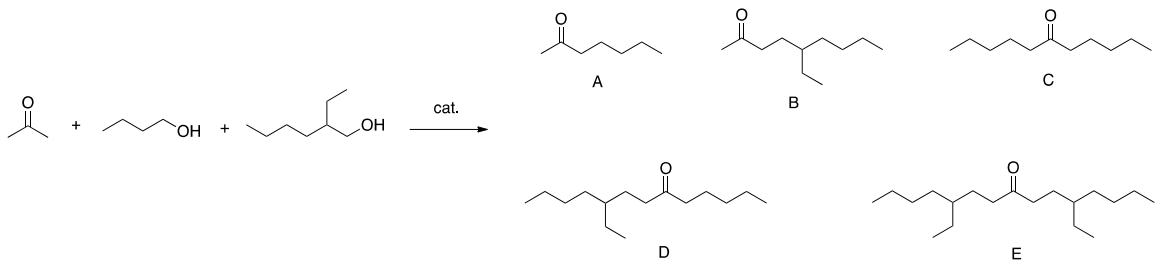

Scheme 3: Condensation of acetone with butanol and 2-ethylhexanol.

The formation of ketone products with a carbon chain longer than C_{11} is desired, since diesel fuel tends to have hydrocarbons from C_{10} to C_{22}, with a peak around C_{16}.

In our previous work, we used IBE instead of ABE fermentation to achieve higher product molecular yields in one pot. On the other hand, butanol and ethanol dimerization has been extensively researched in the literature and there exist a number of strategies for butanol dimerization to 2-ethylhexanol. Conceivably, after separation of the ethanol and butanol from acetone, they could be reacted over one of these catalysts to yield a mixture of butanol and 2-ethylhexanol. The dimers can in turn be in turn reacted with acetone, using the existing catalysts for ABE condensation, to form C_{11+} products (Scheme 3).

To this end, we carried out the aldol condensation reaction using acetone, butanol and 2-ethylhexanol as reactants. In these reactions, we used a 1:1.2:1.2 ratio between acetone, butanol and 2-ethylhexanol. This was based on the assumption that ethanol would completely dimerize to butanol and that 50% of the butanol would dimerize to 2-ethylhexanol. As can be seen in Table 6, high yields were achieved over short reaction times, with high selectivity to the C_{15} ketone product, and low selectivity to the C_7 product. Moreover, TiO_2 appeared to have a promotional effect on the yields, increasing the yield of ABE condensation products and shifting the selectivity to higher products.

Table 6: Percent yields for catalysts in the condensation of acetone with butanol and 2-ethylhexanol. 513 K, 1 mmol acetone, 1.2 mmol butanol, 1.2 mmol 2-ethylhexanol, 350 mg catalyst

Entry	Catalyst	A	B	C	D	E	Total
1	CuHT	29.4	5.4	7.6	2.2	0.1	46
2	PdHT	15.6	5.8	23.1	11.6	1.5	58
3	PdCuHT	20.3	6.9	24.0	12.0	1.5	65
4	PdCuHT + TiO_2	3.1	3.2	21.2	30.3	11.4	71

KINETICS

In order to understand the mechanism of the ABE reaction over the M/HT catalysts, kinetics of ABE condensation reactions over HT, PdHT and CuHT catalysts were investigated. In order to probe the intrinsic reactivity of these catalysts, we used a gas-phase flow reactor.

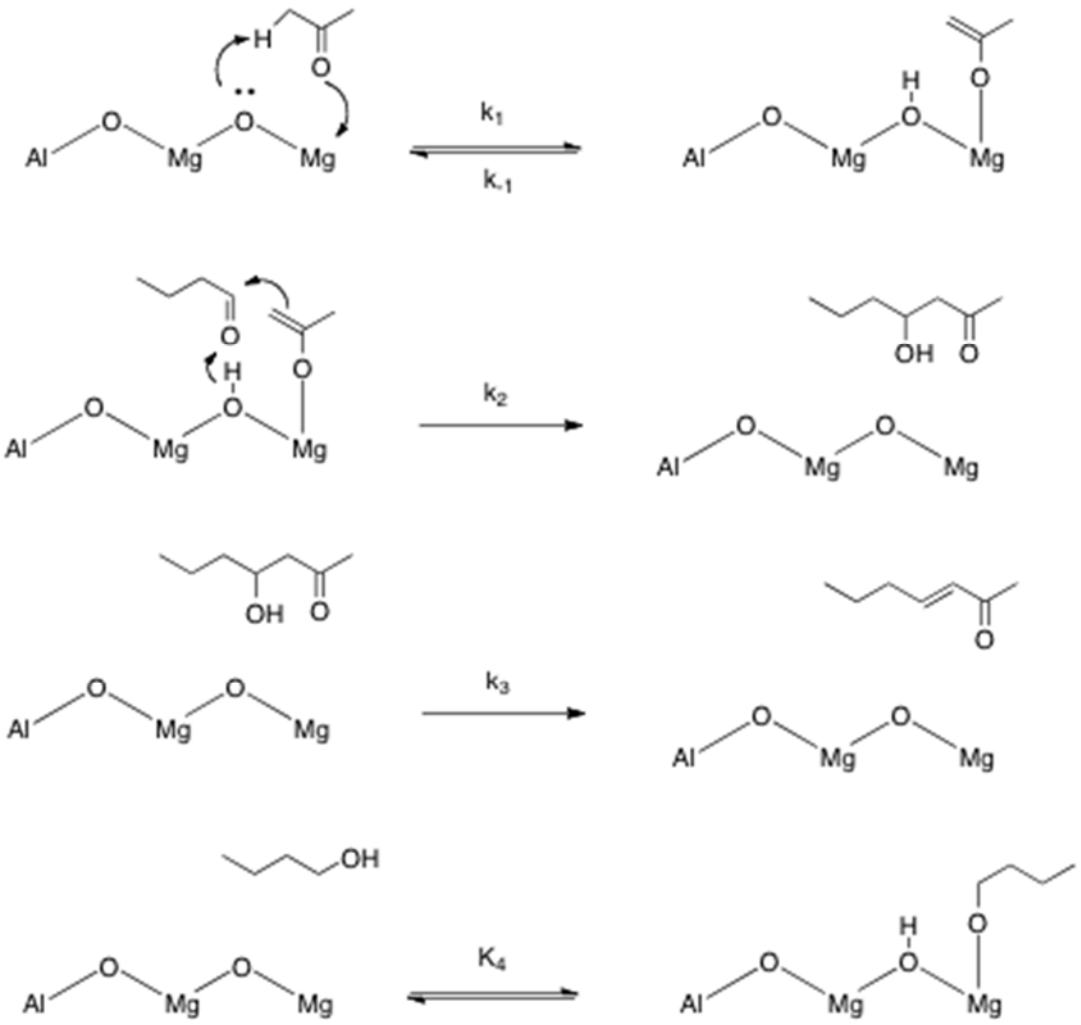

Scheme 4: Condensation of acetone and butyraldehyde over a MgAlO surface.

Transition-metal-free HT catalysts were used to study the mechanism of the aldol condensation. When acetone and butanol were flowed over the catalyst, the cross-coupling product yield at steady state was very low and the effluent was composed mainly of acetone coupling and oligomerization products. This suggests that the transfer (Meerwein-Ponndorf-Verley [25]) hydrogenation from the butanol to the acetone is much slower than the formation of the C-C bond. On the contrary, when the butanol feed was spiked with 5 wt.% butyraldehyde, the main product was the cross-coupling product, 3-hepten-2-one. This reflects the fact that butyraldehyde is a much stronger electrophile than acetone. As a result, the enolate formed from acetone reacts with butyraldehyde much faster than with acetone.

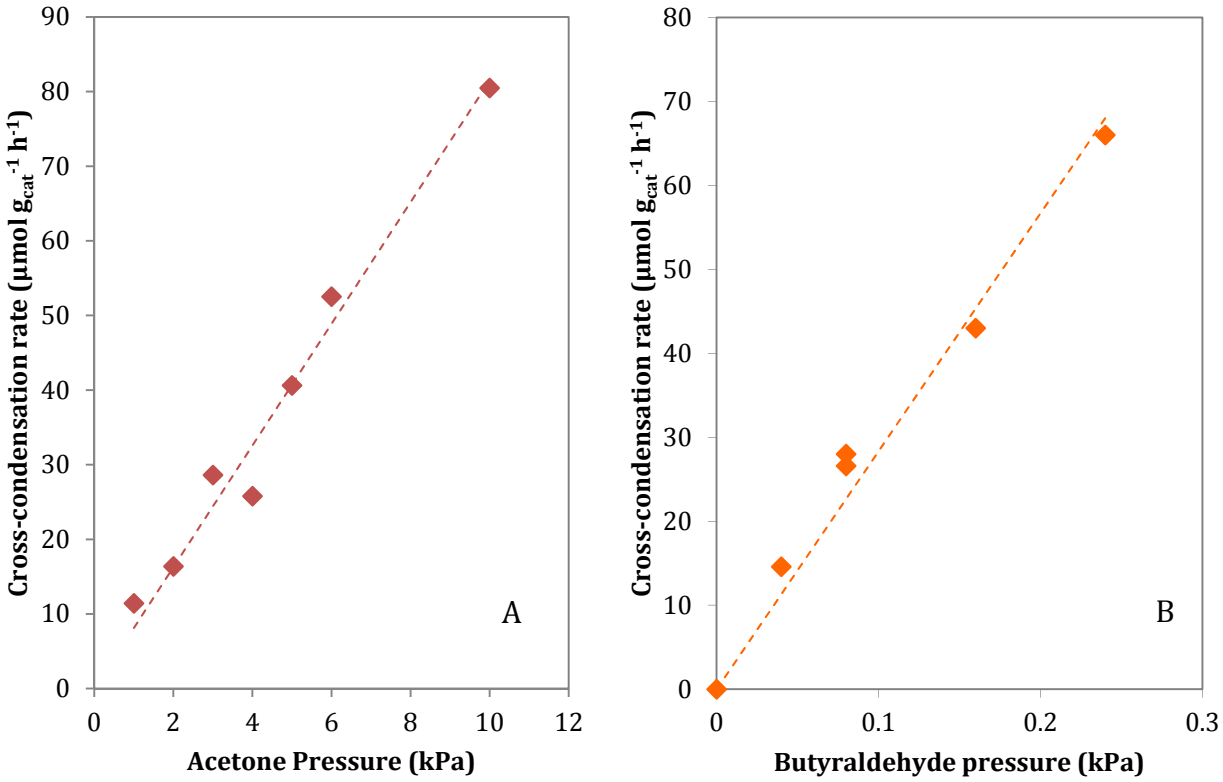

Figure 3: Dependence of cross-condensation rate on acetone pressure and butyraldehyde pressure.

Aldol condensation reactions over basic catalysts are generally believed to take place *via* the abstraction of a proton in the position alpha to the carbonyl to form an enolate, followed by an attack of the electron-rich enolate onto the electrophilic carbonyl carbon. Based on the regioselectivity of the ABE products, we concluded that the enolate is formed only from the acetone. Consistent with this hypothesis, the rate of the coupling reaction between acetone and butyraldehyde showed a first-order dependence on acetone (figure 3A). The dependence on butyraldehyde was also first-order (figure 3B). These observations indicate that the enolate formation step is reversible; an irreversible enolate formation step would result in an aldol condensation rate independent of butyraldehyde pressure. Moreover, the observed KIE with d6-acetone (k_H/k_D = 2.4) indicates that the rate-determining step for the aldol condensation involves the activation of a C-H or O-H bond, and cannot involve the the C-C bond formation between the acetone enolate and butyraldehyde. Since the α-C-H bond activation in acetone has been ruled out as the rate-determining step (the enolate formation step being equilibrated), this observation suggests that the rate-determining step for the aldol condensation is the dehydration of the hydroxy ketone. An alternative explanation for these observations is the proton transfer from the surface to the ketol in the second step is rate-determining for the aldol condensation. In order to distinguish between those two possibilities, we prepared the ketol ex-situ and fed it over the HT catalyst. No ketol was detected in the effluent of the reactor, which indicates that the ketol was rapidly decomposed over the catalyst, thereby ruling this out as a rate-determining step. As such, we

conclude that the rate determining step of the aldol condensation is the concerted C-C bond formation and abstraction of a proton from the surface.

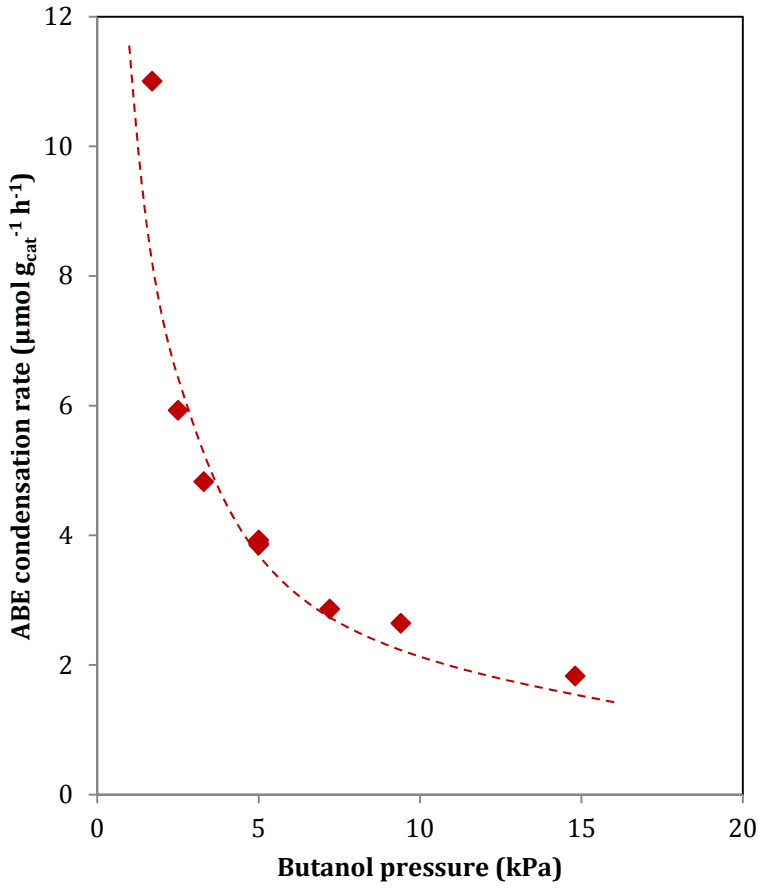

Figure 4: Effects of butanol pressure on aldol condensation rate. Gas-phase flow reactor, 0.4 kPa butyraldehyde, 2 kPa acetone, 2.5% Cu/HT catalyst, 473 K.

Our experiments also indicate that butanol adsorbs competitively to acetone on the catalyst surface. At a constant acetone and butyraldehyde pressure, we observed a reduction of rates as butanol pressure increases. This is consistent with earlier reports, which describe a dissociative adsorption of alcohols over metal oxide surfaces to form alkoxides [26]. This way, unreactive alcohols compete for surface sites with the reactive ketones and aldehydes. In order to check for the consistency of our model, we tried to fit a Langmuir-Hinshelwood rate law on the dependence of the reaction rate on the butanol. From figure S 6, one can see that the inverse rate is proportional to the butanol pressure, which is consistent with a Langmuir-Hinshelwood rate model, in which the butanol competitively adsorbs on surface sites.The apparent activation energy for the aldol condensation reaction over HT is 27 kJ mol^{-1}, as can be seen from the slope of figure S 7.

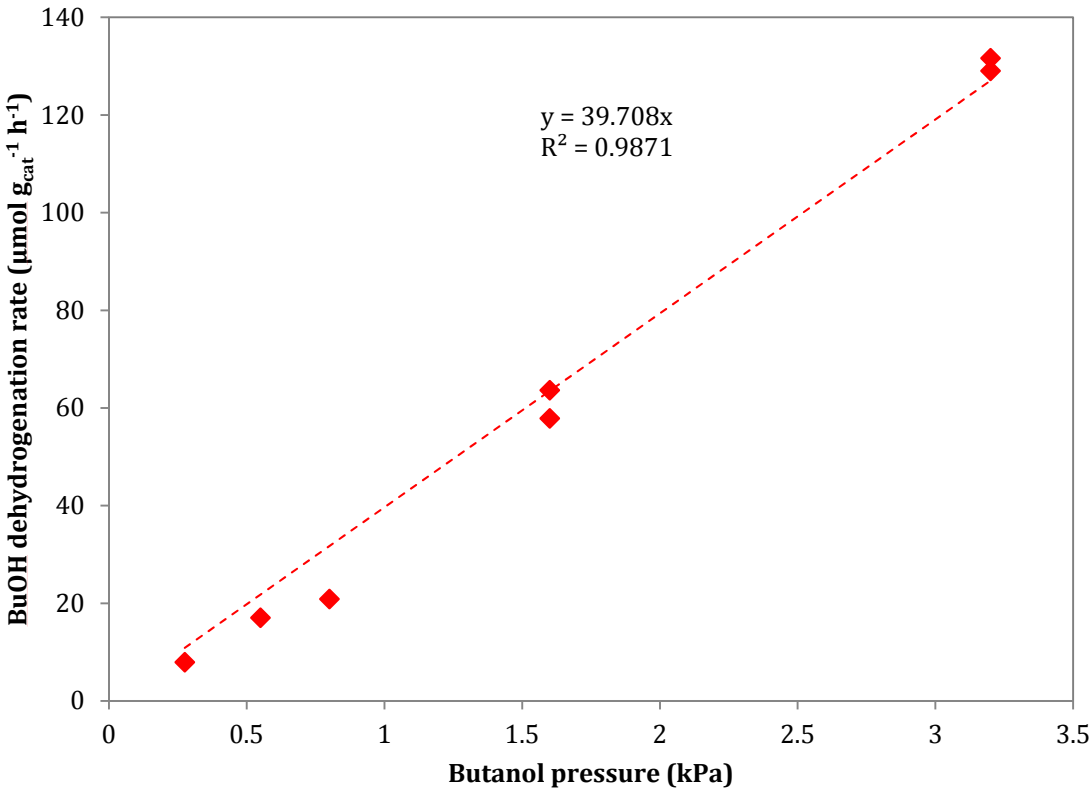

Figure 5: Dependence of butanol dehydrogenation on butanol pressure. 2.5% Cu/HT IWI, 473 K, 2.5 kPa acetone, balance He.

For the CuHT catalysts, we studied a representative 2.5% Cu/HT catalyst. The butanol dehydrogenation rate is proportional to the butanol partial pressure at the low-pressure regime. This is consistent with an earlier report for isopropanol dehydrogenation over Cu/C catalysts, in which Rioux and Vannice [27] suggested that the rate-determining step for alcohol dehydrogenation over Cu surfaces is the O-H bond activation. In order to test this hypothesis, we compared the dehydrogenation rates for butanol and butanol-OD. We observed a KIE equal to 1.1, which is inconsistent with an O-H bond scission as the rate-determining step. This suggests that the C-H bond activation is the rate-determining step for the dehydrogenation of butanol on Cu surfaces. This is consistent with the TPD studies of Bowker and Madix, who showed that O-H activation and alkoxide formation occurs over Cu surfaces at low temperatures, as opposed to C-H bond activation, which occurs at higher temperatures [28, 29].

From the slope of figure S 8, we observe that the apparent activation energy for this reaction is 64 kJ mol^{-1}. This is consistent with earlier kinetic models that predict an alcohol binding energy equal to -6.8 kcal mol^{-1} and an intrinsic activation energy of 22.6 $kcalmol^{-1}$ for isopropanol [27].

In the case of the Pd/HT catalysts, we observe a lower apparent activation energy for the dehydrogenation reaction, equal to 38 kJ mol^{-1}. The ratio of dehydrogenation

to decarbonylation is much more sensitive to temperature, yielding an apparent activation energy of 80 kJ mol^{-1} (figure S 6). Also, at 473 K, the rate of butanol dehydrogenation is independent of pressure at this pressure range, which suggests that the surface is covered by species deriving from butanol. These species could be the butoxides that result from the O-H bond scission or alkyl and formyl fragments from the C-C bond scission that leads to decarbonylation.

CATALYST DESIGN-BIMETALLIC CATALYSTS

In order to combine the high rates of PdHT catalysts with the selectivity of the CuHT catalysts, we made bimetallic versions of these catalysts, supporting mixtures of Cu and Pd onto the hydrotalcite structure. Substituting Cu in Pd-based catalysts has been shown to reduce decarbonylation [30]. In a liquid-phase batch reactor, high yields were achieved with short reaction times, as can be seen in

Table 5.

However, as can be seen from Table 7, the decarbonylation of the aldehydes persisted; the ratio of decarbonylation to aldol condensation did not change appreciably. A possible reason for this behavior is that, at these low Cu mass fractions, the Cu is being trapped inside the structure and is unavailable for reaction, as was the case in CuHT (vide supra).

Table 7: Effects of the support and the alloying on the reaction rates for ABE condensation. Gas-phase flow reactor, 473 K. Rates and selectivity after 4 h time-on-stream.

Catalyst	Dehydrogenation to decarbonylation ratio	Total ABE condensation rate (μmol g_{cat}^{-1} h^{-1})
Pd/HT	3.7	144
PdCu/HT	5.2	217
PdCu/TiO_2	9.0	745
PdCu/HT-C	36	147
PdCu/HAP	13	195

X-ray absorption spectroscopy was performed on the PdCu/HT catalysts to understand the forms of Pd and Cu present in the material. The X-ray absorption near edge (XANES) structures of these materials after H_2 reduction is presented in Figure 6. At the Pd edge (Fig. 6a), the calcined sample does not resemble the bulk PdO reference – the edge is shifted, and the white line has a feature at 24370 eV that is not present in the bulk PdO, suggesting a different phase. Subsequent H_2 treatment causes reduction (shift in the edge position closer to the foil, decrease in white line intensity), but does not completely reduce the Pd in the sample to the metallic state. Similarly, the spectrum of the calcined PdCu/HT at the Cu edge (Fig. 6b) is different than a bulk CuO reference after calcination, closely resembling a hydrated Cu(II) reference. Following treatment in a H_2/He mixture, the Cu shows

characteristics of reduction (appearance of an edge feature at 8980 eV, decrease in white line intensity at energies above 8990 eV), but also does not reduce completely to metallic Cu.

These observed behaviors differ from those of supported Pd and Cu reduced under H_2 under similar conditions. Alumina-supported Pd and Cu are known to reduce to the metallic form below 573 K, and TPR on bimetallic $PdCu/Al_2O_3$ demonstrated reduction of the components at temperatures below 573 K, with reduction of mixed Pd and Cu clusters at temperatures below 100 °C [31, 32]. This resistance to reduction at typical conditions, combined with the differences in the XANES compared to bulk oxides (PdO and CuO) typically formed from calcination of supported Pd and Cu catalysts, suggests that the irreducible Pd and Cu are trapped within the support structure. Ota et al. [33] have shown that Pd can be incorporated into hydrotalcite-like structures and that this incorporation places Pd^{2+} in a distorted octahedral position and renders it inaccessible for reduction. Additionally, literature reports demonstrate that Cu ions can be incorporated into an MgO crystal lattice to form a $Cu_xMg_{1-x}O$ species [34]. The XANES reported here for Cu/HT and PdCu/HT have similar features to those reported in Hilbrand and Martin for a $Cu_xMg_{1-x}O$ [34]. This indicates that a significant proportion of Cu is trapped inside the structure, as was the case with the CuHT catalysts prepared from coprecipitation (vide supra).

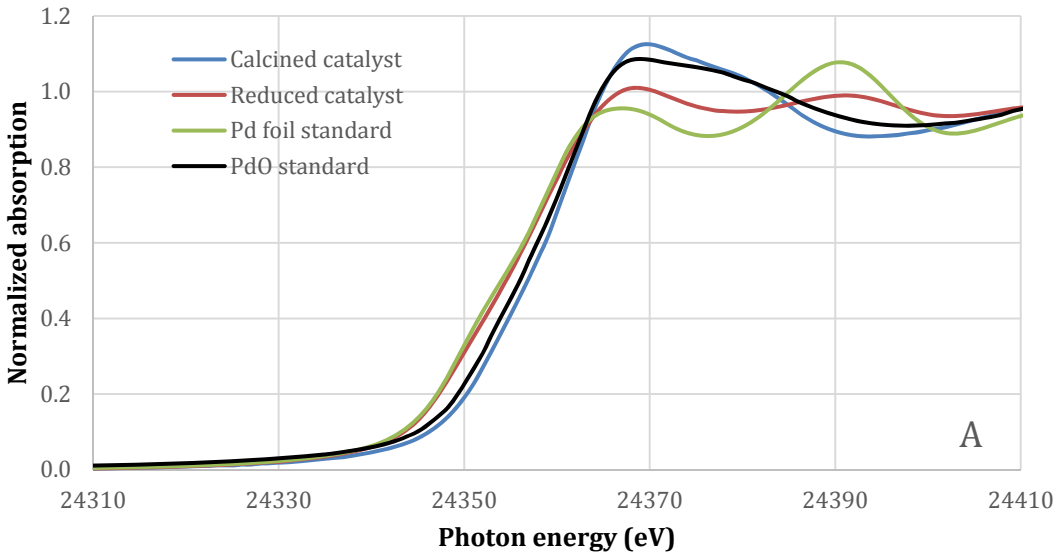

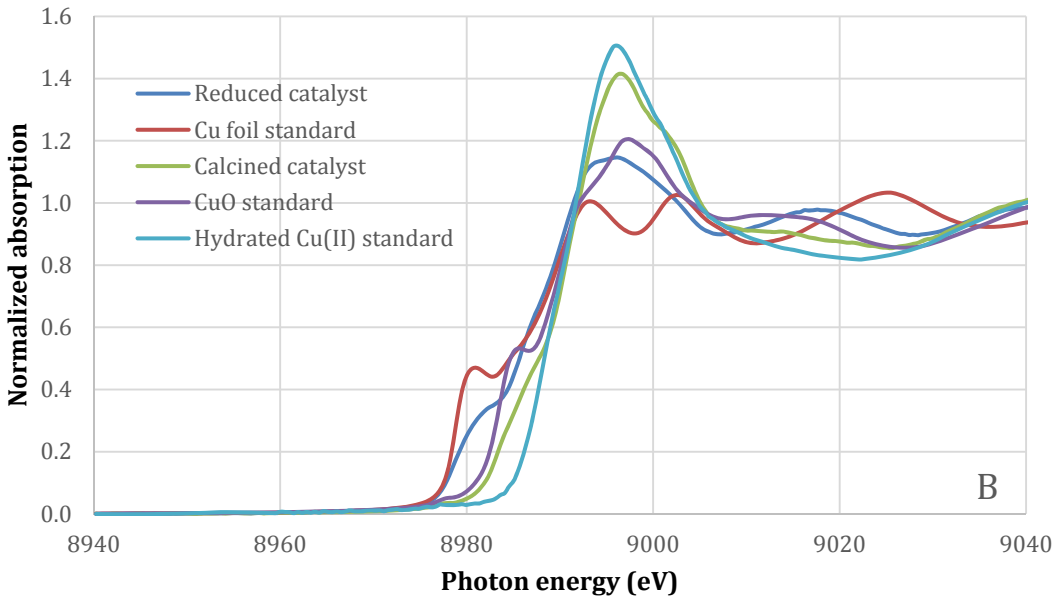

Figure 6: XANES of the Pd edge (A) and the Cu edge (B) of a PdCu/HT catalyst, synthesized by water incipient wetness impregnation and calcined at 823 K in air after calcination and reduction at 523 K.

Contrary to the PdCuHT sample, PdHT is much easier to reduce; the Pd was converted to the metallic form after reduction at 523 K (Fig. S 11), contrary to the PdCu/HT which still showed a fraction of oxidized Pd after an identical pretreatment. This suggests that Cu has a role in increasing the trapping of Pd inside the structure. It is possible that Cu introduces local distortions in the structure, which make the octahedral coordination of Pd more favorable than a purely Mg-Al hydrotalcite structure.

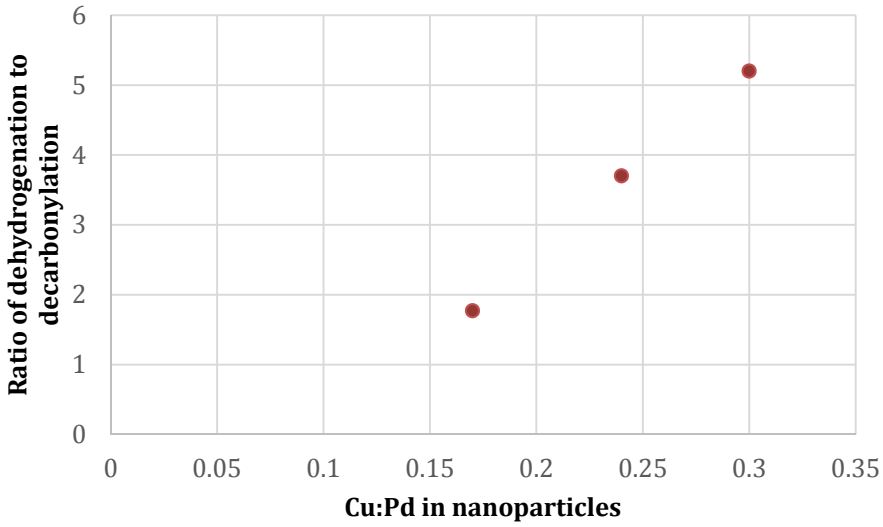

Figure 7: Effects of the Cu:Pd ratio in nanoparticles (as measured by STEM-EDS) on the selectivity of PdCu/MgAlOx catalysts.

A first approach to avoiding trapping was to vary the Mg/Al ratio in the hydrotalcite. This was done in order to ascertain which one of the two elements was responsible for the trapping. In these experiments, the selectivity ratio peaks at 5.2 around an Al fraction equal to 0.25. This is consistent with the maximum Cu/Pd ratio in the PdCu nanoparticles, as determined by TEM-EDS. This observation showed that increasing the alloying increased the selectivity to dehydrogenation over decarbonylation. Interestingly, as can be seen in figure 7, the trend of the ratio of dehydrogenation to aldol condensation with the ratio of Cu/Pd in the nanoparticles extrapolates to negative values. Since there can be no negative reaction rate, this observation suggests that there must be a difference in these catalysts beyond the ratio of the Cu to Pd in the nanoparticles.

Table 8: EXAFS fitting parameters of the metal-metal interactions on the Pd edge for varying PdCu/MgAlOx catalysts. The Pd in the PdCu/$MgAlO_x$ sample was partially oxidized. As a result, the number of fit parameters exceeded the number of data points in the Fourier transform. Because of this, the data were fitted by fixing the distances and the Debye-Waller factor to the average of the two other fits. The oxide percentage was estimated to 29.8% ±4.9% and the Pd-O distance to 2.019 ± 0.017 A

	PdCu/MgO	**PdCu/Mg_3AlO_x**	**PdCu/$MgAlO_x$**
N_{Pd-Cu}	2.057 ± 0.319	1.961 ± 0.411	2.597± 0.363
N_{Pd-Pd}	5.864 ± 0.441	7.476 ± 0.574	5.192 ± 0.434
R_{Pd-Cu} (A)	2.592 ± 0.009	2.589 ± 0.011	2.591
R_{Pd-Pd} (A)	2.700 ± 0.006	2.695 ± 0.006	2.698
σ^2	0.0088 ± 0.0007	0.0088 ± 0.0007	0.0088

A possible reason for these differences is that the MgO sample, which showed the lowest Cu/Pd ratio and lowest selectivity, also shows a lower total coordination number of Pd, based on the EXAFS fitting; while PdCu/Mg_3AlO_x has a Pd coordination number equal to 9.437 ± 0.985, the PdCu/MgO sample has a Pd coordination number equal to 7.921 ± 0.760. The coordination number is correlated to the particle size or the surface segregation of one of the components. Since we know from our TEM results that the size of the nanoparticles is equal in these catalysts, we propose that the reason for this inequality is the fact that the Pd segregates itself to the surface. This way, the Pd-Pd ensembles are not broken by the Cu and the decarbonylation persists.

It is therefore clear that in order to avoid decarbonylation, it is necessary to use a support that does not trap Pd or Cu atoms, so that these are available for reduction and reaction. A possible reason for the extensive trapping of Cu in the MgAlO structure is the fact that Cu^{2+} and Mg^{2+} have similar ionic radii of about 0.73 and 0.72 A, respectively [35]. We would therefore expect a support that shows a chemical or size mismatch to the Cu not to incorporate Cu ions in its structure.

One possibility for achieving this outcome is using carbon as a support, since the bonds in activated carbon are covalent. However, since activated carbon is not a catalyst for the aldol condensation reaction, we support the mixed Mg-Al oxide on the carbon together with the Pd and the Cu. Such an approach has been reported by Winter et al. [36]; they showed that Mg and Al form small particles on the surface. Consistent with these results, our own X-ray diffraction work revealed the existence of small nanoparticles of Mg-Al oxide (approximately 4 nm) and large nanoparticles (average of 24 nm) of Pd and Cu. Moreover, examination of the X-ray absorption spectra showed that Pd and Cu, while supported on HT-modified carbon, are fully reduced after treatment in H_2 at 523 K.

Another approach is to use a support, in which the cation radius is much greater or much smaller than that of Cu^{2+}. Such supports are TiO_2 and hydroxyapatite; the Ti^{4+} ion has an ionic radius of 0.605 A, compared to 0.72 A of Cu. On the other hand, the Ca^{2+} cation in hydroxyapatite is significantly larger (1.03 A) compared to Cu^{2+} As can be seen in figures S 12 onwards, the Cu XANES edge position of the catalyst coincides with that of the Cu foil, thereby confirming that Cu is completely reduced in these samples.

Further confirmation of alloy formation in the HAP, TiO_2 and HT-C supported materials comes from the fitting of the EXAFS oscillations in the Pd edge. In all cases, we note that Pd has Cu atoms in the first shell coordination sphere. We can also see that the ratio of Pd to Cu in the first shell is higher than the nominal 3:1 ratio, ranging from 3.8 to 6. This observation is suggestive of segregation of Cu from Pd. Cu could be forming individual Cu or CuOx nanoparticles or segregating itself to the surface of the nanoparticles. Formation of individual Cu nanoparticles can be ruled out based on the observation that no ester formation is detected during catalysis. Formation of Cu oxides can also be ruled out based on the Cu XANES for the catalysts; the Cu in all catalysts apart from PdCu/HT is fully reduced to the metallic state. This suggests that Cu segregates itself to the surface of the nanoparticles. This is consistent with our investigations into the fundamentals of PdCu alloying, which showed that Cu segregates itself to the surface of PdCu nanoparticles and prevents decarbonylation by breaking up the Pd-Pd ensembles necessary for decarbonylation.

Table 9: EXAFS fitting of the Pd edge of various PdCu catalysts.

	PdCu/HT	PdCu/TiO_2	PdCu/HAP	PdCu/HT-C	Pd foil
Pd-Pd distance	2.679 ± 0.012	2.675 ± 0.003	2.690 ± 0.004	2.689 ± 0.002	2.692± 0.002
Pd-Cu distance	2.607 ± 0.013	2.608 ± 0.010	2.603 ± 0.012	2.605 ± 0.006	-
Pd-O distance	2.006 ± 0.022	-	-	-	-
Pd coordination number	5.93 ± 0.97	8.46 ± 0.32	8.48 ± 0.44	8.76 ± 0.30	12
Cu coordination number	2.85 ± 0.77	1.64 ± 0.22	1.63 ± 0.32	2.30 ± 0.22	-
O coordination number	3.83 ± 0.79	-	-	-	-
σ^2	0.0071 ± 0.0010	0.0080 ± 0.0004	0.0071 ± 0.0004	0.0075 ± 0.0003	0.0053 ± 0.0003

The impact of these approaches on the reactivity and selectivity can be seen in Table 7. We can see that the increase in the extent of reduction trends with the increase in the dehydrogenation to decarbonylation rate. Highest rates were obtained when using the TiO_2-supported materials. At the same time, the selectivity seemed to suffer, more decarbonylation products being observed with TiO_2. Such effects may be attributed to the smaller PdCu clusters being formed over the TiO_2 or to increased surface segregation of Pd, as evidenced by the lower coordination numbers obtained in the EXAFS fittings, compared to those of the HT-C and the HAP catalysts [37]. Similar to the results of Pushkarev et al. [24], the coordinatively unsaturated sites in the corners and edges are probably catalyzing decarbonylation over dehydrogenation.

CONCLUSIONS

In this work, we have screened a number of base-supported metal catalysts for the condensation of acetone with butanol and ethanol to form drop-in diesel fuel precursor ketones. Considerable improvements of the reaction rates were achieved by increasing the surface area of hydrotalcite-supported Cu catalysts. Also, we have shown that supporting Cu onto calcined hydrotalcite materials by incipient wetness impregnation gave catalysts that were tuned to give high selectivity to the ABE ketones without extensive formation of undesirable ester byproducts.

Alcohol dehydrogenation rates over the Cu surfaces are proportional to the alcohol pressure and do not show any kinetic isotope effect with butanol-OD. This suggests that the rate-determining step of the dehydrogenation is the C-H bond activation. On the other hand, the aldol condensation of butyraldehyde with acetone proceeds over the HT surface via an equilibrated enolate formation.

Apart from Cu, high rates were also achieved using Pd-based catalysts. However, these catalysts suffered from extensive decarbonylation of the alcohols. This can be overcome by promoting Pd with Cu. In this context, the support plays a significant role in allowing the formation of alloyed nanoparticles and not structure-trapped Cu. Such supports are TiO_2, hydroxyapatite and hydrotalcite-modified carbon. Using the TiO_2 catalysts, industrially-relevant rates can be achieved for the ABE condensation. We expect this to open the path to the industrial utilization of the ABE process in the future.

REFERENCES

[1] P. Anbarasan, Z. C. Baer, S. Sreekumar, E. Gross, J. B. Binder, H. W. Blanch, D. S. Clark and F. D. Toste, "Integration of chemical catalysis with extractive fermentation to produce fuels," *Nature,* vol. 491, pp. 235-239, 2012.

[2] S. Sreekumar, Z. C. Baer, E. Gross, S. Padmanaban, K. Goulas, G. Gunbas, S. Alayoglu, H. W. Blanch, D. S. Clark and F. D. Toste, "Chemocatalytic Upgrading of Tailored Fermentation Products Toward Biodiesel," *ChemSusChem,* vol. 7, no. 9, pp. 2445-2448, 2014.

[3] E. J. Rode, P. E. Gee, L. N. Marquez, T. Uemura and M. Bazargani, "Aldol condensation of butanal over alkali metal zeolites," *Catalysis Letters,* vol. 9, no. 1, pp. 103-113, 1991.

[4] C. A. Hamilton, S. D. Jackson and G. J. Kelly, "Solid base catalysts and combined solid base hydrogenation catalysts for the aldol condensation of branched and linear aldehydes," *Applied Catalysis A: Environmental,* vol. 263, no. 1, pp. 63-70, 2004.

[5] P. Putanov, E. Kis, G. Boskovic and K. Lázár, "Effects of the method of preparation of MgC_2O_4 as a support precursor on the properties of iron/magnesium oxide catalysts," *Applied Catalysis,* vol. 73, no. 1, pp. 17-26, 1991.

[6] M. J. Climent, A. Corma, S. Iborra and A. Velty, "Activated hydrotalcites as catalysts for the synthesis of chalcones of pharmaceutical interest," *Journal of Catalysis,* vol. 221, no. 2, p. 474–482, 2004.

[7] C.-C. Wang and J. Ying, "Sol–Gel Synthesis and Hydrothermal Processing of Anatase and Rutile Titania Nanocrystals," *Chemistry of Materials,* vol. 11, no. 11, p. 3113–3120, 1999.

[8] K. Wang, G. J. Kennedy and R. A. Cook, "Hydroxyapatite-supported $Rh(CO)_2(acac)$ (acac = acetylacetonate): Structure characterization and catalysis for 1-hexene hydroformylation," *Journal of Molecular Catalysis A: General,* vol. 298, no. 1-2, pp. 88-93, 2009.

[9] P. C. Zonetti, J. Celnik, S. Letichevsky, A. B. Gaspar and L. G. Appel, "Chemicals from ethanol – The dehydrogenative route of the ethyl acetate one-pot synthesis," *Journal of Molecular Catalysis A: Chemical,* vol. 334, p. 29–34, 2011.

[10] K. Inui, T. Kurabayashi and S. Sato, "Direct Synthesis of Ethyl Acetate from Ethanol Carried Out under Pressure," *Journal of Catalysis,* vol. 212, no. 2, pp. 207-215, 2002.

[11] N. Iwasa and N. Takezawa, "Reforming of Ethanol –Dehydrogenation to Ethyl Acetate and Steam Reforming to Acetic Acid over Copper-Based Catalysts," *Bulletin of the Chemical Society of Japan,* vol. 64, no. 9, pp. 2619-2623, 1991.

[12] D. A. Simonetti, E. L. Kunkes and J. A. Dumesic, "Gas-phase conversion of glycerol to synthesis gas over carbon-supported platinum and platinum-

rhenium catalysts," *Journal of Catalysis,* vol. 247, no. 2, pp. 298-306, 2007.

[13] G. W. Huber, R. D. Cortright and J. A. Dumesic, "Renewable Alkanes by Aqueous-Phase Reforming of Biomass-Derived Oxygenates," *Angewandte Chemie International Edition,* vol. 43, no. 12, pp. 1549-1551, 2004.

[14] D. Debecker, E. Gaigneaux and G. Busca, "Exploring, Tuning, and Exploiting the Basicity of Hydrotalcites for Applications in Heterogeneous Catalysis," *Chemistry: A European Journal,* vol. 15, no. 16, pp. 3920-3935, 2009.

[15] V. Rivas and S. Kannan, "Layered double hydroxides with the hydrotalcite-type structure containing Cu^{2+}, Ni^{2+} and Al^{3+}," *Journal of Materials Chemistry,* vol. 10, no. 2, pp. 489-495, 2000.

[16] K. Christensen, D. Chen, R. Lødeng and A. Holmen, "Effect of supports and Ni crystal size on carbon formation and sintering during steam methane reforming," *Applied Catalysis A: General,* vol. 314, no. 1, pp. 9-22, 2006.

[17] S. Galvagno, C. Crisafulli, R. Maggiore, A. Giannetto and J. Schwank, "TPR Investigation of bimetallic Ru-Cu samples supported on SiO_2, Al_2O_3 and MgO," *Journal of Thermal Analysis,* vol. 32, no. 2, pp. 471-483, 1987.

[18] G. Zhang, H. Hattori and K. Tanabe, "Aldol Addition of Acetone, Catalyzed by Solid Base Catalysts: Magnesium Oxide, Calcium Oxide, Strontium Oxide, Barium Oxide, Lanthanum (III) Oxide and Zirconium Oxide," *Applied Catalysis,* vol. 36, pp. 189-197, 1988.

[19] G. Natta and R. Rigamonti, "Studio roentgenografico e chimico dei catalizzatori usati per la produzione del butadiene dall'alcool," *Chimica e Industria,* vol. 29, pp. 239-245, 1947.

[20] J. I. Di Cosimo, V. K. Díez and C. R. Apesteguía, "Base catalysis for the synthesis of α,β-unsaturated ketones from the vapor-phase aldol condensation of acetone," *Applied Catalysis A: General,* vol. 137, no. 1, pp. 149-166, 1996.

[21] W. Shen, G. A. Tompsett, R. Xing, W. C. Conner Jr. and G. W. Huber, "Vapor phase butanal self-condensation over unsupported and supported alkaline earth metal oxides," *Journal of Catalysis,* vol. 286, pp. 248-259, 2012.

[22] J. T. Kozlowski and R. J. Davis, "Heterogeneous Catalysts for the Guerbet Coupling of Alcohols," *ACS Catalysis,* vol. 3, no. 7, pp. 1588-1600, 2013.

[23] E. R. Sacia, B. Madhesan, M. H. Deaner, K. A. Goulas, F. D. Toste and A. T. Bell, "Highly Selective Condensation of Biomass-Derived Methyl Ketones as a Source of Aviation Fuel," *ChemSusChem,* vol. In press, 2015.

[24] V. V. Pushkarev, N. Musselwhite, K. An, S. Alayoglu and G. A. Somorjai, "High structure sensitivity of vapor-phase furfural decarbonylation/hydrogenation reaction network as a function of size and shape of Pt nanoparticles," *Nano Letters,* vol. 12, pp. 5196-5201, 2012.

[25] P. S. Kumbhar, J. Sanchez-Valente, J. Lopez and F. Figueras, "Meerwein–Ponndorf–Verley reduction of carbonyl compounds catalysed by Mg–Al hydrotalcite," *Chemical Communications,* pp. 535-536, 1998.

[26] M. A. Barteau, "Organic Reactions at Well-Defined Oxide Surfaces," *Chemical Reviews,* vol. 96, no. 4, pp. 1413-1430 , 1996.

[27] R. M. Rioux and M. A. Vannice, "Hydrogenation/dehydrogenation reactions: isopropanol dehydrogenation over copper catalysts," *Journal of Catalysis,* vol. 216, no. 1-2, pp. 362-376, 2003.

[28] M. Bowker and R. J. Madix, "XPS, UPS and thermal desorption studies of alcohol adsorption on Cu(110): II. Higher alcohols," *Surface Science,* vol. 116, no. 3, p. 549–572, 1982.

[29] M. Bowker and R. J. Madix, "XPS, UPS and thermal desorption studies of alcohol adsorption on Cu(110): I. Methanol," *Surface Science,* vol. 95, no. 1, p. 190–206, 1980.

[30] S. Sitthisa, T. Pham, T. Prasomsri, T. Sooknoi, R. G. Mallinson and D. E. Resasco, "Conversion of furfural and 2-methylpentanal on Pd/SiO_2 and $Pd–Cu/SiO_2$ catalysts," *Journal of Catalysis,* vol. 280, no. 1, p. 17–27, 2011.

[31] A. Baylet, P. Marécot, D. Duprez, P. Castellazzi, G. Groppi and P. Forzatti, "In situ Raman and in situ XRD analysis of PdO reduction and Pd° oxidation supported on γ-Al_2O_3 catalyst under different atmospheres," *Physical Chemistry - Chemical Physics,* vol. 13, pp. 4607-4613, 2011.

[32] B. J. O'Neill, J. T. Miller, P. J. Dietrich, F. G. Sollberger, F. H. Ribeiro and J. A. Dumesic, "Operando X-ray Absorption Spectroscopy Studies of Sintering for Supported Copper Catalysts during Liquid-phase Reaction," *ChemCatChem,* vol. 6, no. 9, p. 2493–2496, 2014.

[33] A. Ota, E. L. Kunkes, I. Kasatkin, E. Groppo, D. Ferri, B. Poceiro, R. M. Navarro Yerga and M. Behrens, "Comparative study of hydrotalcite-derived supported Pd2Ga and PdZn intermetallic nanoparticles as methanol synthesis and methanol steam reforming catalysts," *Journal of Catalysis,* vol. 293, pp. 27-38, 2012, 293, 27–38.

[34] N. Hilbrandt and M. Martin, "An Extended In Situ Cu–K XAFS and XRD Study on the Site Preference and Valence of Copper Ions in $(Mg_{1-x}Cu_x)O$," *Journal of*

Physical Chemistry B, vol. 103, no. 23, p. 4797–4802, 1999.

[35] R. D. Shannon, "Revised Effective Ionic Radii and Systematic Studies of Interatomic Distances in Halides and Chalcogenides," *Acta Crystallographica,* vol. 32, pp. 751-767, 1976.

[36] F. Winter, A. J. van Dillen and K. P. de Jong, "Supported hydrotalcites as highly active solid base catalysts," *Chemical Communications,* pp. 3977-3979, 2005.

[37] A. I. Frenkel, Q. Wang, S. I. Sanchez, M. W. Small and R. G. Nuzzo, "Short range order in bimetallic nanoalloys: An extended X-ray absorption fine structure study," *The Journal of Chemical Physics,* vol. 138, no. 6, p. 064202, 2013.

Chapter 2: Structural effects of aging in aldol condensation catalysis

INTRODUCTION

In the first chapter of this dissertation, it was shown that alloys of Pd and Cu supported on hydrotalcites and other metal oxides are selective catalysts for the condensation of the ABE mixtures to biodiesel precursor C_7-C_{19} ketones.

However, the possible industrial application of this catalyst system is contingent upon the understanding of the long-term stability of the catalyst [1]. Possible deactivation pathways for metals supported on hydrotalcites and other materials during reaction could include the coking of the catalyst [2], sintering of the metal catalyst [3, 4], structural collapse of the support, leaching of the catalyst [5, 6] and phase change of the support or the metal catalyst [7].

Our approach to understanding the deactivation pathways of the PdCu catalysts tracks changes in the structure and activity of the catalysts over time in batch and flow reaction experiments, in the gas and the liquid phase. This is achieved by means of online monitoring of the product composition of flow reaction, combined with a characterization of the catalysts pre and post-reaction using a variety of experimental techniques, including X-ray diffraction (XRD), X-ray absorption spectroscopy (XAS) and nitrogen physisorption.

MATERIALS AND METHODS

Ion-exchanged Pd and Cu/HT catalysts were obtained by stirring an 1 M aqueous solution of $Pd(NO_3)_2.xH_2O$ or $Cu(CH_3COO)_2.2.5H_2O$ with synthetic hydrotalcite for 1 h at 333 K. The solids were collected by filtration and dried at 373 K [8].

PdCu/HT catalysts were prepared by incipient wetness impregnation of $Pd(NO_3)_2.xH_2O$ and $Cu(NO_3)_2.2.5H_2O$ onto a mixed magnesium-aluminum oxide that was obtained by treatment of a commercial synthetic hydrotalcite sample at 823 K for 4 h (ramp: 1 K min^{-1}) under stagnant ambient air. The resulting material was dried at 373 K and treated under stagnant ambient air at 823 K for 4 h (ramp: 1 K min^{-1}).

HT-C was prepared from incipient wetness impregnation of $Mg(NO_3)_2.6H_2O$ and $Al(NO_3)_3.9H_2O$ onto an activated carbon support (Fisher). The material was subsequently dried at 373 K and treated under flowing He (100 ml min^{-1}) at 823 K for 4 h (ramp: 1 K min^{-1}). PdCu/HT-C catalysts were prepared by incipient wetness impregnation of $Pd(NO_3)_2.xH_2O$ and $Cu(NO_3)_2.2.5H_2O$ onto the HT-C material, followed by drying at 373 K for 24 h and treatment under flowing He (100 ml min^{-1}) at 823 K for 4 h (ramp: 2 K min^{-1}). The PdCu/HT-C catalysts were then reduced under H_2 flow (100 ml min^{-1}) at 523 K for 2 h (ramp: 2 K min^{-1}).

PdCu/TiO_2 catalysts were prepared by incipient wetness impregnation of $Pd(NO_3)_2.xH_2O$ and $Cu(NO_3)_2.2.5H_2O$ onto a TiO_2 material. Those materials were prepared by hydrolysis of

a solution of titanium isopropoxide in ethanol, by slow addition of a water-ethanol mixture and aging for 16 h [9]. The molar ratio of $Ti(OiPr)_4$ to water was 1:100. The solids were subsequently filtered and dried in ambient air at 373 K for 24 h. A portion of the solids was treated in ambient air at 723 K for 4 h (ramp: 5 K min^{-1}). Impregnation was carried out on both the treated and untreated portions of the solids and, after drying for 24 h in ambient air at 373 K, the materials were treated in ambient air at 723 K for 4 h (ramp: 5 K min^{-1}). The material prepared from the calcined solids was designated DC-PdCu/TiO_2 (for double calcination) and the material prepared from the dried solids was designated SC-PdCu/TiO_2 (for single calcination).

In all of the above cases, the total transition metal loading was 2.4% by weight and the atomic ratio of Pd to Cu was 3:1.

For batch reactor studies, a quantity of 100-400 mg of PdCu-based catalyst, 908 μl of ABE mix (a 1:3:6 mixture of ethanol, acetone and butanol by mass, corresponding to the ratio produced by Clostridium acetobutylicum [10]) and approximately 100 μl of dodecane (internal standard) were loaded into a Qtube, which was sealed and heated to 513 K under stirring. After the reaction, the reaction mixture was cooled to room temperature and diluted with tetrahydrofuran. An aliquot of the mixture was analyzed by gas chromatography and the spent catalysts were subsequently removed by centrifugation and dried prior to further analysis.

In gas-phase flow reactor studies, about 300 mg of catalyst were placed on a quartz frit (ID = 8 mm) in the inside of a tubular reactor with plug-flow hydrodynamics. The catalyst was pretreated for 1 h at 523 K under a 50% H_2/He mixture flowing at 100 ml/min and subsequently cooled down to the reaction temperature. Following that, a gas mixture consisting of He and ABE mix (total organic component pressure: 15 kPa) was passed over the catalyst at a temperature of 473 K. The reactor effluent was analyzed by online gas chromatography, using a Shimadzu GC 2014, which was equipped with an HP-1 capillary column and a flame ionization detector.

The liquid-phase plug-flow reactor setup consists of an HPLC pump (Waters 515), transfer lines, a reactor and a back-pressure regulator. The reactor is a 6.35 mm OD stainless steel tube and the catalyst is placed inside it on a stainless steel frit. The pressure inside the reactor was kept above the bubble point of the mixture at the reaction temperature (513 K) using a dome-loaded back pressure regulator (Swagelok) or a spring-loaded valve (Swagelok). The effluent of the reactor was collected, diluted with tetrahydrofuran and analyzed by GC/MS offline, using a Varian CP 3800 gas chromatograph, equipped with VF-5ms columns.

Liquid-phase longevity experiments were conducted using 1.5 g of catalyst and a flow rate of 0.1 ml/min, for a WHSV of 4 ml/g_{cat}h.

X-ray diffraction measurements were obtained using a Bruker D8 diffractometer. Samples were placed on a sample stage under ambient air and the diffractograms were obtained at a rate of $2\theta = 0.02^{o}$/min from $2\theta = 20$ to 60 degrees. Nitrogen physisorption isotherms were obtained using a Micromeritics TriStar 3000 instrument at 77 K and the results quantified

using the BET and BJH formalisms for surface area and pore size distributions, respectively. X-ray absorption measurements were performed at the Advanced Photon Source of the Argonne National lab, in transmission mode, at the Pd and Cu edges.

RESULTS AND DISCUSSION

Figure S 1 shows the changes in crystal structure during the course of the preparation of the materials, as indicated by the X-ray diffractograms. The peak at $2\theta = 43.1^{o}$ suggests that the calcined materials, both before and after metal impregnation, have the cubic periclase structure. In contrast, before calcination, the metal-impregnated material showed the lamellar hydrotalcite structure. This is consistent with the "hydrotalcite memory effect", in which the calcined metal oxide reverts to the lamellar hydrotalcite structure upon exposure to water vapor or to liquid water [11, 12]. On the other hand, ion-exchanged hydrotalcites retain their lamellar structure after the ion-exchange process.

We recently reported high diesel precursor yields from acetone-butanol-ethanol (ABE) and isopropanol-butanol-ethanol (IBE) mixtures over ion-exchanged CuHT and PdHT catalysts [8]. However, small losses in activity were observed with each renewed reaction cycle. In order to understand the phenomena that cause this activity loss, the CuHT ion-exchanged catalysts were tested over a range of reaction times, and the spent catalysts characterized.

Ion-exchanged hydrotalcite catalysts retained the lamellar brucite structure before and after reaction (figure 1). At the same time, the surface area of the spent catalysts increased from 6 m^2/g to 26 m^2/g in the first six hours of the reaction. This increase in surface area could result from reaction products dissolving components of the hydrotalcite structure or the hydrotalcite structure being forced apart by either the reactant alcohols or the water produced during the reaction. In order to test these hypotheses, the same experiment was conducted with the equivalent PdHT material. This material did not show any changes of surface area as a result of the reaction. This observation suggests that products specific to the Cu catalysts are responsible for the observed change in surface area. Given that Cu catalysts produced a large quantity of ester, it is possible that the esters hydrolyze to acids, which in turn attack the structure and form soluble magnesium acetate. As a result, parts of the structure dissolve, increasing the specific surface area of the structure, but rendering the use of ion-exchange materials impractical as aldol condensation catalysts. This is also consistent with the "wormholes" observed in the structure of the spent catalyst using transmission electron microscopy [8]. It is also consistent with the fact that there are no changes in the diffraction line position; such a shift would have indicated a change in lattice spacing due to intercalation. Instead, the diffraction lines become broader, suggesting that the domain size becomes smaller, due to the leaching.

On the other hand, in the case of calcined catalysts, the surface area of monometallic Pd/HT and bimetallic PdCu/HT catalysts decreased as the batch reaction time increased (figure 3 and figure S 3). Also, the X-ray diffraction data (figures 4 and S 4) suggests the catalyst partially changed structure, from the cubic periclase structure, to the lamellar hydrotalcite structure, which generally has a lower surface area [12]. Diffraction patterns of spent

catalysts also tend to show a broad peak centered on 2θ = 38 degrees. It is possible that this broad peak corresponds to an amorphous hydrated magnesium-aluminum oxide phase.

Apart from changes to the oxide support structure, the aging of the catalyst influenced the metal as well. Post-reaction characterization of the intrinsic selectivity of the spent catalyst in a gas-phase flow reactor revealed stark differences between different reaction times. As the reaction time in the liquid phase increased, the selectivity of the PdCu/HT catalyst to the dehydrogenation pathway increased (figure 5). This effect correlates with increased alloying and reducibility of the spent catalysts, based on TEM and EXAFS data (figures 6 and 7, respectively). The former reveals collocation of Pd and Cu in the nanoscale, while the latter shows

In the previous chapter of this work, it was shown that increased alloying and reducibility suppressed deactivation and increased selectivity to the dehydrogenation. However, it could also be due to changes in the PdCu particle size; increased particle size could lead to lower decarbonylation selectivity, in a manner analogous to the observations of Pushkarev et al., who reported increased hydrogenation to decarbonylation ratios for the reaction of furfural over Pt nanoparticle catalysts [13]. In order to distinguish between the two, experiments using the spent Pd/HT catalysts were conducted. Their behavior was almost indistinguishable from the PdCu/HT catalysts. This suggests that the increased alloying is not the dominating reason for the selectivity shifts. Instead, this observation is consistent with particle size effects as the main reason for the increased selectivity.

PdCu/MgO catalysts showed similar behavior. However, the observed loss of surface area during the reaction was sharper (figure 3). Also, contrary to the HT catalyst, a complete loss of the cubic periclase structure was observed within about three hours of reaction, as evidenced by the disappearance of the peak centered on $2\theta = 43.1^{o}$, and the appearance of the layered brucite structure (figure 8). The absence of the broad peak centered around 38 degrees, as was the case in PdCu/HT catalysts, suggests that this peak is due to a poorly crystalline Mg-Al oxide or hydroxide.

The structural transition in the MgAlO materials has been attributed to the formation of water during the reaction and the reaction of this water with the $Mg_6Al_2O_9$ oxide to form the lower-surface-area lamellar structure. In this sense, the observation that structures containing aluminum show less of this transition points to the stabilizing role of aluminum as an additive in the mixed metal oxides.

Further evidence towards the stabilizing role of Al in the Mg-Al oxides can be found in the gas-phase reaction data. In this case, the deactivation observed over a 10-day experiment over a PdCu/HT catalyst (figure 9) was primarily due to the formation of coke. This conclusion is supported by the observation that there is no change in the structure of the catalyst before and after reaction, based on the fact that no new peaks appeared in the X-ray diffractogram and the existing peaks were not broadened (figure S 4). On the contrary, the surface area of the catalyst decreased from 196 m^2/g to 17.9 m^2/g. Together with the surface area loss, a shift of the pore distribution to larger pore sizes was observed, suggesting that the support pores are blocked by carbonaceous deposits from the oligomerization of aldehydes, ketones and other unsaturated species from the ABE mixture [2]. Decreasing the

ratio of aluminum to magnesium in the hydrotalcite resulted in higher rates, but also increased the deactivation rate constant (figure 10). This is consistent with the observation of earlier researchers [14], who reported increased basicity of MgAl oxides with increasing Mg:Al ratio, and suggests that the role of aluminum is structural and not catalytic.

Liquid-phase flow reactor experiments showed an initial drop in reactivity, followed by a steady state for the PdCu/HT catalyst (figure 11). This loss in activity was also accompanied by increased formation of unsaturated products, as evidenced by the GC data. Post-reaction characterization of the spent catalyst revealed a loss of surface area. Also, the X-ray diffraction pattern of the spent PdCu/HT catalyst showed a sharp peak for PdCu. This data suggests metal nanoparticle agglomeration during reaction and is consistent with the batch reaction observation that the selectivity increases with increasing reaction time. Also, this agglomeration and loss of surface area is likely responsible for the increased selectivity to unsaturated products at steady state, compared to the initial data points. Hydrotalcite phase changes were minimal compared to those of the batch reactor experiments. This could be attributed to the low conversion (below 20% conversion of acetone, compared to more than 50%), which results in relatively small amounts of water being produced. The loss in surface area and activity is therefore probably due to coking of the catalyst.

It is worth noting the stark difference between liquid-phase and gas-phase reactions in terms of the extent of coking. We observe that there is approximately a 90% loss of surface area due to coking during gas-phase experiments, as opposed to about 50% loss of surface area and activity in the case of the liquid-phase experiments (figure 11). Given that the conversion is similar and that the reactant fugacity is much lower in the gas phase, the faster formation of coke precursors is likely not the reason for the higher deactivation rate in the gas phase. A possible reason for the lesser amounts of coke-induced deactivation in the case of the liquid phase reactions is that the butanol/acetone mix acts as a solvent to the coke precursors, washing them off the surface of the catalyst and preventing deactivation. On the contrary, in the gas phase reaction system, heavy coke precursors cannot desorb from the surface of the catalyst, due to their low vapor pressure.

The utility of carbon-supported metal oxide catalysts for C-C bond formation reactions has been shown in the previous chapter of this work, wherein they were shown to increase selectivity to the desired products, but also in the work of other groups [15], in which they seemed to promote the water tolerance of the catalysts. Also, C-supported hydrotalcites have been reported to show increased yields and turnover frequencies compared to unsupported materials when used for the synthesis of methyl isobutyl ketone from acetone [16, 17]. Moreover, Faba et al., have reported high yields for the condensation of acetone with furfural (a process similar to ABE condensation) over C-supported Mg-Zr oxides [18].

However, none of the previous groups has investigated the performance of these catalysts in long-term flow reactor experiments or the mechanisms by which they deactivate. In order to understand the mechanism of deactivation, we undertook a similar series of experiments as for the unsupported HT catalysts.

The liquid-phase batch reaction experiments suggest that the PdCu/HT-C catalysts deactivate over the course of the batch reactions. There is a small loss of surface area and a

significant loss of structure during reaction, as evidenced by the BET measurements and the X-ray diffractograms of the spent catalysts (figures S 5 and 12, respectively). Already from the first hour of the reaction, the peak at $2\theta = 43^{o}$ starts to broaden, indicating a loss of the cubic periclase structure. Longer reaction times result in the complete loss of this structure and its replacement by the lamellar hydrotalcite structure. Also, the metal peaks are lost as well, indicating a restructuring of the metal structure or the leaching of the metal into the solution.

The reason for the loss of the metal peaks could well be an effect of the loss of the hydrotalcite layer. As can be seen from the TEM micrographs (figure 13), the mixed oxide forms a uniform layer on top of the carbon support. The restructuring of this support could result in the loss of the supported metal as well.

Also of note is the fact that the restructuring of the periclase phase in the case of the PdCu/HT-C catalyst is much more complete than the restructuring in the case of the PdCu/HT catalysts. This can be ascribed to the smaller domain size of the periclase in the PdCu/HT-C catalysts. This is consistent with literature reports. Based on in-situ XRD measurements of the rehydration of hydrotalcites, the authors of these studies concluded that the restructuring requires wetting of the surface by water prior to nucleation [19, 20]; smaller domain sizes, as is the case in HT-C compared to HT, have higher surface areas and presumably restructure faster than larger domain sizes. This is also consistent with our own work, in which less crystalline hydrotalcites hydrate faster than more crystalline ones (for a fuller discussion of this topic, see Chapter 3 of this work).

When the PdCu/HT-C catalyst is tested in a liquid-phase flow reactor, the conversion decreases initially and then reaches steady state, at about 10% conversion. This behavior is similar to that shown by the PdCuHT catalyst and could be due to the fact that the water formed initially, when the reaction rates are high, causes the restructuring of the catalyst. This, in turn, results in lower rates and slower water formation, thereby averting further restructuring of the catalyst. This hypothesis is consistent with the fact that the extent of the restructuring of the PdCu/HT-C catalyst is minimal during the liquid-phase reaction (see X-ray diffractogram, figure S 6).

Finally, the study of the PdCu/HT-C catalyst in the gas phase shows extensive deactivation. Based on the lack of structural changes in the catalyst, as evidenced by the XRD, we conclude that the cause of deactivation is coking of the catalyst. The extent of deactivation is much smaller in the case of the PdCu/HT-C catalyst than in the case of the PdCu/HT catalyst. The reason for this is that all of the surface of the pores in the HT catalyst is reactive, while a significant proportion of the HT-C surface is carbon, which is not reactive for aldol condensation. As a result, the blockage of the pores due to coking is less extensive in the C-supported catalyst.

Based on our findings, it is clear that we need to use a catalyst that does not interact with water or acids by restructuring or leaching. ZrO_2 [21, 22] and TiO_2 [2, 23, 24] are water-insoluble oxides that are known to catalyze aldol condensation reactions. Between the two, our choice of TiO_2 is influenced by literature reports of the activity of ZrO_2 for esterification

reactions in the presence of metal catalysts [25, 26, 27] and our own observations for high ABE reaction rates over TiO_2, as reported in the previous chapter.

In this context, we tested two different TiO_2-based catalysts: a doubly-calcined TiO_2 catalyst, whereby the anatase structure is formed before the metal impregnation and a singly-calcined one, in which the metal is impregnated into the xerogel formed after drying the TiO_2 solids after sol-gel synthesis [9].

Both catalysts are comprised of the anatase phase of TiO_2. This is desired, as anatase has been reported as the active phase for aldol condensation reactions [28], as opposed to inactive rutile. A more extensive coverage of the phase dependence of aldol condensation reactions over TiO_2 follows in chapter 5 of this work.

During liquid-phase batch experiments, we observe a small surface area loss for both the singly and the doubly calcined catalysts. This loss is accompanied by a sharpening of the anatase peaks in the case of the singly-calcined catalyst. These observations are consistent with the changes that ZrO_2 [21, 22] and TiO_2 [9, 29] catalysts have been reported to undergo during hydrothermal treatment. However, contrary to literature reports [30], no rutile is formed during the reaction. A possible reason for this is that, contrary to the P25 used in the literature study, no rutile exists in the starting material, thereby preventing growth of the rutile phase out of existing rutile.

The structural changes during reaction do not seem to have detrimental effects on the reactivity of the catalyst, based on a 7-day longevity study performed on the singly calcined catalyst. In this study, the conversion of acetone remains constant at 35% over approximately five days, with both 2-heptanone and 6-undecanone formed. After the reaction, the catalyst showed a loss of surface area, from 111 m^2/g to about 66 m^2/g. At the same time, consistent with the batch reaction experiments, there is a sharpening of the anatase peaks. Based on the batch reaction results and the fact that no rate changes are observed after 24 h on stream, we can conclude that all structural changes take place during those initial 24 h.

CONCLUSIONS

In this work, we have demonstrated the feasibility of the long-term operation of flow reactors for the continuous production of diesel fuel precursor ketones. We have shown that hydrotalcites undergo structural changes during reaction in the liquid phase, from the high-surface-area active periclase phase to the low-surface-area lamellar hydrotalcite structure. The presence of aluminum in the hydrotalcite structure inhibits those structural changes, as well as the extensive coking observed in gas-phase reactions.

From the standpoint of longevity and resistance to phase changes, supporting hydrotalcites on activated carbon does not offer any benefits. On the contrary, we observe much more extensive phase transitions when using hydrotalcites supported on carbon.

Based on the minimal extent of structural transitions during reaction, as well as the fact that the ABE condensation rates remain constant over a period of five days on stream, we conclude that TiO_2-supported PdCu catalysts show the highest promise for use in industrial conditions.

REFERENCES

[1] T. J. Schwartz, B. J. O'Neill, B. H. Shanks and J. A. Dumesic, "Bridging the Chemical and Biological Catalysis Gap: Challenges and Outlooks for Producing Sustainable Chemicals," *ACS Catalysis,* vol. 4, no. 6, p. 2060–2069, 2014.

[2] J. E. Rekoske and M. A. Barteau, "Kinetics, Selectivity, and Deactivation in the Aldol Condensation of Acetaldehyde on Anatase Titanium Dioxide," *Industrial and Engineering Chemistry Research,* vol. 50, no. 1, pp. 41-51, 2010.

[3] M. Kurtz, H. Wilmer, T. Genger, O. Hinrichsen and M. Muhler, "Deactivation of supported copper catalysts for methanol synthesis," *Catalysis Letters,* vol. 86, no. 1-3, pp. 77-80, 2003.

[4] Y. Schuurman, B. F. M. Kuster, K. van der Wiele and G. B. Marin, "Selective oxidation of methyl α-d-glucoside on carbon supported platinum: III. Catalyst deactivation," *Applied Catalysis A: General,* vol. 89, no. 1, pp. 47-68, 1992.

[5] F. R. Venema, J. A. Peters and H. van Bekkum, "Platinum-catalyzed oxidation of aldopentoses to aldaric acids," *Journal of Molecular Catalysis,* vol. 77, no. 1, pp. 75-85, 1992.

[6] M. Besson and P. Gallezot, "Selective oxidation of alcohols and aldehydes on metal catalysts," *Catalysis Today,* vol. 57, no. 1-2, pp. 127-141, 2000.

[7] C. N. Satterfield, Heterogeneous Catalysis in Practice, McGraw-Hill, 1980.

[8] S. Sreekumar, Z. C. Baer, E. Gross, S. Padmanaban, K. Goulas, G. Gunbas, S. Alayoglu, H. W. Blanch, D. S. Clark and F. D. Toste, "Chemocatalytic Upgrading of Tailored Fermentation Products Toward Biodiesel," *ChemSusChem,* vol. 7, no. 9, pp. 2445-2448, 2014.

[9] C.-C. Wang and J. Ying, "Sol–Gel Synthesis and Hydrothermal Processing of Anatase and Rutile Titania Nanocrystals," *Chemistry of Materials,* vol. 11, no. 11, p. 3113–3120, 1999.

[10] P. Anbarasan, Z. C. Baer, S. Sreekumar, E. Gross, J. B. Binder, H. W. Blanch, D. S. Clark and F. D. Toste, "Integration of chemical catalysis with extractive fermentation to produce fuels," *Nature,* vol. 491, pp. 235-239, 2012.

[11] D. Debecker, E. Gaigneaux and G. Busca, "Exploring, Tuning, and Exploiting the Basicity of Hydrotalcites for Applications in Heterogeneous Catalysis," *Chemistry: A European Journal,* vol. 15, no. 16, pp. 3920-3935, 2009.

[12] M. J. Climent, A. Corma, S. Iborra and A. Velty, "Activated hydrotalcites as catalysts for the synthesis of chalcones of pharmaceutical interest," *Journal of Catalysis,* vol. 221, no. 2, p. 474–482, 2004.

[13] V. V. Pushkarev, N. Musselwhite, K. An, S. Alayoglu and G. A. Somorjai, "High structure sensitivity of vapor-phase furfural decarbonylation/hydrogenation reaction network as a function of size and shape of Pt nanoparticles," *Nano Letters,* vol. 12, pp. 5196-5201, 2012.

[14] J. I. Di Cosimo, V. K. Diez, M. Xu, E. Iglesia and C. R. Apesteguia, "Structure and Surface and Catalytic Properties of Mg-Al Basic Oxides," *Journal of Catalysis,* vol. 178, p. 499–510, 1998.

[15] T. N. Pham, D. Shi, T. Sooknoi and D. E. Resasco, "Aqueous-phase ketonization of acetic acid over Ru/TiO_2/carbon catalysts," *Journal of Catalysis,* vol. 295, pp. 169-178, 2012.

[16] F. Winter, A. J. van Dillen and K. P. de Jong, "Supported hydrotalcites as highly active solid base catalysts," *Chemical Communications,* pp. 3977-3979, 2005.

[17] F. Winter, V. Koot, A. J. van Dillen, J. W. Geus and K. P. de Jong, "Hydrotalcites supported on carbon nanofibers as solid base catalysts for the synthesis of MIBK," *Journal of Catalysis,* vol. 236, no. 1, pp. 91-100, 2012.

[18] L. Faba, E. Díaz and S. Ordóñez, "Improvement on the Catalytic Performance of Mg–Zr Mixed Oxides for Furfural–Acetone Aldol Condensation by Supporting on Mesoporous Carbons," *ChemSusChem,* vol. 6, no. 3, pp. 463-473, 2013.

[19] J. Perez-Ramirez, S. Abello and N. M. van der Pers, "Memory Effect of Activated Mg–Al Hydrotalcite: In Situ XRD Studies during Decomposition and Gas-Phase Reconstruction," *Chemistry - A European Journal,* vol. 13, no. 3, p. 870–878, 2007.

[20] F. Millange, R. I. Walton and D. O'Hare, "Time-resolved in situ X-ray diffraction study of the liquid-phase reconstruction of Mg–Al–carbonate hydrotalcite-like compounds," *Journal of Materials Chemistry,* vol. 10, pp. 1713-1720, 2000.

[21] P. D. L. Mercera, J. G. Van Ommen, E. B. M. Doesburg, A. J. Burggraaf and J. R. H. Ross, "Influence of ethanol washing of the hydrous precursor on the textural and structural properties of zirconia," *Journal of Materials Science,* vol. 27, pp. 4890-4898 , 1992.

[22] P. D. L. Mercera, J. G. Van Ommen, E. B. M. Doesburg, A. J. Burggraaf and J. R. H. Ross, "Zirconia as a support for catalysts Influence of additives on the thermal stability of the porous texture of monoclinic zirconia," *Applied Catalysis,* vol. 71, no. 2, pp. 363-391, 1991.

[23] S. Luo and J. L. Falconer, "Acetone and acetaldehyde oligomerization on TiO_2 surfaces," *Journal of Catalysis,* vol. 185, no. 2, pp. 393-407, 1999.

[24] S. Luo and J. L. Falconer, "Aldol condensation of acetaldehyde to form high molecular weight compounds on TiO_2," *Catalysis Letters,* vol. 57, no. 3, pp. 89-93, 1999.

[25] K. Inui, T. Kurabayashi and S. Sato, "Direct Synthesis of Ethyl Acetate from Ethanol Carried Out under Pressure," *Journal of Catalysis,* vol. 212, no. 2, pp. 207-215, 2002.

[26] N. Iwasa and N. Takezawa, "Reforming of Ethanol –Dehydrogenation to Ethyl Acetate and Steam Reforming to Acetic Acid over Copper-Based Catalysts," *Bulletin of the Chemical Society of Japan,* vol. 64, no. 9, pp. 2619-2623, 1991.

[27] P. C. Zonetti, J. Celnik, S. Letichevsky, A. B. Gaspar and L. G. Appel, "Chemicals from ethanol – The dehydrogenative route of the ethyl acetate one-pot synthesis," *Journal of Molecular Catalysis A: Chemical,* vol. 334, p. 29–34, 2011.

[28] J. E. Rekoske and M. A. Barteau, "Competition between acetaldehyde and crotonaldehyde during adsorption and reaction on anatase and rutile titanium dioxide," *Langmuir,* vol. 15, no. 6, pp. 2061-2070, 1999.

[29] M. Andersson, L. Österlund, S. Ljungström and A. Palmqvist, "Preparation of Nanosize Anatase and Rutile TiO_2 by Hydrothermal Treatment of Microemulsions and Their Activity for Photocatalytic Wet Oxidation of Phenol," *Journal of Physical Chemistry B,* vol. 106, no. 41, p. 10674–10679, 2002.

[30] J.-G. Yu, H.-G. Yu, B. Cheng, X.-J. Zhao, J. C. Yu and W.-K. Ho, "The Effect of Calcination Temperature on the Surface Microstructure and Photocatalytic Activity of TiO_2 Thin Films Prepared by Liquid Phase Deposition," *Journal of Physical Chemistry B,* vol. 107, no. 50, p. 13871–13879, 2003.

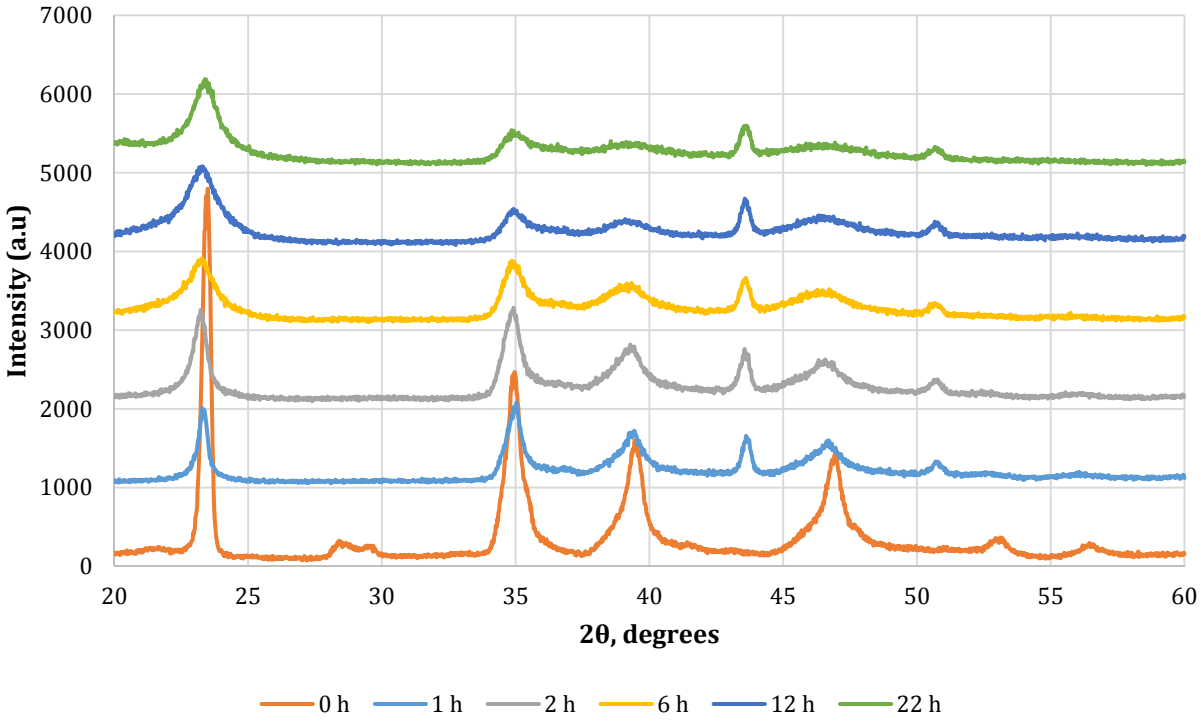

Figure 1: Change of the structure of ion-exchanged HT catalysts during ABE reaction. [Batch reactions, 513 K, acetone (2.3 mmol), butanol (2 mL), ethanol (1 mmol)]

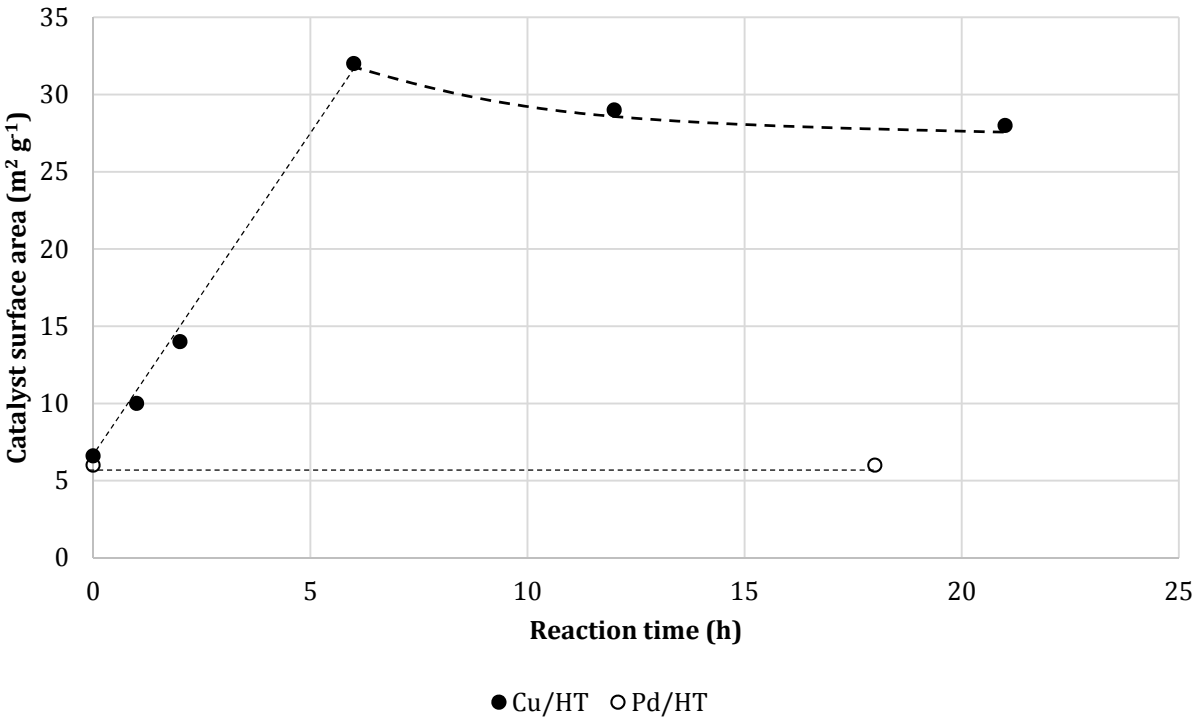

Figure 2: Evolution of the surface area of ion-exchanged, hydrotalcite-supported Pd and Cu catalysts over the course of the reaction. [Batch reactions, 513 K, acetone (2.3 mmol), butanol (2 mL), ethanol (1 mmol)]. Dashed lines indicate qualitative trends.

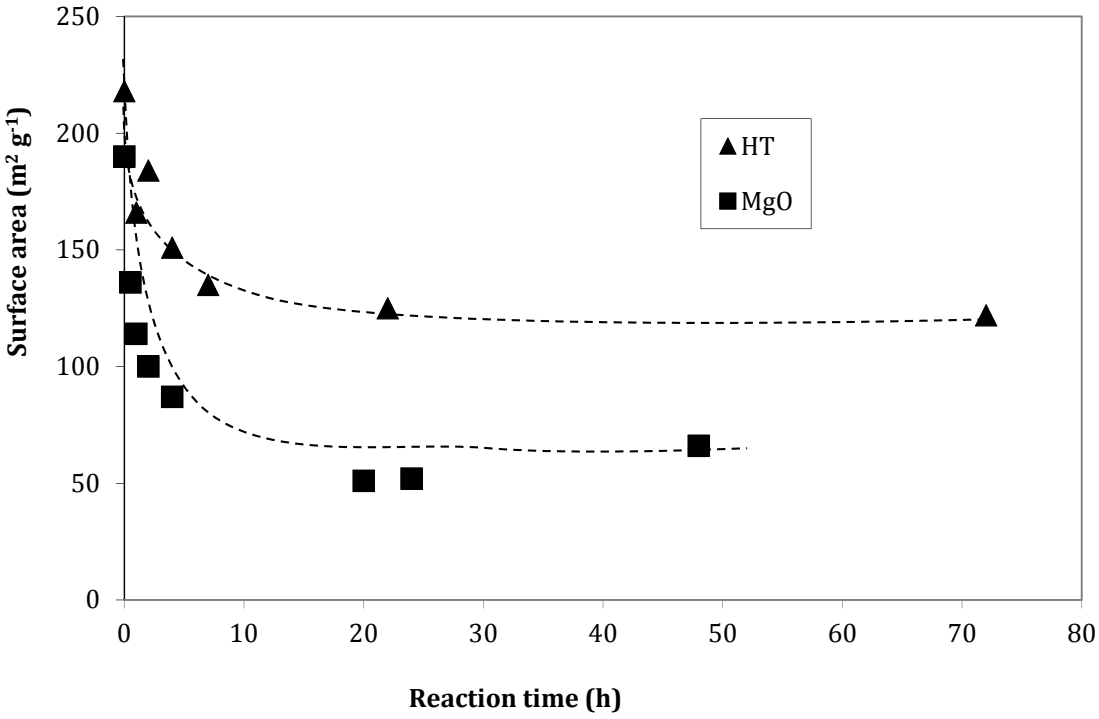

Figure 3: Evolution of the surface area of PdCu catalysts supported on periclase.[Batch reactions, 513 K, acetone (2.3 mmol), butanol (2 mL), ethanol (1 mmol)]. The dashed lines represent qualitative trends.

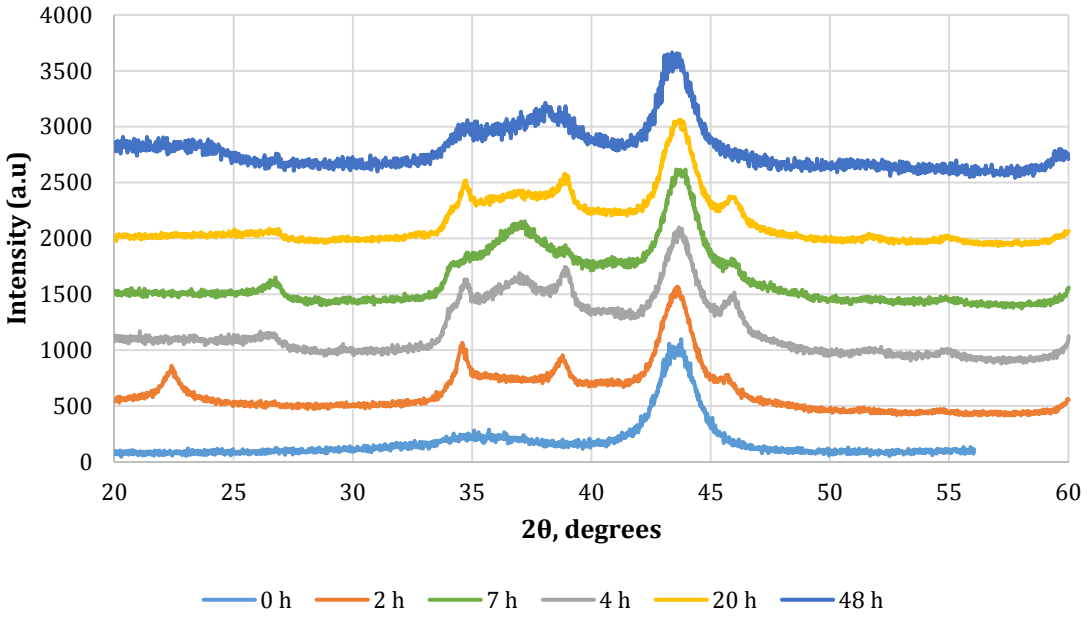

Figure 4: Evolution of the crystal structure of MgAlO-supported PdCu catalysts. [Batch reactions, 513 K, acetone (3.7 mmol), butanol (6 mmol), ethanol (1.6 mmol)].

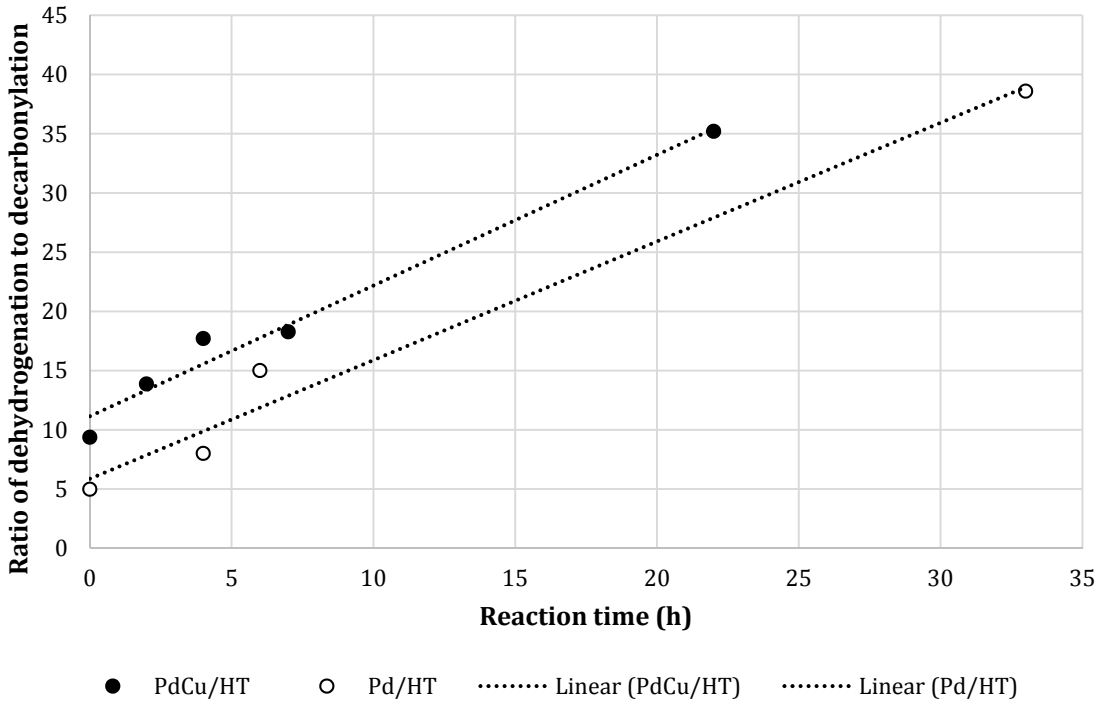

Figure 5: Effects of batch-phase reaction time on the intrinsic selectivity of PdCu/HT and Pd/HT catalysts. Gas phase flow reaction, 85 kPa He, 15 kPa ABE mix 0.2 ml/h, 150 mg catalyst, 473 K.

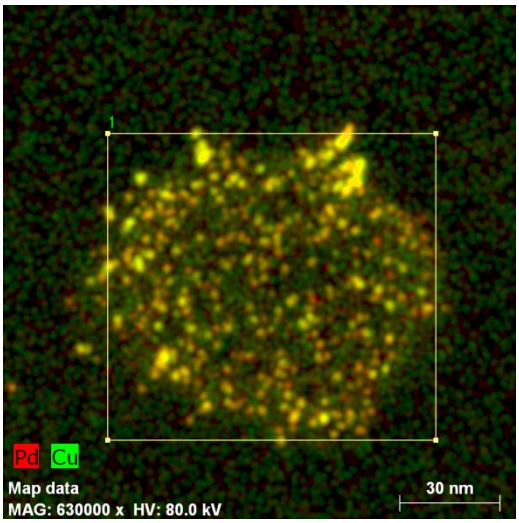

Figure 6: TEM-EDS image of catalyst after reaction.

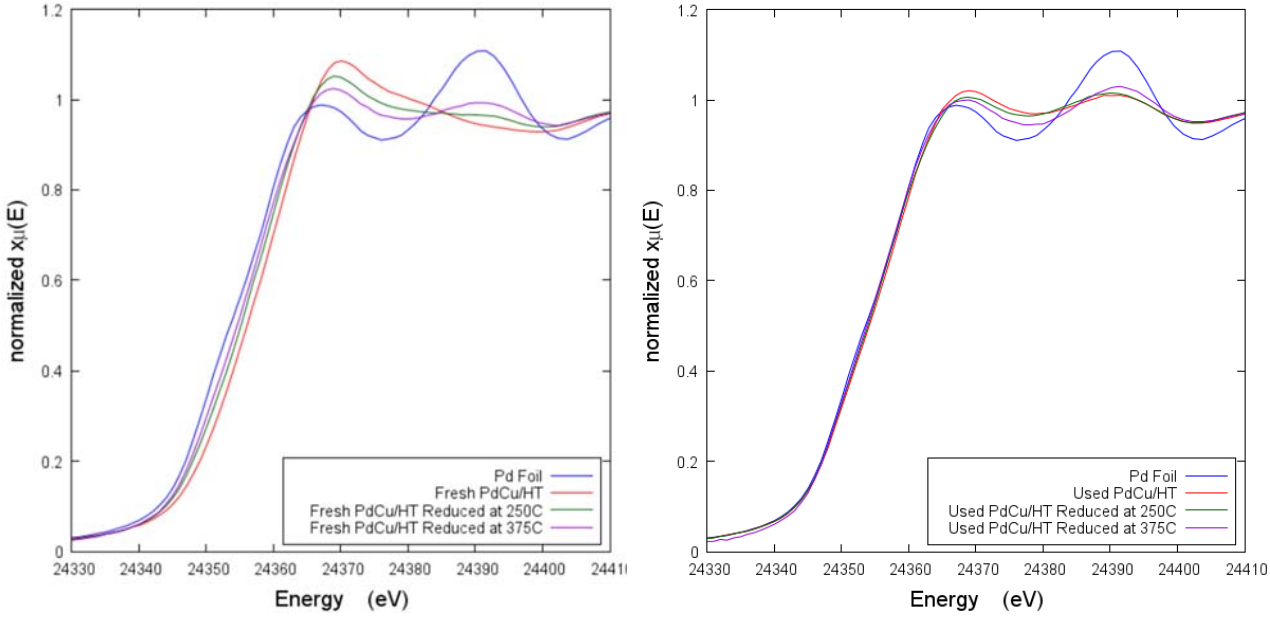

Figure 7: Pd edge XANES for the fresh PdCu/HT catalyst and a PdCu/HT catalyst used in a batch reaction for 2h.

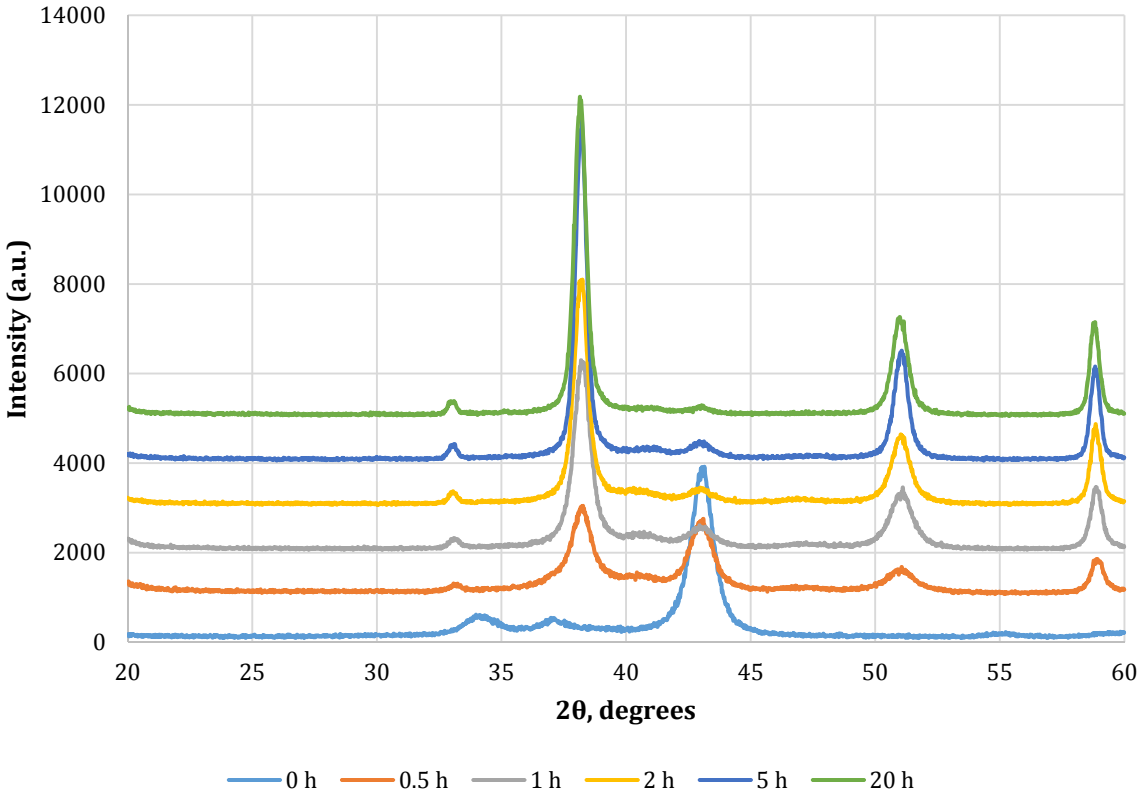

Figure 8: Evolution of the crystal structure of the MgO-supported PdCu catalysts. [Batch reactions, 513 K, acetone (3.7 mmol), butanol (6 mmol), ethanol (1.6 mmol)].

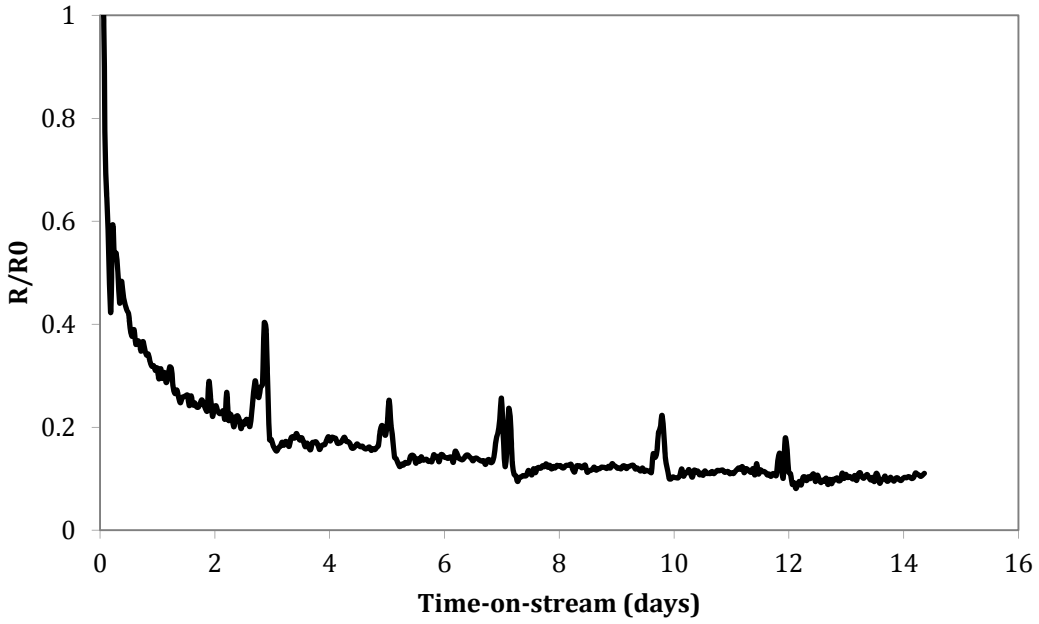

Figure 9: Stability study for PdCu/HT in the gas phase. 85 kPa He, 15 kPa ABE mix 0.2 ml/h, 473 K.

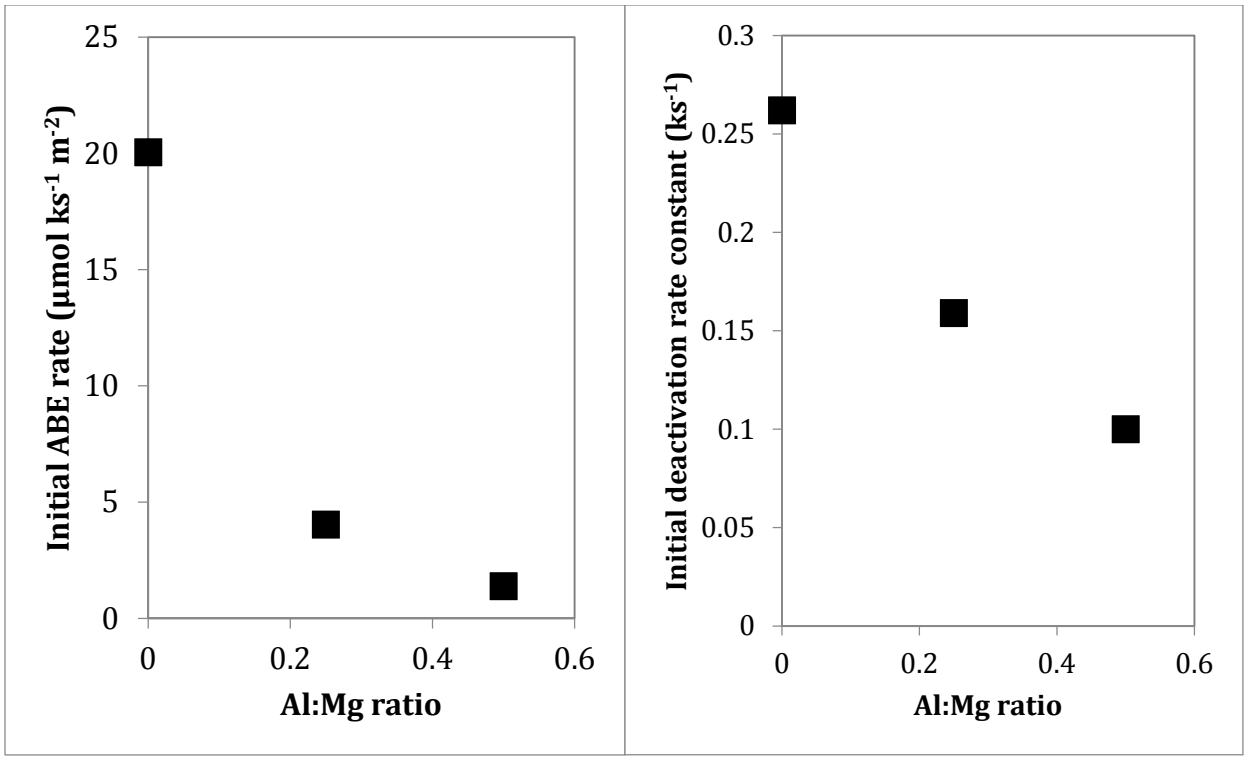

Figure 10: Effects of the Al:Mg ratio on the reaction rate and the deactivation rate. Gas phase flow reaction, 85 kPa He, 15 kPa ABE mix 0.2 ml/h, 150 mg catalyst, 473 K.

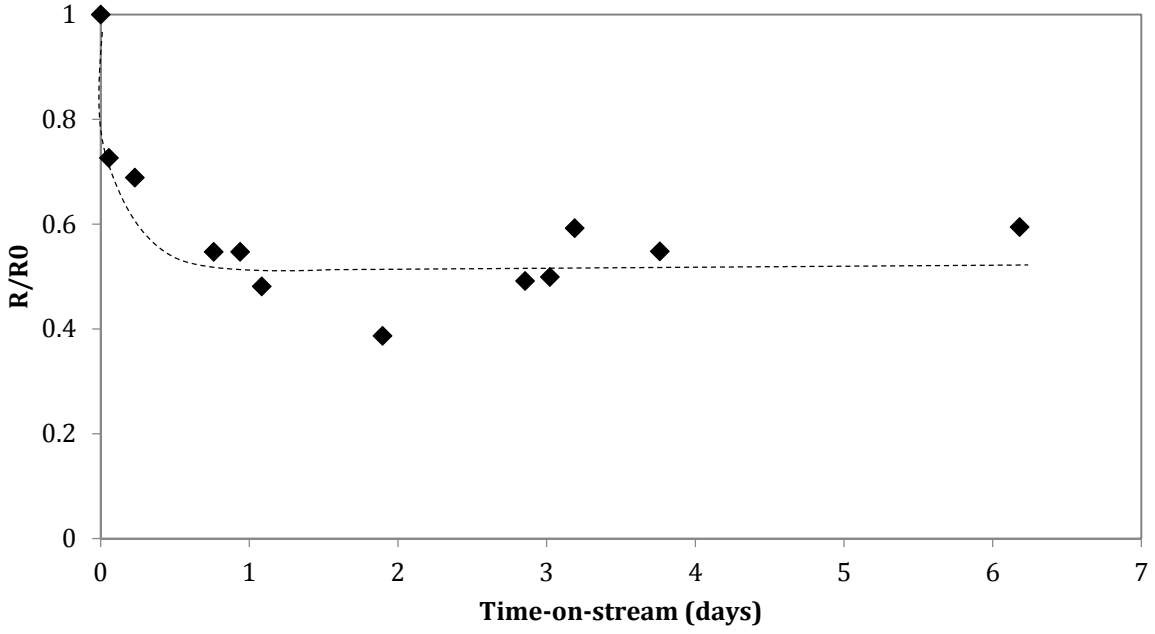

Figure 11: Time-on-stream plot for the ABE reaction over a PdCuHT catalyst. 1 g catalyst, 0.2 ml/min ABE mix, 513 K. The dashed line represents a qualitative trend.

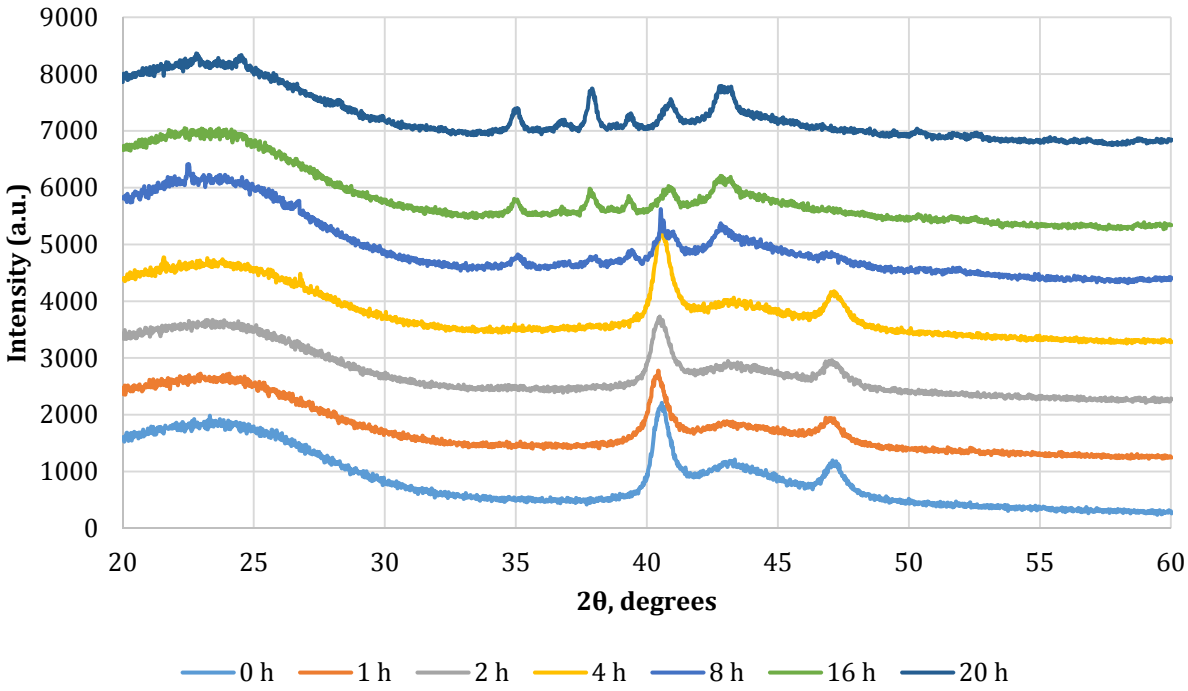

Figure 12: Evolution of the structure of PdCu/HT-C over the course of batch reactions.

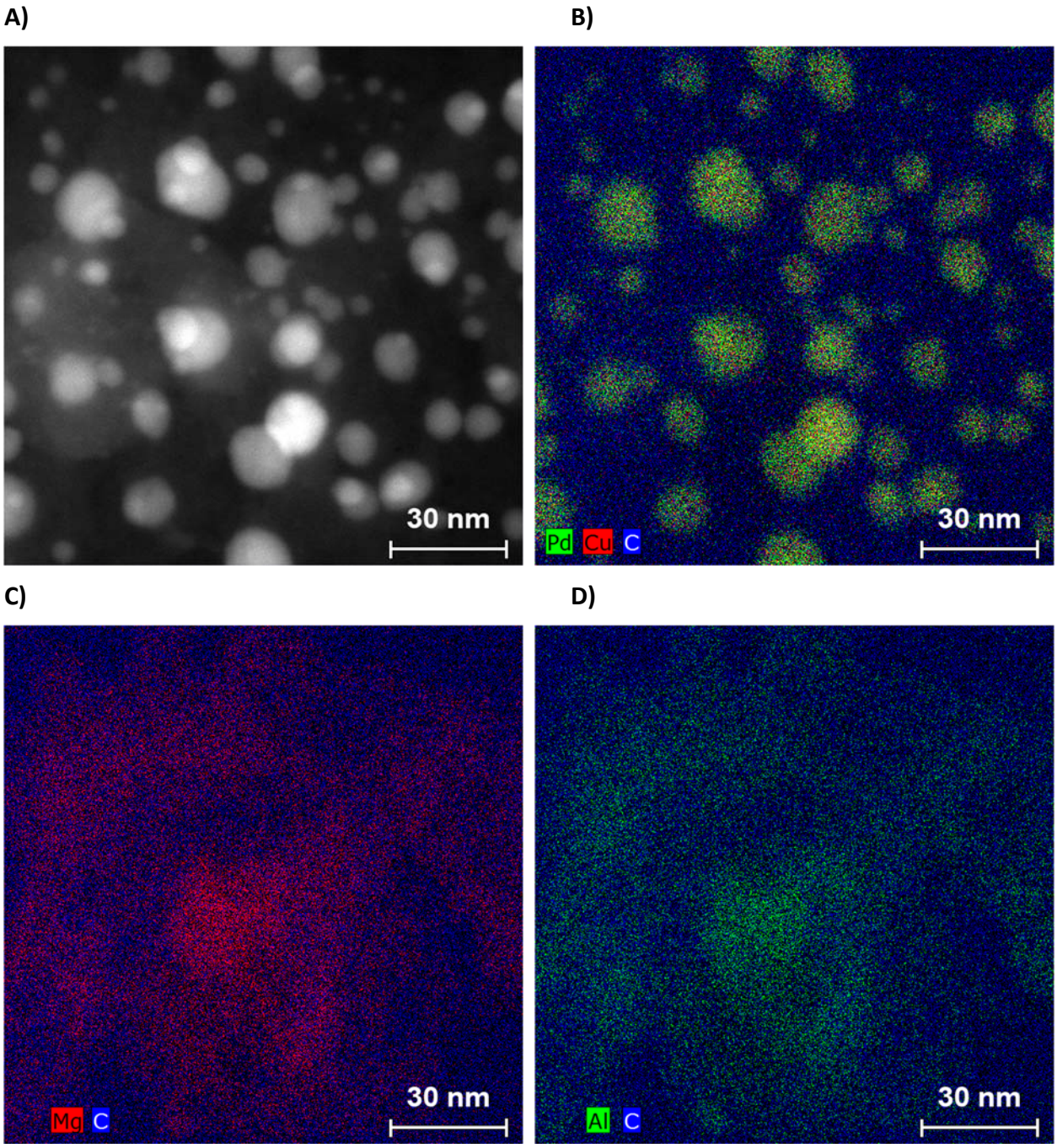

Figure 13: HAADF-STEM image (A) and STEM-EDS elemental maps (B, C, and D) of the PdCu/HT-C catalyst

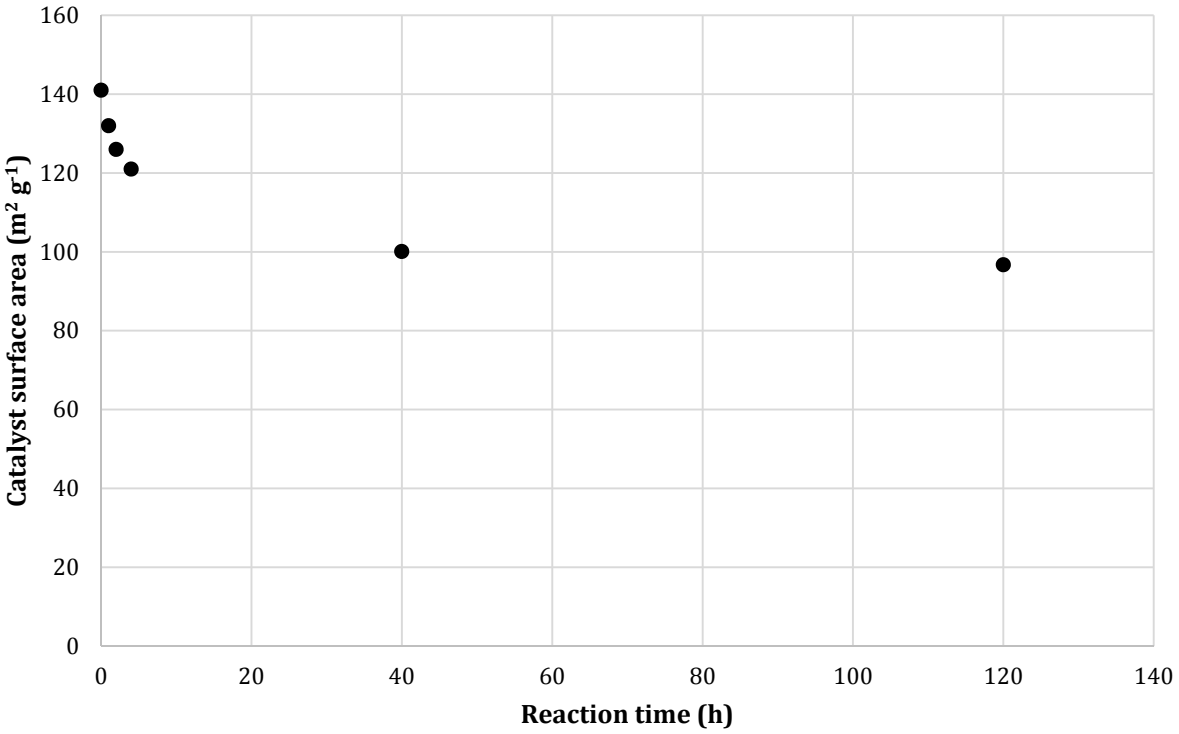

Figure 14: Effects of batch reaction time on the surface area of $PdCu/TiO_2$.

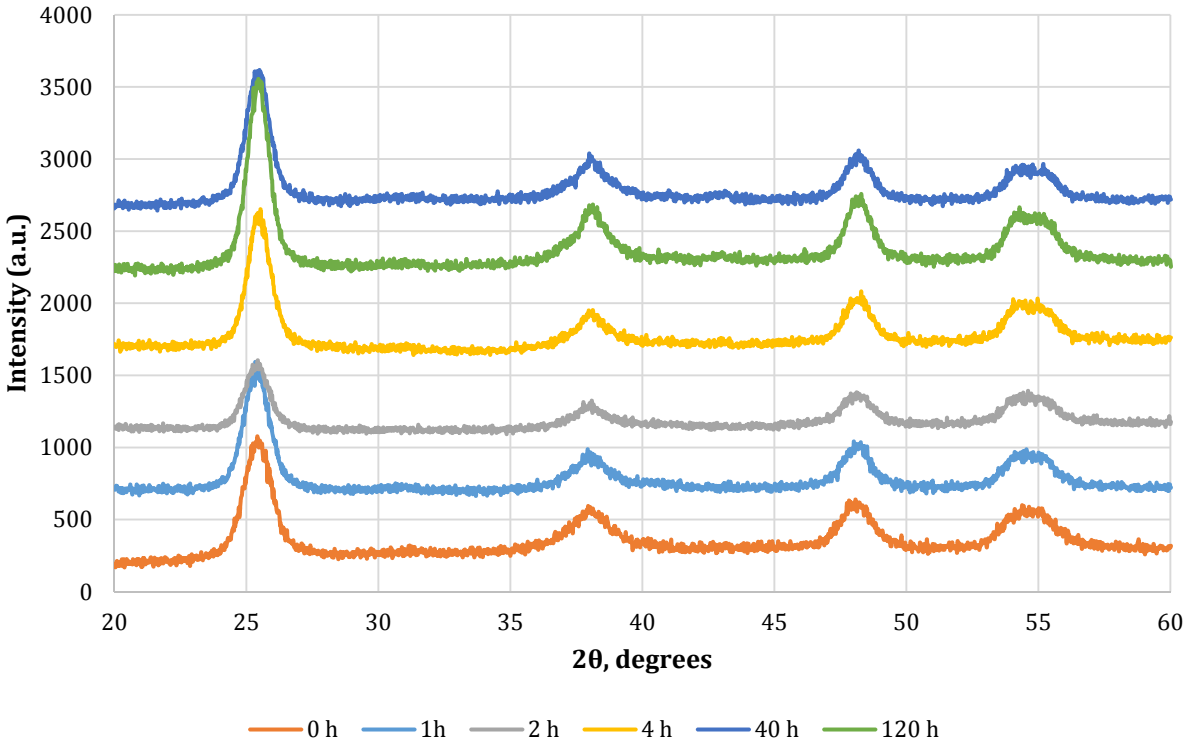

Figure 15: Evolution of the structure of $PdCu/TiO_2$ over the course of batch reactions.

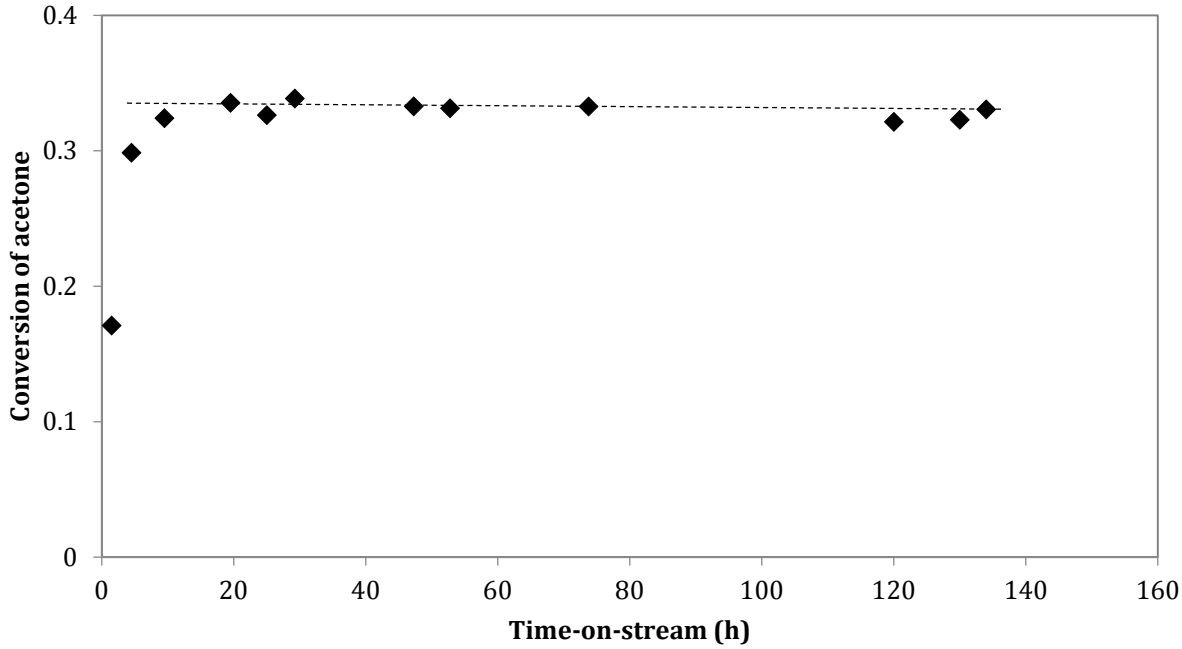

Figure 16: Longevity of the $PdCu/TiO_2$ catalyst in a liquid-phase flow reaction.

Chapter 3: Effects of Crystallinity and Heat Treatment on the Reactivity, Selectivity and Stability of Hydrotalcite-based catalysts

INTRODUCTION

Hydrotalcite materials and the mixed oxides derived thereof have been widely used as catalysts for a variety of chemical reactions [1]. More specifically, they have been used as basic catalysts for aldol condensation-like reactions, such as the ethanol Guerbet reaction [2], the Claisen-Schmidt condensation [3] and methyl ketone trimerizations [4]. They have also been used as supports for metal catalysts in the context of a wide variety of reactions. For example, Ni-substituted hydrotalcites have been shown to be very active catalysts for the reforming of methane [5, 6] and of ethanol [7]. Hydrotalcite-supported Pd catalysts have been used extensively in the literature for hydrogenation/dehydrogenation reactions [8, 9] and also in organic chemical synthesis [10].

In our previous work [11] and in earlier chapters of this dissertation, we have shown the utility of hydrotalcite-supported Pd and PdCu catalysts for the ABE condensation reaction. We also reported the challenges associated with the restructuring of the hydrotalcite during reaction, as well as the trapping of Cu in the structure. The former resulted in deactivation of the catalyst, while the latter resulted in losses of starting material through the decarbonylation of aldehyde intermediates over the Pd surfaces.

Based on these observations, we decided to perform a detailed study of the effects of temperature on the reactivity and selectivity of a metal-free HT catalyst and of a PdCu/HT catalyst. Based on the aforementioned considerations, we expected the higher temperatures to lead to a more crystalline material, which would be more stable under reaction conditions. Also, we expected higher calcination temperatures to lead to less trapping of the transition metals, as their native oxides have square planar geometries around the metal, which contrasts with the hydrotalcite material that has octahedral geometry at the metal site.

MATERIALS AND METHODS

Metal-free hydrotalcite catalysts were prepared by calcination of synthetic hydrotalcite in stagnant ambient air.

To synthesize hydrotalcite supported PdCu catalysts, we used the incipient wetness impregnation method, using water and tetrahydrofuran (THF) as solvents. Synthetic hydrotalcite was calcined under ambient air at 823 K (ramp rate 1 K min^{-1}) and was impregnated with palladium and copper nitrates in a 3:1 molar ratio. The resulting solid was dried at 373 K and calcined at various temperatures under stagnant ambient air.

In situ X-ray diffraction experiments were carried out in a Bruker D8 diffractometer using a flow cell. The flow of nitrogen was regulated at 85 ml min^{-1} using a rotameter. Water was injected into the nitrogen stream, using a syringe pump, and the flow rate was calculated to give 3 kPa of water, the saturation pressure of water at ambient temperature. Diffractograms were collected every 12 minutes. Ten diffractograms were added for one data point and the extent of the conversion of hydrotalcite was calculated by dividing the area under the peak at 43.1° with the initial area of that peak.

The protocols for reaction and characterization of the catalysts have been described extensively in Chapters 1 and 2 of this dissertation.

RESULTS AND DISCUSSION

Consistent with literature reports [3], the calcined hydrotalcite is a cubic periclase structure and restructures to the lamellar hydrotalcite, under a flow of water-saturated nitrogen (figure 1). The increasing peaks at 12.5°, 23.7° and 29.6° correspond to the (003), (006) and (009) reflections of the hydrotalcite structure, while the shoulder observed at 60.7° corresponds to the (110) reflection. The decreasing peak at 43.1° corresponds to the (200) reflection of the periclase structure, while the one at 62.8° corresponds to the (220) reflection [12].

As is easily seen from the comparison of figures 1 and 2, the reconstruction of the mixed metal oxide to the hydrotalcite was considerably slower in the case of the material that was calcined at 973 K, compared to the material calcined at 723 K. The extent of reconstruction (α) of the latter material was about 35%, while the former showed an α of about 10% after 9 h.

Perez-Ramirez et al. [13], as well as Millange et al. [12] showed that the reconstruction of hydrotalcites in the presence of liquid water or water vapor follows the Avrami-Erofeev model, based on *in situ* XRD studies of the calcination and reconstruction of Mg-Al hydrotalcites. This model correlates the extent of a solid-state reaction (α) with the time (t) and kinetic parameters of transformation (k, n) [14, 15].

$$a = 1 - \exp\{-(kt)^n\}$$

and can be linearized as follows [16]:

$$\ln[-\ln(1-\alpha)] = n\ln t + n\ln k$$

The linearized Avrami-Erofeev model provides a good fit for the reconstruction of the oxide calcined at 973 K. However, the reconstruction of the material calcined at 723 K does not follow the same trend. A possible reason for this is that the intrinsic reactivity of the material changes during the reaction; the line breadth decreases during reaction, indicating that the crystallinity of the starting material increases during the reconstruction (need to

add figure here). For this reason, in order to obtain the intrinsic rate of reconstruction, we used the first three points of the curve.

In figure 5A, one can see the effects of the calcination temperature on the reconstruction rate. Since the calcination temperature is not an intrinsic property of the material, it is instructive to use a measure of crystallinity as the independent variable. This could be the full width at half maximum (FWHM) for the (200) peak of the periclase structure, which decreased from 2.087^{o} for the sample calcined at 723 K to 1.720^{o} for the sample calcined at 973 K, indicating lower crystallinity at lower calcination temperatures. The reconstruction rate constant increased with the breadth of the periclase structure peak, from 0.016 h^{-1} to 0.067 h^{-1} (figure 5B).

The catalytic consequences of the rate of reconstruction have been reported by Sacia et al. in the context of the aldol condensation of hexanedione to 2-methylcylopentenone. In that system, the reactivity trends were dependent on the reaction medium; in organic solvent, the yields trend with surface area. In contrast, in a biphasic water-toluene mixture, the yields trend with calcination temperature [17]. During reaction in toluene, the catalyst retained the high-surface-area periclase structure, while in water the catalyst reconstructed to the hydrotalcite phase. The rate of this transformation is what drives the reactivity in the biphasic system. As can be seen in figure 5, the yield in the water-toluene mixture decreases as the rate of reconstruction increases.

Having shown the consequences of crystallinity on a monofunctional catalytic system, we undertook a similar study for a bifunctional catalyst system. We chose the PdCu/HT system, which has been shown to be an active catalyst for the ABE condensation reaction in the earlier chapters of this work.

Increasing the calcination temperature of the bifunctional catalysts above 723 K results in lower surface area materials. Below 723 K, the calcination at 673 K results in a material with lower surface area. The reason for this is that the crystallization of the periclase phase is slower at low temperatures. This is also consistent with the X-ray diffractograms of these materials, in which we see a drop in the peak broadening when the calcination temperature is increasing, (figure 6).

One of our goals in this study was to understand the trapping of transition metal ions in the structure and devise methods to prevent it. In chapter 1 of this work, we showed that catalysts prepared by incipient wetness impregnation showed higher ABE yields compared to those prepared by coprecipitation. We showed that this improvement is due to the higher reducibility of the Cu in the catalyst. We propose here that if reconstruction of the mixed metal oxide in the impregnation is avoided, then the extent of trapping of the transition metals is reduced. For this reason, in addition to the catalysts prepared by water IWI, we prepared a series of catalysts with THF as the IWI solvent. Using THF as a solvent resulted in the retention of the periclase structure during IWI. This is also the reason that the surface area of the finished catalyst does not change significantly with changes in calcination temperature (figure 7). This is also consistent with the reduced peak

broadening of the (200) peak for the THF-impregnated catalysts compared to the water-impregnated ones.

The effects of the heat treatment on the reducibility of the catalyst were investigated by X-ray absorption spectroscopy and are presented in figures 8 - 12. On the Pd edge, the calcined catalysts were all in a 2+ oxidation state, based on the edge position. The catalysts that were prepared using THF as an IWI solvent and the water-impregnated catalyst calcined at 1023 K are consistent with a bulk PdO phase, both in the XANES (figure 8) and the EXAFS (figure 9). On the other hand, the two water-impregnated catalysts that have been calcined at 673 and 823 K show a sharper white line feature in the XANES region and also much weaker second shell Pd-Pd scattering features. We propose that the Pd in these materials is predominately trapped inside the periclase structure. The shorter M-O distances of the periclase structure, compared to PdO, are consistent with the sharper white line, while the weaker Pd-M second-shell scattering could be due to scattering by Mg and Al instead of Pd. Such structures have been suggested in the past for Pd/HT materials by Ota et al. [18].

After reduction at 523 K, all catalysts show an edge consistent with the metallic Pd state. However, the existence of a white line in the EXAFS compared to the reference foil (figure 10) and the scattering features at R < 1.8 Å suggest that there is residual Pd-O coordination (figure 11). The catalysts that show characteristics of Pd trapped in the periclase structure also less Pd-Pd coordination in the reduced state. This is consistent with those materials having smaller nanoparticles. A possible reason for this is that the diffusion of the Pd^{2+} ions through the Mg-Al oxide matrix is much slower than the surface diffusion of these species. Trapping of transition metal species in hydrotalcite matrices through the formation of a solid solution has been used in the past in the case of Ni-hydrotalcite catalysts and been reported to result in the formation of small nanoparticles that are resistant to sintering [6].

Similarly, in the Cu edge, the calcined catalysts show a mixture of CuO and $Cu_xMg_{1-x}O$ structures. Linear combination fitting of the XANES region suggests that the IWI solvent has relatively small effects on the proportion of one phase versus the other, as is shown in table 1. After reduction, the presence of three phases complicates fitting significantly. However, conclusions can be drawn by inspection of the edge position; as was the case in the Pd edge, lower calcination temperatures and the use of THF as incipient wetness impregnation solvent resulted in greater extents of reduction.

The catalytic consequences of these approaches are presented in figures 13, and 14. We observe an increase of the dehydrogenation to decarbonylation ratio as a function of the calcination temperature. The reason for this increase is not the extent of Cu incorporation in the nanoparticles, as increasing temperatures tend to increase the amount of Cu that exists in a Cu-Mg-Al oxide solid solution, as we have shown above. Instead, the reason for the increased selectivity is the increased nanoparticle size. Based on the X-ray absorption experiments, we have shown that the Pd-M coordination increases with increasing calcination temperature. This in turn has the effect of increasing the number of terrace

sites relative to corner and edge sites, resulting in increased selectivity for dehydrogenation.

The increased particle size with increasing temperature is consistent with the decrease in the gas-phase reaction rates (per unit mass of catalyst), as dispersion decreases. Since there is no catalyst restructuring in the gas phase, the extrapolation to zero time-on-stream gives the reaction rate for the fresh catalyst. Contrary to the gas-phase rates, the liquid phase yields showed a maximum at the 723 K calcination temperature. This is due to the competing effects of decreasing reaction rates due to the larger nanoparticles and the increasing stability of the catalyst due to the higher crystallinity.

CONCLUSIONS

Increasing calcination temperatures of monofunctional HT catalysts results in greater tolerance for the presence of water in the reaction medium. This manifests itself in higher yields for the intramolecular aldol condensation of hexanedione. In the case of the bifunctional PdCu/HT catalysts, the increasing calcination temperature results in more extensive trapping of the Cu in the structure. At the same time, the PdCu nanoparticle size is increasing, which results in selectivity improvements. Consistent with this, gas phase reaction rates, as normalized by the catalyst mass, are decreasing. However, the liquid phase batch reaction yields are peaking at 723 K; lower calcination temperatures result in poor HT crystallinity, which in turn results in a less water-tolerant material.

REFERENCES

[1] D. Debecker, E. Gaigneaux and G. Busca, "Exploring, Tuning, and Exploiting the Basicity of Hydrotalcites for Applications in Heterogeneous Catalysis," *Chemistry: A European Journal,* vol. 15, no. 16, pp. 3920-3935, 2009.

[2] J. T. Kozlowski and R. J. Davis, "Heterogeneous Catalysts for the Guerbet Coupling of Alcohols," *ACS Catalysis,* vol. 3, no. 7, pp. 1588-1600, 2013.

[3] M. J. Climent, A. Corma, S. Iborra and A. Velty, "Activated hydrotalcites as catalysts for the synthesis of chalcones of pharmaceutical interest," *Journal of Catalysis,* vol. 221, no. 2, p. 474–482, 2004.

[4] E. R. Sacia, B. Madhesan, M. H. Deaner, K. A. Goulas, F. D. Toste and A. T. Bell, "Highly Selective Condensation of Biomass-Derived Methyl Ketones as a Source of Aviation

Fuel," *ChemSusChem,* vol. In press, 2015.

[5] C. Resini, T. Montanari, L. Barattini, G. Ramis, G. Busca, S. Presto, P. Rianic, R. Marazza, M. Sisani, F. Marmottini and U. Costantino, "Hydrogen production by ethanol steam reforming over Ni catalysts derived from hydrotalcite-like precursors: Catalyst characterization, catalytic activity and reaction path," *Applied Catalysis A: General,* vol. 355, no. 1-2, p. 83–93, 2009.

[6] A. I. Tsyganok, T. Tsunoda, S. Hamakawa, K. Suzuki, K. Takehira and T. Hayakawa, "Dry reforming of methane over catalysts derived from nickel-containing Mg–Al layered double hydroxides," *Journal of Catalysis,* vol. 213, no. 2, pp. 191-203, 2003.

[7] A. N. Fatsikostas, D. I. Kondarides and X. E. Verykios, "Production of hydrogen for fuel cells by reformation of biomass-derived ethanol," *Catalysis Today,* vol. 75, no. 1-4, pp. 145-155, 2002.

[8] Y. Z. Chen, C. W. Liaw and L. I. Lee, "Selective hydrogenation of phenol to cyclohexanone over palladium supported on calcined Mg/Al hydrotalcite," *Applied Catalysis A: General,* vol. 177, no. 1, pp. 1-8, 1999.

[9] P. Sangeetha, P. Seetharamulu, K. Shanthia, S. Narayanan and K. S. Rama Rao, "Studies on Mg-Al oxide hydrotalcite supported Pd catalysts for vapor phase hydrogenation of nitrobenzene," *Journal of Molecular Catalysis A: Chemical,* vol. 273, no. 1-2, pp. 244-249, 2007.

[10] B. M. Choudary, S. Madhi, N. S. Chowdari, M. L. Kantam and B. Sreedhar, "Layered Double Hydroxide Supported Nanopalladium Catalyst for Heck-, Suzuki-, Sonogashira-, and Stille-Type Coupling Reactions of Chloroarenes," *Journal of the American Chemical Society,* vol. 124, no. 47, pp. 14127-14136, 2002.

[11] S. Sreekumar, Z. C. Baer, E. Gross, S. Padmanaban, K. Goulas, G. Gunbas, S. Alayoglu, H. W. Blanch, D. S. Clark and F. D. Toste, "Chemocatalytic Upgrading of Tailored Fermentation Products Toward Biodiesel," *ChemSusChem,* vol. 7, no. 9, pp. 2445-2448, 2014.

[12] F. Millange, R. I. Walton and D. O'Hare, "Time-resolved in situ X-ray diffraction study of the liquid-phase reconstruction of Mg–Al–carbonate hydrotalcite-like compounds," *Journal of Materials Chemistry,* vol. 10, pp. 1713-1720, 2000.

[13] J. Perez-Ramirez, S. Abello and N. M. van der Pers, "Memory Effect of Activated Mg–Al Hydrotalcite: In Situ XRD Studies during Decomposition and Gas-Phase Reconstruction," *Chemistry - A European Journal,* vol. 13, no. 3, p. 870–878, 2007.

[14] M. Avrami, "Kinetics of Phase Change. I: General Theory," *Journal of Chemical Physics,*

vol. 7, pp. 1103-1112, 1939.

[15] B. V. Erofeev, "A generalized equation of chemical kinetics and its application in reactions involving solids," *Comptes rendus de l' Academie des Sciences de l' URSS,* vol. 52, pp. 511-514, 1946.

[16] J. D. Hancock and J. H. Sharp, "Method of Comparing Solid-State Kinetic Data and Its Application to the Decomposition of Kaolinite, Brucite, and $BaCO_3$," *Journal of the American Ceramic Society,* vol. 55, no. 2, pp. 74-77, 1972.

[17] E. R. Sacia, M. H. Deaner, Y. L. Louie and A. T. Bell, "Synthesis of biomass-derived methylcyclopentane as a gasoline additive via aldol condensation/hydrodeoxygenation of 2,5-hexanedione," *Green Chemistry,* vol. 17, pp. 2393-2397, 2015 .

[18] A. Ota, E. L. Kunkes, I. Kasatkin, E. Groppo, D. Ferri, B. Poceiro, R. M. Navarro Yerga and M. Behrens, "Comparative study of hydrotalcite-derived supported Pd_2Ga and PdZn intermetallic nanoparticles as methanol synthesis and methanol steam reforming catalysts," *Journal of Catalysis,* vol. 293, pp. 27-38, 2012, 293, 27–38.

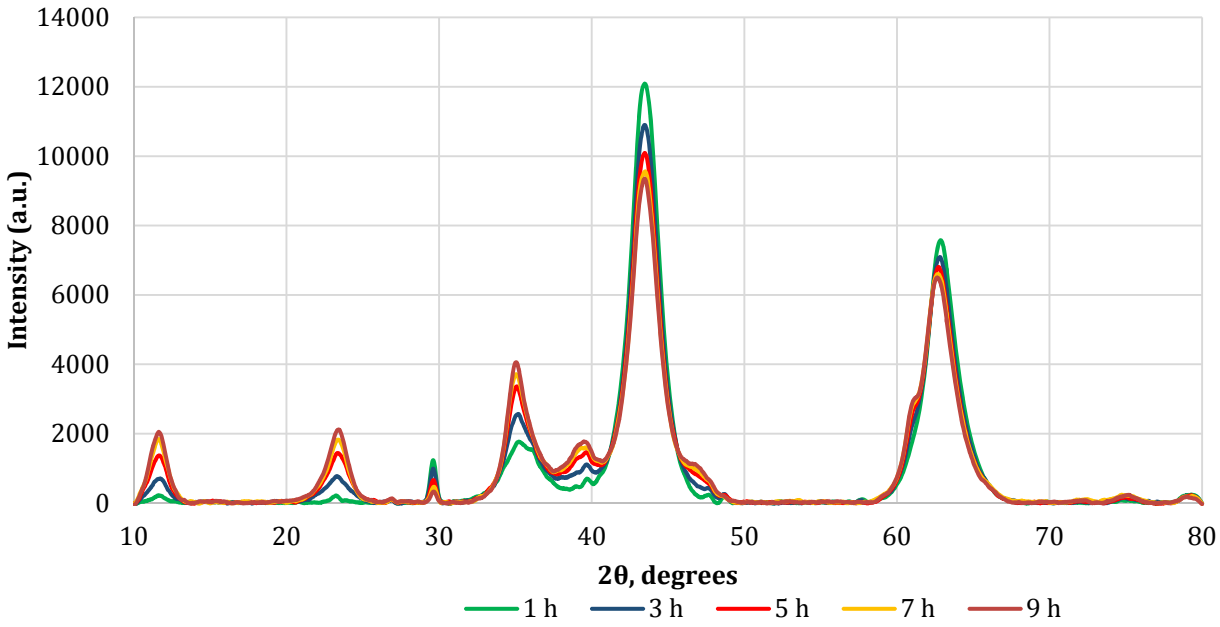

Figure 1: Reconstruction of a HT catalyst calcined at 723 K. 80 ml min^{-1} 3 kPa H_2O in N_2, 295 K

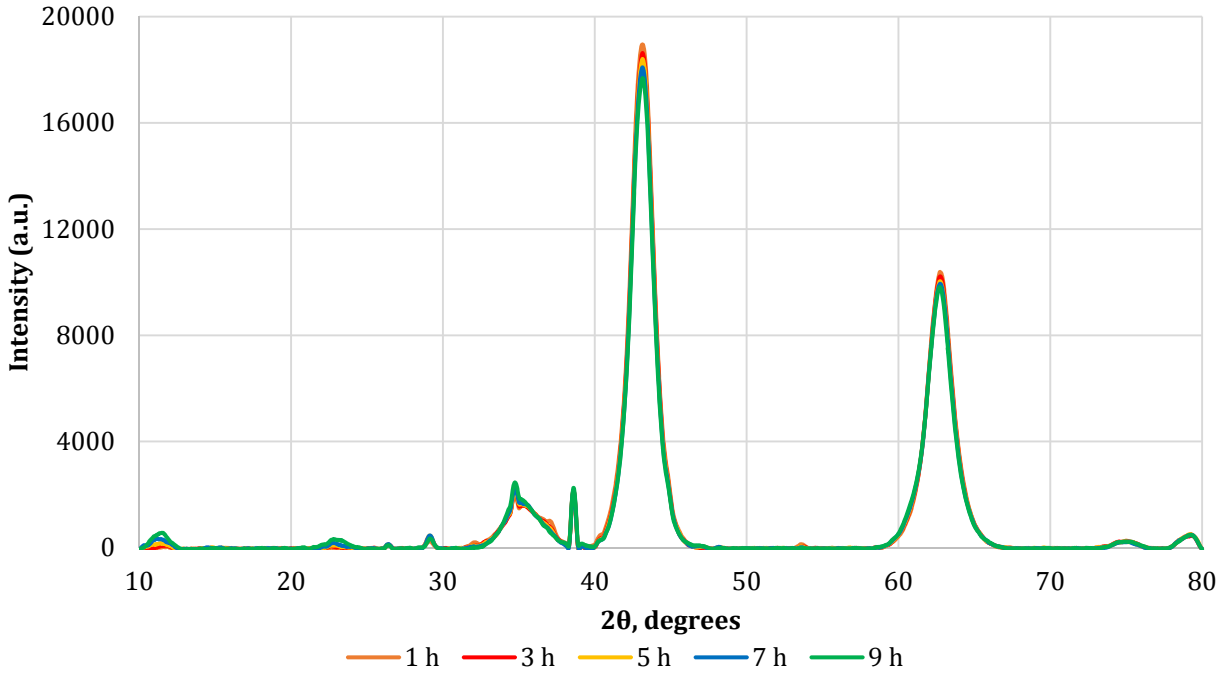

Figure 2: Reconstruction of a HT catalyst calcined at 973 K. 80 ml min^{-1} 3 kPa H_2O in N_2, 295 K

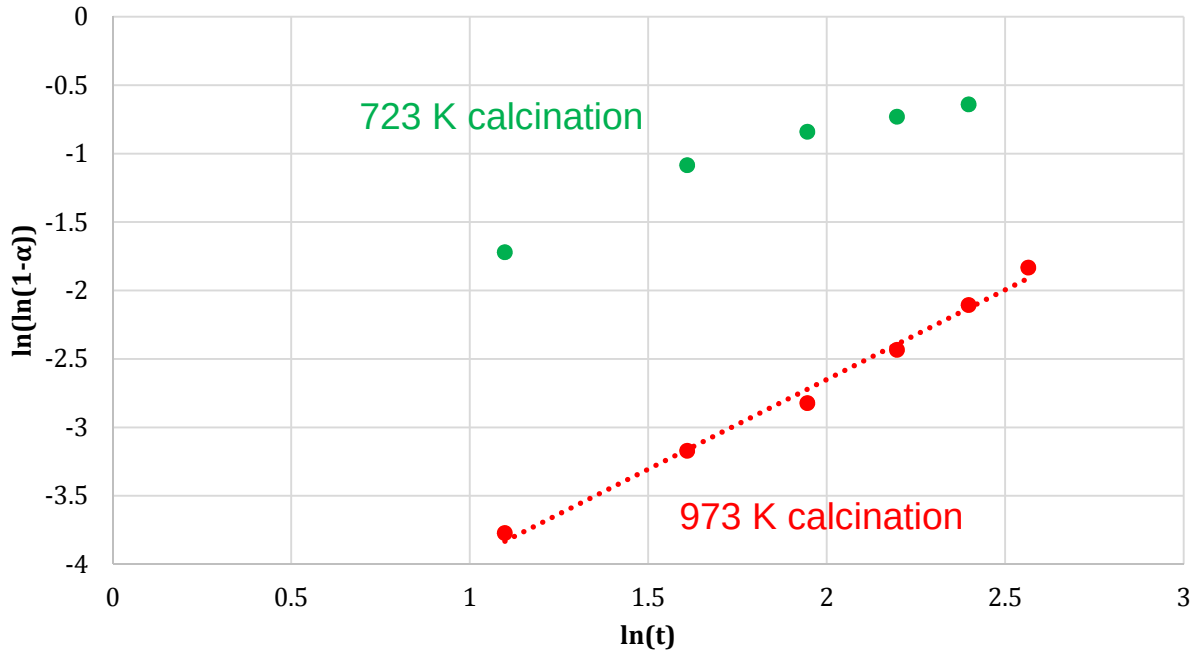

Figure 3: Sharp-Hancock plots for hydrotalcites calcined at 723 K and 973 K

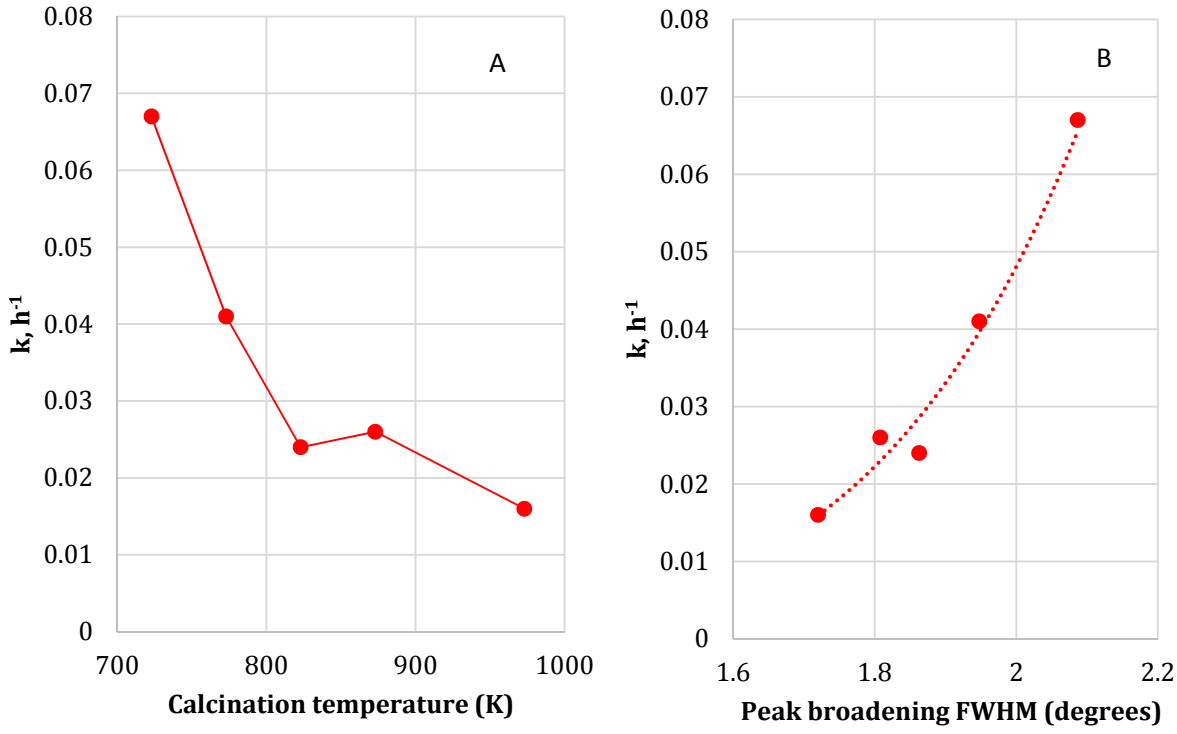

Figure 4: Effect of calcination temperature (A) and the resulting crystallinity (B, expressed as the initial broadening of the (200) peak of the cubic metal oxide material) on the reconstruction rate constant.

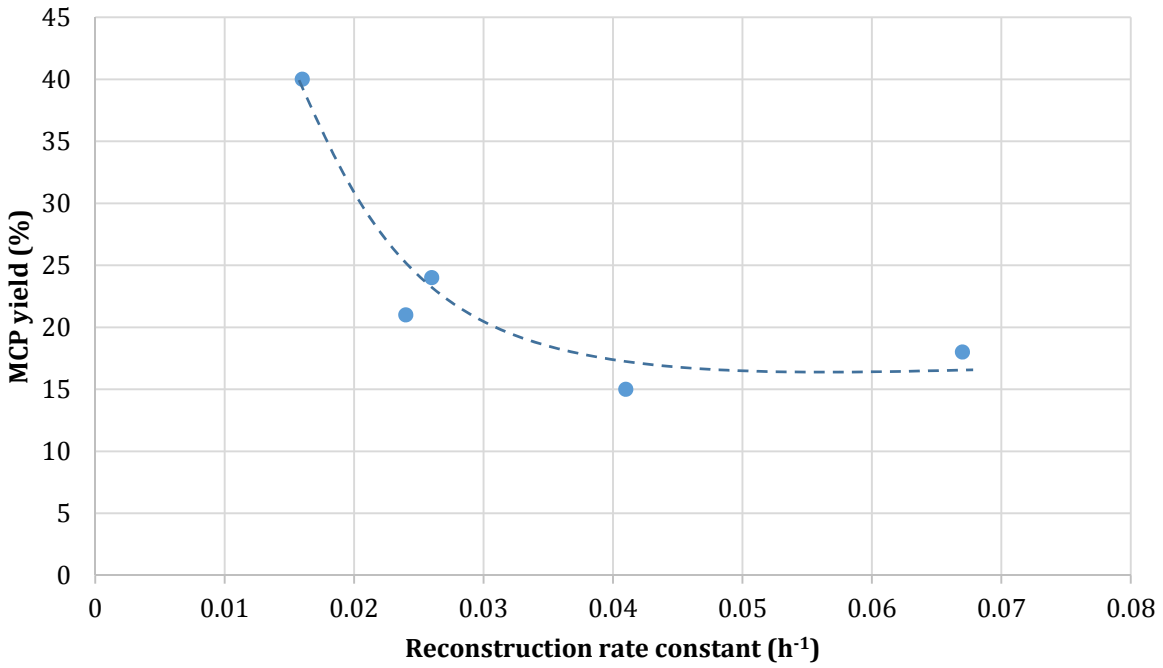

Figure 5: Effect of the reconstruction rate on the MCP yield during catalysis in a biphasic mixture. Kinetic data from Sacia et al. [17].

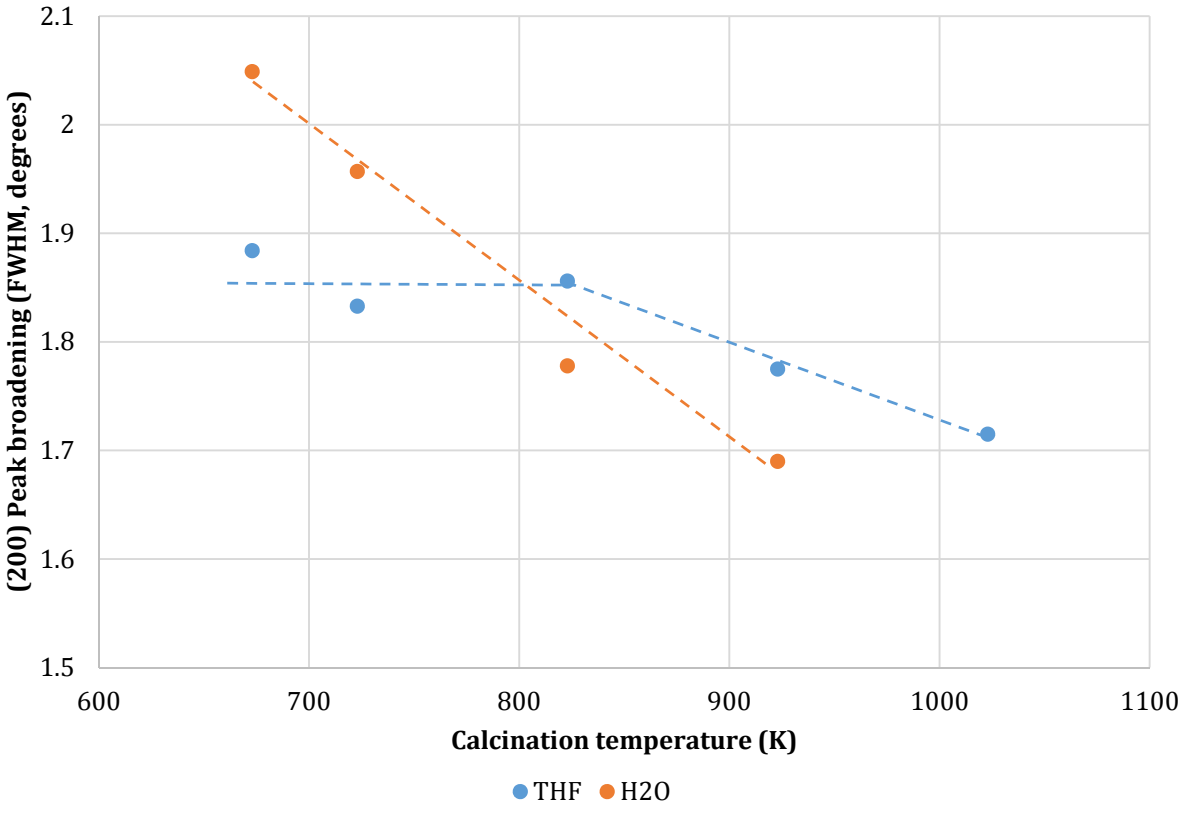

Figure 6: Effect of the calcination temperature on the crystallinity of PdCu/HT catalyst.

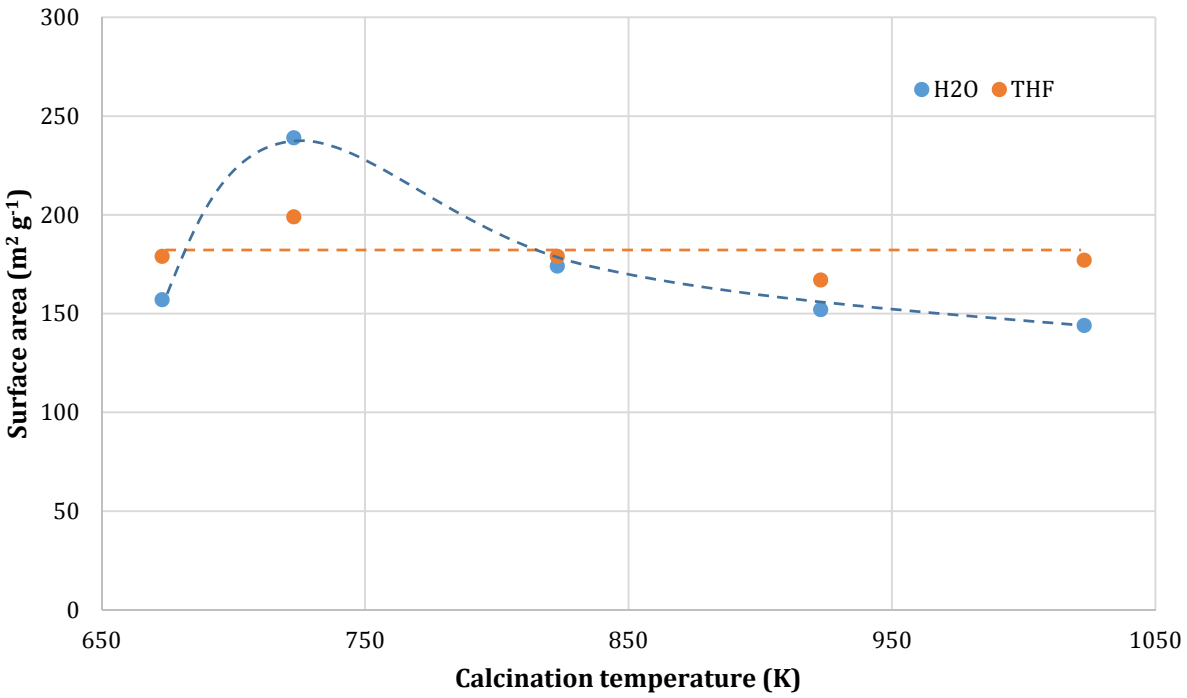

Figure 7: Effects of the calcination temperature on the surface area of PdCu/HT catalysts, prepared with water and tetrahydrofuran as incipient wetness impregnation solvents.

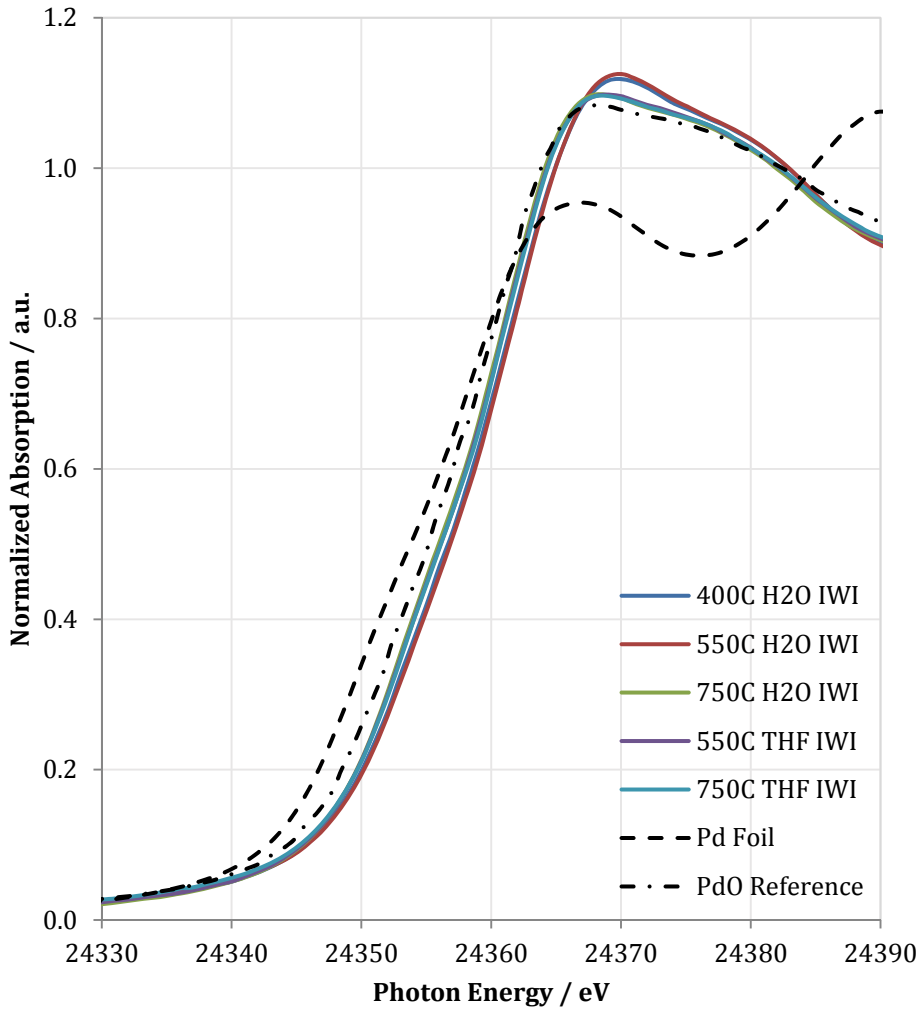

Figure 8: Pd K edge XANES region as a function of PdCuHT catalyst calcination temperature. Spectra recorded in transmission at room temperature under He.

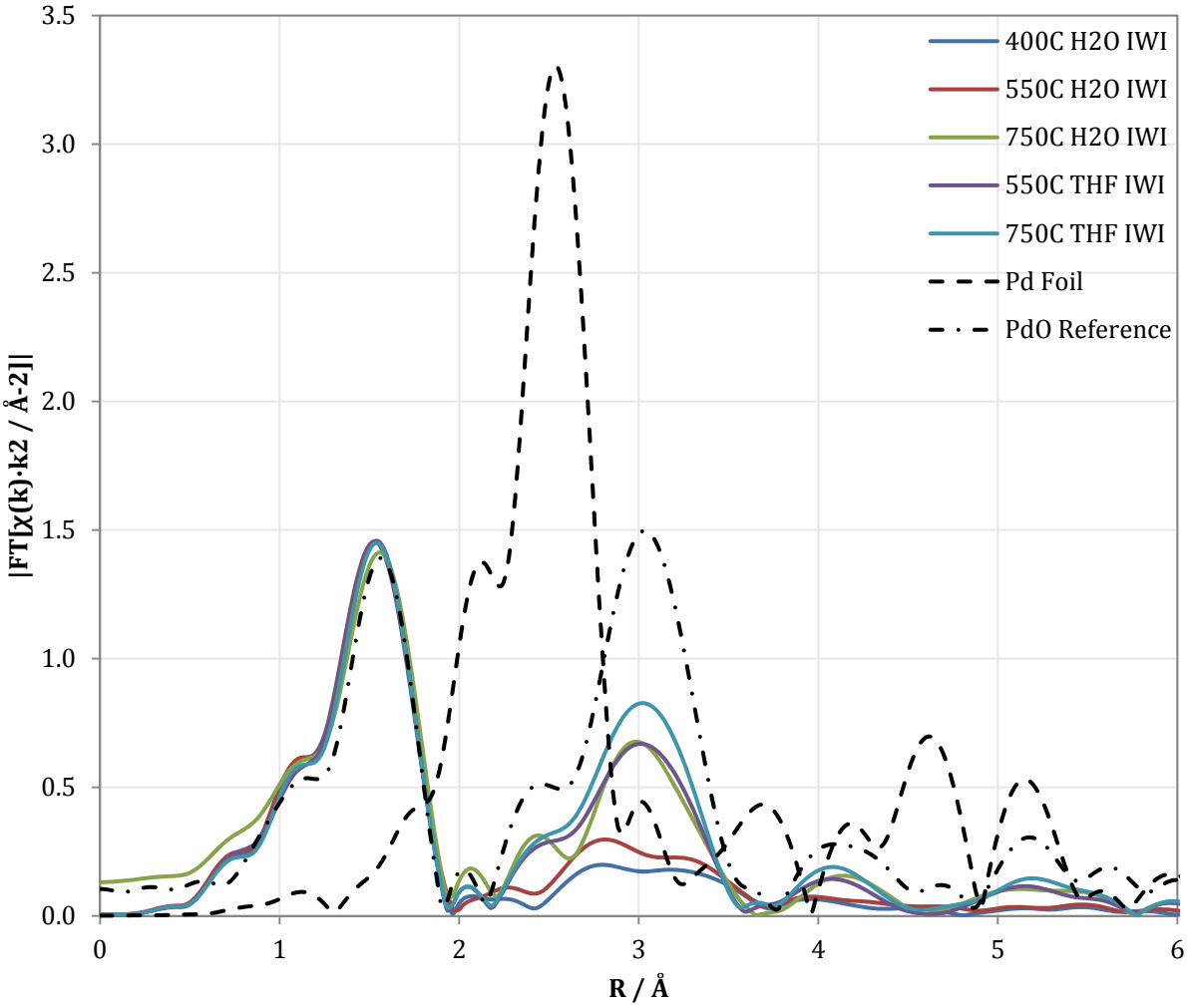

Figure 9: Magnitude of the Fourier transform of the EXAFS of the Pd edge of the calcined catalysts.

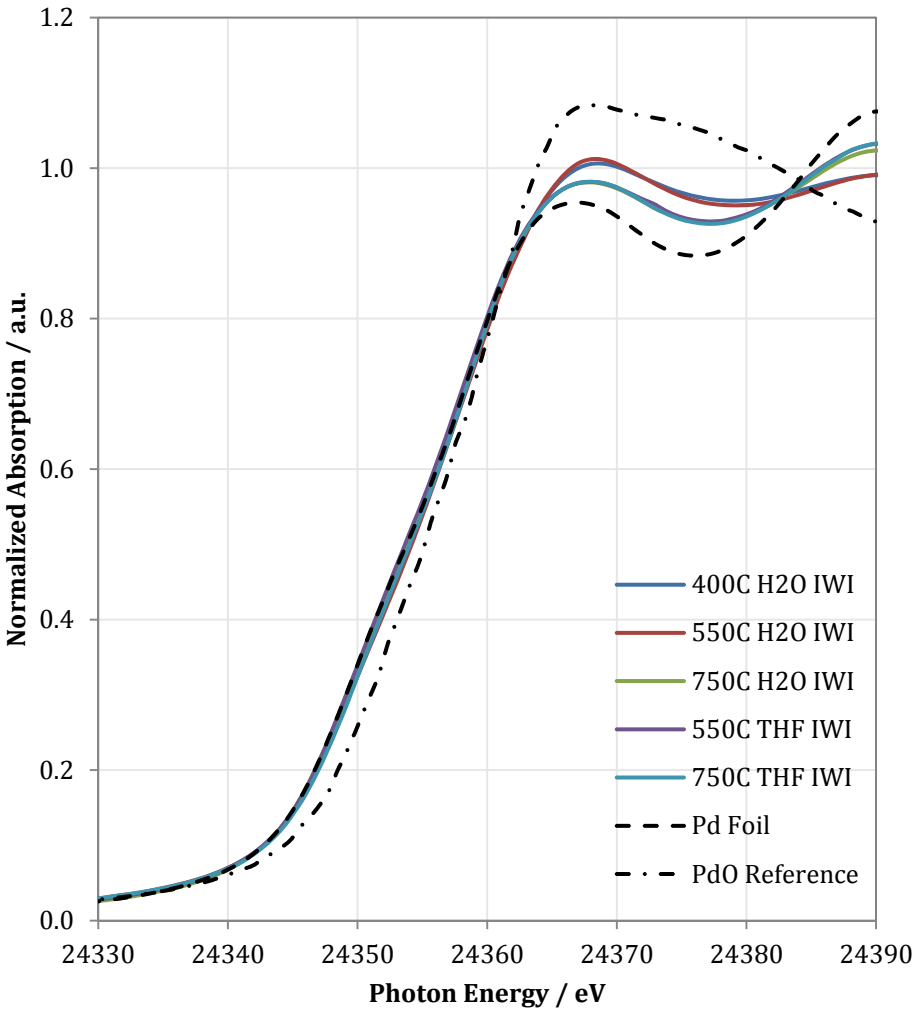

Figure 10: Pd K edge XANES of the PdCuHT catalysts after reduction at 523 K. Spectra recorded in transmission at room temperature under He.

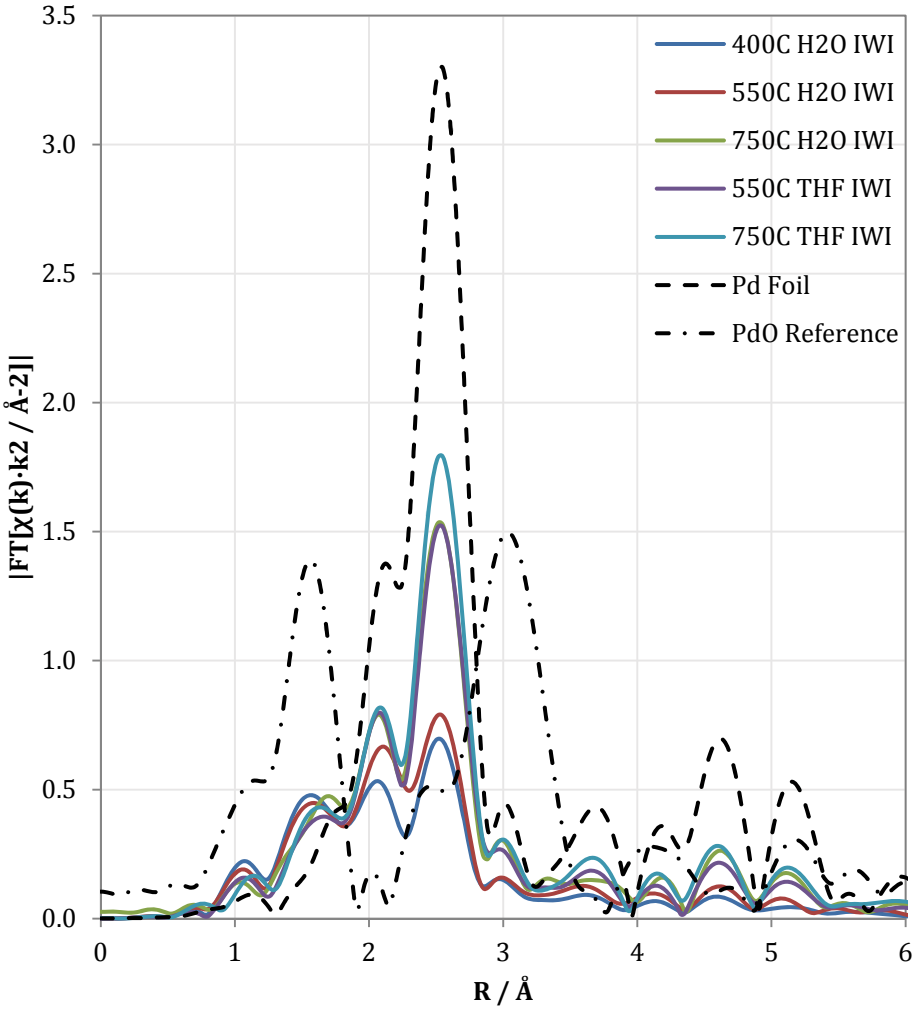

Figure 11: Magnitude of the Fourier transform of the EXAFS region of the Pd K edge spectrum of the reduced catalysts.

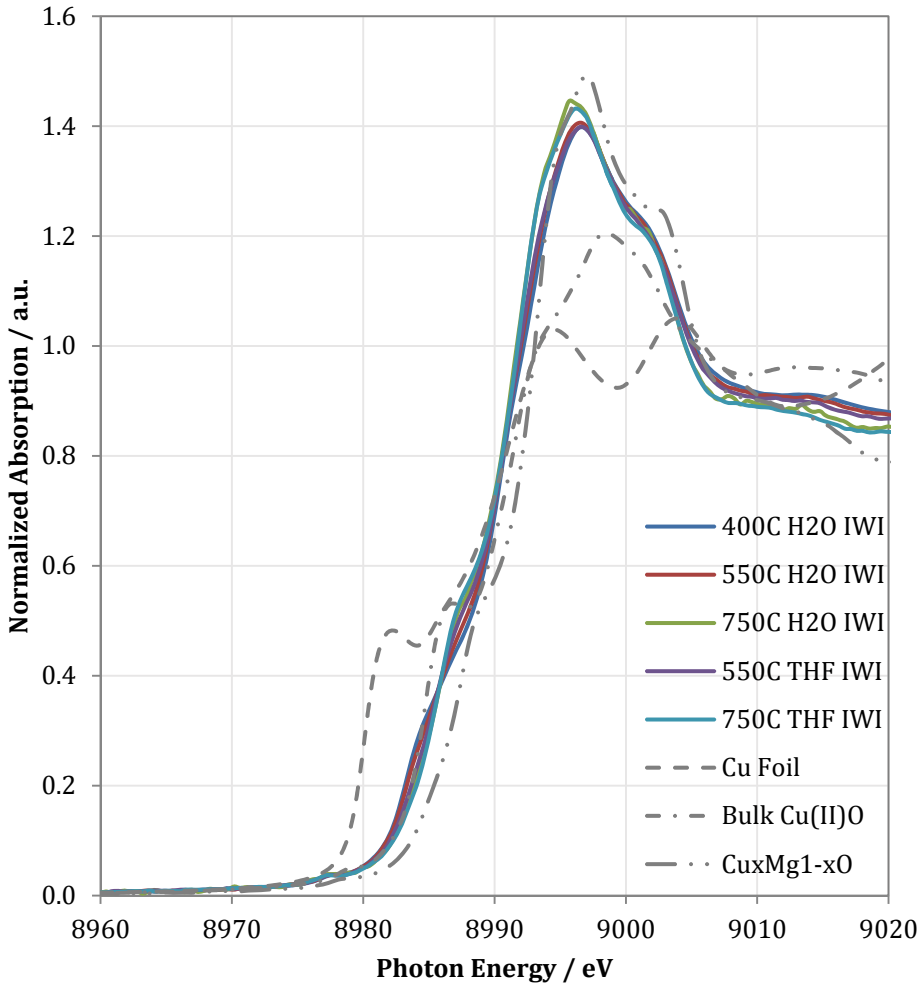

Figure 12: Cu K edge XANES spectra of the calcined PdCu/HT catalysts.

Table 1: Linear combination fitting of the XANES part of the Cu K edge X-ray absorption spectrum

Sample	Treatment	% Cu(0)	% Bulk CuO	% $Cu_xMg_{1-x}O$
Cu Foil	Air RT	100	0	0
CuO Standard	Air RT	0	100	0
$Cu_xMg_{1-x}O$ Standard	Air RT	0	0	100
823 K Calc, H_2O IWI	Air RT	0	24	76
	Reduced at 523 K	No Satisfactory Fit		
1023 K Calc, H_2O IWI	Air RT	0	14	86
	Reduced at 523 K	No Satisfactory Fit		
823 K Calc, THF IWI	Air RT	0	26	74
	Reduced at 523 K	No Satisfactory Fit		
1023 K Calc, THF IWI	Air RT	0	15	85
	Reduced at 523 K	No Satisfactory Fit		

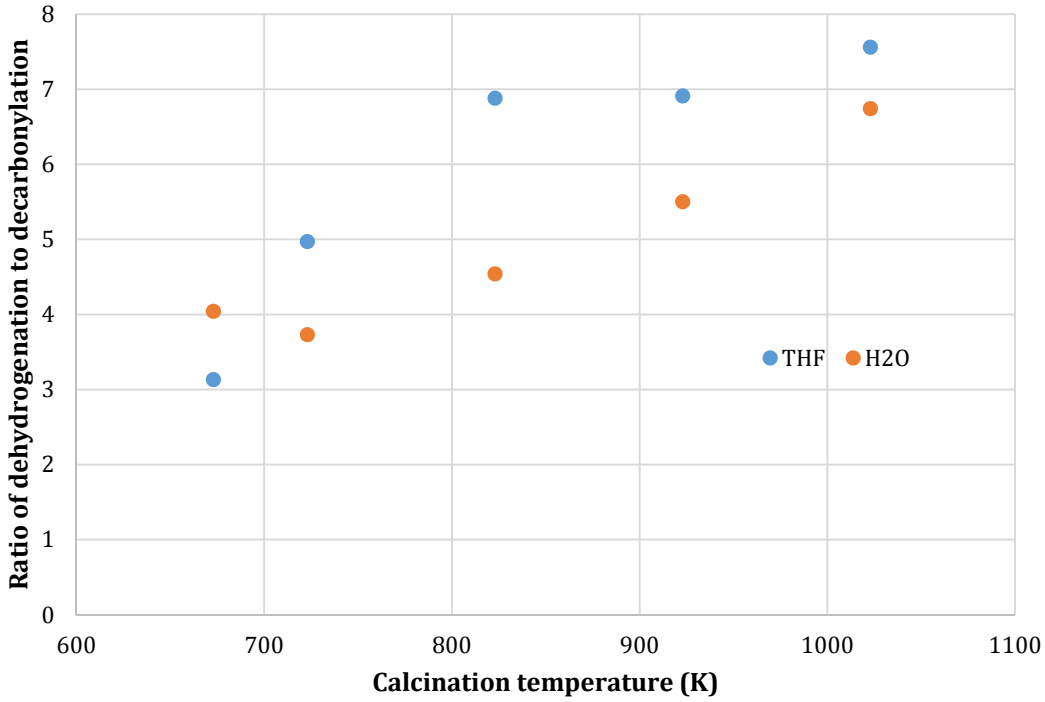

Figure 13: Effects of the calcination temperature on the selectivity of the PdCu/HT catalysts in the gas phase. Flow reaction, gas phase. 150 mg catalyst, 0.4 ml/h mg ABE mix, 50 ml/min He, 473 K

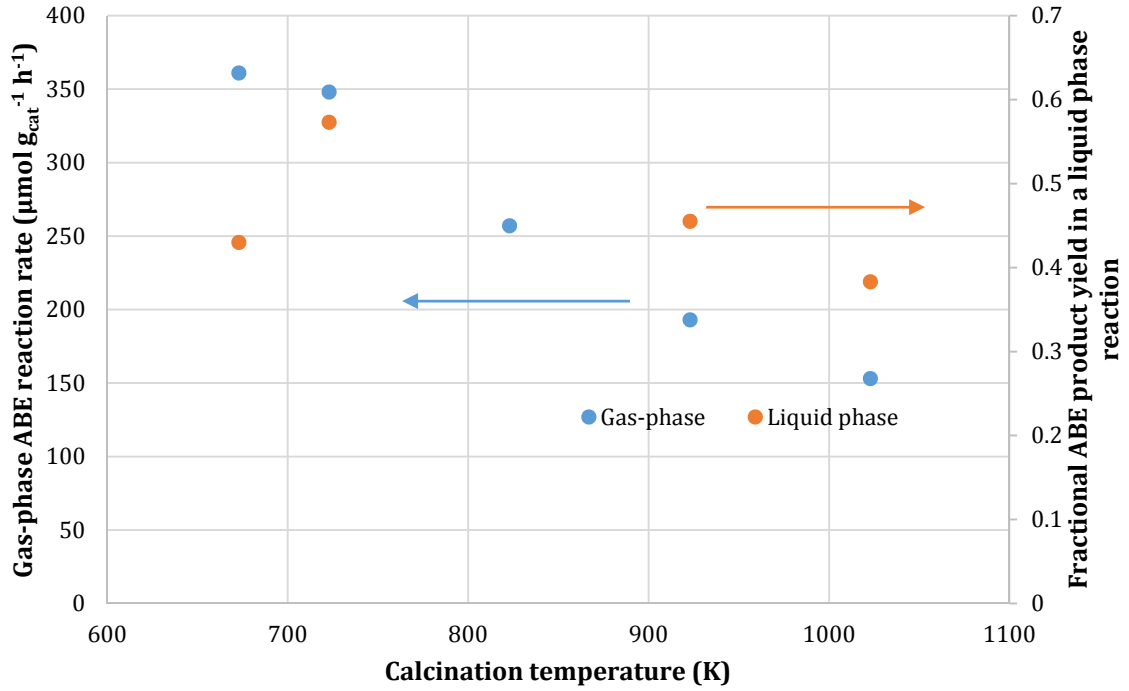

Figure 14: Effects of calcination temperature on the reaction rate of the ABE condensation over PdCuHT catalysts. Flow reaction, gas phase: 150 mg catalyst, 0.4 ml/h mg ABE mix, 50 ml/min He, 473 K. Liquid phase, batch reaction: 150 mg catalyst, 720 mg ABE mix, 75 mg dodecane (int. std.). 513 K, 1 h

Chapter 4: Kinetics of furfural condensation with aliphatic alcohols

INTRODUCTION

Furfural and hydroxymethyl furfural have garnered significant interest as building blocks for biomass-derived fuels in the quest for reduction of CO_2 emissions from transportation fuels.

Chheda et al. [1] reported high yields of furfural and hydroxymethyl furfural (HMF) from monosaccharides and polysaccharides using biphasic batch reactions. Xing et al. [2] have reported a process yielding 90% of theoretical furfural from hemicellulose, using a biphasic continuous flow reactor. Both of these methods use dilute mineral acid as the catalyst. Other researchers have reported the production of furfural from xylose using solid acid catalysts, such as Amberlyst 15 [3], Nafion [4], heteropolyacids [5] and zeolites [6].

Other research groups have focused on the conversion of furfural to fuel and chemical precursors. Modified hydrotalcites have been used to catalyze the Knoevenagel condensation of furfural with malononitrile [3]. Another approach to high value-added products involves the hydrogenation of furfural to saturated derivatives [7], such as furan and furfuryl alcohol. Furfuryl alcohol may subsequently undergo esterification to form levulinic acid esters [8], which then are easily converted to gamma-valerolactone [9]. The condensation of furfural [10] with acetone and that of its hydrogenation products [11] with a range of nucleophiles has been studied and has been shown to give alkanes [12] and other components [13] blendable with diesel fuel after hydrodeoxygenation of the products.

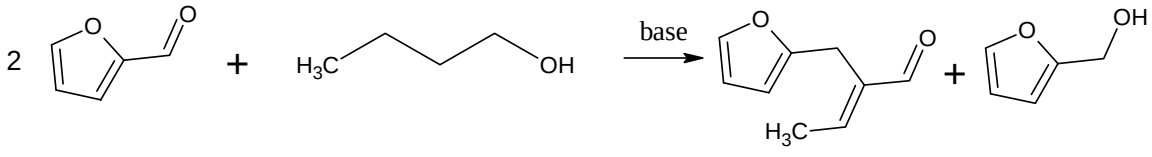

Scheme 1: Reaction of furfural with butanol.

In our recent work [14], we showed that the condensation of furfural with aliphatic alcohols (Scheme 1) yielded unsaturated furfuryl aldehydes that were subsequently converted to gasoline, diesel and jet fuel blendstocks. This sequence achieves a net decrease in greenhouse gas emissions of 50 to 70%, depending on the source of the hydrogen and the alcohols. However, in that paper, there was no attempt to elucidate the mechanism of the reaction.

In this chapter, we use liquid-phase and gas-phase kinetic experiments to investigate the mechanism of the condensation of furfural and alcohols.

MATERIALS AND METHODS

Preparation of Ni-substituted hydrotalcites was carried out by modifying a method described by Climent et al. [15]. Briefly, layered hydroxycarbonates were precipitated from a solution of Ni, Mg and Al nitrates (1.5 M total metal concentration, 3:1 Mg:Al) with an equal volume of a NH_4OH and $(NH_4)_2CO_3$ solution (3.375 M and 1 M, respectively). After precipitation at 333 K, the solids were filtered and washed with copious amounts of warm (323 K) water. The solids were then dried at ambient air at 368 K and calcined at 823 K for 4 h, with a ramp rate of 1 K/min.

Liquid-phase kinetic experiments were performed in 12 mL batch reactors (Qtube, Sigma-Aldrich). In these experiments, the reactants, furfural and butanol were loaded with an appropriate amount of catalyst under air, sealed and heater under stirring to the reaction temperature. After the reaction was complete, the reactor was cooled, the pressure was released and the contents diluted with toluene or THF. The solids were separated and aliquots of the liquid were taken for analysis by GC-MS and GC-FID (Varian 3800, VF-5MS capillary columns).

Gas-phase kinetic experiments were performed in a gas-phase flow reactor setup. Helium and hydrogen gases (Praxair 99.999%) were introduced into the system through mass flow controllers (Parker model 201). Liquid reactants, furfural (Sigma-Aldrich), butanol (Sigma-Aldrich CHROMASOLV ®) and butyraldehyde (TCI America), were introduced into the gas stream through syringe pumps (KD Scientific Legato 100). Transfer lines were heated to above 403 K to prevent condensation of reactants and products. The catalyst bed was supported on a borosilicate glass frit in a tubular reactor with plug-flow hydrodynamics. The temperature of the reactor was kept constant at 413-443 K by an electric furnace (APS PA), controlled by a PID controller (Watlow). The reaction products were analyzed by gas chromatography (Shimadzu GC 2014). Prior to reaction, the catalyst was treated in a 50% H_2/He mixture at 523 K for 1h.

RESULTS AND DISCUSSION

The kinetics of the transfer hydrogenation-aldol condensation reaction over the $Ni(dppe)Cl_2$ and K_2CO_3 catalyst were investigated in the liquid phase.

The reaction progress study over this system showed an induction period over the first few hours of reaction. In this region, no addition product was observed, but butanol was being consumed. This suggests that the formation of an intermediate is taking place. This intermediate could either be the active form of the catalyst, such as the replacement of the Cl^- ligands by butoxide ligands, or an actual intermediate in the reaction pathway. The former hypothesis can be discarded based on the observation that about 0.2 mol of butanol was consumed by the end of the induction period, whereas complete replacement of Cl^- ligands by butoxide would only require the consumption of 0.1 mol of butanol. In control experiments (table 1), no reaction

was observed with butanol and furfural in the absence of the Ni complex, suggesting that its role is the dehydrogenation of the butanol. Consistent with earlier reports [16], the condensation of the furfural with the butyraldehyde proceeded readily over K_2CO_3, both in the presence and the absence of Ni; however, the reaction yields were lower, on the order of 40%, compared to the 80% yield achieved in the original system. This could be due to oligomerization of butyraldehyde and/or furfural at this temperature and high butyraldehyde concentration.

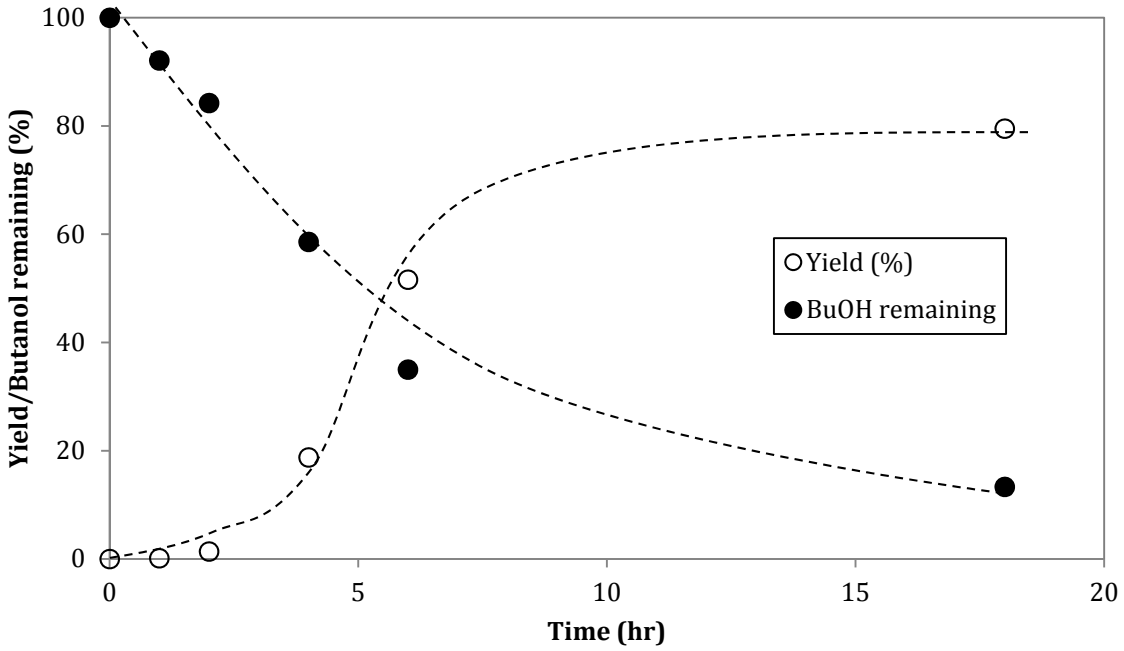

Figure 1: Liquid-phase reaction progress study of the addition of butanol to furfural. 1 mmol butanol, 2 mmol furfural, 1 mL toluene, 423 K. 26.4 mg Ni(dppe)Cl_2, 49.6 mg K_2CO_3. Dashed lines represent qualitative trends.

Table 1: Control experiments for the condensation of furfural with butanol over Ni(dppe)Cl_2 and K_2CO_3. 1 mmol C_4 aliphatic oxygenates, 2 mmol furfural, 423 K.

Catalyst	Reactants	Yield of adduct (%)
0.05 mmol Ni(dppe)Cl_2, 0.3 mmol K_2CO_3	Butanol, furfural	79
0.05 mmol Ni(dppe)Cl_2, 0.3 mmol K_2CO_3	Butyraldehyde, furfural	38
0.3 mmol K_2CO_3	Butyraldehyde, furfural	42
0.3 mmol K_2CO_3	Butanol, furfural	2

It is known that radical mechanisms can be involved in nickel reactions [17] [18]. In order to test this possibility, we added a radical inhibitor, BHT. No reduction of the yield was observed, compared to the control experiment. This observation suggests that a radical mechanism can likely be ruled out.

Metal hydride mechanisms have been invoked as intermediates for the dehydrogenation of alcohols to aldehydes [19] [20]. In order to investigate the possibility of Ni hydrides being intermediates of the reaction, we sampled the headspace of the reaction and analyzed it using GC/TCD. The absence of hydrogen gas in this experiment is an indication that a hydride mechanism is not active in this reaction.

Instead of a Ni-hydride mechanism, we propose that the Ni complex acts as a Lewis acid to coordinate the furfural, which receives a hydride from a Ni n-butoxide intermediate. Such butoxides may be formed by the deprotonation of alcohol by the base (K_2CO_3) and the substitution of one or two chloride ligands on the Ni.

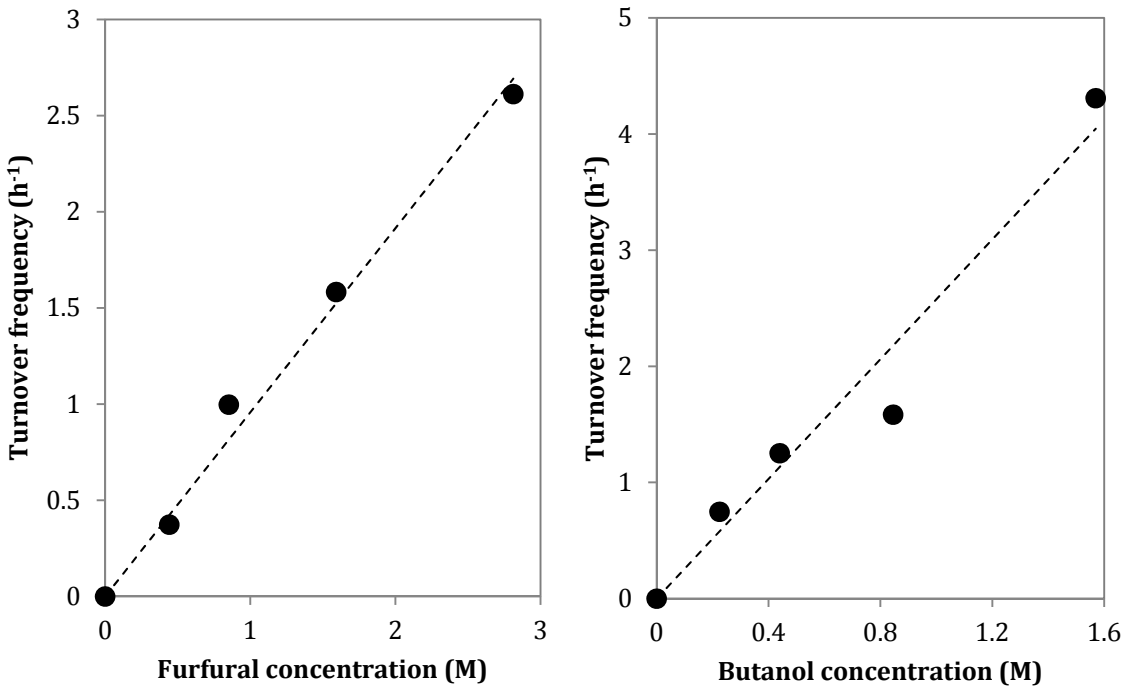

Figure 2: Rate of butanol dehydrogenation as a function of furfural and butanol concentrations. 0.05 mmol Ni(dppe)Cl_2, 0.3 mmol K_2CO_3, 423 K.

No butanol was converted to butyraldehyde in the absence of furfural. This, combined with the observation (fig. 2) that the butanol consumption rate in the induction period was proportional to the furfural pressure is further evidence as to the existence of a transfer hydrogenation mechanism. These observations suggests that the rate-determining step of the catalytic cycle, as depicted in scheme 2, is the transfer of the hydride from the butoxide to the furfural. This transfer is plausible, as it can occur via a favorable six-member transition state.

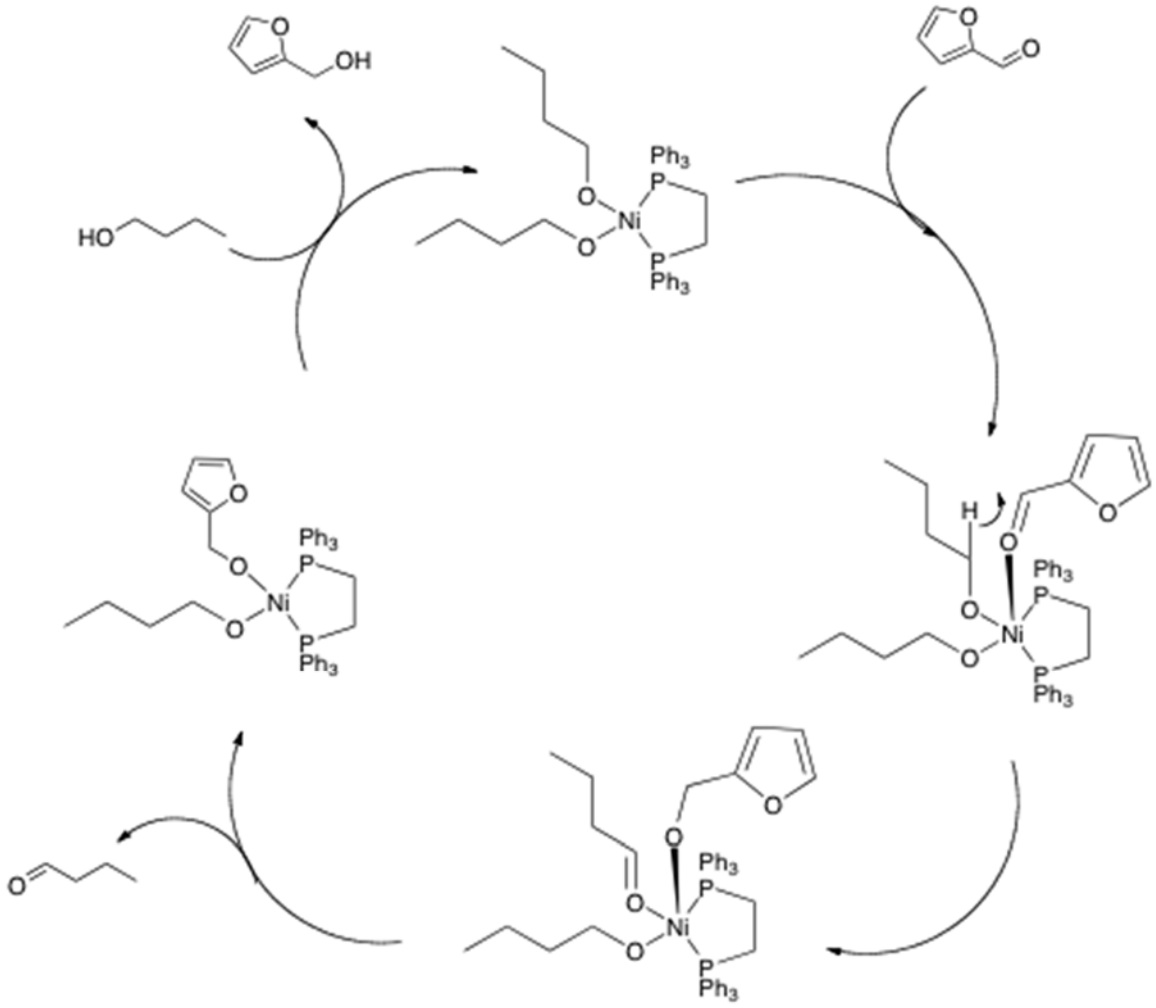

Scheme 2: Mechanism of dehydrogenation of butanol to butyraldehyde via hydride transfer to furfural.

Heterogeneous catalysts are generally preferred in the industry to homogeneous ones, as they are generally more robust and easier to handle. For this reason, we investigated a heterogeneous Ni^{2+} material combined with a base by making a Ni-MgO-Al_2O_3 catalyst from a Ni-substituted hydrotalcite precursor. We also elected to use a gas-phase reaction system to probe the reaction, with the end goal of using a two-bed reactor system to carry out the condensation and the hydrodeoxygenation reactions.

Figure 3 shows the effects of the Ni loading on the reaction rates. Remarkably, both the aldol condensation rate and the dehydrogenation rate decreased with increasing Ni loading on the catalyst, reducing by about a factor of 2, from 0% Ni to 9.6% Ni. This shows that Ni is not required for the reaction to take place. On the contrary, presence of Ni is detrimental to the reaction. The reason for this could be that both reactions take place over basic sites, the intensity of which is reduced upon substitution of Mg^{2+} by Ni^{2+}. Basic solids have been shown to catalyze the dehydrogenation of alcohols via a hydride transfer to a carbonyl group and a

mechanism like this could be in play here as well [21] [22] [23]. Therefore, in order to probe this hypothesis, we carried out a set of kinetic experiments in the reactor.

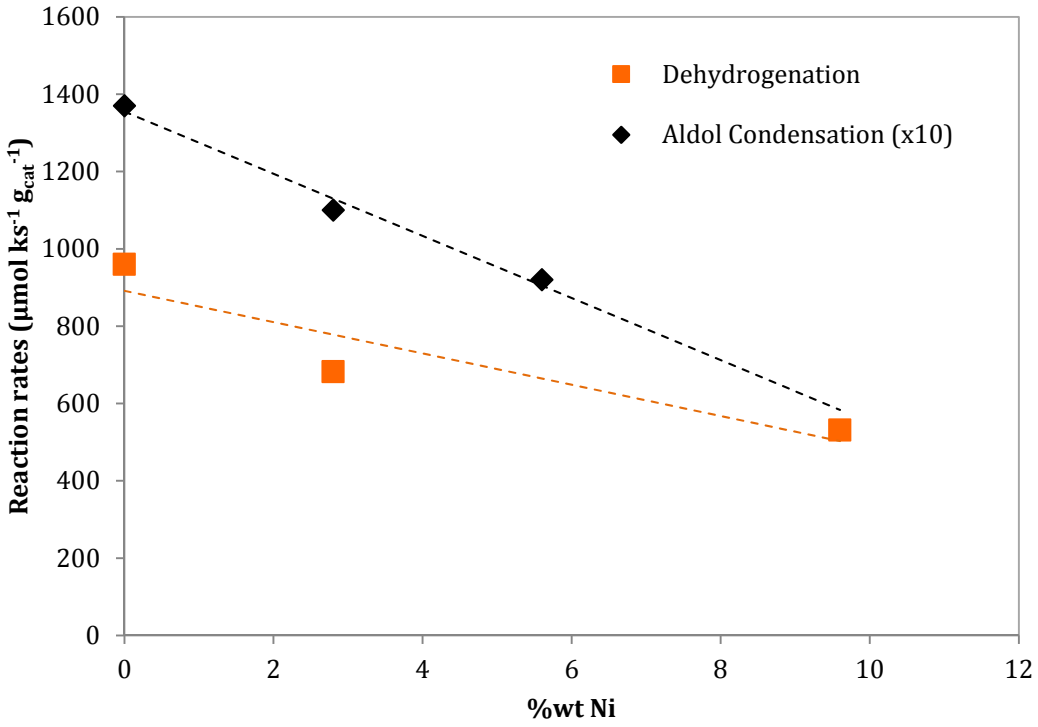

Figure 3: Effects of Ni loading on dehydrogenation and aldol condensation rates. Dashed lines indicate qualitative trends.

Figure 4 shows the selectivity of the reaction as a function of the butanol conversion (controlled by the residence time). At low butanol conversion values, the main product was butyraldehyde. At higher butanol conversion values, selectivity shifts towards the butyraldehyde-furfural adduct. These observations suggest that butanol is first dehydrogenated to the reactive butyraldehyde, which in turn reacts with furfural to form the adduct.

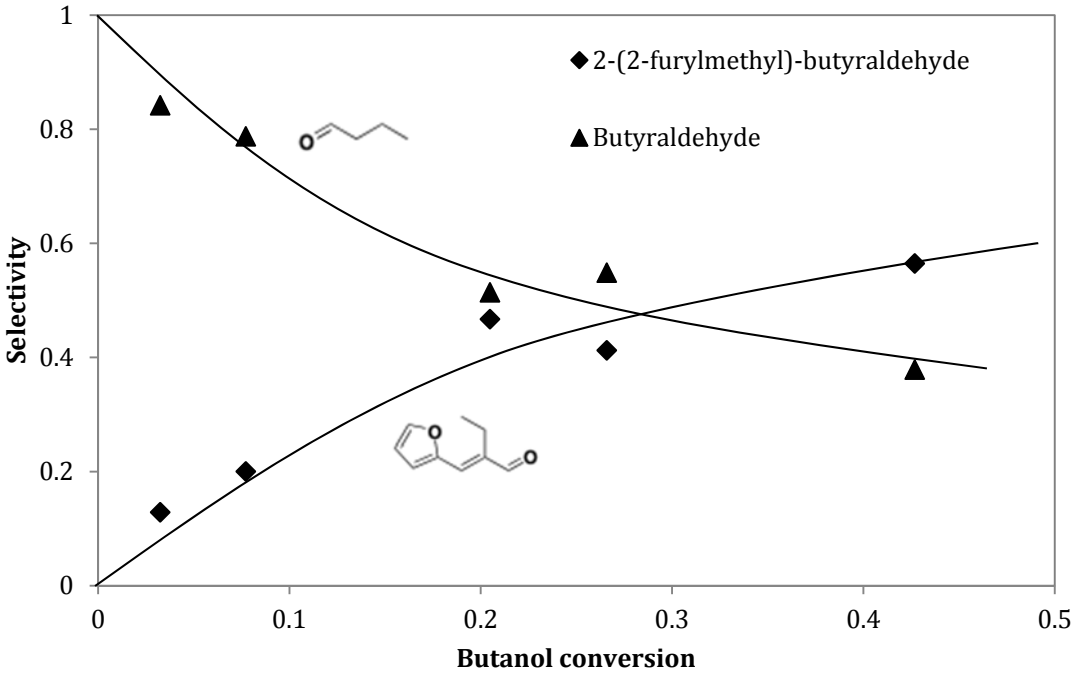

Figure 4: Effects of residence time on the selectivity of the condensation of butanol and furfural.

Figure 4 shows the dependence of the rate of butanol dehydrogenation on furfural and butanol pressures. As was the case in the liquid phase Ni(dppe)Cl_2-catalyzed reaction, the dehydrogenation rate is first-order in furfural. On the other hand, the dependence on butanol pressure shows a first-order dependence at low butanol pressures and is independent of butanol pressure at the higher pressure regime. This is consistent with saturation kinetics, probably arising from increased butoxide coverage in the surface, since basic solids are known to dissociatively adsorb alcohols on their surface, forming alkoxides [24].

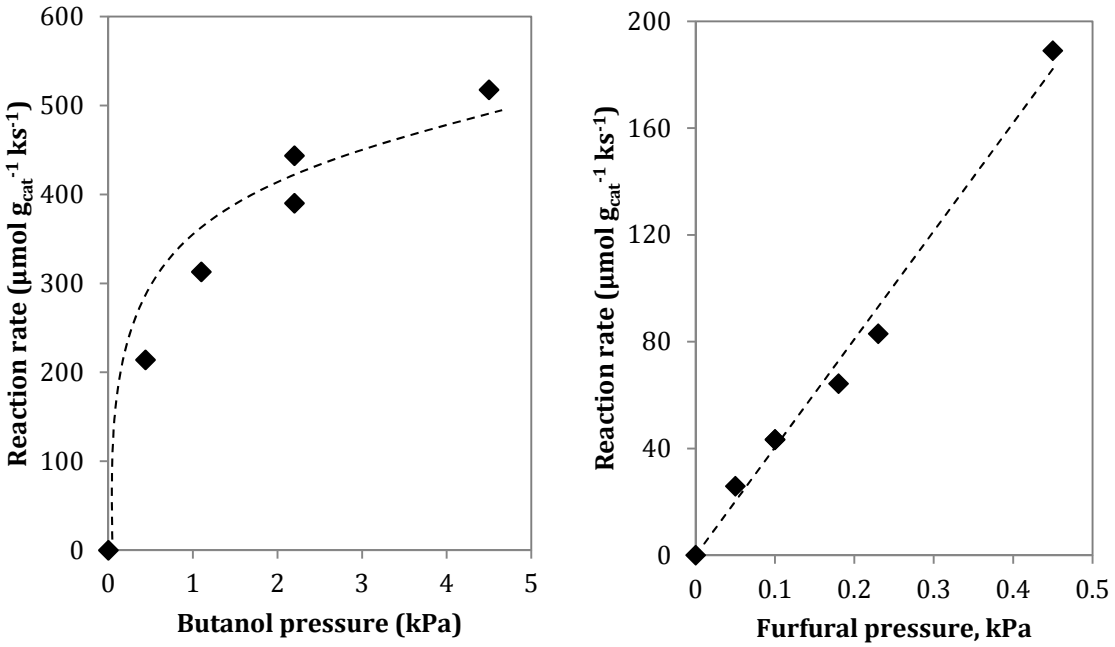

Figure 5: Effects of butanol and furfural pressure on the butanol dehydrogenation rate.

These observations suggest that furfural participates in the rate-limiting step of the butanol dehydrogenation reaction. This is consistent with a Meerwein-Ponndorf-Verley transfer hydrogenation, in which a butoxide on the surface transfers a hydride atom to a molecule of furfural, forming furfuryl alcohol and butyraldehyde. In order to test this hypothesis, we performed kinetic isotope effect experiments, using 1,1-d_2-butanol and butanol-OD. No kinetic isotope effect was detected in the case of butanol deuterated in the OH group. However, in the case of the C_1 di-deuterated butanol, we measured a KIE equal to 2.0. This is consistent with a primary kinetic isotope effect and is suggestive of an C_1-H bond scission in the rate-determining step. The combination of kinetics and isotope effects support the hypothesis that the rate-determining step of this sequence is the hydride transfer from the butoxide to the furfural. The reaction sequence for the transfer hydrogenation is shown in scheme 3 and the proposed transition state is shown in scheme 4.

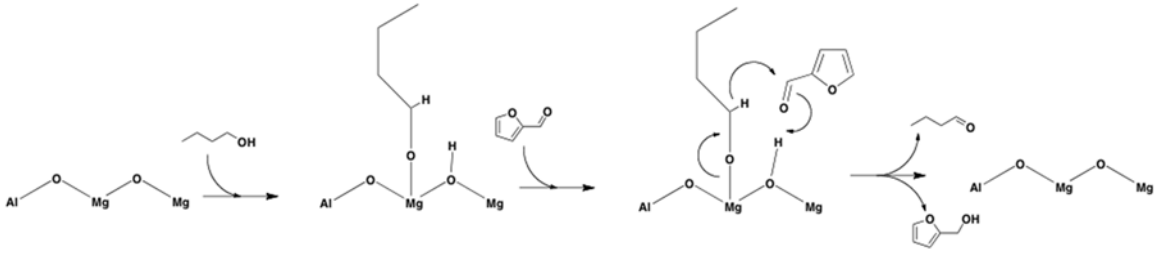

Scheme 3: Mechanism of transfer hydrogenation over a basic catalyst.

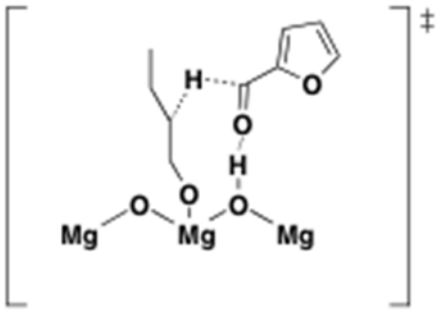

Scheme 4: Proposed transition state for the transfer hydrogenation.

In the condensation step, we propose that the reaction proceeds through an aldol-type mechanism, in which an enolate is formed from butyraldehyde and attacks the electrophilic carbonyl carbon of the furfural, based on the regioselectivity of the product. The condensation mechanism is shown in scheme 5.

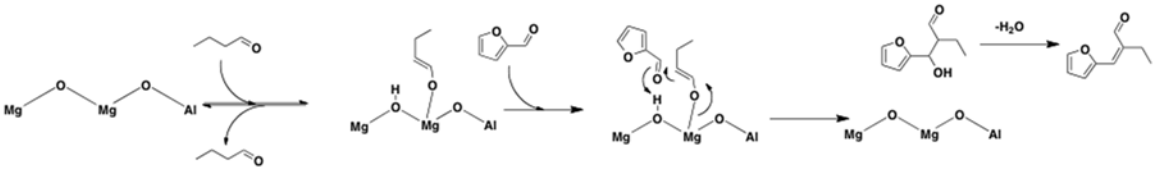

Scheme 5: Mechanism of aldol condensation of butyraldehyde and furfural over calcined hydrotalcite.

The rate of aldol condensation was independent of the butyraldehyde pressure, as can be seen in figure 6. Since the reaction pathway requires the participation of butyraldehyde in every step, this observation shows that butyraldehyde participates in the kinetically relevant step and, at the same time, that it is the most abundant surface intermediate during condensation reactions. It is also noteworthy that the pressure at which butyraldehyde covers the surface completely is much lower than that at which butanol covers the surface completely. This is consistent with the observations of Hanspal et al. [25], who showed that during the ethanol Guerbet reaction, aldehyde species are bound more strongly to an MgO surface than alcohol species, based on Steady State Isotopic Transient Kinetic Analysis (SSITKA) experiments

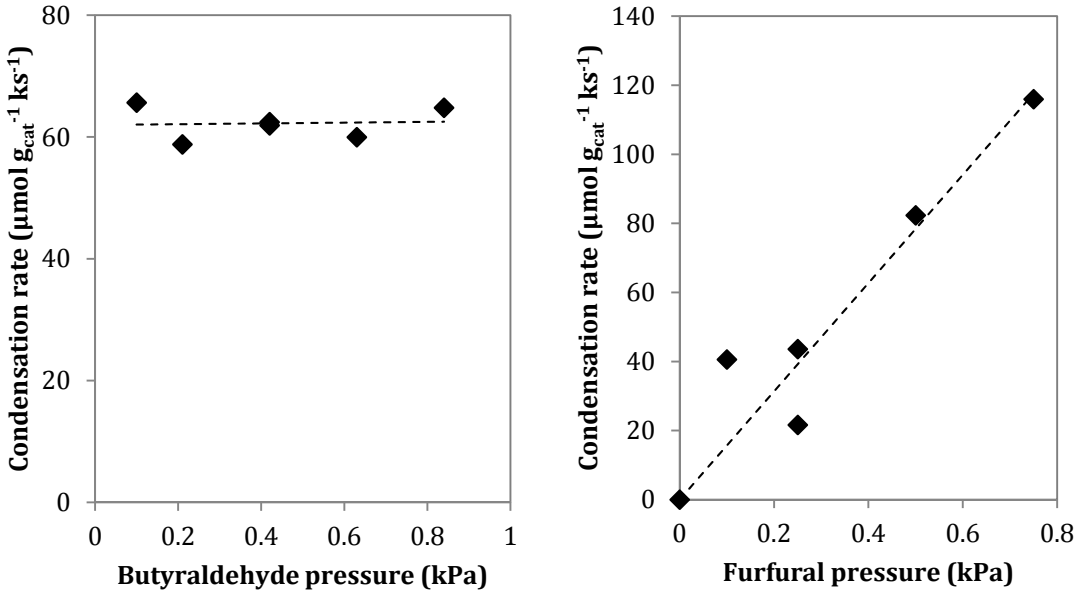

Figure 6: Dependence of aldol condensation rate on butyraldehyde and furfural pressure.

We also observe that the aldol condensation rate showed a first-order dependence on the furfural pressure. This observation enabled us to distinguish between a rate-determining enolate formation step and an equilibrated enolate formation step. In particular, the observation indicates that furfural participates in the rate-determining step of the aldol condensation between furfural and butyraldehyde, signifying an equilibrated enolate formation. This is consistent with the kinetics in chapter 1 of this dissertation, on the condensation of acetone with butyraldehyde and acetaldehyde. There, it was shown that the enolate formation from the acetone is equilibrated with gas-phase acetone. In this case, the observation that furfural participates in the rate-determining step shows that the enolate formation from butyraldehyde is equilibrated and that the C-C bond formation is rate-determining for the condensation of furfural and butyraldehyde.

CONCLUSIONS

In this work, we have shown that the coupling of furfural with aliphatic alcohols proceeds via a transfer hydrogenation-aldol condensation mechanism. The transfer of a hydride from an alkoxide to the furfural is the rate-limiting step in both the homogeneous and heterogeneous cases, as can be shown by kinetic experiments and the kinetic isotope effects. In the heterogeneous system, both the transfer hydrogenation and the aldol condensation are catalyzed by the basic sites on the mixed Mg-Al oxide. On the other hand, in the homogeneous system, the K_2CO_3 base is not strong enough to catalyze the transfer hydrogenation, necessitating the presence of the Ni complex that acts as a Lewis acid to coordinate the furfural and the butoxide and catalyze the hydride transfer.

REFERENCES

[1] J. N. Chheda, Y. Roman-Leshkov and J. A. Dumesic, "Production of 5-hydroxymethylfurfural and furfural by dehydration of biomass-derived mono- and poly-saccharides," *Green Chemistry,* vol. 9, pp. 342-350, 2007.

[2] R. Xing, W. Qi and G. W. Huber, "Production of furfural and carboxylic acids from waste aqueous hemicellulose solutions from the pulp and paper and cellulosic ethanol industries," *Energy and Environmental Science,* vol. 4, pp. 2193-2205, 2011.

[3] M. Shirotori, S. Nishimura and K. Ebitani, "One-pot synthesis of furfural derivatives from pentoses using solid acid and base catalysts," *Catalysis Science and Technology,* vol. 4, pp. 971-978, 2014.

[4] E. Lam, E. Majid, A. C. W. Leung, J. H. Chong, K. A. Mahmoud and J. H. T. Luong, "Synthesis of Furfural from Xylose by Heterogeneous and Reusable Nafion Catalysts," *ChemSusChem,* vol. 4, no. 4, p. 535–541, 2011.

[5] A. S. Dias, M. Martyn Pillinger and A. A. Valente, "Liquid phase dehydration of d-xylose in the presence of Keggin-type heteropolyacids," *Applied Catalysis A: General,* vol. 285, no. 1-2, p. 126–131, 2005.

[6] V. Choudhary, A. B. Pinar, S. I. Sandler, D. G. Vlachos and R. F. Lobo, "Xylose Isomerization to Xylulose and its Dehydration to Furfural in Aqueous Media," *ACS Catalysis,* vol. 1, no. 12, p. 1724–1728, 2011.

[7] P. Gallezot, "Conversion of biomass to selected chemical products," *Chemical Society Reviews,* vol. 41, pp. 1538-1558, 2012.

[8] G. M. González Maldonado, R. S. Assary, J. Dumesic and L. A. Curtiss, "Acid-Catalyzed Conversion of Furfuryl Alcohol to Ethyl Levulinate in Liquid Ethanol," *Energy and Environmental Science,* vol. 5, no. 10, p. 8990–8997, 2012.

[9] D. M. Alonso, S. G. Wettstein and J. A. Dumesic, "Gamma-valerolactone, a sustainable platform molecule derived from lignocellulosic biomass," *Green Chemistry,* vol. 15, pp. 584-595, 2013.

[10] G. W. Huber, J. N. Chheda, C. J. Barrett and J. A. Dumesic, "Production of Liquid Alkanes by Aqueous-Phase Processing of Biomass-Derived Carbohydrates," *Science,* vol. 308, pp. 1446-1450, 2005.

[11] A. Corma, O. de la Torre and M. Renz, "Production of high quality diesel from cellulose and hemicellulose by the Sylvan process: catalysts and process variables," *Energy and Environmental Science,* vol. 5, pp. 6328-6344, 2012.

[12] A. Corma, O. de la Torre, M. Renz and N. Villandier, "Production of High-Quality Diesel from Biomass Waste Products," *Angewandte Chemie,* vol. 123, no. 10, p. 2423–2426, 2011.

[13] M. Balakrishnan, E. R. Sacia and A. T. Bell, "Selective Hydrogenation of Furan-Containing Condensation Products as a Source of Biomass-Derived Diesel Additives," *ChemSusChem,* vol. 7, no. 10, p. 2796–2800, 2014.

[14] S. Sreekumar, M. Balakrishnan, K. A. Goulas, G. Gunbas, A. A. Gokhale, L. Louie, A. T. Bell and F. D. Toste.

[15] M. J. Climent, A. Corma, S. Iborra and A. Velty, "Activated hydrotalcites as catalysts for the synthesis of chalcones of pharmaceutical interest," *Journal of Catalysis,* vol. 221, no. 2, p. 474–482, 2004.

[16] G. M. Strunz and C.-M. Yu, "On the crossed-aldol reaction of cyclohexane-l,2-dione with acetone, and the preparation of pyrroline derivatives from the product," *Canadian Journal of Chemistry,* vol. 66, pp. 1081-1083, 66, 1081 (1988). .

[17] C. Granel, P. Dubois, R. Jérôme and P. Teyssié, "Controlled Radical Polymerization of Methacrylic Monomers in the Presence of a Bis(ortho-chelated) Arylnickel(II) Complex and Different Activated Alkyl Halides," *Macromolecules,* vol. 29, no. 27, p. 8576–8582, 1996.

[18] G. Moineau, M. Minet, P. Dubois, P. Teyssie, T. Senninger and R. Jerome, "Controlled Radical Polymerization of (Meth)acrylates by ATRP with $NiBr_2(PPh_3)_2$ as Catalyst".

[19] F. Shi, M. K. Tse, X. Cui, D. Gördes, D. Michalik, K. Thurow, Y. Deng and M. Beller, "Copper-Catalyzed Alkylation of Sulfonamides with Alcohols," *Angewandte Chemie International Edition,* vol. 48, no. 32, p. 5912–5915, 2009.

[20] C. Li, H. Kawada, X. Sun, H. Xu, Y. Yoneyama and N. Tsubaki, "Highly Efficient Alcohol Oxidation on Nanoporous VSB-5 Nickel Phosphate Catalyst Functionalized by NaOH Treatment," *ChemCatChem,* vol. 3, no. 4, p. 684–689, 2011.

[21] P. S. Kumbhar, J. Sanchez-Valente, J. Lopez and F. Figueras, "Meerwein–Ponndorf–Verley reduction of carbonyl compounds catalysed by Mg–Al hydrotalcite," *Chemical Communications,* pp. 535-536, 1998.

[22] J. R. Ruiz, C. Jiménez-Sanchidrián, J. M. Hidalgo and J. M. Marinas, "Reduction of ketones and aldehydes to alcohols with magnesium–aluminium mixed oxide and 2-propanol," *Journal of Molecular Catalysis A: Chemical,* vol. 246, no. 1-2, p.

190–194, 2006.

[23] Y. Zhu, S. Liu, S. Jaenicke and G. Chuah, "Zirconia catalysts in Meerwein-Ponndorf-Verley reduction of citral," *Catalysis Today,* vol. 97, no. 4, p. 249–255, 2004.

[24] M. A. Barteau, "Organic Reactions at Well-Defined Oxide Surfaces," *Chemical Reviews,* vol. 96, no. 4, pp. 1413-1430 , 1996.

[25] S. Hanspal, Z. D. Young, H. Shou and R. J. Davis, "Multiproduct Steady-State Isotopic Transient Kinetic Analysis of the Ethanol Coupling Reaction over Hydroxyapatite and Magnesia," *ACS Catalysis,* vol. 5, no. 3, p. 1737–1746, 2015.

Chapter 5: Bifunctional pathways of catalytic C-O and C-C bond formation over Cu and TiO_2

INTRODUCTION

As has been shown in the previous chapters of this work and also by multiple researchers in the literature [1, 2, 3], aldol condensation is a viable pathway for upgrading small organic molecules to fuel-grade components through the formation of C-C bonds and the rejection of oxygen as water, with the advantage that aldol condensation reactions of alkanols do not require an external hydrogen source.

Other than the ABE condensation, another possible application of biomass upgrading through aldol condensation is the oligomerization of lignocellulosic ethanol to molecules suitable for mixing with diesel fuel, as their production using current commercial technologies competes with food stocks [4].

Aldol condensation reactions over TiO_2 have been studied under steady state [5] and batch catalysis [6], as well as during temperature programmed experiments [7, 8, 9]. However, extensive deactivation, due to carbonaceous deposits on the surface, has prevented a full understanding of the mechanism and the practical utilization of this process [5].

In previous investigations, Cu-based catalysts have been shown to catalyze the dehydrogenation of alkanols to alkanals. Sad et al. [10] showed that alkanols and alkanals are at equilibrium, the position of which was determined by the hydrogen pressure, for all experimental conditions in their experiments. They also reported that aldol condensation and esterification of propanol and propanal takes place on monofunctional Cu catalysts supported on C, ZnO/Al_2O_3 and on SiO_2. In the course of their investigation, they proposed that the participation of the support in the reaction is negligible and that all the chemistry occurs on Cu.

Other investigators have shown that conversion of lower alkanols and carbonyl compounds can be catalyzed by metals supported on hydrotalcite supports, the role of the metal being the hydrogenation of unsaturated products and the consequent improvement of the thermodynamics for the entire process [1, 11, 12, 13].

In this chapter, we propose combining the functions of a Cu-based catalyst with a TiO_2 catalyst in order to achieve high conversions of an alkanol feed to aldol condensation products of higher molecular weight and carbon to oxygen ratio. In order to achieve this, we propose using the hydrogenation and dehydrogenation functions of the Cu catalysts to equilibrate alkanols and alkanals [12] in the reactants and the products, to prevent deactivation of TiO_2 by hydrogenating unsaturated products of aldol condensation on the TiO_2 catalyst, and to drive the thermodynamics of the process by hydrogenating unsaturated intermediate products. This approach is similar to the one taken by Corma et al. [14] for alkylation reactions over Pd/MgO catalysts. In the course of our investigation, we

measure the effects of the mixing ratio of the Cu and TiO_2 based catalysts, as well as the effects of the partial pressures of reactants and products on the rate of aldol condensation and esterification reactions on the TiO_2. We combine the results of this study with titration experiments in order to propose a mechanism for aldol condensation and esterification reactions on TiO_2.

MATERIALS AND METHODS

Commercial copper catalysts supported on zinc/aluminum oxide ($Cu/ZnO/Al_2O_3$) were obtained from Alfa Aesar (HiFUEL W220).

Single-phase titanium dioxide catalysts were prepared using the methods proposed by Wang and Ying [15]. 50 ml of a 1 M solution of titanium isopropoxide (Sigma Aldrich, 99.99%) in ethanol (Sigma Aldrich, 99.9%) was added dropwise to a solution of 50 ml of ethanol and water under stirring. After at least 2 h of stirring, the mixture was separated by centrifugation. To obtain anatase, the solids were dried overnight at 353 K in stagnant ambient air and subsequently treated in flowing air (Praxair, extra dry) at 723 K (0.083 K s^{-1}) for 2 h. To obtain rutile, the solids were treated in 30 ml of 1 M HNO_3 (Merck) solution for 7 days at 453 K and then filtered and dried at 353 K. After this treatment, they were treated in flowing air at 673 K for 2 h.

Titanium dioxide catalysts were also prepared from Degussa P25 titanium dioxide powder, for purposes of comparison. The TiO_2 powder was washed in deionized water and dried in a static oven at 393 K overnight and then treated in air at 723 K (0.083 K s^{-1}) for 6 h. After this treatment, the powder was hydrated, dried in similar conditions as before and treated in air at 673 K (0.083 K s^{-1}) for 5 h and in hydrogen at 553 K (0.033 K s^{-1}) for 2 h.

Portions of the TiO_2 catalysts were subsequently treated in air for a second time, at higher temperatures (0.083 K s^{-1}, 5 h) to change the anatase to rutile ratio and the surface area. The anatase to rutile ratio after the treatment is shown in table 1.

Platinum and copper were supported on silica using the incipient wetness impregnation procedures outlined in [16] and [10], respectively. Fumed silica (Cab-O-Sil, S = 650 m^2 g^{-1}) was dispersed in deionized water and stirred for 1 h. The solids were recovered by centrifugation and dried in stagnant air for at least 8 h at 383 K. The dried solids or silica gel (Sigma-Aldrich, Davisil grade 62, 60-200 μm) were treated in flowing air at 923 K (0.083 K s^{-1}) for 4 h.

For the 1% Pt/SiO_2 sample, the silicon dioxide was impregnated with aqueous hexachloroplatinic acid (Sigma-Aldrich, 99%). The sample was dried in ambient air at 383 K and subsequently treated in hydrogen at 873 K and passivated a 1% O_2/He mixture at ambient temperature for 1 h.

For the 10% Cu/SiO_2 samples, SiO_2 was impregnated with aqueous copper nitrate hemipentahydrate (Sigma-Aldrich, 99.99% trace metals basis). The impregnated samples were dried in ambient air at 383 K and then treated in flowing dry air at 723 K, in order to decompose the precursor. The samples were then reduced in hydrogen at 553 K and passivated a 1% O_2/He mixture at ambient temperature for 1 h.

After synthesis, the catalysts were sieved down to a particle size of 125 to 250 μm. This is done in order to prevent excessive pressure drop across the catalyst bed during reaction experiments.

Surface areas of all catalysts were measured using automatic Micromeritics ASAP 2020 or Tristar 3000 physisorption analyzers. The BET surface area was obtained using nitrogen physisorption at 77 K.

The phase composition of the metal oxide catalysts was measured by X-ray diffraction in a Siemens D5000 powder diffractometer, using a Cu K_α radiation source and a step size of 0.02 ^{o}/s.

To calculate the anatase to rutile ratio in the TiO_2 catalysts, we used the correlation proposed by Spurr and Myers [17]:

$$x_{anatase} = \frac{1}{1+1.26\frac{I_R}{I_A}}$$

where I_R is the intensity of the rutile peak at $2\theta = 27.5^o$, I_A is the intensity of the anatase peak at $2\theta = 25.4^o$ and $x_{anatase}$ is the mass fraction of anatase in the sample, shown in table 1.

Kinetic measurements were conducted in a tubular plug-flow reactor setup. Helium, hydrogen, and carbon dioxide (all Praxair 99.999% pure) are contained in gas cylinders and were fed to the reactor through mass flow controllers, whereas liquid reactants were fed to the reactor through an injection port. Their flow rate was adjusted by means of an infusion pump and varies between 0.05 and 1.6 ml h^{-1}. The reactor was made of quartz and was placed inside a three-zone furnace, whose temperature was monitored by a thermocouple and adjusted with temperature controllers connected to the heated zones of the furnace. The catalyst bed was supported on a quartz frit inside the reactor. All the transfer lines were heated to above 373 K to avoid condensation of reactants and products.

The effluent of the reactor was injected into a Shimadzu GC 2014 gas chromatograph (GC) using a ten-port Valco sampling valve. Organic products were separated and detected using a polysiloxane capillary column (Agilent Technologies HP-1, 50 m x 320 μm x 1.05 μm) connected to a flame ionization detector (FID). Permanent gases were quantified using a 5 m Porapak Q column (Grace – Davison)

and a thermal conductivity detector (TCD). Each GC run lasted approximately 20 minutes and corresponds to a single data point. Helium was used as carrier gas for both columns.

Before every experiment, the catalyst was treated in a stream of 7% H_2 in He for 2 h at 523 K (unless otherwise noted) before cooling to the reaction temperature. This was done in order to ensure that the Cu or Pt metal was fully reduced prior to the start of the reaction.

RESULTS AND DISCUSSION

SURFACE AREA AND PHASE COMPOSITION

As can be seen in table 1, increasing the treatment temperature of P25-based materials results in a reduction of the surface area and an increase of the rutile phase, consistent with what previous investigators have reported [18, 19, 20].

Investigation of the anatase particle size effects on the reaction was achieved by systematically changing the ratio of titanium isopropoxide to water during the hydrolysis reaction. Higher water contents in the reaction mixture resulted in higher surface area in the finished material (table 2). This has been proposed to be due to the acceleration of the hydrolysis reaction over the agglomeration reactions [15].

MONOFUNCTIONAL CATALYSIS: Cu

Sad et al. [10] have shown that propanol and propanal react over Cu-based catalysts to form coupling products by C-C and C-O bond formation. Cu surfaces have been shown to catalyze the alcohol/carbonyl equilibrium in earlier publications and are also used in the industry for hydrogenation/dehydrogenation reactions involving oxygenates [21, 22, 23]. In particular, under conditions similar to our experimental conditions, alcohols can be assumed to be equilibrated with aldehydes or ketones. As such, the mixture of C_3 oxygenates can be treated as a reactant pool, with the ratio of alcohol to aldehyde/ketone set by the H_2 pressure [10].

If we assume that reaction occurs on the Cu surface [10], we can write a Langmuir-Hinshelwood rate law as follows:

$$\frac{r}{L} = \frac{k(A_1^*)^{n_1}(A_2^*)^{n_2}(A_3^*)^{n_3}}{\left(1+(A_1^*)+(A_2^*)+(A_3^*)\right)^m} \quad (1)$$

where r is the reaction rate, L is the total number of sites, A_i is the surface concentration of species i and k is the intrinsic rate constant of the rate-determining step in the catalytic cycle. The exponent n_i can be equal to 0, 1 or 2 and it reflects the

participation of zero, one or two molecules of species i in the rate-determining step. In this analysis, species 1 is alcohol, species 2 is the surface alkoxide and species 3 is the aldehyde. We have assumed that the hydrogen coverage of the Cu surface is small compared to that of the oxygenates and the empty sites, based on relevant temperature-programmed desorption [24]and kinetic investigations [21, 25] of Cu catalysts.

Alcohol dehydrogenation on Cu has been shown to involve alkoxide intermediates [26]. Since alcohols and aldehydes are equilibrated in our system, the alkoxide intermediates should also be in equilibrium with alcohols and aldehydes. Based on this hypothesis and assuming equilibrated absorption and desorption of aldehydes and alcohols, the rate law can be written as:

$$\frac{r}{L} = \frac{k_1 (K_1 p_1)^{n_1} \left(K_2 \sqrt{p_3 p_1}\right)^{n_2} (K_3 p_3)^{n_3}}{\left(1 + K_1 p_1 + K_2 \sqrt{p_3 p_1} + K_3 p_3\right)^m} \quad (2)$$

We can express all terms as a function of aldehyde pressure and hydrogen pressure:

$$\frac{r}{L} = \frac{k_1 \left(p_3 p_{H_2}\right)^{n_1} \left(p_3 p_{H_2}^{0.5}\right)^{n_2} (p_3)^{n_3}}{\left(1 + K_1 p_3 p_{H_2} + K_2 p_3 p_{H_2}^{0.5} + K_3 p_3\right)^m} = \frac{k_1 \left(p_3^{n_1+n_2+n_3} p_{H_2}^{n_1+0.5n_2}\right)}{\left(1 + p_3 \left(K_1 p_{H_2} + K_2 p_{H_2}^{0.5} + K_3\right)\right)^m} \quad (3)$$

If the hydrogen pressure is constant, the ratio of alcohol to aldehyde is constant, so the rate law can be simplified as:

$$\frac{r}{L} = \frac{k_{obs} p_3^{\,n_1+n_2+n_3}}{\left(1 + K_{obs} p_3\right)^m} = \frac{k_{obs} p_3^{\,n}}{\left(1 + K_{obs} p_3\right)^m} \quad (4)$$

where $n = n_1 + n_2 + n_3$.

At high oxygenate pressures $K_{obs}p_3 >> 1$:

$$\frac{r}{L} = \frac{k_{obs} p_3^{\,n_1+n_2+n_3}}{\left(1 + K_{obs} p_3\right)^m} = \frac{k_{obs} p_3^{\,n}}{\left(K_{obs} p_3\right)^m} \quad (5)$$

Fig. 1 shows that at aldehyde pressures higher than 0.1 kPa, the rate was independent of the aldehyde pressure. This means that the exponents of the pressure terms in the numerator and the denominator are equal: m = n. Going back to the previous rate law and substituting, we obtain:

$$\frac{r}{L} = \frac{k_1 \left(p_3^m p_{H_2}^{n_1+0.5n_2}\right)}{\left(1 + p_3 \left(K_1 p_{H_2} + K_2 p_{H_2}^{0.5} + K_3\right)\right)^m} \quad (6)$$

The trivial case of m = 0 can be ruled out on the basis of the observation that the reaction rates increase with oxygenate pressure at the low-pressure regime.

If we assume that there is only one oxygenate species that covers the surface the rate law can be simplified:

$$\frac{r}{L} = \frac{k_1\left(p_3^m p_{H_2}^{n_1+0.5n_2}\right)}{\left(1+ p_3 K_{obs} p_{H_2}^{0.5n_4}\right)^m} \quad (7)$$

where the parameter n_4 can take the values of 0, 1 and 2 and expresses how many hydrogen atoms are added to the aldehyde to form the MASI.

At high oxygenate pressures, $p_3 K_{obs} p_{H_2}^{0.5n_4} >> 1$, so:

$$\frac{r}{L} = \frac{k_1\left(p_3^m p_{H_2}^{n_1+0.5n_2}\right)}{\left(p_3 K_{obs} p_{H_2}^{0.5n_4}\right)^m} = K p_{H_2}^{n_1+0.5n_2-0.5mn_4} = K p_{H_2}^{j} \quad (8)$$

The j integer expresses the difference in the hydrogen dependences of the numerator and the denominator and can take integer or half-integer values. From figure 2, after fitting, the optimal value of j is close to 1.

$$j = n_1 + \frac{n_2}{2} - \frac{mn_4}{2} = 1 \quad (9)$$

Case 1: m = 1, n_1 = 1 n_2 = 0 n_3 = 0 n_4 = 0

Case 1 corresponds to a unimolecular reaction of an alcohol over one Cu site, with aldehyde being the MASI.

Case 2: m = 2, n_1 = 1 n_2 = 0 n_3 = 1 n_4 = 0

Case 2 corresponds to a bimolecular reaction of an aldehyde and an alcohol over two adjacent Cu sites, with aldehyde being the MASI.

Case 3: m = 2, n_1 = 0 n_2 = 2 n_3 = 0 n_4 = 0

Case 3 corresponds to a bimolecular reaction of two alkoxides over two adjacent Cu sites, with aldehyde being the MASI.

Case 4: m = 2, n_1 = 2 n_2 = 0 n_3 = 0 n_4 = 1

Case 4 corresponds to a bimolecular reaction of two alcohols over two adjacent Cu sites, with alkoxide being the MASI.

We also observed no kinetic isotope effect when deuterated alcohol was used as the reactant together with H_2 in the gas phase. Therefore, we conclude that the rate-determining step over $Cu/ZnO/Al_2O_3$ does not involve an H atom abstraction or that the H atom involved in the rate-determining step is rapidly exchanged. Based on this observation, we can rule out case 1. Case 1 involves the activation of an alcohol, on a

single Cu site, which would presumably be the abstraction of a hydrogen atom. Case 2 can also be ruled out on the basis of this observation.

Case 4 can be ruled out, as the stoichiometry would result in an improbable $C_6H_{16}O_2$ intermediate.

If case 3 were true, it would require the following rate law:

$$\frac{r}{L} = \frac{k_{obs}(p_1 p_3)}{(1 + K_{obs} p_3)^2} (10)$$

Again, if the ratio of alcohol to aldehyde is constant, the rate law becomes:

$$\frac{r}{L} = \frac{k'_{obs}\, p_3^2}{(1 + K'_{obs}\, p_3)^2} (11)$$

which can be written as:

$$\frac{p_3}{\sqrt{r}} = \frac{1}{\sqrt{k'_{obs}}} + \frac{K'_{obs}}{\sqrt{k'_{obs}}} p_3 (12)$$

In figure 3, one can see that this rate law can describe the observed data. This suggests that the coupling of two alkoxides over a Cu surface mostly covered by aldehydes could be the rate-determining step.

BIFUNCTIONAL CATALYSIS-DEACTIVATION

During aldol condensation of aldehydes and ketones over TiO_2 catalysts, extensive deactivation has been known to take place [5, 8, 9]. This deactivation has been attributed to the formation of carbonaceous deposits on the surface of the catalysts [5], on the basis of gravimetric studies. In our experiments, we have also observed extensive deactivation of the catalysts during aldol condensation, concurrent with increased selectivity to mesitylene and other C_9 aromatic species. Heavier aromatic species, formed by the same pathways as mesitylene, remain on the catalyst surface and result in its deactivation.

As can be seen in table 3, the presence of a metal catalyst, such as Cu or Pt, and the introduction of hydrogen to the feed stream prevents catalyst deactivation. Additionally, increasing the pressure of H_2 over the catalyst decreases the deactivation rate constant. Following these observations, we propose that the mechanism for the prevention of deactivation when Pt or Cu are introduced into the system involves the hydrogenation of a C=C bond of an unsaturated intermediate to aromatic products. In their absence, these reactive unsaturated intermediates undergo successive aldol condensations and Michael additions to yield

carbonaceous oligomers that are deposited on the surface, deactivating the active sites [5, 9].

ALCOHOL-CARBONYL EQUILIBRIA

Experiments with physical mixtures of monofunctional $Cu/ZnO/Al_2O_3$ and TiO_2 show that hydrogenation/dehydrogenation reactions approached equilibrium as the Cu content in the bed increased (Fig. 4), for constant space velocity with respect to TiO_2. In contrast, Pt did not catalyze the alcohol/carbonyl equilibrium as readily as Cu. During reactions of propanal over physical mixtures of TiO_2 and Pt-based catalysts, approached to equilibrium for propanal hydrogenation was less than 0.1. Over Pt, propanal hydrogenation rates increased with the hydrogen pressure (fig. 5)

ESTERIFICATION AND ALDOL CONDENSATION

Aldol condensation and esterification take place on both TiO_2 and Cu. Aldol condensation of propanol/propanal over $Cu/ZnO/Al_2O_3$ gave equilibrated mixtures of 2-methyl-3-pentanone and 2-methyl-3-pentanol, whereas aldol condensation of the same molecules occurred over TiO_2 gives 2-methyl-2-pentenal. When $Cu/ZnO/Al_2O_3$ or Pt were added to the TiO_2, we obtained 2-methylpentanal and 2-methyl-1-pentanol, with less or no α,β-unsaturated aldehyde detected. This is consistent with the proposed pathway, of aldol condensation over TiO_2 and hydrogenation over the metal catalyst.

When propanol was fed over TiO_2 or physical mixtures of Pt and TiO_2, no aldol condensation was observed. This suggests that propanal reacts over TiO_2 to form the aldol condensation products and that there are no Guerbet-like direct pathways of propanol to higher alcohols over TiO_2 at our experimental conditions. This observation is also consistent with the trend visible in figure 4, which shows that the total pool conversion rate increases when the Cu content increases: higher Cu content in the bed leads to equilibration earlier, hence higher effective concentration of aldehyde throughout the reactor.

Our results also show that ester was formed over physical mixtures. The increased ester rates in the case of a physical mixture as compared to the $Cu/ZnO/Al_2O_3$, suggests that an esterification pathway that involves the TiO_2 is active (fig. 6 and scheme 1). Ester formation has been reported in the literature over catalysts and reaction conditions similar to the reaction conditions in our experiments. Sad et al. [10] reported the formation of esters over monofunctional Cu catalysts, proposing that surface alkoxides attack physisorbed aldehyde molecules on Cu surfaces. On the other hand, Idriss and Seebauer [27] reported the formation of ethyl acetate during the oxidation of ethanol to acetaldehyde over a TiO_2 surface. They proposed that the ester forms on the TiO_2 surface via a Tishchenko reaction involving two alkanals. However, our results do not agree with this proposal. More specifically, we did not

observe ester formation when pure propionaldehyde was fed over a monofunctional TiO_2 catalyst. If esterification proceeded through the reaction of two surface alkanals, propyl propionate would have been observed in these experiments. In our experiments, we note that the simultaneous presence of alkanol and alkanal is required for esterification to take place over TiO_2. This suggests that the mechanism for the ester formation involves species that derive both from alkanols and alkanals.

The absence of esterification over pure TiO_2 and low rates of esterification over physical mixtures of TiO_2 and Pt/SiO_2, when equilibrated mixtures of aldehydes and alcohols were fed over the catalyst, imply that the presence of Cu is also necessary for esterification over TiO_2-based catalysts. This observation suggests that a step in the esterification reaction takes place over a Cu surface. A possible pathway for esterification over Cu and TiO_2 physical mixtures involves the formation of a hemiacetal over the TiO_2 surface and its dehydrogenation over a Cu surface. Hemiacetal formation and dehydrogenation has been proposed as the mechanism for ester formation over physical mixtures of Cu and ZrO_2-based catalysts [28]. The dehydrogenation of the hemiacetal is a hydroxyl dehydrogenation to a carbonyl, a reaction that is akin to the dehydrogenation of an alcohol to a ketone. For this reason, we would expect this reaction to be faster over a Cu surface than over a Pt surface. This is consistent with the low rates of ester formation observed over Pt and TiO_2 physical mixtures; if alkanol dehydrogenation is slow over a particular catalyst, so should be hemiacetal dehydrogenation.

Figure 7 shows that the esterification rate over TiO_2 increases as the Cu content in the bed increases. If we assume that aldol condensation and esterification stem from a common surface titanium enolate intermediate, we can write a pseudo-steady-state approximation for the hemiacetal:

$$m_{TiO_2} k_1 (ENOL^*) p_{PrOH} = m_{TiO_2} k_{-1} (HA) + m_{Cu} k_2 (HA) \quad (13)$$

Solving for the hemiacetal concentration:

$$(HA) = \frac{m_{TiO_2} k_1 (ENOL^*) p_{PrOH}}{m_{TiO_2} k_{-1} + m_{Cu} k_2} \quad (14)$$

Where (HA) is the hemiacetal pressure, m_{Cu} and m_{TiO2} are the masses of the Cu and TiO_2 catalysts in the bed, respectively. The pressure of propanol and propanal are noted as p_{PrOH} and $p_{Pr=O}$, respectively, and the kinetic rate constants are defined in scheme 2. The assumption that the hemiacetal is a reactive intermediate is backed by the fact that none of it is detected in the gas chromatograph.

The ratio of esterification to aldol condensation can therefore be written:

$$\frac{r_{Est}}{r_{AC}} = \frac{m_{Cu} k_2 (HA)}{m_{TiO_2} k_3 (ENOL^*) p_{Pr=O}} \quad (15)$$

$$\frac{r_{Est}}{r_{AC}} = \frac{m_{Cu}k_2 \dfrac{m_{TiO_2}k_1(ENOL^*)(\mathrm{Pr}OH)}{m_{TiO_2}k_{-1} + m_{Cu}k_2}}{m_{TiO_2}k_3(ENOL^*)(\mathrm{Pr}=O)} \quad (16)$$

And simplifying:

$$\frac{r_{Est}}{r_{AC}} = \frac{m_{Cu}k_1}{m_{TiO_2}k_{-1} + m_{Cu}k_2} \frac{k_2(\mathrm{Pr}OH)}{k_3(\mathrm{Pr}=O)} \quad (17)$$

If the alcohols and aldehydes are equilibrated throughout the reactor:

$$\frac{r_{Est}}{r_{AC}} = \frac{m_{Cu}k_1}{m_{TiO_2}k_{-1} + m_{Cu}k_2} \frac{k_2K_4p_{H_2}}{k_3} \quad (18)$$

And if the hydrogen pressure is constant:

$$\frac{r_{Est}}{r_{AC}} = \frac{m_{Cu}}{m_{TiO_2} + m_{Cu}k_2/k_{-1}} K_{obs} \quad (19)$$

$$\frac{r_{AC}}{r_{Est}} = \frac{k_2}{k_{-1}K_{obs}} + \frac{1}{K_{obs}} \frac{m_{TiO_2}}{m_{Cu}} \quad (20)$$

If this rate law holds, then plotting the ratio of the rates of aldol condensation and esterification at a constant hydrogen pressure against the ratio of the masses of Cu and TiO_2 will give a straight line, which from fig. 8 we can see is the case. Thus, the ratio of esterification to aldol condesation over a physical mixture of Cu and TiO_2-based catalysts can be tuned by the composition of the mixture.

SITE REQUIREMENTS

There has been debate in the literature as to the nature of the site required for aldol condensation over TiO_2. We investigated the possibility of surface alkoxides on TiO_2 catalyzing the aldol condensation and esterification reactions, as surface alkoxides have been reported to catalyze aldol condensation and esterification [10]. To this end, we co-fed *tert*-butanol with ethanol as a co-reactant. A reduction of rates was observed; this suggests that alkoxides are not a catalyst for esterification or aldol condensation. Instead, surface alkoxides inhibit the reaction by occupying surface sites on the TiO_2.

Reduced centers (oxygen vacancies) have been proposed by Benz et al. [29] as the active sites for the self-condensation of benzaldehyde to stilbene. Benz et al. followed this reaction using scanning tunneling microscopy (STM) in ultra-high vacuum conditions. Oxygen vacancies have also been reported to catalyze the formation of alkenes from oxygenates [8]. In this kind of reaction, the oxygen of the

organic oxygenates remains on the surface, covering the vacancy and, simultaneously, alkenes desorb. In our reaction system, the selectivity to light hydrocarbons was less than 0.2%. This suggests that no reduced centers exist in our system. Moreover, increasing the pre-reduction temperature does not result in increased reaction rates. On the contrary, the increase of the pre-reduction temperature to 623 K results in a decrease of the reaction rate . The reason for the decrease is likely that Cu catalysts sinter at higher temperatures. This agrees with the observations of Luo and Falconer [8], who found no difference in aldol condensation reactivity between oxidized and reduced P25 titanium dioxide.

Brønsted and Lewis acid sites have been proposed by Singh et al. [7] as the sites required on TiO_2, on the basis of infrared spectroscopy. Lewis sites have also been proposed by Garro et al. for Mukaiyama aldol condensation over mixed Ti-Si oxides [30]. In order to investigate these possibilities, we used an in-situ titration technique, using 2,6-di-*tert*-butylpyridine (DTBP) as a titrant for the Brønsted acid sites; this molecule has been shown to bind irreversibly to these sites and render them unavailable for reaction [31, 32]. However, in our experiments, no DTBP uptake was detected and the rates did not change upon the introduction of propanol spiked with DTBP. These results suggest that Brønsted acid sites are not present in our sample and do not participate in the reaction under these conditions. Similarly, pyridine was used to titrate the Lewis acid sites and, again, neither titrant uptake nor any reduction in rates was detected. These experiments shows that monofunctional Lewis acid sites also do not participate in the reaction. It also suggests that these sites are not strong enough to bind pyridine at this temperature.

Basic sites have also been proposed as the reactive sites for aldol condensation reactions over metal oxides [1, 33]. Basic sites have been reported to bind acidic molecules, such as CO_2 in different modes, depending on their strength [34]. If monofunctional basic sites are indeed the sites responsible for aldol condensation catalysis over TiO_2, introduction of CO_2 in the feed stream will decrease the rates, as CO_2 binds to the active sites. However, no change in reaction rates was observed upon introduction of CO_2, which implies that monofunctional basic sites do not participate in the aldol condensation reaction over TiO_2.

On the contrary, upon introduction of a protic acidic molecule (propionic acid) reaction rates decreased immediately. This decrease cannot be attributed to coverage of the Cu surface, as the ratio of alkanol to alkanal did not change after the introduction of the acid. Instead, the reduction is attributed to the acid occupying sites on the TiO_2 surface. This observation is consistent with a mechanism in which acid-base pairs catalyze the reaction. Acid-base pairs have been proposed as active sites for reactions such as the anti-Zaitsev dehydration of 2-butanol and for H_2-D_2 exchange [35]. In these reactions, covalent bonds are heterolytically broken, with the resulting anion attaching to an acidic metal atom and the cation attaching to the basic oxygen atom [35]. Combined acid and base sites of intermediate strength have also been proposed as the active sites for aldol condensation over hydrotalcite [36]

and over mixed metal oxides [37], based on temperature-programmed desorption data and kinetic studies.

Protic acids can titrate Lewis acid-base pairs as they can dissociate and titrate the acid and the base in a concerted fashion, the proton attaching to the Lewis basic oxygen and the conjugate base attaching to the Lewis-acidic metal atom, in this case Ti.

PHASE REQUIREMENTS

In experiments over bifunctional TiO_2 and Cu catalyst mixtures, reaction rates decrease with increasing rutile in the sample (Figure 9). In a pure low-surface area rutile sample, prepared by treating P25 at 1073 K, no aldol condensation on TiO_2 was detected. The aldol condensation rate on the TiO_2 was also negligible in the case of a high-surface area rutile sample, prepared according to Wang and Ying [15]. This indicates that anatase is the active phase for aldol condensation and esterification under our experimental conditions. Similarly, over mixtures of TiO_2 and Pt catalysts, we observed much higher reaction rates for anatase than for rutile (figure 10).

This seemingly goes against the conclusions of Rekoske and Barteau [38], who report that both anatase and rutile can catalyze aldol condensation at a temperature range of 313 – 373 K. They also propose that the activation energy for aldol condensation was higher on anatase than on rutile and suggest that anatase surfaces have a higher number of sites capable of catalyzing aldol condensation. As an alternative, they propose that rutile sites are not capable of catalytic turnover, deactivating after one reaction. Our experiments support the latter hypothesis, since very little catalytic reaction is observed over rutile.

INFRARED SPECTROSCOPY

We utilized infrared spectroscopy to investigate the differences between anatase and rutile in operando. During steady-state catalytic conversion of acetone, we observed an increase of the broad band centered at 1576 cm^{-1} (figure 11), which is consistent with an aromatic or conjugated C=C bond stretch. The breadth of the band could be due to the superposition of the absorptions of a set of different aromatic molecules on the surface. This band persisted after the flow of acetone was stopped, indicating that this is a surface species that cannot desorb at the experimental conditions. On the contrary, no change in the spectrum over time was observed over rutile (figure 12). This behavior is consistent with the higher reactivity of anatase and the deactivation of the catalyst reported earlier in this work.

PARTICLE SIZE EFFECTS

The anatase particle size effects were investigated, using both a bifunctional mixture of $Cu/ZnO/Al_2O_3$ and TiO_2, with ethanol as the reactant, as well as a Pt/SiO_2 and

TiO_2 mixture, with acetone as the reactant. In these experiments, we see two different effects: in the bifunctional system, with ethanol as the reactant, the anatase surface was mostly clean. In contrast, under the conditions of the monofunctional system, the most abundant surface intermediate was the acetone. Smaller anatase particles will tend to be more reactive towards enolate formation and will also bind oxygenates more strongly. This is a possible reason for the trends observed in figure 13: In the case of the acetone, the ketone pressure is much higher than the aldehyde pressure in the case of the $Cu/ZnO/Al_2O_3$ and TiO_2 physical mixtures, so we would expect the adsorption to play a more important role in that system.

EFFECTS OF REACTANT PRESSURE AND SPACE VELOCITY

The ratio of aldol condensation to esterification depends linearly on the ratio of alkanol to alkanal pressure for a range of space velocities and alkanol pressures (Fig. 14, 15). This indicates that both reactions happen on the same site and proceed from a common intermediate that reacts with an alkanol to form the ester or with an alkanal to form the aldol condensation products. Further support for this argument comes from the observation that the introduction of various inhibitors, such as m-cresol and t-butanol did not result in a change in the esterification to aldol condensation rate ratio.

In metal-metal oxide physical mixtures, decreasing the space velocity resulted in higher ratios of C_{3n} to C_{2n} products, as seen in Fig. 16. This observation indicates that the C_{3n} products are formed by C_{2n} products returning to the surface and reacting with the C_n reactants, in a manner consistent with an A→B→E mechanism, where A is C_n, B is C_{2n} and E is C_{3n}.

In contrast, in the absence of a metal that hydrogenates the C=C bonds, the ratio of C_9 to C_6 products was independent of space velocity, as seen in fig. 17. This result indicates that 2-methyl-2-pentenal, the only C_6 aldol condensation product of propanal, does not react further to form C_9 products. The reason for this is that 2-methyl-2-pentenal does not have an acidic α-H atom that can be abstracted to give an enolate.

As the space velocity was decreased, the reaction rates also decreases, as seen in Fig. 18, suggesting product inhibition. A possible inhibiting product is water, which has been reported to inhibit aldol condensation in similar systems [1], as it dissociates to form surface hydroxyls [39]. If water is the product that inhibits, then co-feeding water at a concentration an order of magnitude higher than the water produced from the reaction will eliminate the space velocity effects. However, as can be seen in figure 18, cofeeding water did not eliminate space velocity effects, despite the fact that the rates were reduced. This suggests that another product or group of products also causes a reduction in rates, a possible candidate being the higher esterification and aldol condensation products.

WATER EFFECTS

Cofeeding water over $Cu/ZnO/Al_2O_3$ and TiO_2 physical mixtures and also over $Cu/ZnO/Al_2O_3$ monofunctional catalysts resulted in carboxylic acid formation. Over both catalyst systems, the carboxylic acid formation rate was proportional to the partial pressure of the aldehyde (figures 19 and 20). Over the TiO_2 and $Cu/ZnO/Al_2O_3$ physical mixture, the carboxylic acid formation rate was proportional to the water pressure to the half power (figure 20). This suggests that the aldehyde is reacting with hydroxyl groups and not water molecules. Therefore, it is possible that the propionic acid formation takes place on TiO_2, as a water molecule reacting with an acid-base pair will give a pair of surface hydroxyls on the TiO_2 surface. It is to note that the trendlines for the dependence of propionic acid formation on water or propionaldehyde do not go through the origin. The discrepancy could arise from the fact that propionic acid tends to bind onto the gas chromatograph column and give poor results, especially in low concentrations [40].

Interestingly, increasing the space velocity over a bifunctional catalyst resulted in higher propionic acid formation rates (figure 21). This increase cannot be attributed to product inhibition, as the ratio of ester to acid increases linearly with pool conversion (figure 22). The reason for this increase could be that the acid reacts with an alcohol over either the Cu or the TiO_2 surface to form the ester, hence providing another pathway to esterification.

Cofeeding water also resulted in a slight decrease of the esterification to aldol condensation rate ratio. This is possibly due to the propionic acid or the water binding selectively to Cu sites: on figure 23 one can see that the Cu is strongly affected by increased H_2O pressures. As mentioned previously, decreasing the effective ratio of Cu to TiO_2 sites decreased the esterification to aldol condensation rate ratio, both by decreasing the hemiacetal dehydrogenation as well as the direct esterification over $Cu/ZnO/Al_2O_3$.

REACTANT PRESSURE EFFECTS

Over TiO_2 catalysts, the total reaction rate depends mainly on the carbonyl compound pressure and the space velocity, as mentioned above. The effect of the carbonyl compound pressure can be seen in fig 24 for the physical mixtures with $Cu/ZnO/Al_2O_3$ and in fig 25 for the physical mixtures with Pt/SiO_2. It can be seen from fig. 24 that there is an inhibitory effect of the alkanol, which can be attributed to the alkanol competing for sites on the TiO_2 with the alkanal. The same phenomenon also accounts for the lower reaction rates at higher hydrogen pressures (fig 25 and 26); as stated before, higher hydrogen pressures result in higher alkanol formation rates. Molecular and dissociative adsorption of alkanols on TiO_2 to form surface alkoxides has been reported in a number of earlier studies [41, 42, 43].

We propose that dissociative adsorption is the mechanism with which the alkanols inhibit the rate, as molecularly adsorbed alcohols desorb at temperatures much lower than the reaction temperature [41]. A mechanism in which the alkanols inhibit the reactions by taking up sites on the Cu surface was also considered, but rejected on the basis that the ratio of the esterification to the aldol condensation rates did not change with the introduction of a tertiary alcohol; if the increasing alkanol partial pressures inhibited the hydrogenation/dehydrogenation functions on the Cu, the result would be a different product distribution, as Cu takes part in the esterification pathway but not in the aldol condensation pathway.

PROPOSED MECHANISM AND RATE LAW

Based on the titration results and the aforementioned rate data, we propose a mechanism involving the formation of a surface titanium enolate (scheme 3). In step 0, the oxygen of the alkanal (base) coordinates on the Ti atom (Lewis acid). The coordination of the aldehyde through the carbonyl oxygen, with concurrent reduction of the double bond character between C and O has been shown in infrared studies [38]. Following that, in step 1, the acidic α-hydrogen of the alkanal is abstracted by the surface O atom, which acts as a base. This concerted enolate formation step is followed by a nucleophilic attack from the enolate on the carbon of the carbonyl group of a gas-phase or weakly adsorbed alkanal (step 2), forming the aldol, which is rapidly dehydrated (step 3) or by the reaction of the enolate and an alkanol, which results in the formation of the hemiacetal and subsequently the ester, after dehydrogenation of the hemiacetal intermediate over Cu, as described previously. (step 4)

After the dehydration of the aldol, the resulting α,β-unsaturated aldehyde is hydrogenated on the Cu surface to an equilibrated alkanol/alkanal mixture. The alkanal in this mixture reacts further on the TiO_2 surface to form heavier products, which are the C_{3n} aldol condensation and ester products.

Assuming a differential reactor and a rapid dehydration of the aldol, we can write a kinetic rate expression for the formation of the aldol and the hemiacetal, in keeping with the aforementioned mechanism:

$$r = k_2[Enolate*]p_{aldehyde} + k_4[Enolate*]p_{alcohol} \quad (21)$$

For this rate expression, we apply the quasi-steady-state approximation for the surface enolates.

$$\frac{d[Enolate*]}{dt} = 0 = k_1[Aldehyde*] - k_{-1}[Enolate*] - k_2[Enolate*]p_{aldehyde} - k_4[Enolate*]p_{alcohol} \quad (22)$$

There are two limiting cases to the previous equation. In the first, the enolate formation is irreversible and in the second, the enolate formation is completely

equilibrated. Applying these limiting cases to the rate law, and using a site balance we obtain two different possible kinetic models, equations 23a and 23b.

$$\frac{r}{[L]} = \frac{K_0 k_1 p_{aldehyde}}{1 + K_0 p_{aldehyde} + K_5 p_{alcohol} + K_6 \left(p_{alcohol} + p_{aldehyde}\right) x_{pool}} \quad (23a)$$

$$\frac{r}{[L]} = \frac{K_0 K_1 p_{aldehyde} \left(p_{aldehyde} + p_{alcohol}\right)}{1 + K_0 p_{aldehyde} + K_5 p_{alcohol} + K_6 \left(p_{alcohol} + p_{aldehyde}\right) x_{pool}} \quad (23b)$$

To account for the reduction of rates with increasing conversion, we included a fourth term in the denominator: $K_6 x_{pool}(p_{alcohol}+p_{aldehyde})$. This term corresponds to products competing for sites on the TiO_2 surface.

To distinguish between the two possible models, we used the Athena modeling software on a set (n=43) of kinetic data for 1-propanol. The modeling results yielded a very satisfactory correlation for the irreversible enolate formation (R^2 = 0.987) and a very poor correlation in the case of the equilibrated enolate formation (R^2 = 0.582). In table 5, one can see the results of the kinetic modeling for the irreversible enolate formation case.

It can be seen that the term corresponding to the product adsorption is larger than the term for the aldehyde adsorption. This is consistent with the observation that reaction rates decrease with increasing conversion, due to product inhibition. For this to happen, the products must adsorb more strongly to the surface than the reactants. It is also consistent with the relevant observations of Rekoske and Barteau [38], who reported competitive adsorption of crotonaldehyde with acetaldehyde on both anatase and rutile, based on infrared studies.

We also measured the activation energy for self-condensation of acetone over a physical mixture of TiO_2 and Pt/SiO_2 catalyst, as well as the activation energy for enolate formation in the case of a physical mixture of TiO_2 and $Cu/ZnO/Al_2O_3$ catalysts. In the former case, rate values were interpolated to 5 kPa acetone and a conversion of 2%. At 463 K, the rate did not depend on acetone pressure for $p_{acetone}$ > 2 kPa. Assuming a Langmuir-Hinshelwood mechanism as mentioned above, at the flat region, the reaction rate will be approximately equal to the intrinsic kinetic rate constant for the α-H abstraction. From this Arrhenius plot (fig. 27), we calculated activation energy equal to 36±3 kJ/mol.

Similarly, for the Cu and TiO_2 physical mixture system (figure 28), we measured the reaction rate for aldol condensation over a physical mixture of TiO_2 and $Cu/ZnO/Al_2O_3$ and corrected it by the ratio of alkanol to alkanal, in order to obtain the total enolate formation rate. In this case, the activation energy of enolate formation is equal to 38±3 kJ/mol.

Further evidence as to the irreversibility of the α-H abstraction can be found at the kinetic isotope effect experiments. In these experiments, we measured the

difference of the intrinsic kinetic rate constant, when using acetone and perdeuterated acetone. Defining the kinetic isotope effect (KIE) as:

$$KIE = \frac{k_H}{k_D},$$

where k_H and k_D are the kinetic rate constants for the natural-abundance reactant and for the perdeuterated reactant, respectively, we obtained a KIE for the aldol condensation of acetone equal to 2.1 (figure 29). This is within the range for a primary kinetic isotope effect, which indicates that a bond to a hydrogen atom is broken in the kinetically relevant step. This is consistent with the hypothesis that the rate-determining step is the α-H abstraction.

POSSIBLE APPLICATIONS

Increasing the reaction temperature increases both the intrinsic rate constant, through an Arrhenius-type expression, as well as the concentration of the reactant alkanal, as higher temperatures favor dehydrogenation of the alkanol. In this way, the system can be used practically for the conversion of ethanol to diesel-range components. Indeed, the conversion of the C_2 oxygenate pool increases with increasing temperature. Reducing the space velocity can also increase the conversion of the C_2 pool and increase the selectivity to higher products, as mentioned before. In Table 6, one can see the effects of increasing space velocity and temperature on the conversion and the selectivity patterns. Conversions of the C_2 pool up to 88.3% can be achieved at space velocities of 7.6×10^{-3} $mol_{ethanol}$ $(g_{TiO2}ks)^{-1}$ and temperatures of 573 K. There is no observable catalyst deactivation up to 543 K. At higher temperatures, a reduction of rates with time-on-stream is observed, combined with lower approaches to equilibrium. This deactivation is presumed to be due to deactivation of the Cu component of the physical mixture, as suggested by the lower approach to equilibrium. The most probable mechanism for this observed deactivation is the sintering of the Cu particles, which are known to deactivate at higher temperatures [44].

During aldol condensation, oxygen is rejected from the organic molecules as water. As a result, the heavier products have a lower O/C ratio (Figure 30) and are consequently hydrophobic. Because of this, the liquid in the condensate trap separates spontaneously into two phases, a hydrophobic and an aqueous one, facilitating separation of the desired heavy products from the undesired aqueous phase. The gas phase contains H_2 and unreacted light (C_2-C_6) oxygenates (inset in figure 30), which in practice would be returned to the reactor to react further.

CONCLUSIONS

In this study, we investigated the behavior of aldol condensation and esterification reactions of alcohols, aldehydes and ketones over physical mixtures of Cu, Pt and TiO_2 based catalysts. The presence of metals and hydrogen has been shown to stabilize the reaction rates, preventing deactivation by hydrogenating reactive unsaturated intermediates. In these systems, Cu dehydrogenates the alkanol to equilibrium and the resulting alkanal or ketone undergoes self-aldol condensation or esterification with an alkanol over the TiO_2 catalyst. The unsaturated products from the aldol condensation are in turn hydrogenated over the Cu or Pt catalyst. Based on titration and kinetic experiment results, the required site for aldol condensation and esterification is a Lewis acid-base pair on the anatase TiO_2 surface. The rate-determining step in the reaction sequence is the formation of a surface enolate. This enolate participates in a nucleophilic attack on the carbonyl carbon of an alkanal to give the α,β-unsaturated alkanal or in a reaction with an alkanol to give a hemiacetal, which is in turn dehydrogenated over a Cu surface to form the ester. The rate of this step is controlled by the Cu content in the bed. This way, the ester to aldol condensation product ratio can be tuned by changing the ratio of the Cu to TiO_2 catalyst in the bed.

REFERENCES

[1] E. L. Kunkes, E. I. Gürbüz and J. A. Dumesic, "Vapour-phase C–C coupling reactions of biomass-derived oxygenates over Pd/$CeZrO_x$ catalysts," *Journal of Catalysis,* vol. 266, no. 2, pp. 236-249, 2009.

[2] E. I. Gürbüz, E. L. Kunkes and J. A. Dumesic, "Integration of C–C coupling reactions of biomass-derived oxygenates to fuel-grade compounds," *Applied Catalysis B: Environmental,* vol. 94, no. 1-2, pp. 134-141, 2010.

[3] G. S. Salvapati, K. V. Ramanamurty and M. Janardanarao, "Selective catalytic self-condensation of acetone," *Journal of Molecular Catalysis,* vol. 54, no. 1, pp. 9-30, 1989.

[4] G. W. Huber, S. Iborra and A. Corma, "Synthesis of Transportation Fuels from Biomass: Chemistry, Catalysts, and Engineering," *Chemical Reviews,* vol. 106, no. 9, p. 4044–4098, 2006.

[5] J. E. Rekoske and M. A. Barteau, "Kinetics, Selectivity, and Deactivation in the Aldol Condensation of Acetaldehyde on Anatase Titanium Dioxide," *Industrial and Engineering Chemistry Research,* vol. 50, no. 1, pp. 41-51, 2010.

[6] A. Fischer, P. Makowski, J.-O. Mueller, M. Antonietti, A. Thomas and F. Goettmann, "High-Surface-Area TiO_2 and TiN as Catalysts for the C-C Coupling

of Alcohols and Ketones," *ChemSusChem,* vol. 1, no. 5, pp. 444-449, 2008.

[7] M. Singh, N. Zhou, D. K. Paul and K. J. Klabunde, "IR spectral evidence of aldol condensation: Acetaldehyde adsorption over TiO_2 surface," *Journal of Catalysis,* vol. 260, no. 2, pp. 371-379, 2008.

[8] S. Luo and J. L. Falconer, "Acetone and acetaldehyde oligomerization on TiO_2 surfaces," *Journal of Catalysis,* vol. 185, no. 2, pp. 393-407, 1999.

[9] S. Luo and J. L. Falconer, "Aldol condensation of acetaldehyde to form high molecular weight compounds on TiO_2," *Catalysis Letters,* vol. 57, no. 3, pp. 89-93, 1999.

[10] M. E. Sad, M. N. Neurock and E. Iglesia, "Formation of C-C and C-O bonds and oxygen removal in reactions of alkanediols, alkanols, and alkanals on copper catalysts," *Journal of the American Chemical Society,* vol. 133, no. 50, pp. 20384-20398, 2011.

[11] A. A. Nikolopoulos, B. W. L. Jang and J. J. Spivey, "Acetone condensation and selective hydrogenation to MIBK on Pd and Pt hydrotalcite-derived Mgsingle bondAl mixed oxide catalysts," *Applied Catalysis A: General,* vol. 296, no. 1, pp. 128-136, 2005.

[12] J. I. Di Cosimo, G. Torres and A. C. R, "One-Step MIBK Synthesis: A New Process from 2-Propanol," *Journal of Catalysis,* vol. 208, no. 1, pp. 114-123, 2002.

[13] M. J. L. Gines and E. Iglesia, "Bifunctional Condensation Reactions of Alcohols on Basic Oxides Modified by Copper and Potassium," *Journal of Catalysis,* vol. 176, pp. 155-172, 1998.

[14] T. R. M. J. S. Avelino Corma, "Monoalkylations with alcohols by a cascade reaction on bifunctional solid catalysts: Reaction kinetics and mechanism," *Journal of Catalysis,* vol. 279, no. 2, pp. 319-327, 2011.

[15] C.-C. Wang and J. Ying, "Sol–Gel Synthesis and Hydrothermal Processing of Anatase and Rutile Titania Nanocrystals," *Chemistry of Materials,* vol. 11, no. 11, p. 3113–3120, 1999.

[16] Y.-H. Chin, C. Buda and E. Iglesia, "Selectivity of chemisorbed oxygen in C–H bond activation and CO oxidation and kinetic consequences for CH_4–O_2 catalysis on Pt and Rh clusters," *Journal of Catalysis,* vol. 283, no. 1, pp. 10-24, 2011.

[17] R. A. Spurr and H. Myers, "Quantitative Analysis of Anatase-Rutile Mixtures with an X-Ray Diffractometer," *Analytical Chemistry,* vol. 29, no. 5, pp. 760-762,

1957.

[18] A. W. Czanderna, C. N. Ramachandra Rao and J. M. Honig, "The anatase-rutile transition. Part 1.—Kinetics of the transformation of pure anatase," *Transactions of the Faraday Society,* vol. 54, pp. 1068-1071, 1958.

[19] A. A. Gribb and J. F. Banfield, "Particle size effects on transformation kinetics and phase stability in nanocrystalline TiO_2" *American Mineralogist,* vol. 82, p. 717–728, 1997.

[20] A. S. Barnard and L. A. Curtiss, "Prediction of TiO_2 Nanoparticle Phase and Shape Transitions Controlled by Surface Chemistry," *Nano Letters,* vol. 5, no. 7, pp. 1261-1266, 2005.

[21] R. M. Rioux and M. A. Vannice, "Hydrogenation/dehydrogenation reactions: isopropanol dehydrogenation over copper catalysts," *Journal of Catalysis,* vol. 216, no. 1-2, pp. 362-376, 2003.

[22] N. F. Bálsamo, C. M. Chanquía, E. R. Herrero, S. G. Casuscelli, M. E. Crivello and G. A. Eimer, "Dehydrogenation of Isopropanol on Copper-Containing Mesoporous Catalysts," *Industrial and Engineering Chemistry Research,* vol. 49, no. 24, p. 12365–12370, 2010.

[23] V. Z. Fridman and A. A. Davydov, "Dehydrogenation of Cyclohexanol on Copper-Containing Catalysts: I. The Influence of the Oxidation State of Copper on the Activity of Copper Sites," *Journal of Catalysis,* vol. 195, no. 1, pp. 20-30, 2000.

[24] M. Muhler, L. P. Nielsen, E. Törnqvist, B. S. Clausen and H. Topsøe, "Temperature-programmed desorption of H_2 as a tool to determine metal surface areas of Cu catalysts," *Catalysis Letters,* vol. 14, no. 3-4, pp. 241-249, 1992.

[25] R. J. Madon, D. Braden, S. Kandoi, P. Nagel, M. Mavrikakis and J. A. Dumesic, "Microkinetic analysis and mechanism of the water gas shift reaction over copper catalysts," *Journal of Catalysis,* vol. 281, no. 1, pp. 1-11, 2011.

[26] M. Bowker and R. J. Madix, "XPS, UPS and thermal desorption studies of alcohol adsorption on Cu(110): II. Higher alcohols," *Surface Science,* vol. 116, no. 3, p. 549–572, 1982.

[27] H. Idriss and E. G. Seebauer, "Reactions of ethanol over metal oxides," *Journal of Molecular Catalysis A: Chemical,* vol. 152, no. 1-2, pp. 201-212, 2000.

[28] P. C. Zonetti, J. Celnik, S. Letichevsky, A. B. Gaspar and L. G. Appel, "Chemicals from ethanol – The dehydrogenative route of the ethyl acetate one-pot

synthesis," *Journal of Molecular Catalysis A: Chemical,* vol. 334, p. 29–34, 2011.

[29] L. Benz, J. Haubrich, S. C. Jensen and C. M. Friend, "Molecular Imaging of Reductive Coupling Reactions: Interstitial-Mediated Coupling of Benzaldehyde on Reduced TiO_2(110)," *ACS Nano,* vol. 5, no. 2, pp. 834-843, 2011.

[30] R. Garro, M. T. Navarro, J. Primo and A. Corma, "Lewis acid-containing mesoporous molecular sieves as solid efficient catalysts for solvent-free Mukaiyama-type aldol condensation," *Journal of Catalysis,* vol. 233, no. 2, pp. 342-350, 2005.

[31] J. G. Santiesteban, J. C. Vartuli, S. Han, R. D. Bastian and C. D. Chang, "Influence of the Preparative Method on the Activity of Highly Acidic WO_x/ZrO_2 and the Relative Acid Activity Compared with Zeolites," *Journal of Catalysis,* vol. 168, no. 2, pp. 431-441, 1997.

[32] G. A. Mills, E. R. Boedeker and A. G. Oblad, "Chemical Characterization of Catalysts. I. Poisoning of Cracking Catalysts by Nitrogen Compounds and Potassium Ion," *Journal of the American Chemical Society,* vol. 72, no. 4, pp. 1554-1560, 1950.

[33] V. K. Díez, C. R. Apesteguía and J. I. Di Cosimo, "Aldol condensation of citral with acetone on MgO and alkali-promoted MgO catalysts," *Journal of Catalysis,* vol. 240, no. 2, pp. 235-244, 2006.

[34] J. C. Lavalley, "Infrared spectrometric studies of the surface basicity of metal oxides and zeolites using adsorbed probe molecules," *Catalysis Today,* vol. 27, no. 3-4, pp. 377-401, 1996.

[35] K. Tanabe, Acid-Base Catalysis, Tokyo: Kodansha-VCH, 1989.

[36] G. Torres, C. R. Apesteguía and J. I. Di Cosimo, "One-step methyl isobutyl ketone (MIBK) synthesis from 2-propanol: Catalyst and reaction condition optimization," *Applied Catalysis A: General,* vol. 317, no. 2, pp. 161-170, 2007.

[37] W. Shen, G. A. Tompsett, R. Xing, W. C. Conner Jr. and G. W. Huber, "Vapor phase butanal self-condensation over unsupported and supported alkaline earth metal oxides," *Journal of Catalysis,* vol. 286, pp. 248-259, 2012.

[38] J. E. Rekoske and M. A. Barteau, "Competition between acetaldehyde and crotonaldehyde during adsorption and reaction on anatase and rutile titanium dioxide," *Langmuir,* vol. 15, no. 6, pp. 2061-2070, 1999.

[39] M. A. Barteau, "Organic Reactions at Well-Defined Oxide Surfaces," *Chemical Reviews,* vol. 96, no. 4, pp. 1413-1430 , 1996.

[40] V. Mahadevan and L. Stenroos, "Quantitative analysis of volatile fatty acids in aqueous solution by gas chromatography," *Analytical Chemistry,* vol. 39, no. 13, pp. 1652-1654, 1967.

[41] K. S. Kim, M. A. Barteau and W. E. Farneth, "Adsorption and decomposition of aliphatic alcohols on titania," *Langmuir,* vol. 4, no. 3, pp. 533-543, 1988.

[42] Z. Li, R. S. Smith, Kay, B. D and Z. Dohnálek, "Determination of Absolute Coverages for Small Aliphatic Alcohols on TiO_2(110)," *Journal of Physical Chemistry C,* vol. 115, no. 45, p. 22534–22539, 2011.

[43] P. M. Jayaweera, E. L. Quah and H. Idriss, "Photoreaction of Ethanol on TiO_2(110) Single-Crystal Surface," *Journal of Physical Chemistry C,* vol. 111, no. 4, p. 1764–1769, 2007.

[44] J. C. J. Bart and R. P. A. Sneeden, "Copper-zinc oxide-alumina methanol catalysts revisited," *Catalysis Today,* vol. 2, no. 1, pp. 1-124, 1987.

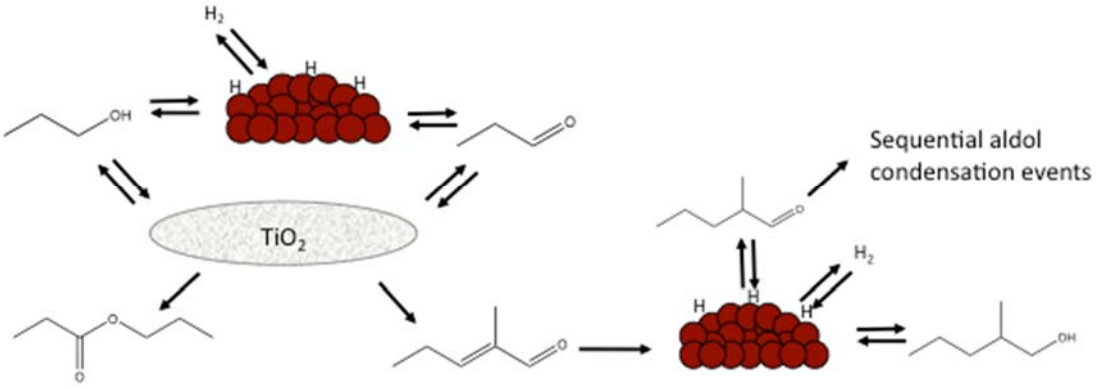

Scheme 1: Reaction network of propanol on physical mixtures of TiO_2 and Cu-based catalysts

Table 1: Effects of treatment temperature on rutile content and surface area of catalysts based on P25 TiO_2

Treatment temperature (K)	Rutile (% mass)	Surface area ($m^2\ g^{-1}$)
723	25±3	43.9±0.4
773	28±3	40.1±0.3
873	36±3	38.9±0.3
973	89±3	11.1±0.1
1073	100±3	2.7±0.1

Table 2: Effects of water to alkoxide concentration in the hydrolysis mixture temperature on the surface area of anatase catalysts. Treatment temperature 773 K (flowing air, 4 h).

Ratio of water to titanium isopropoxide (K)	Surface area ($m^2\ g^{-1}$)
3	1.65±0.1
15	19.4±0.2
50	77.4±0.8
100	99.2±0.8
150	124±1.0

Table 3: Effects of Cu mass fraction and H_2 pressure on deactivation. (Propanal, 0.24 kPa, 473 K, 50 mg TiO_2). Deactivation constant is definced as: $\frac{dr}{dt} = -k_d r$ or in the integrated form $\frac{r}{r_0} = \exp(-k_d t)$ (2). Where r is the total reaction rate, r_0 is the initial reaction rate and t is the time on stream. During the experiments, it is calculated by fitting an exponential curve to the experimental rate data.

Cu or Pt-based catalyst fraction (mass)	H_2 pressure (kPa)	First-order deactivation rate constant k_d (ks^{-1})	Trimethylbenzene Selectivity (%, C-basis)
0 (Cu)	40	0.09	30
0.8 (Cu)	25	0.01	5
0.8 (Cu)	40	<0.01	< 1
0.5 (Pt)	40	<0.01	<1

Table 4: Titration experiments. (473 K, 4 kPa propanol, 40 kPa H_2, physical mixture $Cu/ZnO/Al_2O_3$ and TiO_2 (P25) (4:1 mass)).

Titrant	Titrant pressure (Pa)	Steady-state aldol condensation rate after titrant introduction μmol g_{TiO2}^{-1} ks^{-1}
None	--	242
DTBP	12	240
Pyridine	12	236
CO_2	$3x10^4$	234
Propionic acid	400	15

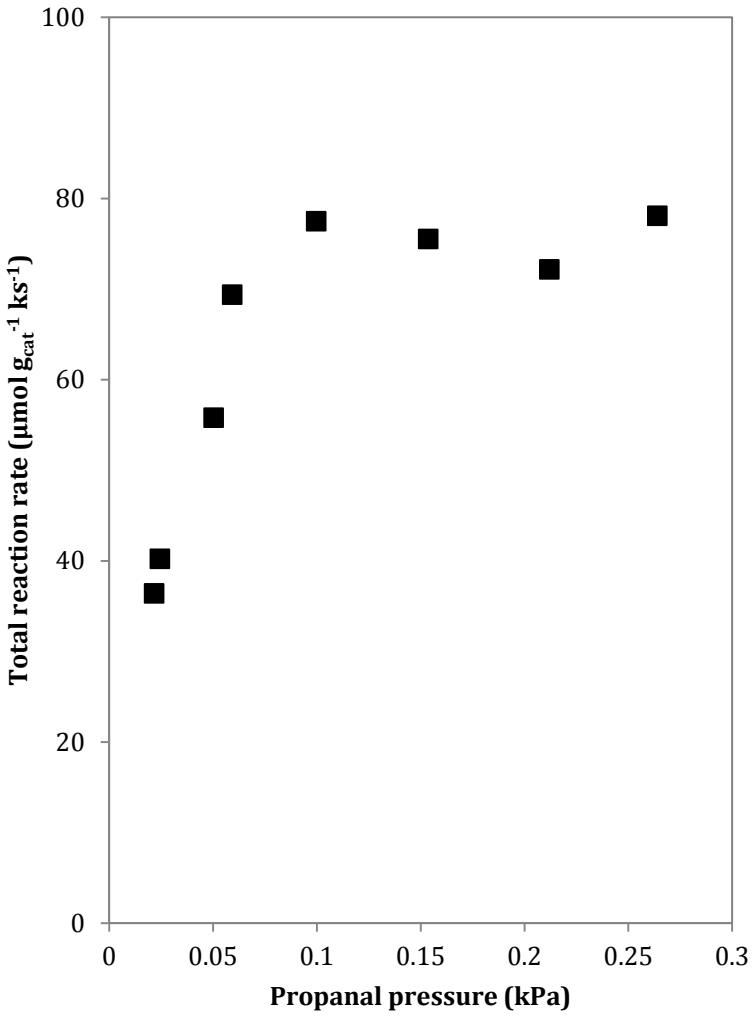

Figure 1: Total reaction rate over $Cu/ZnO/Al_2O_3$ as a function of propanal pressure. 473 K, 40 kPa H_2, 690 ks g_{cat} $mol_{propanol}^{-1}$.

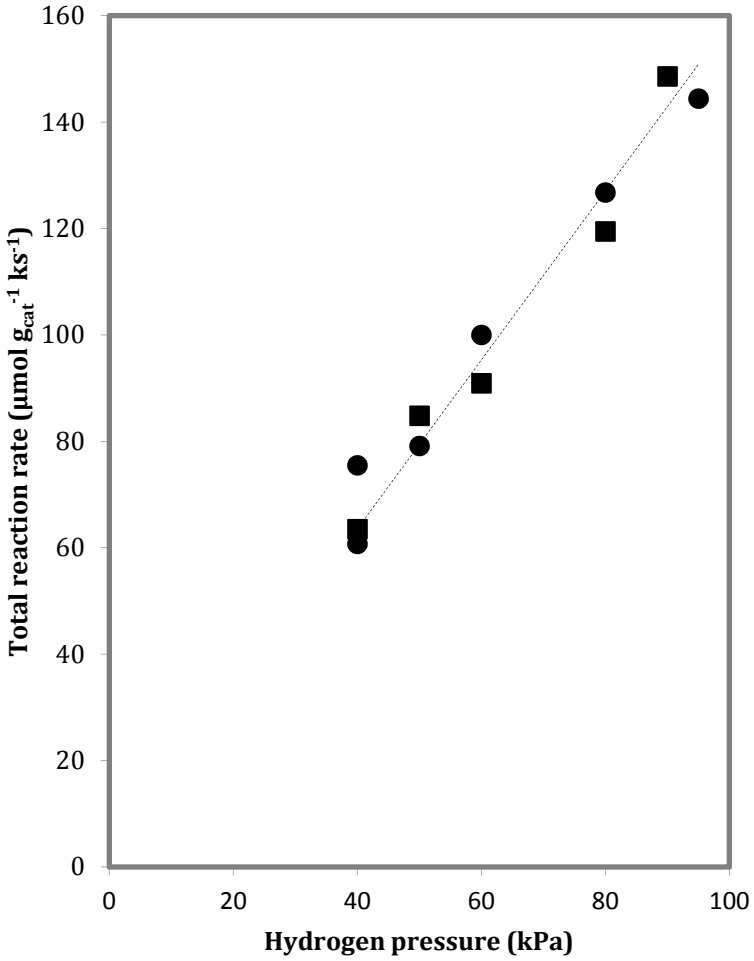

Figure 2: Total reaction rate over $Cu/ZnO/Al_2O_3$ as a function of hydrogen pressure. 473 K, 40 kPa H_2, 690 ks g_{cat} $mol_{propanol}^{-1}$.

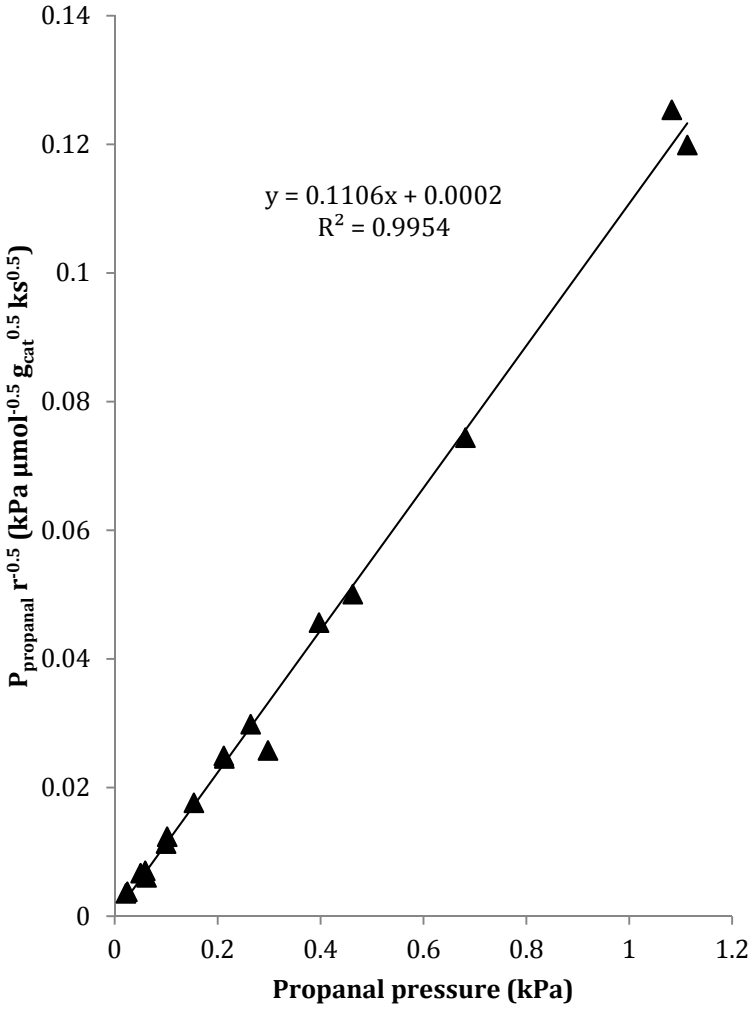

Figure 3: Fitting of rate law to experimental data. 473 K, 40 kPa H_2, 170-690 ks g_{cat} $mol_{propanol}^{-1}$.

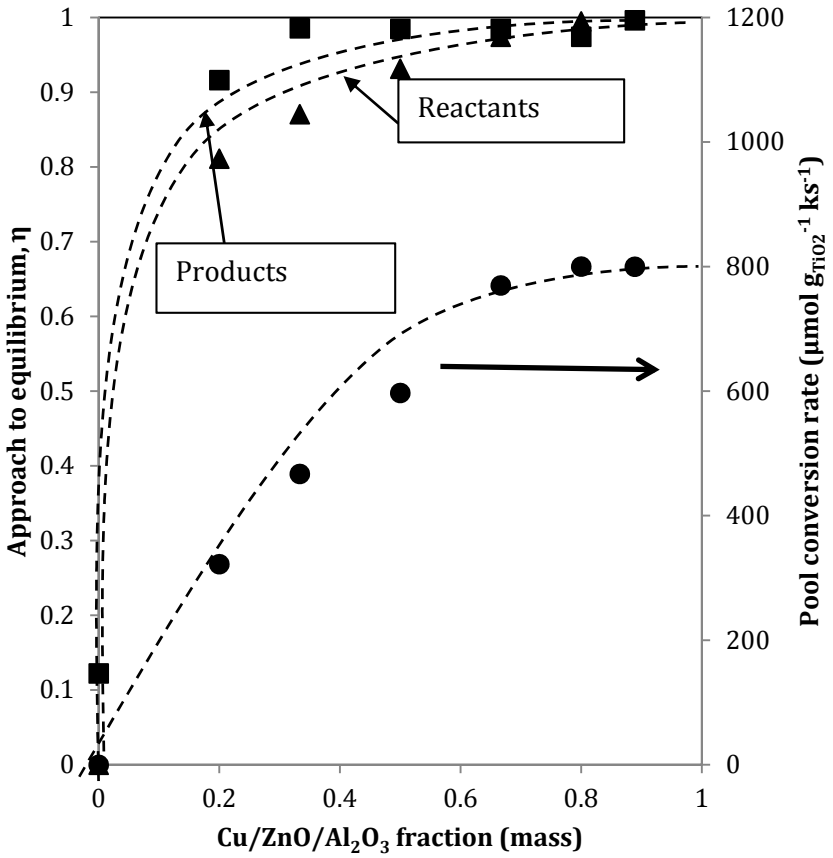

Figure 4: Effects of the mass fraction of Cu and TiO_2 on the approach to equilibrium for reactants (propanol/propanal ▲) and condensation products (2-methylpentanal/2-methyl-1-pentanol -■), as well as the total pool conversion rate 4 kPa propanol, 40 kPa H_2, 473 K

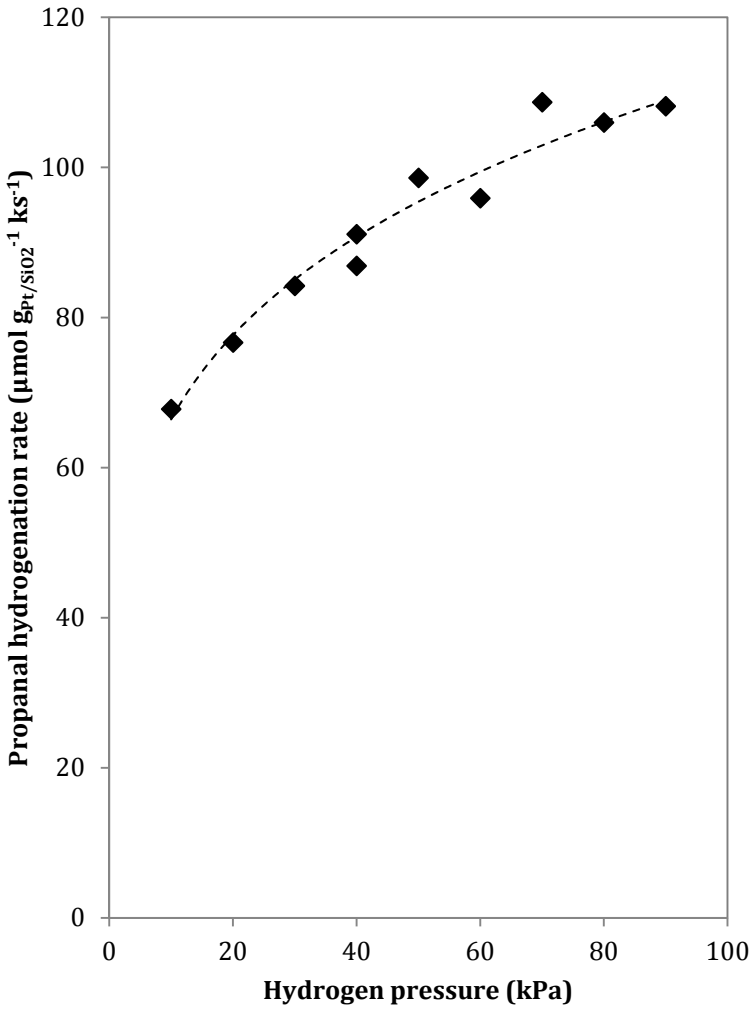

Figure 5: Dependence of propanal hydrogenation rate on hydrogen pressure. 473 K, 3 kPa propanal, 0.6 ml/h, 20 mg Pt/SiO_2.

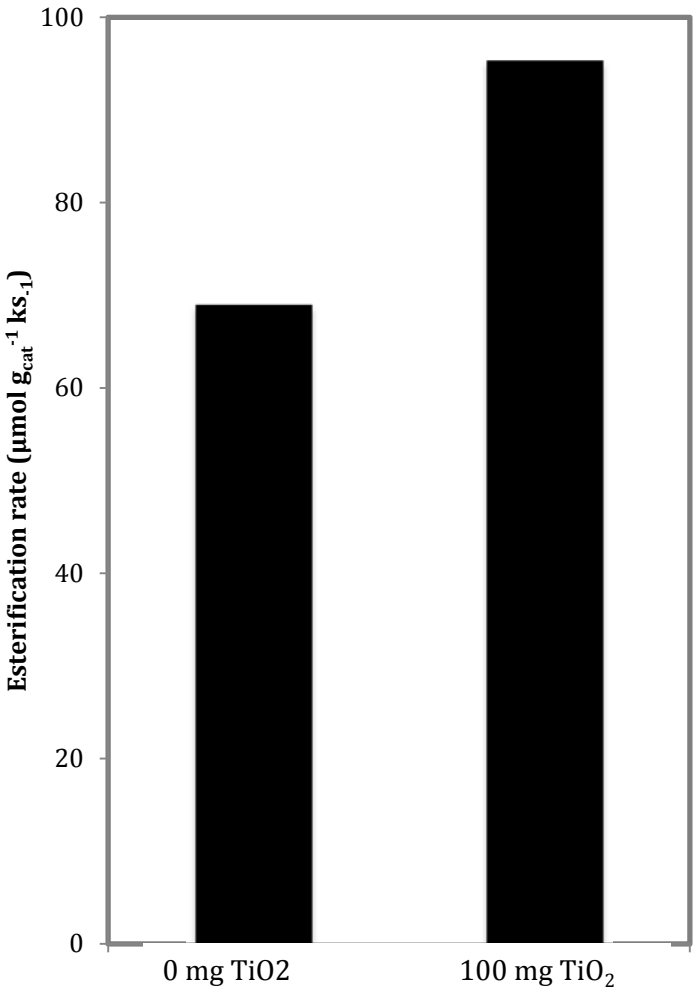

.

Figure 6: Esterification rate in the presence and absence of TiO_2. 4 kPa propanol, 40 kPa H_2, 473 K, 200 mg $Cu/ZnO/Al_2O_3$.

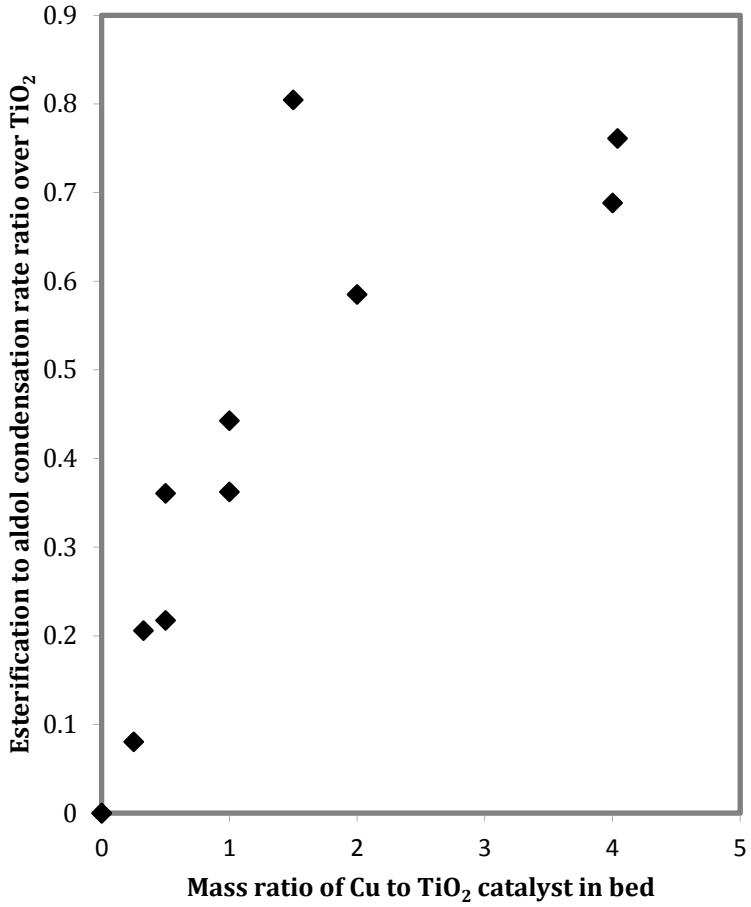

Figure 7: Dependence of the ratio of aldol condensation to esterification over TiO_2 on the mass ratio of $Cu/ZnO/Al_2O_3$ to TiO_2 in the bed. 473 K, 4 kPa propanol, 40 kPa H_2.

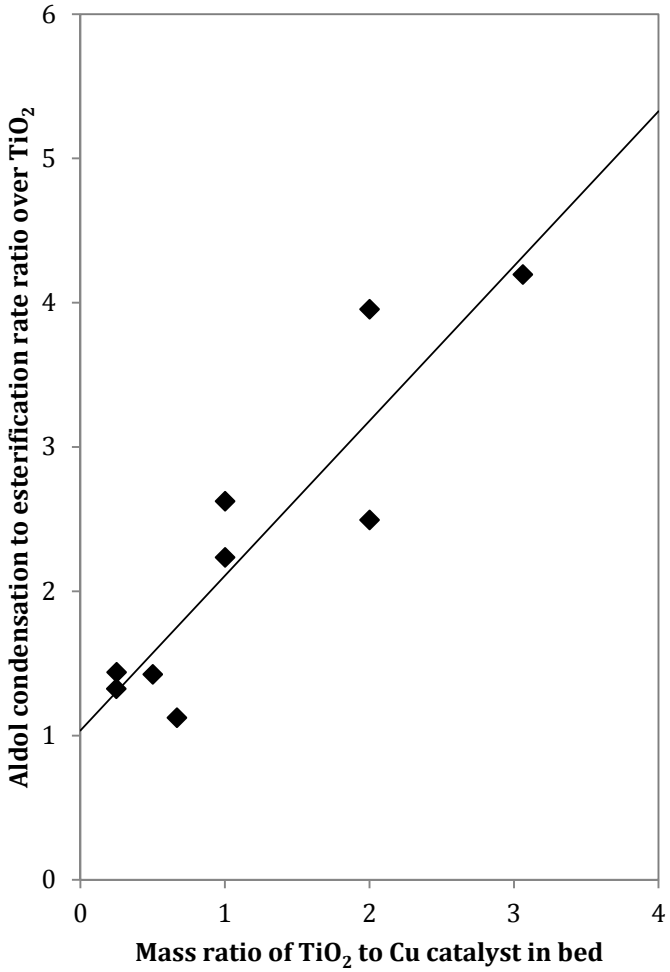

Figure 8: Dependence of the ratio of aldol condensation to esterification over TiO_2 on the mass ratio of $Cu/ZnO/Al_2O_3$ to TiO_2 in the bed. 473 K, 4 kPa propanol, 40 kPa H_2.

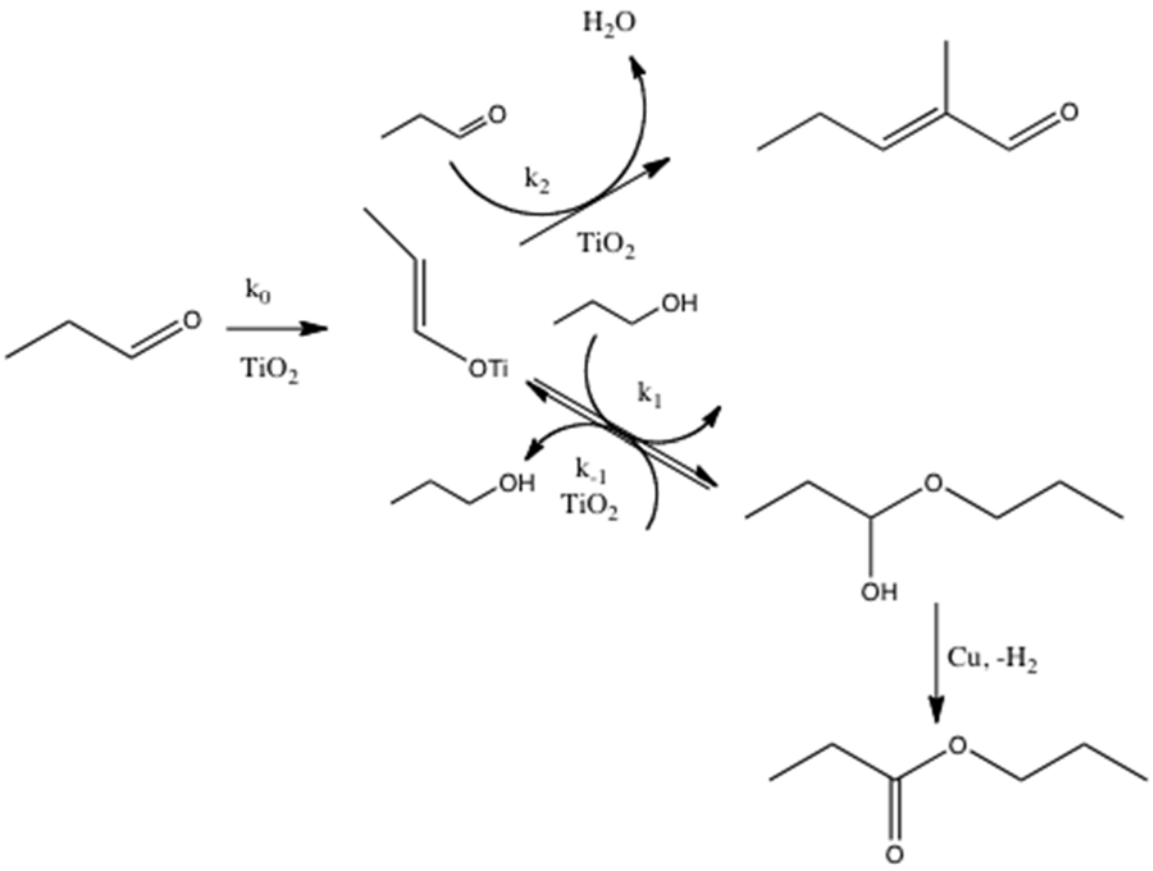

Scheme 2: Esterification and aldol condensation pathways over TiO_2 and Cu physical mixtures

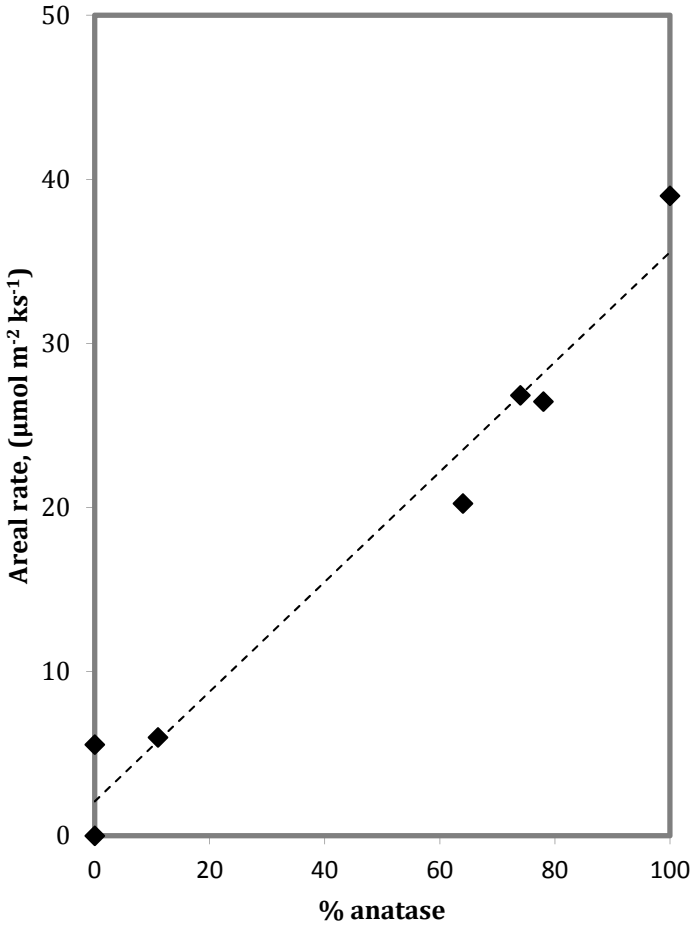

Figure 9: Areal rates as a function of anatase content in TiO_2. (4 kPa Ethanol, 473 K, physical mixture $Cu/ZnO/Al_2O_3$ and TiO_2 (4:1 mass))

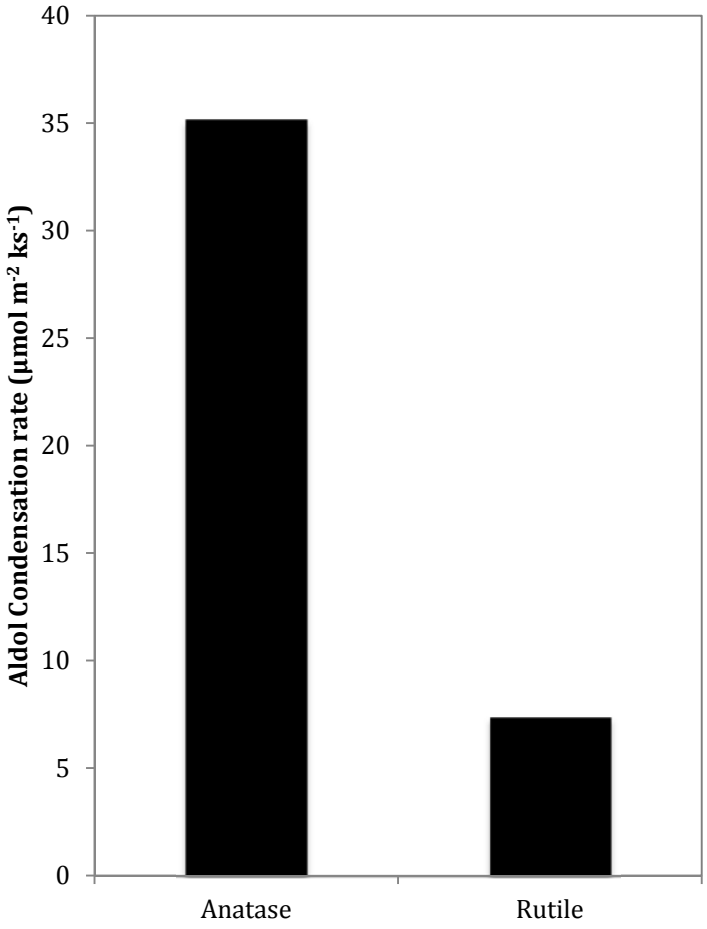

Figure 10: Aldol condensation rates over rutile and anatase in the presence of Pt. 2 kPa acetone, 473 K. For anatase: 0.784 m^2 anatase, 25 mg Pt/SiO_2. For rutile: 0.414 m^2 rutile, 38 mg Pt/SiO_2.

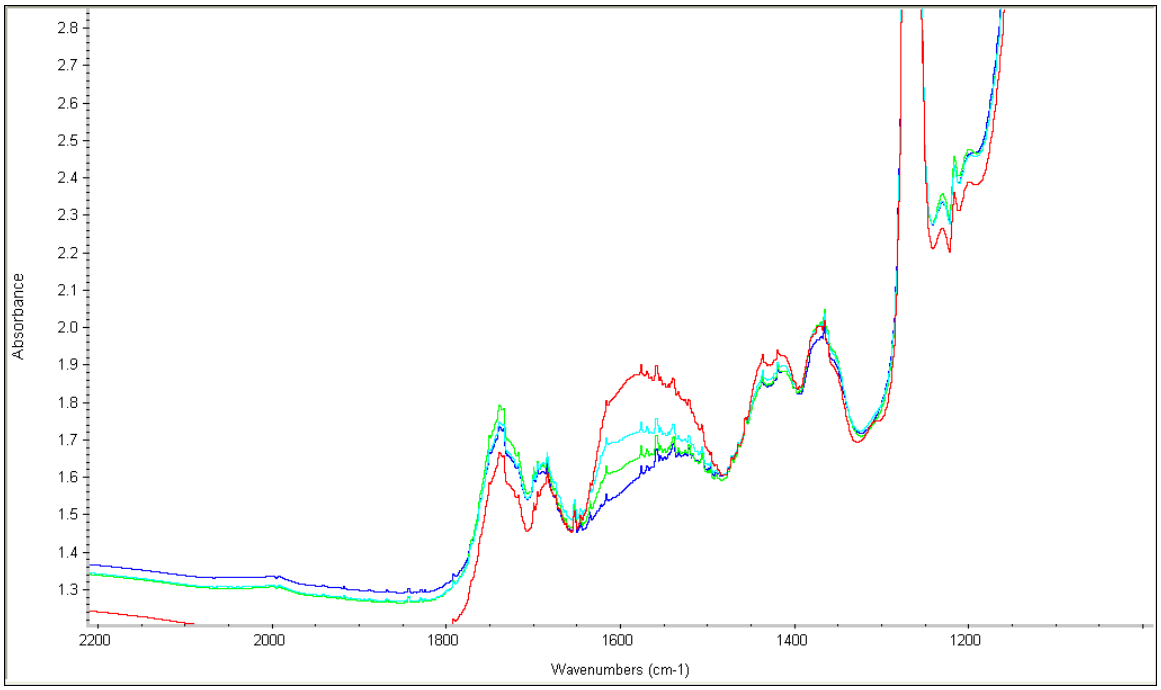

Figure 11: Time change of anatase surface under catalytic conditions: Blue: t = 0, green t = 8 min, cyan t = 16 min, red t = 82 min. At time t = 0, the flow of acetone is started (2 kPa, 0.4 ml/h, balance He, 473 K, anatase pellet).

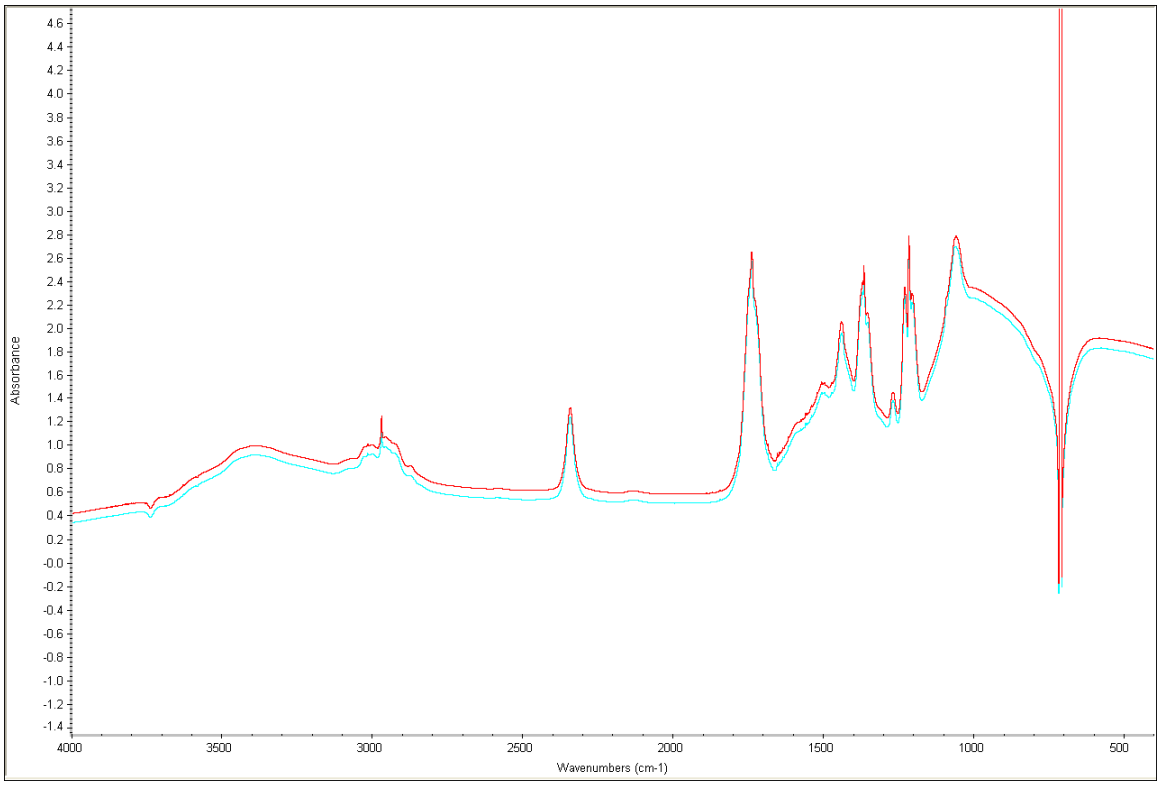

Figure 12: Time change of rutile surface under catalytic conditions. Cyan t = 0, red t = 40. At time t = 0, the flow of acetone is started (2 kPa, 0.4 ml/h, balance He, 473 K, anatase pellet).

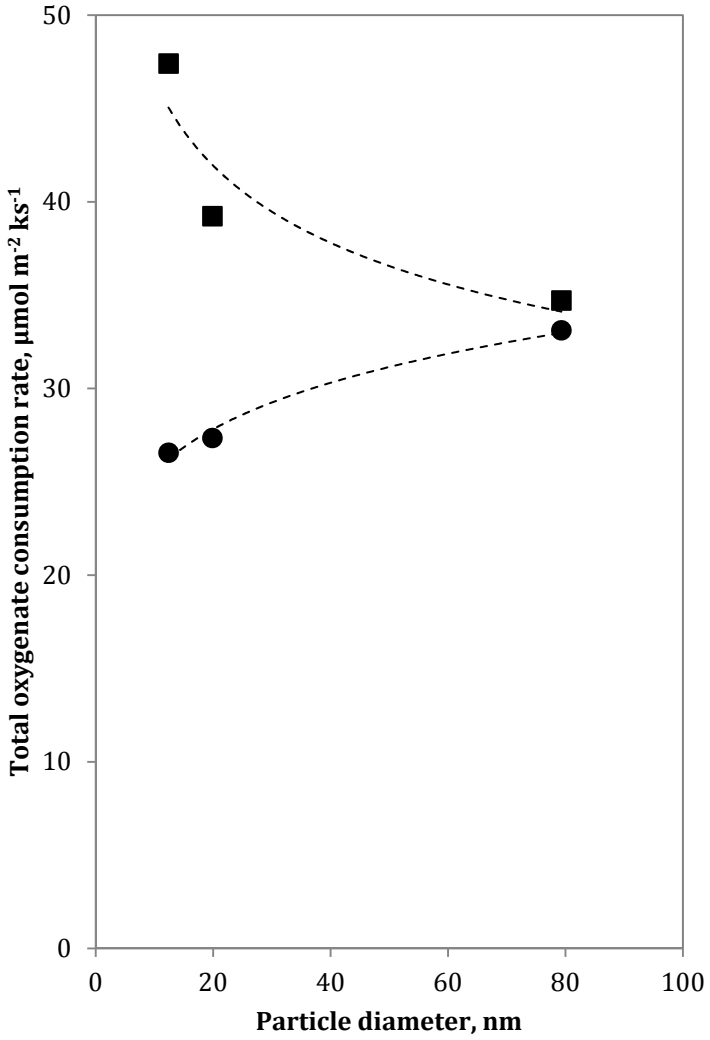

Figure 13: Effects of anatase particle size on oxygenate reaction rate. 40 kPa H_2. Circles: Physical mixture of TiO2 and $Cu/ZnO/Al_2O_3$, 0.2 $g_{CuZnAl}/m_{anatase}^2$, 4 kPa ethanol, 1 kPa H_2O, 40 kPa H_2, 473 K. Squares: Physical mixture of TiO2 and Pt/SiO_2, 0.25 $mg_{Pt}/m_{anatase}^2$, 2 kPa acetone, 40 kPa H_2, 473 K.

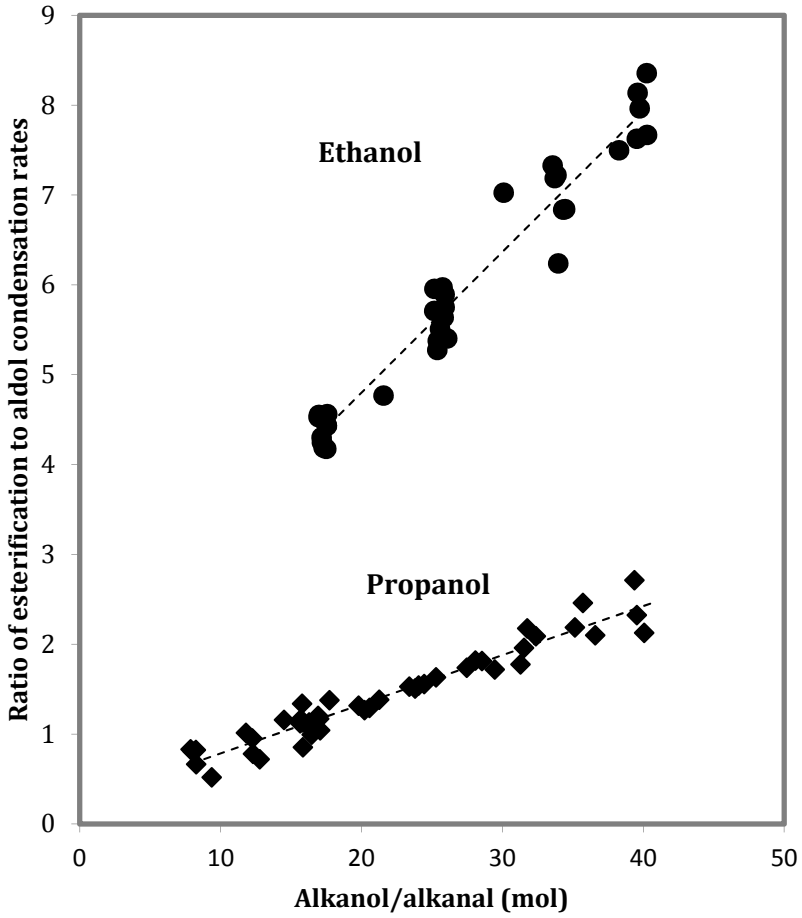

Figure 14: Effects of the ratio of alkanol to alkanal on the ratio of esterification and aldol condensation. (▲) 0.6-2.4 kPa propanol (●) 3-6 kPa ethanol. 473 K, residence time (τ): 67.4 ks g_{TiO2} $mol_{propanol}^{-1}$, 20-95 kPa H_2.

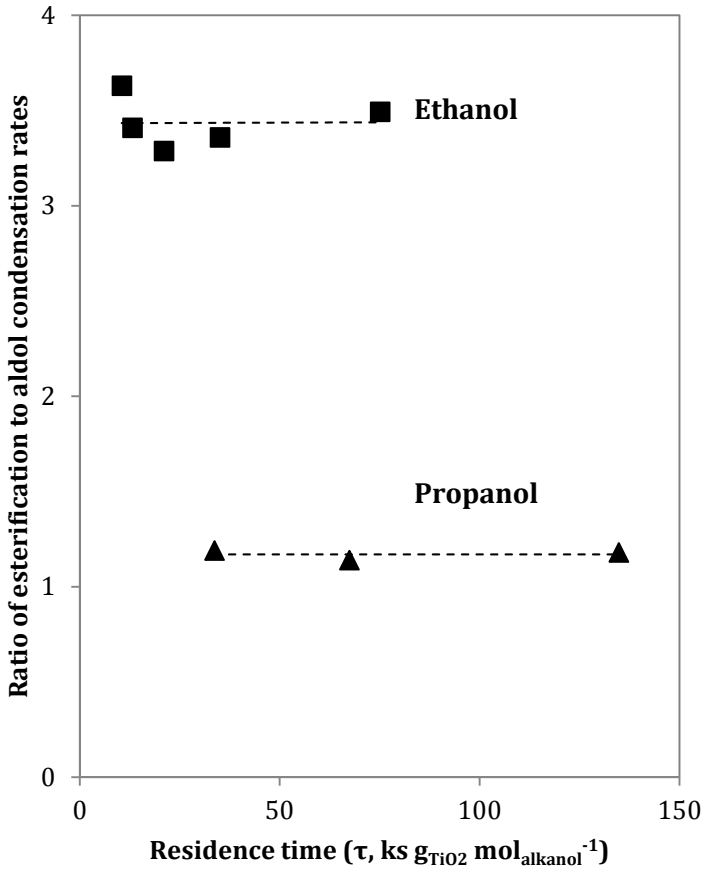

Figure 15: Effects of residence time on the ratio of esterification to aldol condensation rates. (▲) 2.4 kPa propanol (■) 4 kPa ethanol. 40 kPa H2, 473 K, physical mixture Cu/ZnO/Al_2O_3 and TiO_2 (P25) (4:1 mass). Dashed curve represents qualitative trend

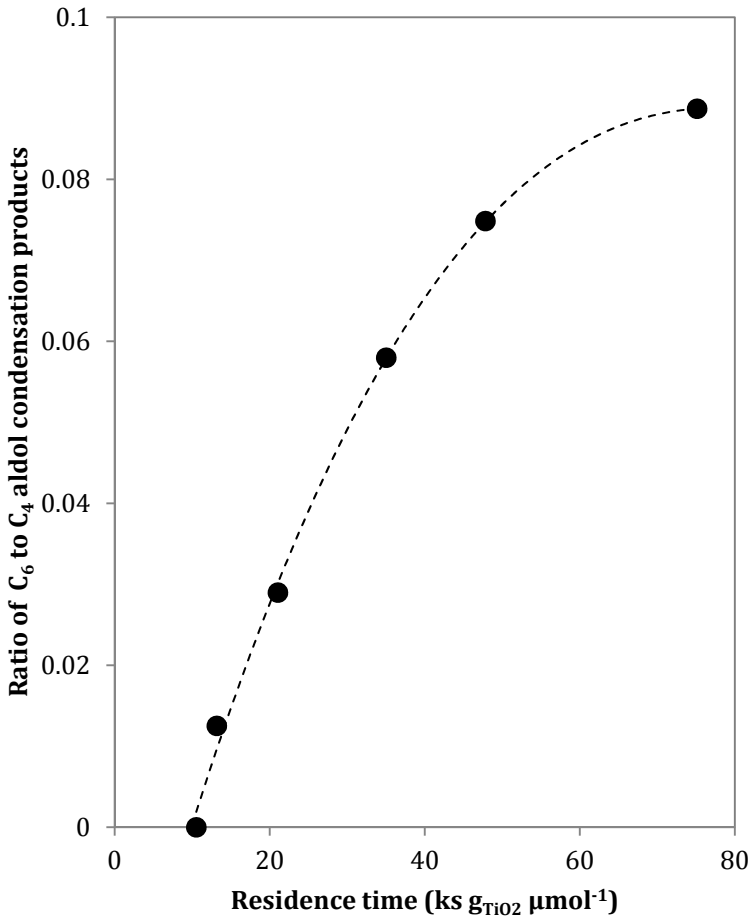

Figure 16: Effects of the residence time on the ratio of secondary to primary products (C_6 and C_4 species, respectively) of acetaldehyde self-condensation reactions. (4 kPa ethanol, 40 kPa H_2, physical mixture $Cu/ZnO/Al_2O_3$ and TiO_2 (P25) (4:1 mass)). Dashed curve represents qualitative trend.

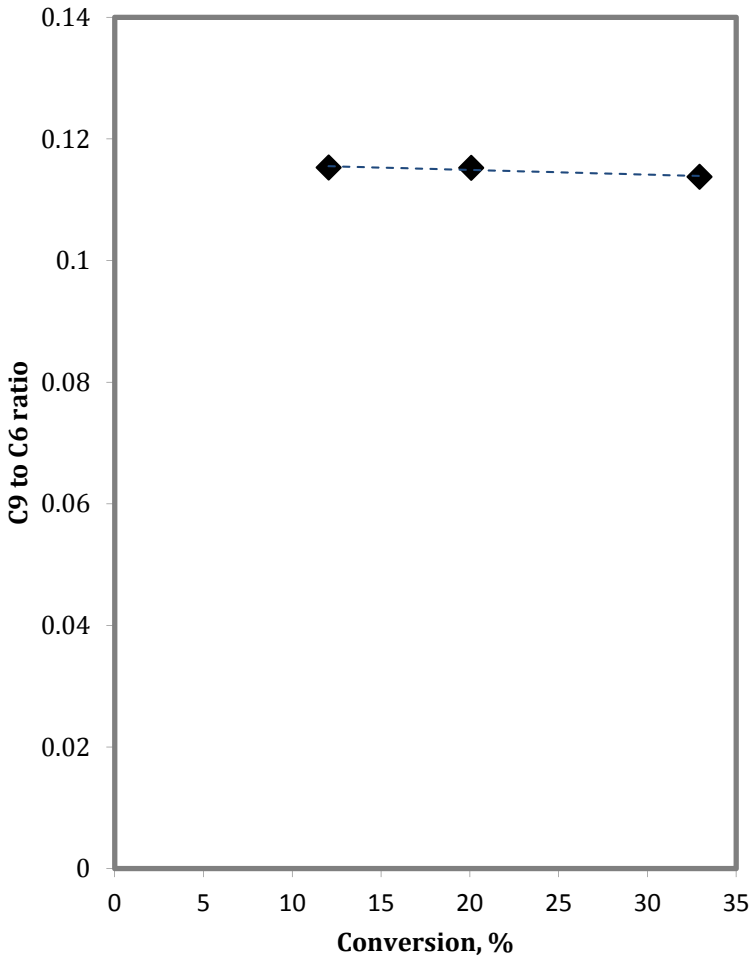

Figure 17: Effects of the residence time on the ratio of secondary to primary products (C_9 and C_6 species, respectively) of propanal self-condensation reactions. (0.25 kPa propanal, 40 kPa H_2, TiO_2 (P25)). Dashed curve represents qualitative trend.

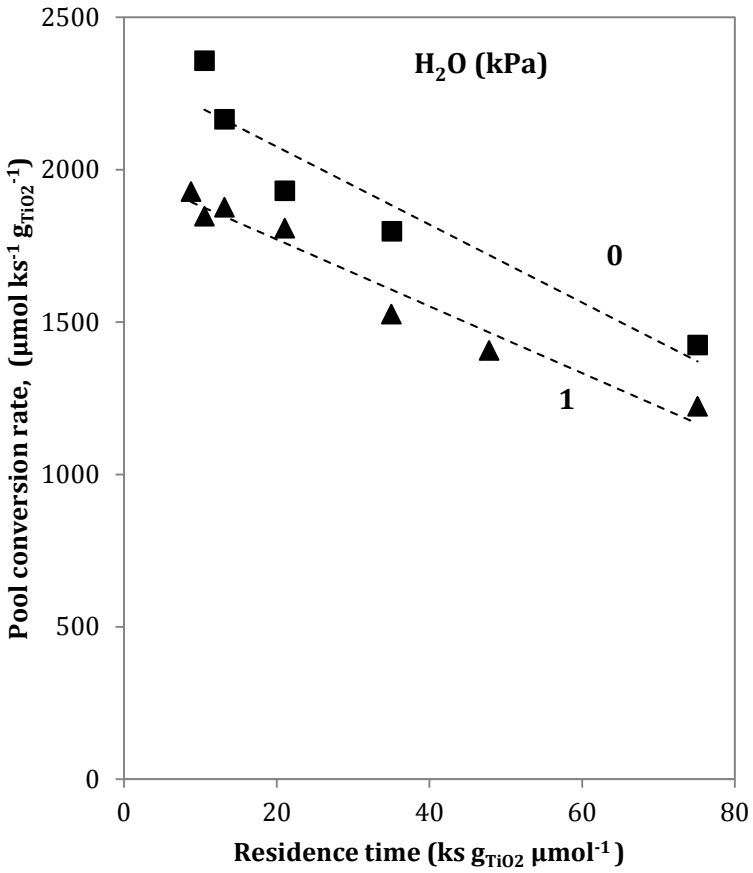

Figure 18: Effects of residence time on pool conversion reaction rates, with 1 kPa (▲) and 0 kPa (■) H_2O. (473 K, 4 kPa ethanol, 40 kPa H_2, physical mixture $Cu/ZnO/Al_2O_3$ and TiO_2 (P25) (4:1 mass)).

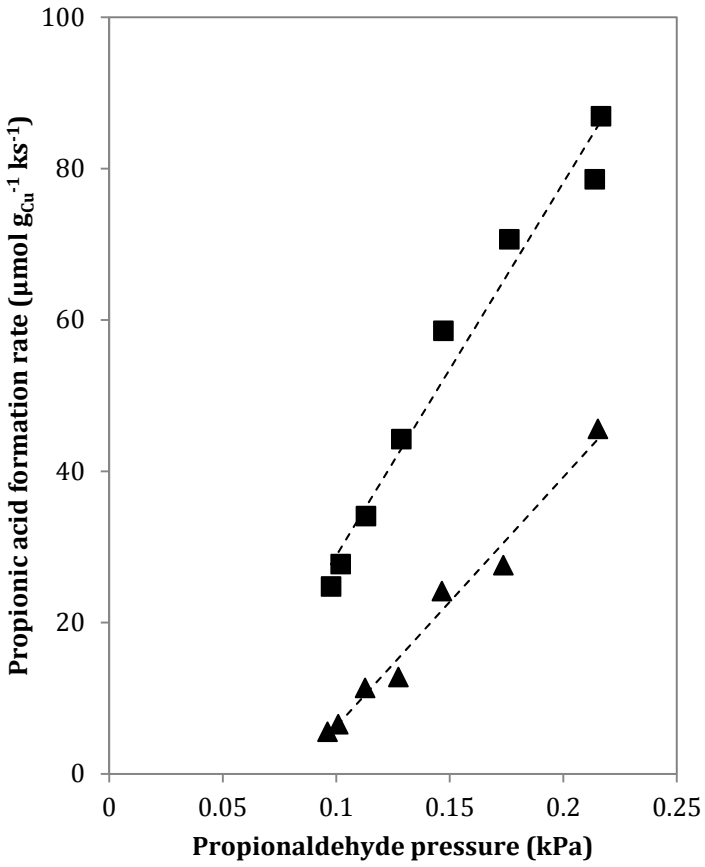

Figure 19: Effects of water and propanal pressure on propionic acid formation over Cu. (4 kPa propanol, 1 kPa (▲) – 4 kPa (■) water, 40 kPa H_2, 473 K, $Cu/ZnO/Al_2O_3$, 140 g_{Cu} ks $mol_{propanol}^{-1}$)

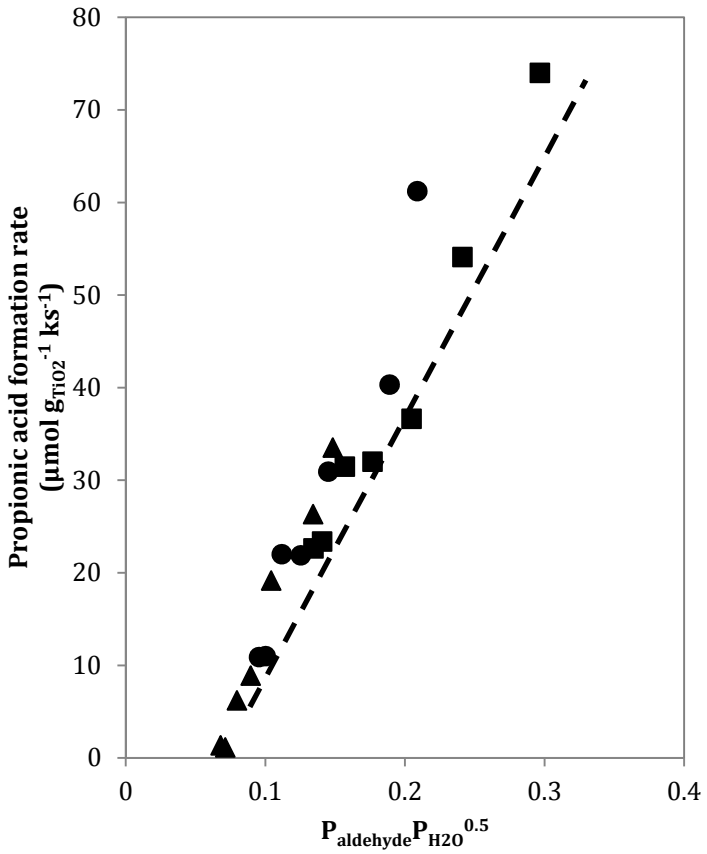

Figure 20: Dependence of propionic acid formation rate over TiO_2 and $Cu/ZnO/Al_2O_3$ on water and propionaldehyde. 4 kPa propanol, 40-95 kPa H2, 473 K physical mixture $Cu/ZnO/Al_2O_3$ and TiO_2 (P25) (4:1 mass). Circles: 1 kPa water. Squares: 2 kPa water. Triangles: 0.5 kPa water.

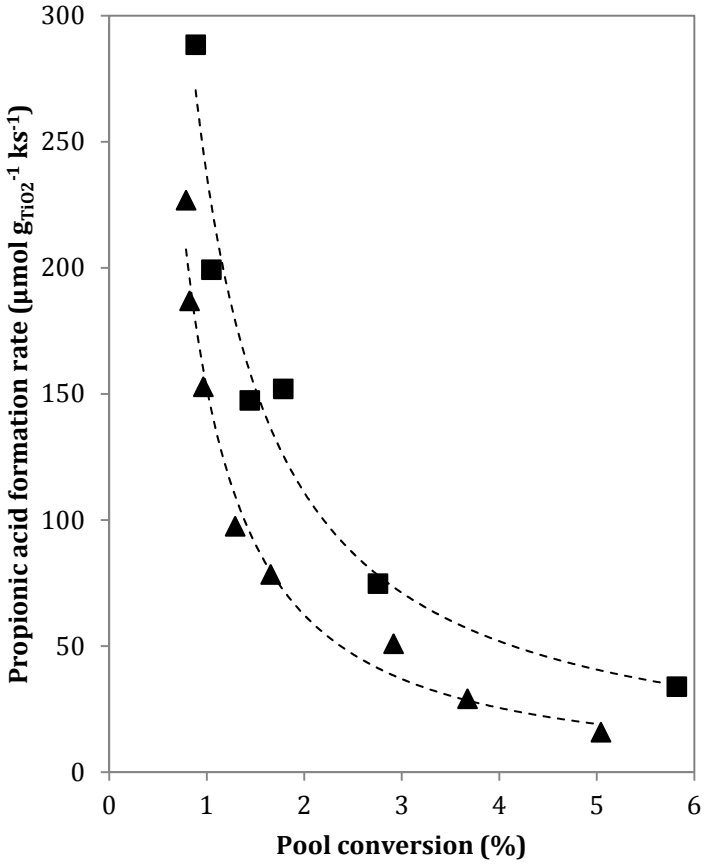

Figure 21: Dependence of propionic acid formation rate on space velocity. 4 kPa propanol, 40 kPa H_2, 473 K physical mixture Cu/ZnO/Al_2O_3 and TiO_2 (P25) (4:1 mass), 1 kPa (▲) – 2 kPa (■) water

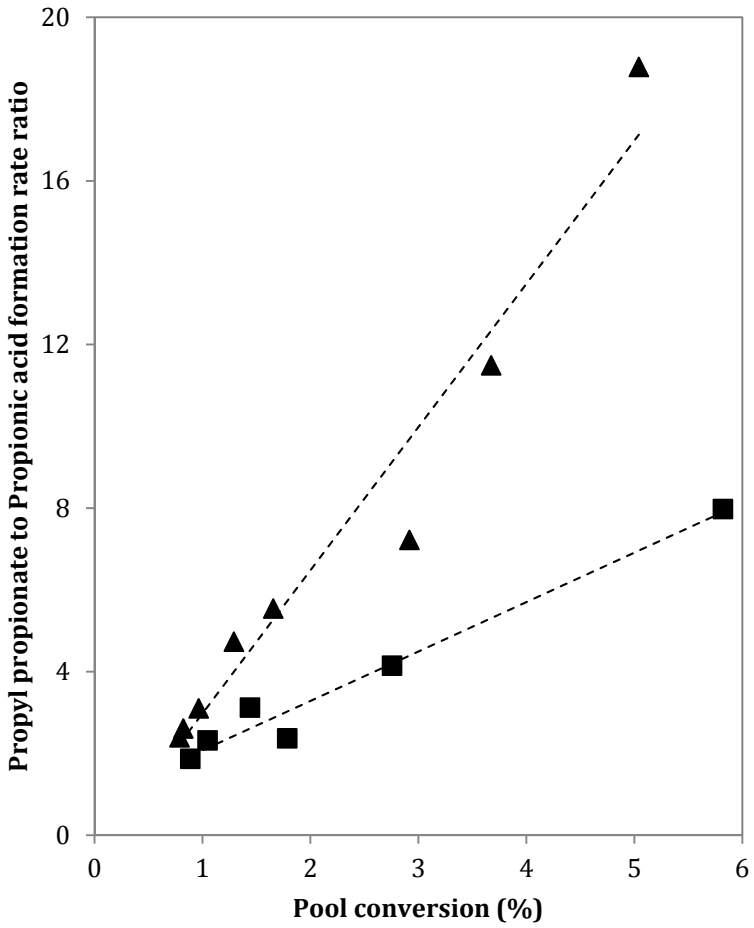

Figure 22: Dependence of the ratio of ester to propionic acid formation rate on space velocity. 4 kPa propanol, 40 kPa H_2, 473 K physical mixture $Cu/ZnO/Al_2O_3$ and TiO_2 (P25) (4:1 mass), 1 kPa (▲) – 2 kPa (■) water.

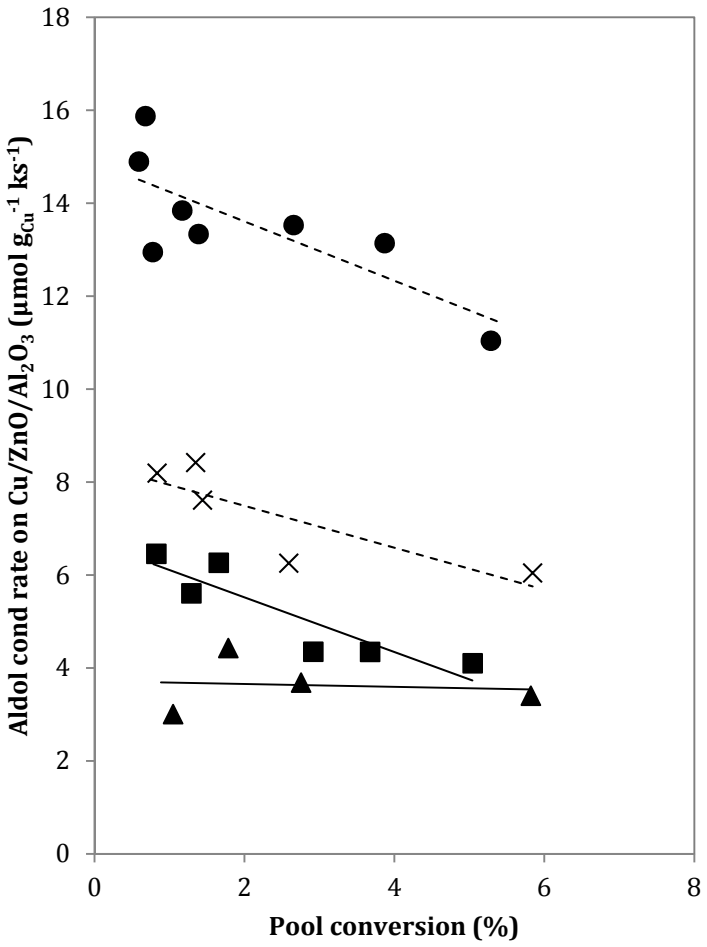

Figure 23: Effects of cofed water (0 kPa (●), 0.5 kPa (X), 1 kPa (■) and 2 kPa (▲)) and pool conversion on the aldol condensation rate over Cu/ZnO/Al2O3. (473 K, 4 kPa propanol, 40 kPa H_2, physical mixture Cu/ZnO/Al_2O_3 and TiO_2 (P25) (4:1 mass)).

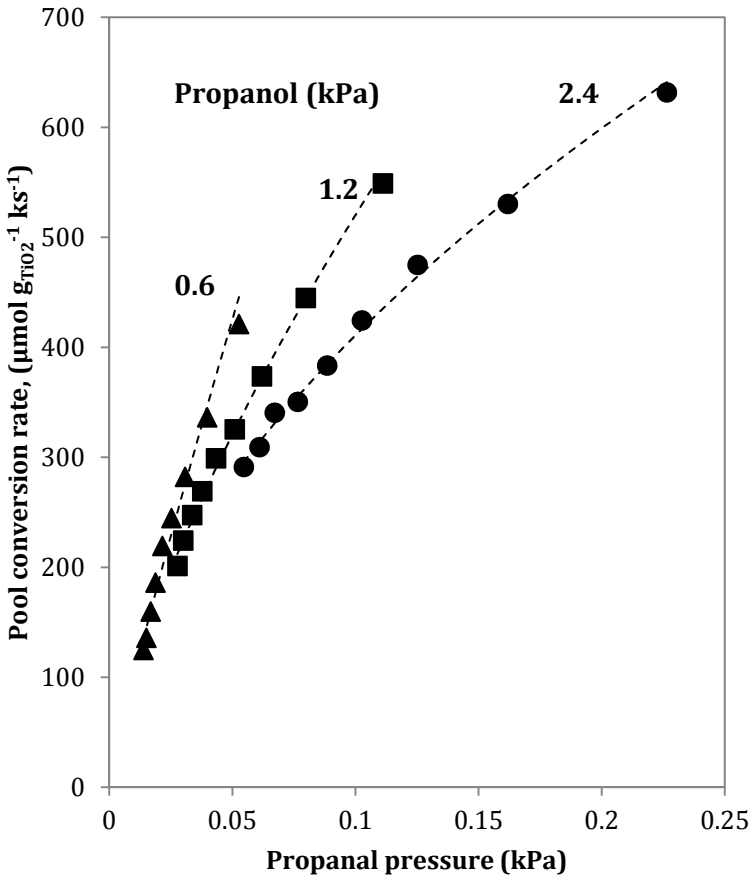

Figure 24: Effects of 1-propanol and propanal pressure on reaction rates. (▲) 0.6 kPa propanol (■) 1.2 kPa propanol (●) 2.4 kPa propanol. 473 K, τ = 67.4 ks g_{TiO2} $mol_{propanol}^{-1}$, 20-95 kPa H_2 on physical mixture Cu/ZnO/Al_2O_3 and TiO_2 (P25) (4:1 mass). Dashed curves represent trends.

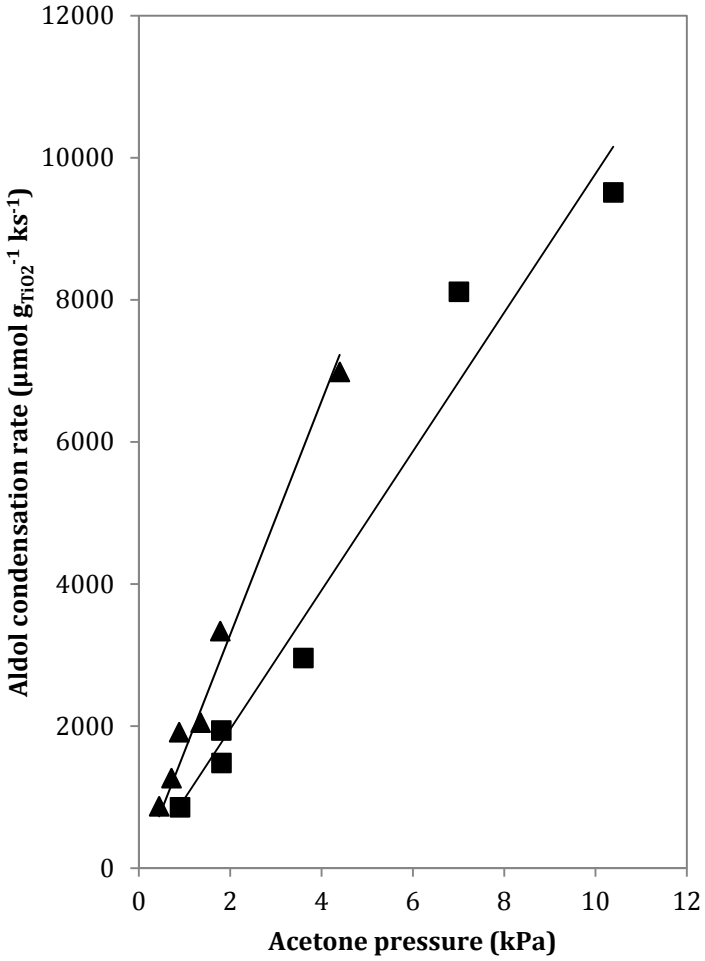

Figure 25: Dependence of aldol condensation of acetone over a physical mixture of Pt and TiO_2 on acetone pressure. 473 K, 8 ks g_{TiO2} $mol_{acetone}^{-1}$, . (▲) 40 kPa H_2 (■) 95 kPa H_2.

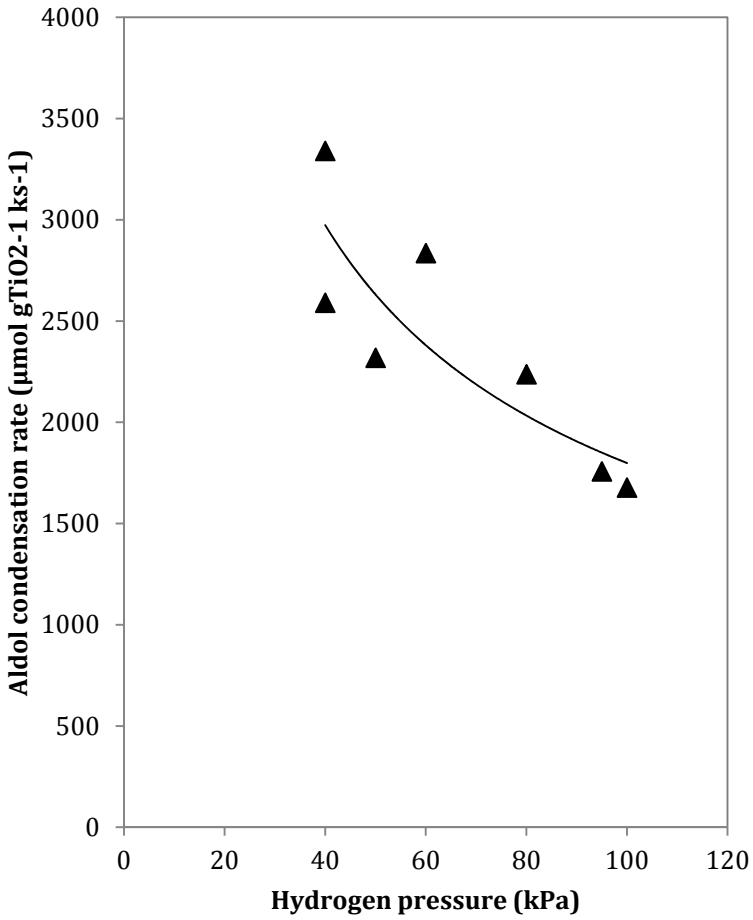

Figure 26: Dependence of aldol condensation of acetone over a physical mixture of Pt and TiO_2 on hydrogen pressure. 473 K, 8 ks g_{TiO2} $mol_{acetone}^{-1}$,, 2 kPa acetone.

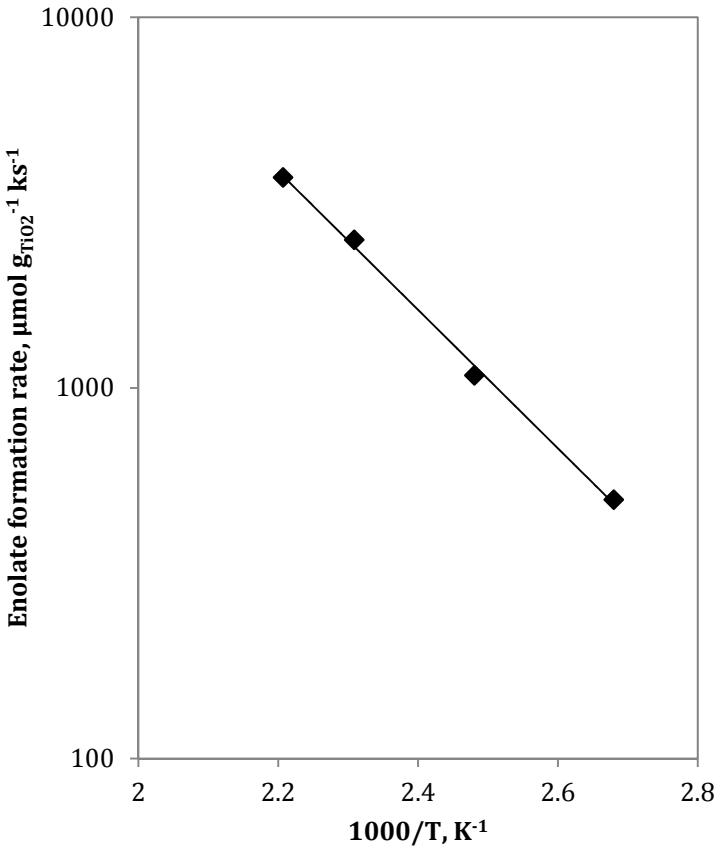

Figure 27: Arrhenius plot for acetone condensation over Pt/SiO_2 and TiO_2. 40 kPa H_2, rate values extrapolated to 5 kPa acetone pressure and 2% conversion.

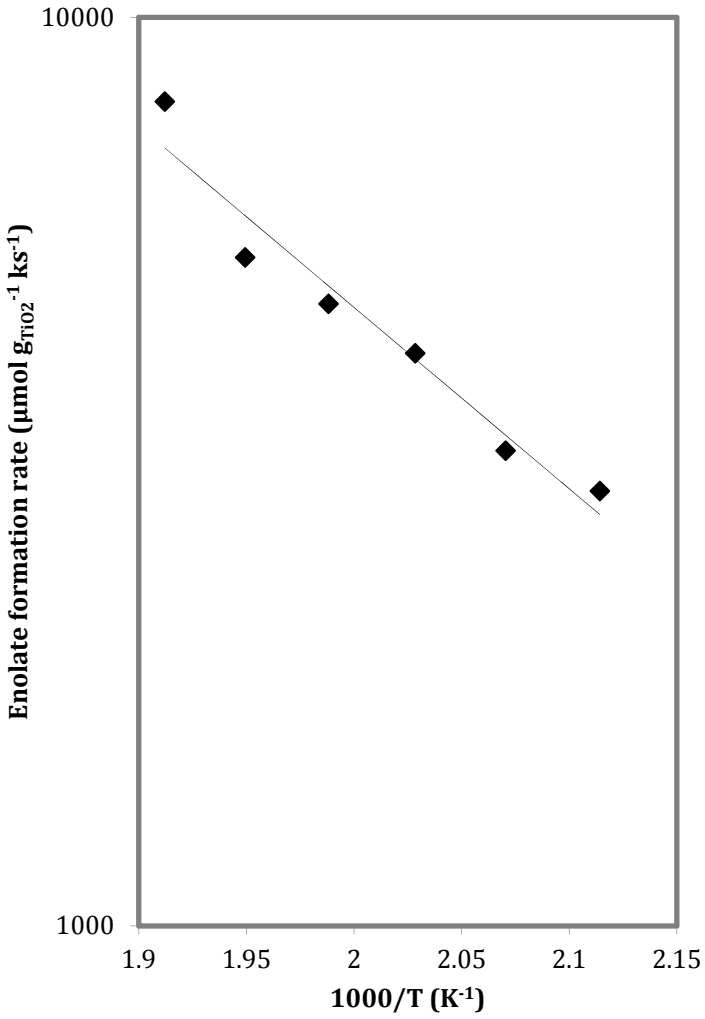

Figure 28 Arrhenius plot for propanal condensation over $Cu/ZnO/Al_2O_3$ and TiO_2. 40 kPa H_2, 10 kPa Propanol, 1 ml/h on physical mixture $Cu/ZnO/Al_2O_3$ and TiO_2 (P25) (4:1 mass).

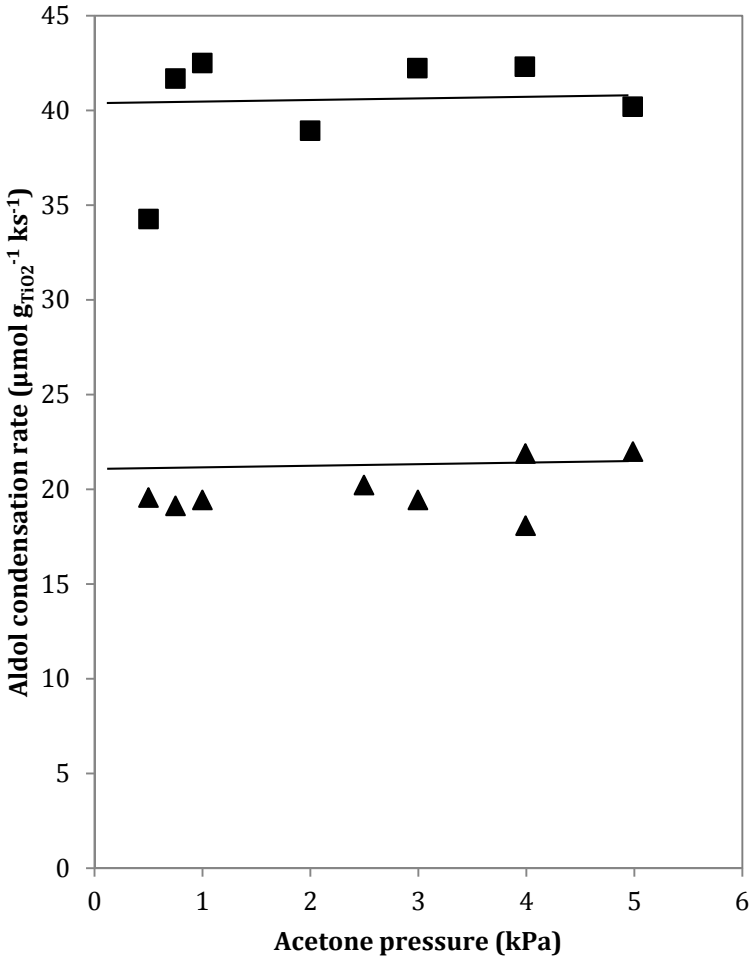

Figure 29: Kinetic isotope effect experiment for acetone aldol condensation. 403 K, 40 kPa H_2, physical mixture of TiO_2 (P25) and Pt/SiO_2. (▲) perdeuterated acetone (■) natural-abundance acetone.

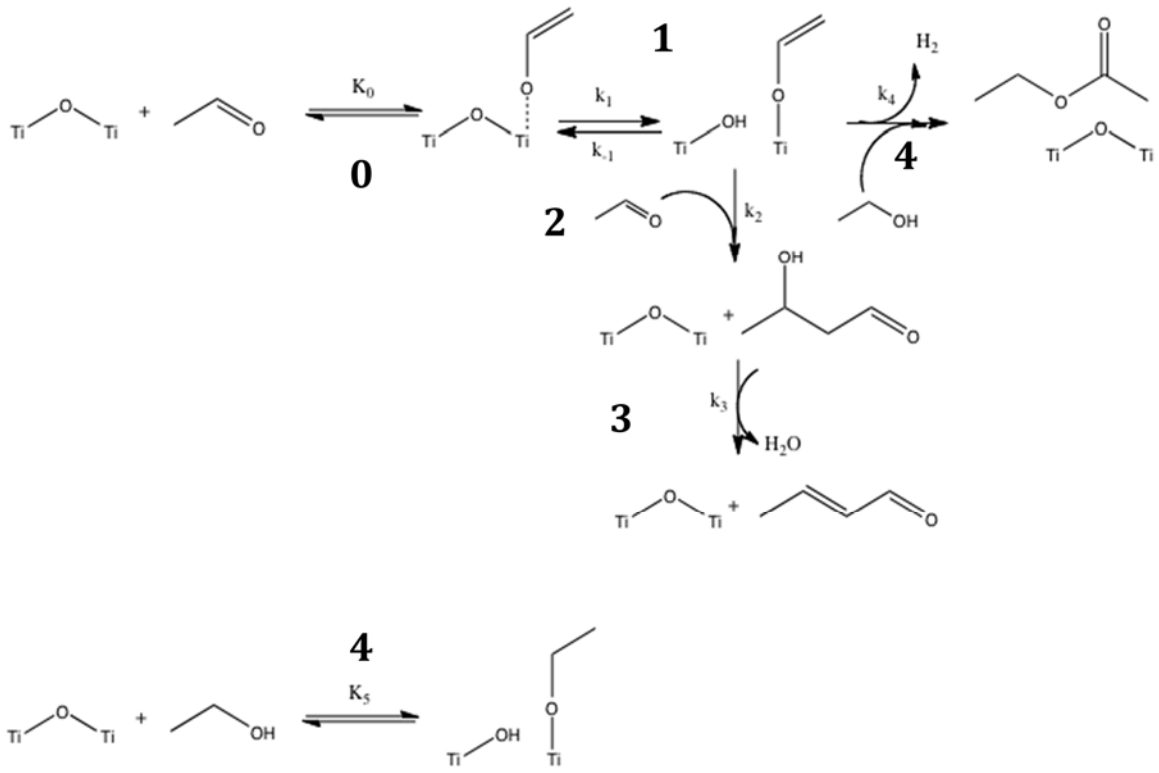

Scheme 3: Elementary steps for aldol condensation and esterification on Ti-O acid-base pairs on TiO_2 surfaces

Table 5: Estimated rate constants for enolate formation (as defined in Scheme 2). (Propanol. 473 K, physical mixture $Cu/ZnO/Al_2O_3$ and TiO_2 (P25) (4:1 mass))

Reactant	K_0k_1 ($mol_{propanol}ks^{-1}$ g_{TiO2}^{-1} kPa^{-2})	K_0 (kPa^{-1})	K_4 (kPa^{-1})	K_5 (kPa^{-1})
1-Propanol	$1.33x10^4$	8.02	$8.8x10^{-2}$	19.6

Table 6: Effects of temperature and residence time on conversion and selectivity (4 kPa propanol, 40 kPa H_2, physical mixture $Cu/ZnO/Al_2O_3$ and TiO_2 (P25) (1:1 mass)).

Reaction temperature (K)	473	473	523	523	573
Residence time (g_{TiO2} ks $mol_{ethanol}^{-1}$)	131	526	131	526	131
Conversion of C_2 pool (%)	9.8	23	54	80	88
Selectivity, (%, C-basis)					
C_4	63	51	20	7.5	5.9
C_6	14	25	20	21	16
C_8	9.4	20	24	33	29
C_{9+}	14	7.1	33	38	47

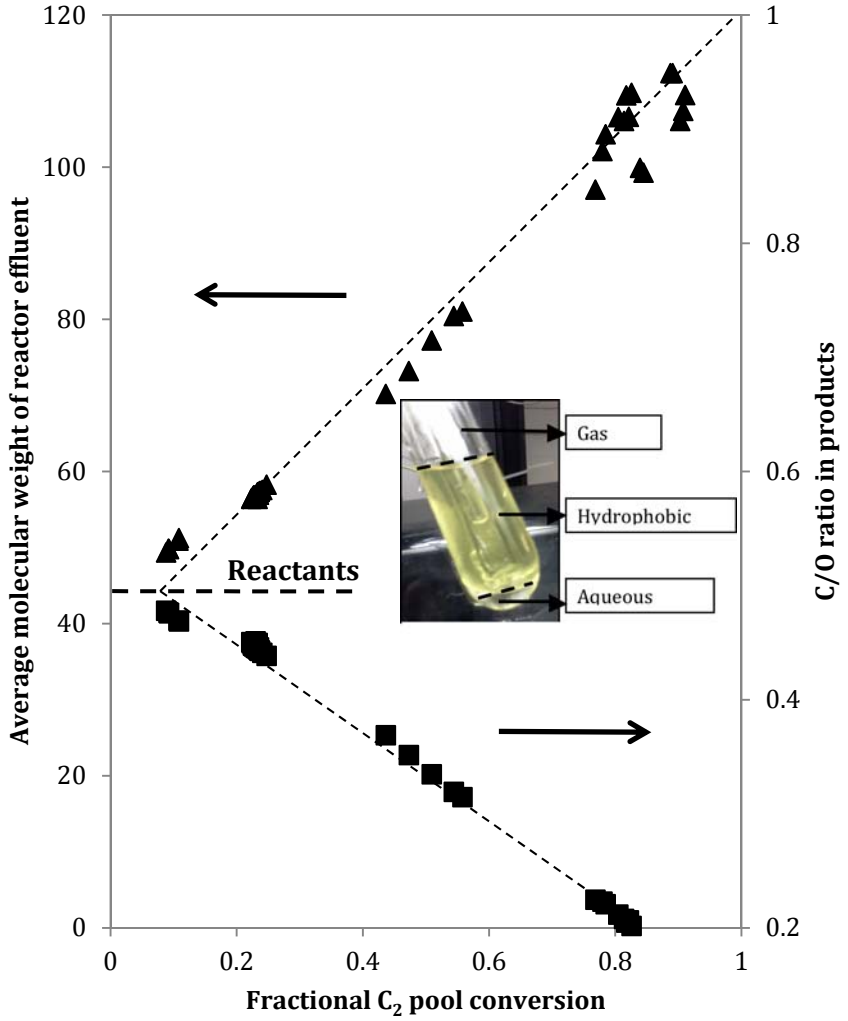

Figure 30: Effect of increasing conversion on the average molecular weight of the effluent (▲) and its oxygen to carbon ratio (■). (473-573 K, Residence time: 131-526 g_{TiO2} ks $mol_{ethanol}^{-1}$, 4 kPa propanol, 40 kPa H_2, physical mixture Cu/ZnO/Al_2O_3 and TiO_2 (P25) (1:1 mass)). Inset: Phase separator downstream of reactor

Chapter 6: C-C and C-O bond formation reactions over physical mixtures of ZrO_2 and metal-based catalysts

INTRODUCTION

The use of heterogeneous catalysts in the manufacture of ethyl acetate simplifies the production process, as no expensive catalyst separation step is required after the reaction. In recent years, copper and palladium-based heterogeneous catalysts have been shown to catalyze a single-step ethyl acetate synthesis from ethanol [1, 2, 3]. This process has garnered considerable interest, since it does not require the use of corrosive acids as reactants or catalysts, like the three major industrial processes: the Fisher esterification [4], the Tishchenko coupling of acetaldehyde [4] and the addition of acetic acid to ethylene [5, 6]. It could also be utilized for the manufacture of 'green' ethyl acetate because ethanol can be sourced from either sugarcane or lignocellulosic feedstocks.

In this process, the addition of ZrO_2 as part of the support has been reported to increase the ethanol conversion rate to ethyl acetate [7]. Subsequent mechanistic studies over mixed metal oxide catalysts and physical mixtures have attributed this increase to the formation of a hemiacetal on the ZrO_2 surface and its subsequent dehydrogenation on the Cu or Pd catalyst [8]. The mechanism of hemiacetal formation on ZrO_2 is proposed to be the reaction of a surface zirconium alkoxide with a vicinally adsorbed alkanal [9].

Pure ZrO_2 [10, 11, 12], as well as ZrO_2 doped with CeO_2 [11, 12, 13], has been reported to catalyze aldol condensation reactions. More specifically, Kunkes et al. [13] investigated the kinetics of aldol condensation reactions over a $Pd/Ce_{0.5}Zr_{0.5}O_2$ catalyst and showed that single and double aldol adducts can be formed with very good selectivity and rates from C_6 ketones.

However, to the best of our knowledge, there has been no investigation of the effects of the ZrO_2 phase on its reactivity for C-C and C-O bond formation reactions. As a result, this study aims to investigate the relationship between phase and reactivity of zirconia. Also, we intend to investigate the effects of the metal co-catalyst and of the reactant pressure on the selectivity and rates, with an ultimate goal of elucidating the surface species and reactive intermediates that participate in the reaction. Finally, we investigate the possibility of using Pt as hydrogenation and dehydrogenation catalyst, due to its resistance to sintering at higher temperatures compared to Cu.

MATERIALS AND METHODS

Zirconium oxide catalysts were prepared by hydrolysis of zirconium oxychloride (Sigma-Aldrich) tetrachloride (Sigma-Aldrich) salts by a method that has been outlined by Barton et al. [14]. In this process, a concentrated ammonia solution (Merck) was added under stirring at ambient conditions dropwise to a 0.5 M solution of the salt until the pH reaches 9. The solids were separated from the liquid by vacuum filtration and redispersed in an ammonia solution of pH = 9. The filtration and redispersion cycles were repeated until no chloride ions were detected in the filtrate by addition of 1 ml of a 3 M silver nitrate (Sigma-Aldrich) aquatic solution.

After filtration, the solids were dried in stagnant ambient air at 383 K. The dried solids were subsequently treated in air at or above 723 K, in order to tune the surface area and phase composition of the catalysts. Zirconia-based catalysts were designated as ZRXXX, where XXX is the treatment temperature in ^{o}C.

A 1% Pt/SiO_2 sample was prepared by impregnation of silica gel with aqueous hexachloroplatinic acid (Sigma-Aldrich, 99%). The sample was dried in ambient air at 383 K and subsequently treated in hydrogen at 873 K and passivated a 1% O_2/He mixture at ambient temperature for 1 h.

Commercial CuO/ZnO/Al_2O_3 catalysts were obtained from Alfa Aesar (HiFUEL W220) and used without further treatment.

Surface areas of all ZrO_2 catalysts were measured using automatic Micromeritics ASAP 2020 or Tristar 3000 physisorption analyzers. The BET surface area was obtained using nitrogen physisorption at 77 K and was used to normalize the rates.

The phase composition of the metal oxide catalysts was measured by X-ray diffraction in a Siemens D5000 powder diffractometer, using a Cu K_α radiation source and a step size of 0.02 ^{o}/s.

The monoclinic-to-tetragonal ratio for the ZrO_2 catalysts was calculated using the formula proposed by Toraya et al. [15]. First, the integrated intensity ratio X_m was calculated from integrating the relevant peaks and subsequently, the volume fraction v_m of monoclinic zirconia:

$$X_m = \frac{I_m(\bar{1}11) + I_m(111)}{I_m(\bar{1}11) + I_m(111) + I_t(101)}$$

$$v_m = \frac{1.311X_m}{1 + 0.311X_m}$$

In the above equations, $I_m(\bar{1}11)$ is the intensity of the peak from monoclinic ZrO_2 at 2θ = 28.2^{o}, $I_m(111)$ the intensity of the peak at 2θ = 31.5^{o} and $I_t(101)$ the intensity of the peak from the tetragonal phase at 2θ = 30.2^{o}.

All reactions were conducted in a quartz cylindrical plug-flow reactor at conversions smaller than 10%, unless otherwise noted. The catalyst was located on a quartz frit with a diameter of 8 mm. Hydrogen and helium (Praxair, UHP grade) were fed through mass flow controllers (Porter model 201) and liquid reactants (Sigma Aldrich, ACS grade) were introduced by means of syringe pumps (KD scientific). The reaction products were analyzed online by a Shimadzu GC 2014 gas chromatograph.

RESULTS AND DISCUSSION

EFFECTS OF THE PRETREATMENT ON THE PHASE OF ZIRCONIA

Consistent with reports by previous researchers, heat treatment of zirconium hydroxide and oxide materials at high temperatures resulted in a reduction of surface area and the volume fraction of the tetragonal phase [14]. The effects of the heat treatment on the phase composition and the surface area of the materials are shown in Table 1.

REACTION NETWORK

The reaction of propanol over a physical mixture of $Cu/ZnO/Al_2O_3$ and ZrO_2 afforded primarily the ester. Secondary products included 2-methyl-1-pentanol and 2-methylvaleraldehyde, from the aldol condensation of the propionaldehyde. Under the reaction conditions, the alcohols and the aldehydes are at equilibrium, as has been previously reported for similar systems [15] and has been mentioned earlier in this dissertation. Also, the hydrogenation of 2-methyl-2-pentenal was rapid, as none was detected by GC.

As has been shown in chapter 5 of this dissertation, reacting propionaldehyde over physical mixtures of ZrO_2 and Pt/SiO_2 yielded primarily the 2-methylvaleraldehyde, along with smaller quantities of 2-methyl-2-pentenal. No alcohol was observed, reflecting the low selectivity of Pt-based catalysts for C=O bond hydrogenation. On the contrary, extensive decarbonylation was observed.

When acetone was fed over ZrO_2 and Pt/SiO_2, the main products observed were mesityl oxide and methyl isobutyl ketone. We also obtain C_9 products, such as isovalerone and cyclic ketones.

In the absence of Cu, no esterification was observed, even when mixtures of alcohols and aldehydes were fed over the catalyst. This is consistent with earlier reports that Cu is necessary to dehydrogenate the hemiacetal that results from the reaction of an aldehyde and an alcohol [2, 8].

EFFECTS OF METAL AND CATALYST MIXING RATIO

In order to investigate the site where the rate-determining step for esterification takes place, we investigated the effects of changing the Cu to ZrO_2 catalyst mixing ratio. As can be seen in Figure 1, ester formation rates over ZrO_2 (after subtraction

of the autogenous $Cu/ZnO/Al_2O_3$ contributions), as normalized by ZrO_2, increased linearly with the fraction of Cu in the bed. This relationship suggests that the rate-determining step of the sequence takes place over the Cu surface. The dehydrogenation of the alcohol can be ruled out as rate-determining step, since alcohols and aldehydes are in equilibrium under the reaction conditions, as has also been previously demonstrated. This conclusion suggests that the dehydrogenation of the hemiacetal is the rate-limiting step in the sequence and that the hemiacetal is in equilibrium with the alcohol and aldehyde in the presence of a ZrO_2 catalyst.

EFFECTS OF REACTANT PRESSURE

Esterification rates over ZR500 were proportional to the aldehyde pressure and decreased slightly with increasing alcohol pressure (Figure 2). We have already shown that the rate-determining step for the esterification is the dehydrogenation of the hemiacetal over the Cu catalyst. As a result, the hemiacetal formation step can be considered to be a pre-equilibrium. Consequently, the partial pressure of the hemiacetal in the reactor will be proportional to the product of the aldehyde pressure and the alcohol pressure. Bearing that in mind, the aforementioned observation can be due to the fact that the hemiacetal dehydrogenation is a first-order reaction in hemiacetal pressure. While there is no direct kinetic evidence for this conclusion, parallels between hemiacetal and alcohol dehydrogenation reactions support this hypothesis [17]. The reduction of the reaction rate with increasing alcohol pressure can be ascribed to the fact that the Cu surface is covered by alkoxides. This observation is consistent with the work of previous researchers [16, 17].

A possible mechanism for aldol condensation over ZrO_2 is shown in Scheme 1. This mechanism is similar to the ones proposed by Zaki et al. [18]. In this, an acetone molecule is adsorbed on the ZrO_2 surface and an enolate is formed by the abstraction of an α-H atom. This enolate reacts in turn with a gas-phase acetone molecule to form diacetone alcohol. Since no diacetone alcohol was detected in the products of the reaction, we conclude that this species is dehydrated rapidly over ZrO_2. The resulting mesityl oxide is hydrogenated to methyl isobutyl ketone over the Pt surface.

There are two extreme cases for the enolate formation, which is the step denoted by k_1: an equilibrated one and an irreversible one. The former has been reported for the condensation of acetone over MgO and La_2O_3 catalysts [19], as well as over HT in Chapter 1 of the present work, and the latter has been proposed for aldol condensation over TiO_2 [20].

Since the enolate is a short-lived intermediate, one can use the pseudo-steady-state approximation for it. Thus:

$$K_0 k_1 p_{acetone}(*) = k_2(enolate*)p_{acetone} + k_{-1}(enolate*)$$

$$(enolate*) = \frac{K_0 k_1 p_{acetone}(*)}{k_2 p_{acetone} + k_{-1}}$$

The rate of product formation can be written as:

$$r = k_2 k_3 (enolate*) p_{acetone} = \frac{K_0 k_1 k_2 k_3 p_{acetone}(*)}{k_2 p_{acetone} + k_{-1}} p_{acetone} = \frac{K_0 k_1 k_2 k_3 p_{acetone}(*)}{k_2 p_{acetone} + k_{-1}} \frac{p_{acetone}}{1 + K_0 p_{acetone}}$$

In the equilibrated case, $k_{-1} >> k_2 p_{acetone}$. In this case, one would not observe a zero-order regime at higher acetone pressures, but a first-order dependence, as the order of the numerator would be larger than that of the numerator at all conditions. Therefore, the observed zero-order dependence (Figure 3) is strong evidence for an irreversible enolate formation. Thus, the rate law can be written as:

$$r = \frac{K_0 k_1 k_2 k_3 p_{acetone}}{1 + K_0 p_{acetone}}$$

A good fit can be obtained for this rate law, with $K_0 k_1 k_2 k_3 = 0.9$ mmol g_{ZrO2}^{-1} ks^{-1} kPa^{-1} and $K_0 = 1.6$ kPa^{-1} , with a $R^2 = 0.962$.

An important question that must be addressed is the possibility of the ester and aldol condensation products coming from a single intermediate. If both the ester and the aldol adducts came from the same intermediate, the rate of esterification in the presence of Cu would be similar to the rate of aldol condensation in the absence of Cu, since in the former case, the amount of intermediate diverted to the ester would be equal to the amount of intermediate forming the aldol adduct. As seen from Figure 4, the aldol condensation rate in the presence and the absence of copper was similar. However, the ester formation rate was much higher than that of the aldol condensation rate (Figure 5). As such, we conclude that the esterification and aldol condensation pathways operate independently from each other.

PHASE DEPENDENCE OF ALDOL CONDENSATION RATE OVER ZrO_2

As seen in Figure 6, aldol condensation rates over ZrO_2 increased with increasing monoclinic volume fraction. This trend contrasts to the one observed in earlier publications on zirconia, in which the tetragonal phase gave the highest reactivity. These phenomena can be attributed to the fact that tetragonal zirconia tends to be more acidic than monoclinic zirconia [11]. As a result, base-catalyzed reactions, such as aldol condensation, occur preferentially over monoclinic zirconia.

CONCLUSIONS

In this study, we have shown that esterification over physical mixtures of ZrO_2 and Cu-based catalysts occurs via an equilibrated hemiacetal formation step over ZrO_2. The kinetically relevant step for esterification is the dehydrogenation of the

hemiacetal over an alkoxide-covered Cu surface. Aldol condensation reactions take place preferentially over monoclinic ZrO_2 via an irreversible enolate formation step and subsequent C-C bond formation.

REFERENCES

[1] K. Inui, T. Kurabayashi and S. Sato, "Direct Synthesis of Ethyl Acetate from Ethanol Carried Out under Pressure," *Journal of Catalysis,* vol. 212, no. 2, pp. 207-215, 2002.

[2] A. B. Gaspar, F. G. Barbosa, S. Letichevsky and L. G. Appel, "The one-pot ethyl acetate syntheses: The role of the support in the oxidative and the dehydrogenative routes," *Applied Catalysis A: General,* vol. 380, no. 1-2, pp. 113-117, 2010.

[3] N. Iwasa and N. Takezawa, "Reforming of Ethanol –Dehydrogenation to Ethyl Acetate and Steam Reforming to Acetic Acid over Copper-Based Catalysts," *Bulletin of the Chemical Society of Japan,* vol. 64, no. 9, pp. 2619-2623, 1991.

[4] W. Riemenschneider and H. M. Bolt, "Esters, Organic," in *Ullmann's Encyclopedia of Industrial Chemistry*, Weinheim, Wiley-VCH, 2005.

[5] K. Sano, M. Nishiyama, T. Suzuki, S. Wakabayashi and K. Miyahara, "Process for preparation of lower fatty acid ester". European Union Patent EP 0562139, 29 09 1993.

[6] M. P. Atkins and B. Sharma, "Ester Synthesis". European Union Patent EP 0757027, 05 02 1997.

[7] K. Inui, T. Kurabayashi and T. Takahashi, "Novel catalyst for gas-phase ester production comprises zirconium oxide, copper, and at least one from zinc oxide, chromium oxide, aluminum oxide and silicon oxide". United States of America Patent US2004242917-A1, 15 11 2002.

[8] P. C. Zonetti, J. Celnik, S. Letichevsky, A. B. Gaspar and L. G. Appel, "Chemicals from ethanol – The dehydrogenative route of the ethyl acetate one-pot synthesis," *Journal of Molecular Catalysis A: Chemical,* vol. 334, p. 29–34, 2011.

[9] K. Inui, T. Kurabayashi, S. Sato and N. Ichikawa, "Effective formation of ethyl acetate from ethanol over Cu-Zn-Zr-Al-O catalyst," *Journal of Molecular Catalysis A: Chemical,* vol. 216, no. 1, p. 147–156, 2004.

[10] K. Takanabe, K.-I. Aika, K. Seshan and L. Lefferts, "Catalyst deactivation during steam reforming of acetic acid over Pt/ZrO_2," *Chemical Engineering Journal,* vol. 120, no. 1-2, pp. 133-137, 2006.

[11] A. Gangadharan, M. Shen, T. Sooknoi, D. E. Resasco and R. G. Mallinson, "Condensation reactions of propanal over $Ce_xZr_{1-x}O_2$ mixed oxide catalysts," *Applied Catalysis A: General,* vol. 385, no. 1-2, pp. 80-91, 2010.

[12] E. I. Gürbüz, E. L. Kunkes and J. A. Dumesic, "Integration of C–C coupling reactions of biomass-derived oxygenates to fuel-grade compounds," *Applied Catalysis B: Environmental,* vol. 94, no. 1-2, pp. 134-141, 2010.

[13] E. L. Kunkes, E. I. Gürbüz and J. A. Dumesic, "Vapour-phase C–C coupling reactions of biomass-derived oxygenates over $Pd/CeZrO_x$ catalysts," *Journal of Catalysis,* vol. 266, no. 2, pp. 236-249, 2009.

[14] D. G. Barton, S. L. Soled, G. D. Meitzner, G. A. Fuentes and E. Iglesia, "Structural and Catalytic Characterization of Solid Acids Based on Zirconia Modified by Tungsten Oxide," *Journal of Catalysis,* vol. 181, no. 1, pp. 57-72, 1999.

[15] H. Toraya, M. Yoshimura and S. Somiya, "Quantitative Analysis of Monoclinic-Stabilized Cubic ZrO2 Systems by X-Ray Diffraction," *Journal of the American Ceramic Society,* vol. 67, no. 9, pp. C183-C184, 1984.

[16] M. E. Sad, M. N. Neurock and E. Iglesia, "Formation of C-C and C-O bonds and oxygen removal in reactions of alkanediols, alkanols, and alkanals on copper catalysts," *Journal of the American Chemical Society,* vol. 133, no. 50, pp. 20384-20398, 2011.

[17] R. M. Rioux and M. A. Vannice, "Hydrogenation/dehydrogenation reactions: isopropanol dehydrogenation over copper catalysts," *Journal of Catalysis,* vol. 216, no. 1-2, pp. 362-376, 2003.

[18] M. I. Zaki, M. A. Hasan and L. Pasupulety, "Surface Reactions of Acetone on Al_2O_3, TiO_2, ZrO_2, and CeO_2: IR Spectroscopic Assessment of Impacts of the Surface Acid–Base Properties," *Langmuir,* vol. 17, no. 3, p. 768–774, 1999.

[19] G. Zhang, H. Hattori and K. Tanabe, "Aldol Addition of Acetone, Catalyzed by Solid Base Catalysts: Magnesium Oxide, Calcium Oxide, Strontium Oxide, Barium Oxide, Lanthanum (III) Oxide and Zirconium Oxide," *Applied Catalysis,* vol. 36, pp. 189-197, 1988.

[20] J. E. Rekoske and M. A. Barteau, "Kinetics, Selectivity, and Deactivation in the Aldol Condensation of Acetaldehyde on Anatase Titanium Dioxide," *Industrial and Engineering Chemistry Research,* vol. 50, no. 1, pp. 41-51, 2010.

Table 1: Effects of treatment temperature on the phase and surface area of zirconium oxide samples.

Catalyst	Treatment temperature (K)	Surface area ($m^2\ g^{-1}$)	Monoclinic volume fraction (%)
ZR500	773	102	72.9
ZR550	823	96.7	75.3
ZR600	873	80.4	79.0
ZR650	923	54	85.7
ZR700	973	27	87.3
ZR800	1073	10	92.2

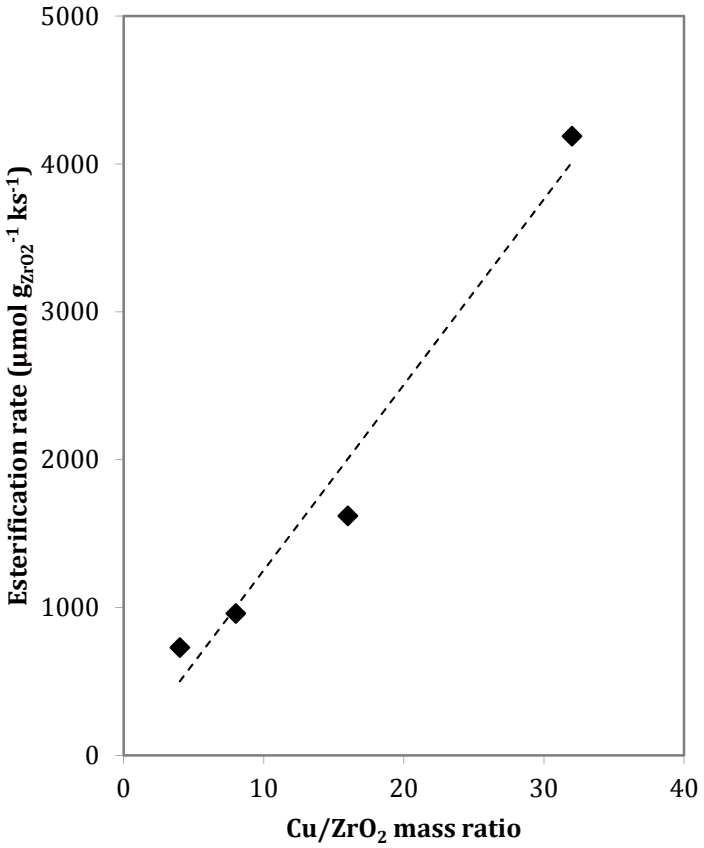

Figure 1: Effects of the Cu to ZrO_2 mass ratio on the esterification rate over ZrO_2. (4 kPa propanol, 40 kPa H_2, 473 K).

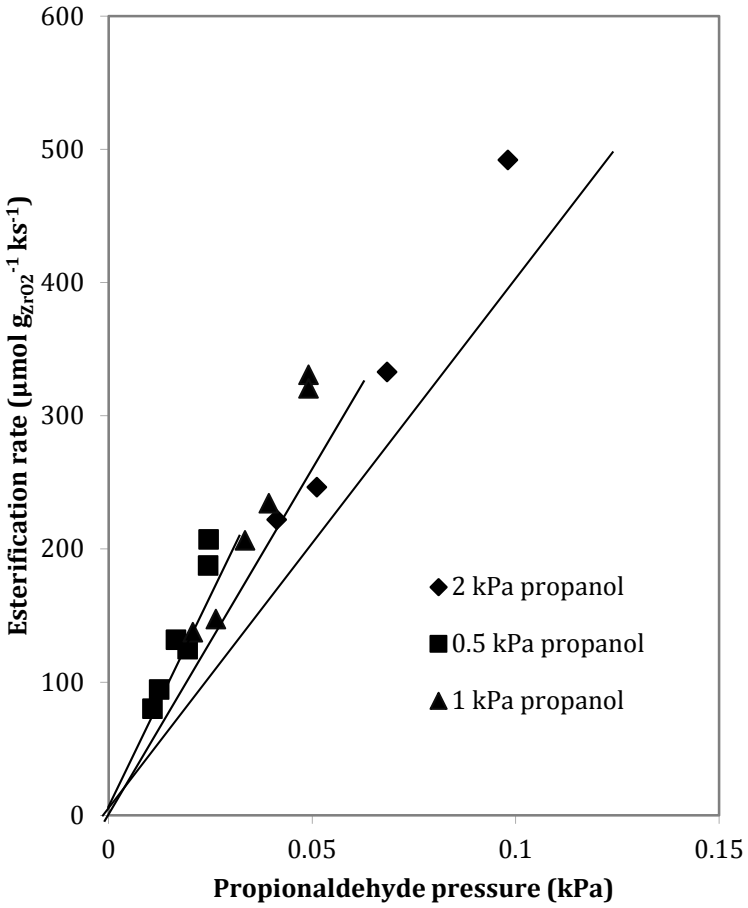

Figure 2: Effects of aldehyde and alcohol pressure on the esterification rate. 473 K 40-100 kPa H_2, 0.05 ml/h propanol, 50 mg ZR500, 200 mg Cu/ZnO/Al_2O_3.

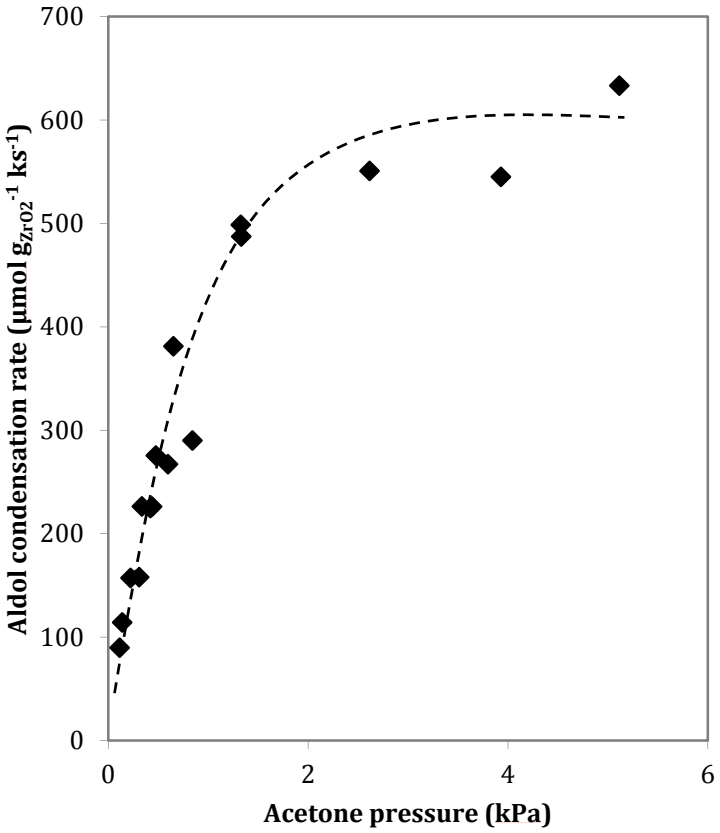

Figure 3: Dependence of aldol condensation rate on the acetone pressure. 473 K, 40 kPa H_2, physical mixture of ZR500 and Pt/SiO_2, 5.5 µg Pt/m^2 ZrO_2

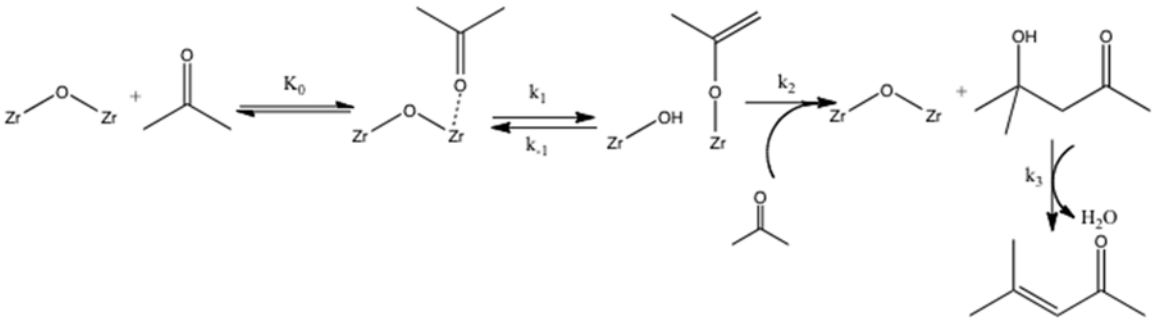

Scheme 1: Reaction mechanism for aldol condensation over ZrO_2.

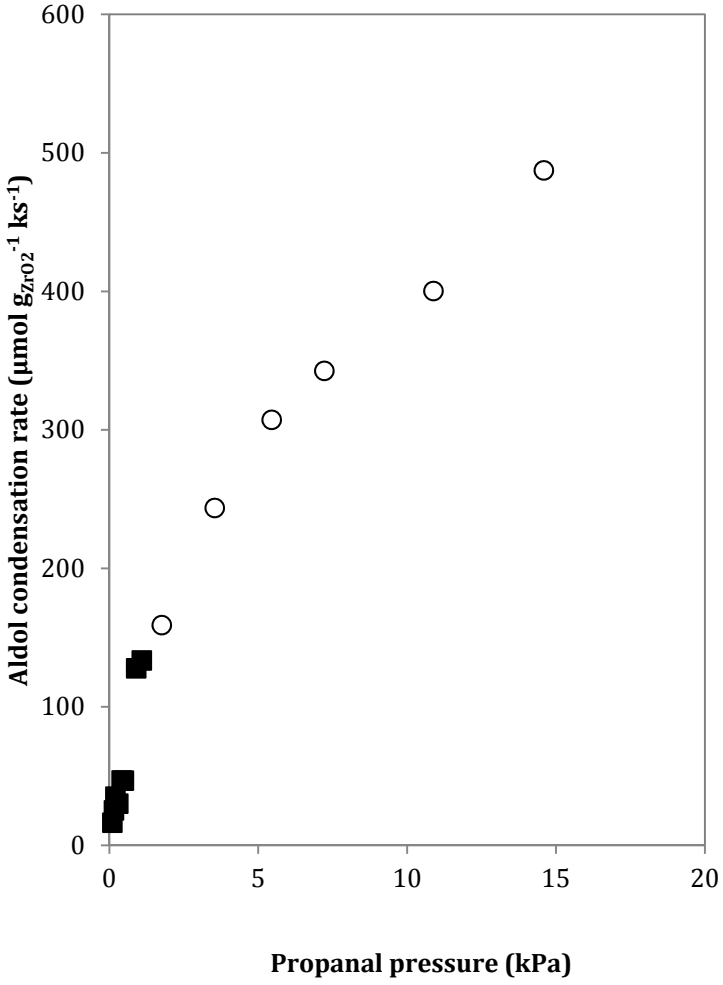

Figure 4: Aldol condensation rate of propanal in the presence (filled squares) and the absence (empty circles) of Cu. 473 K, 40 kPa H_2, 4-20 kPa propanol and physical mixture of $Cu/ZnO/Al_2O_3$ and ZrO_2 or 2-16 kPa propanal, physical mixture of Pt/SiO_2 and ZrO_2.

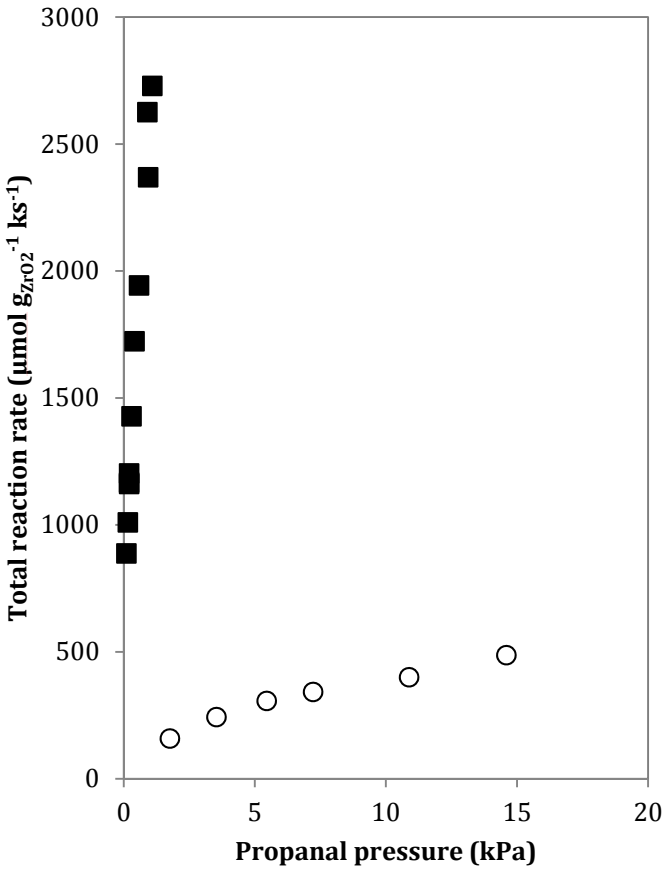

Figure 5: Total reaction rate in the presence (filled squares) and the absence (empty circles) of Cu.473 K, 40 kPa H_2, 4-20 kPa propanol and physical mixture of $Cu/ZnO/Al_2O_3$ and ZrO_2 or 2-16 kPa propanal, physical mixture of Pt/SiO_2 and ZrO_2.

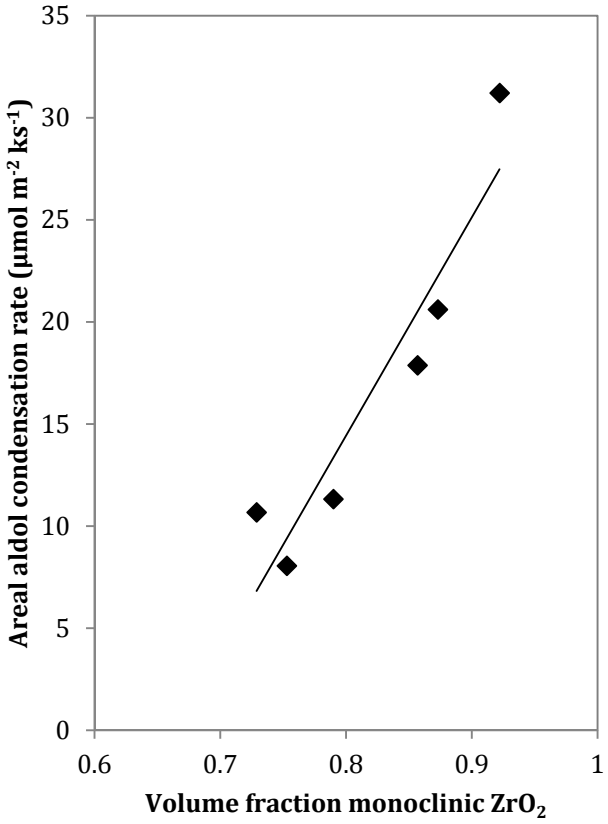

Figure 6: Dependence of aldol condensation rates on the volume fraction of ZrO_2. 0.8 kPa acetone, 473 K, 40 kPa H_2, physical mixture of ZrO_2 and Pt/SiO_2 , 12 µg Pt/m^2 ZrO_2

APPENDIX A: SUPPORTING INFORMATION FOR CHAPTER 1

Table S 1: Effects of Cu loading on BET surface area of coprecipitated Cu/HT catalysts.

Cu loading	BET surface area
1%	200
1.9%	178
2.4%	185
4.6%	164
9.1%	143

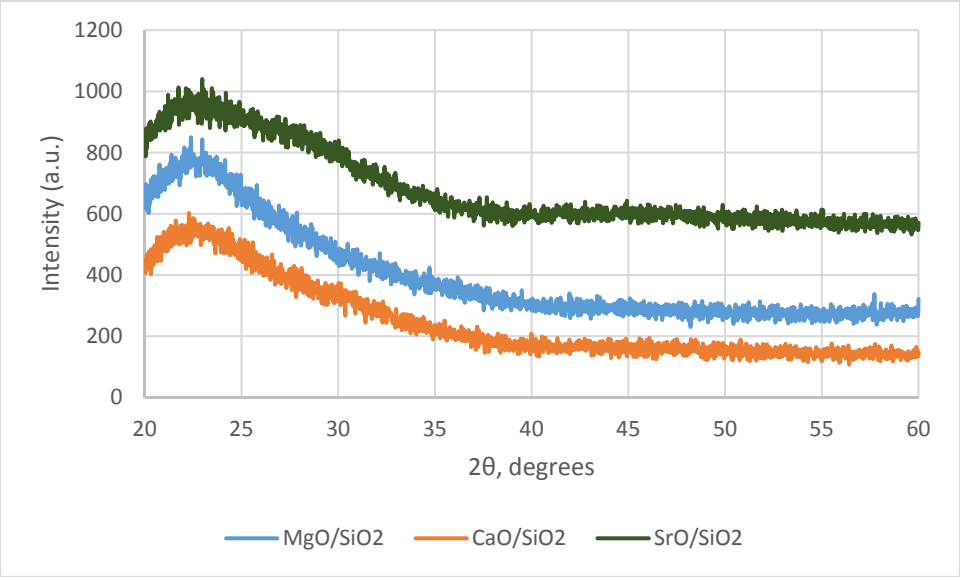

Figure S 1: X-ray diffractograms for SiO_2-supported IIA metal oxides.

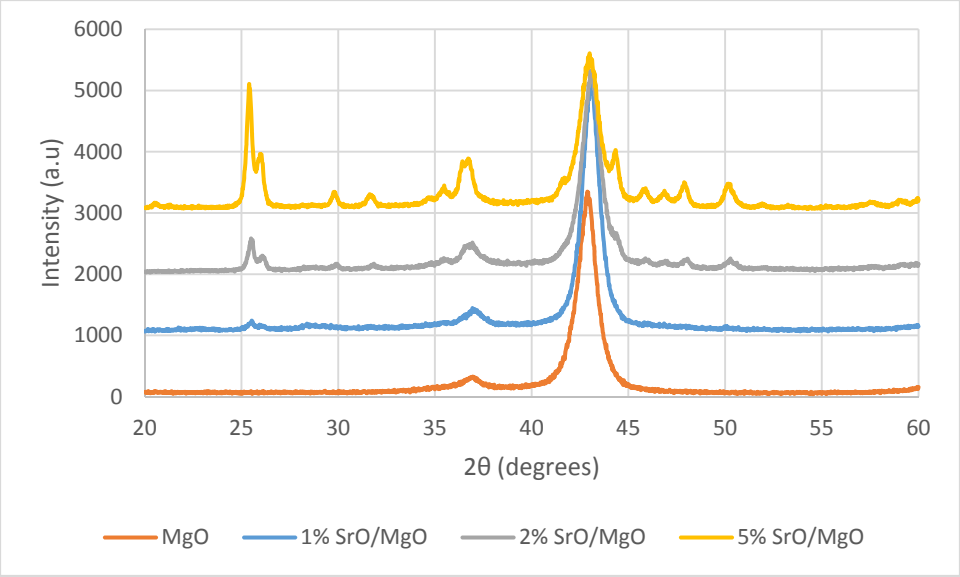

Figure S 2: Effects of SrO substitution on the structure of MgO materials

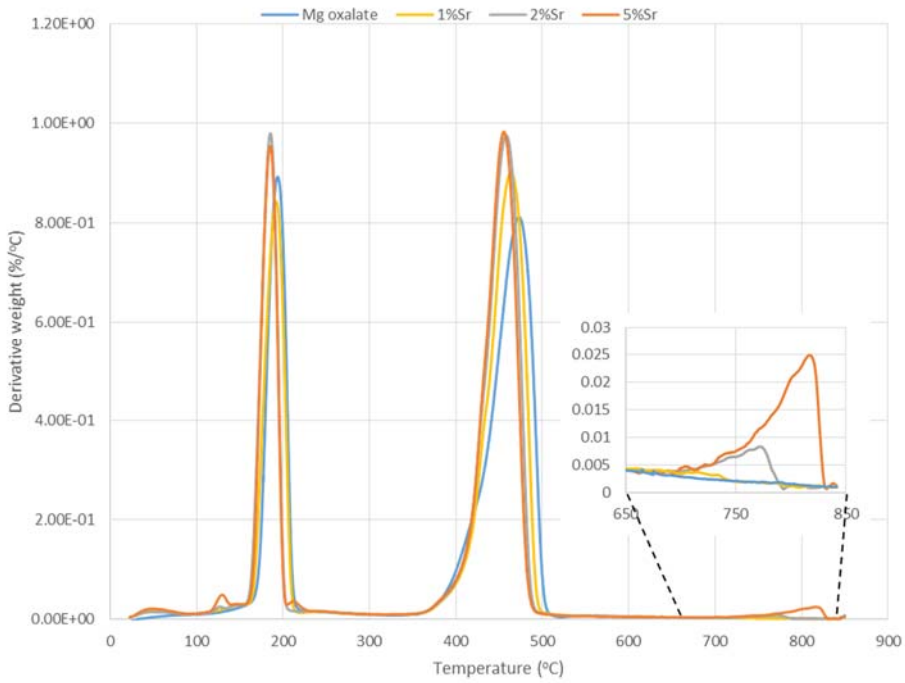

Figure S 3: Effects of SrO substitution on the TGA of magnesium oxalate-derived materials

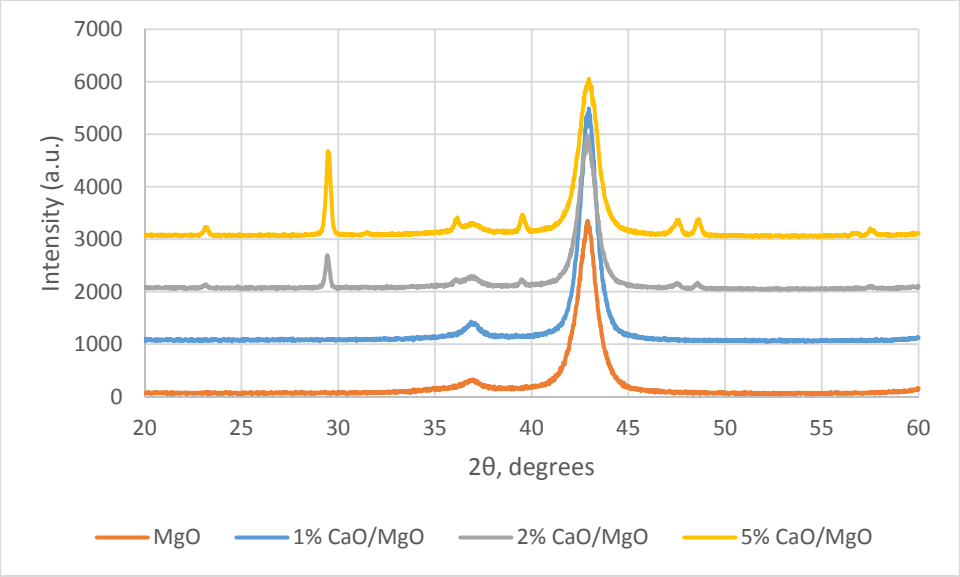

Figure S 4: Effects of CaO substitution on the structure of MgO materials.

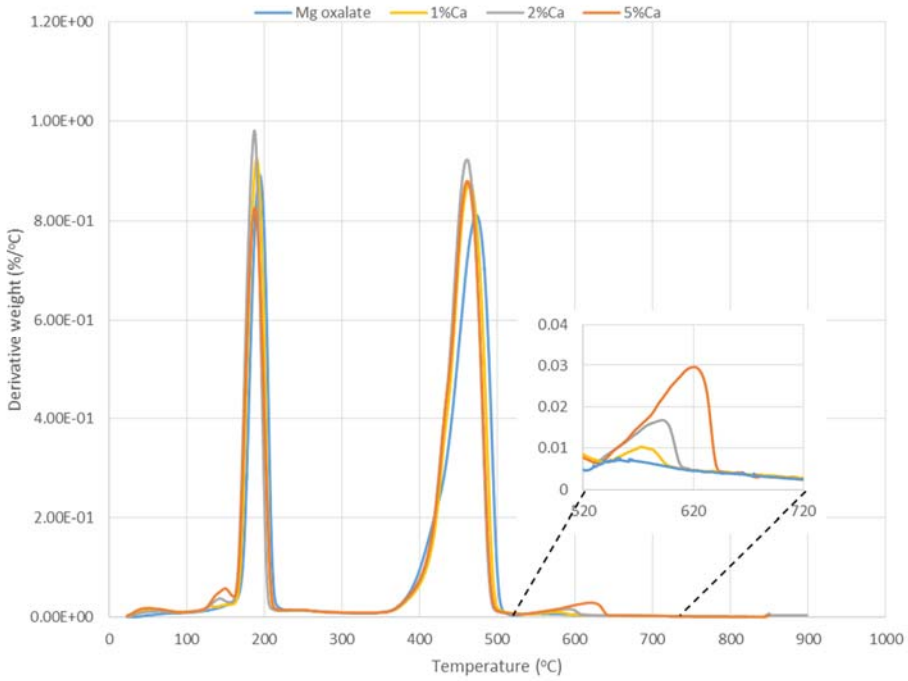

Figure S 5: Effects of CaO substitution in the structure of magnesium oxalate-derived catalysts

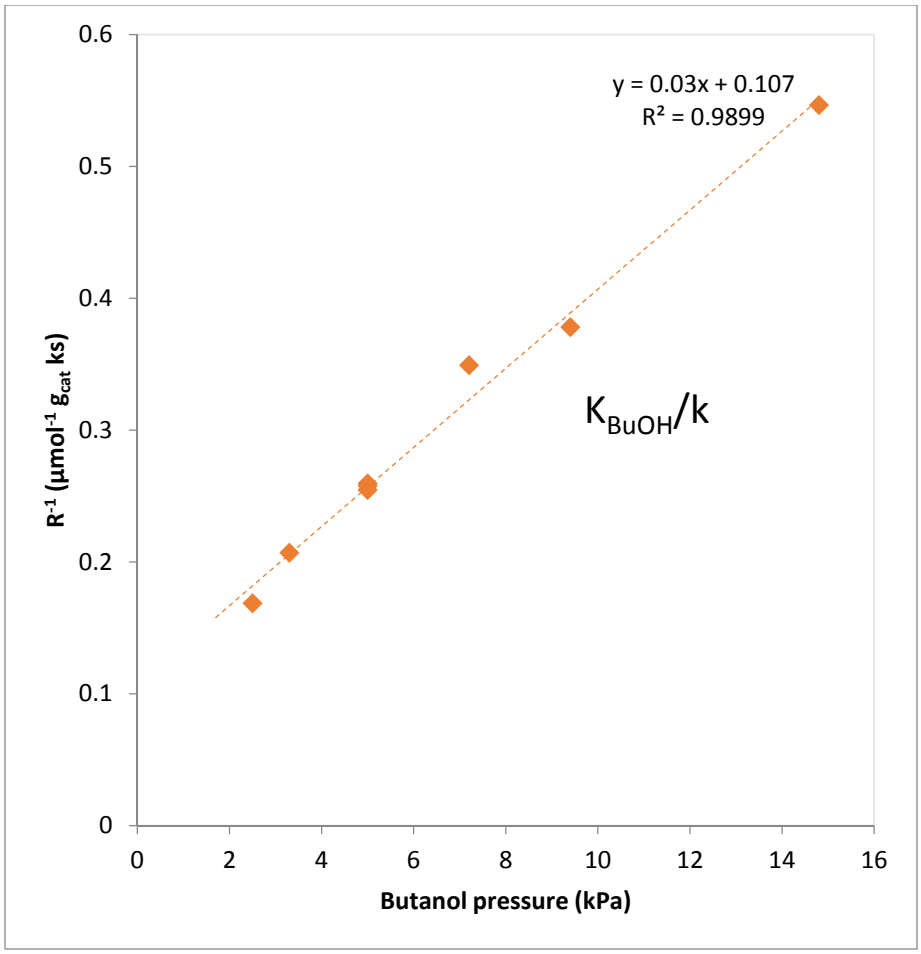

Figure S 6: Dependence of ABE condensation rate on pressure of butanol.

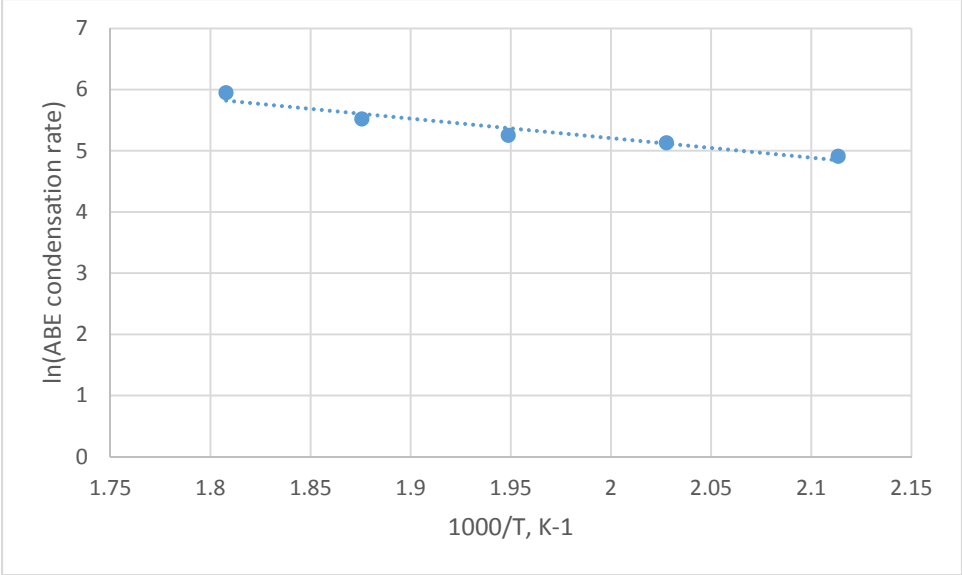

Figure S 7: Arrhenius plot for the condensation of acetone and butyraldehyde in the presence of butanol.

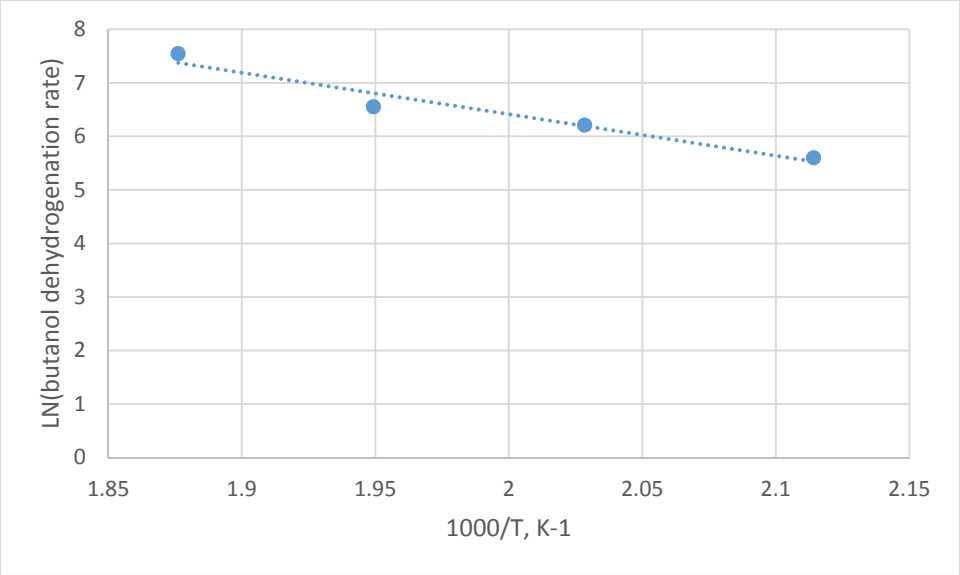

Figure S 8:Arrhenius plot for the dehydrogenation of butanol over a CuHT catalyst.

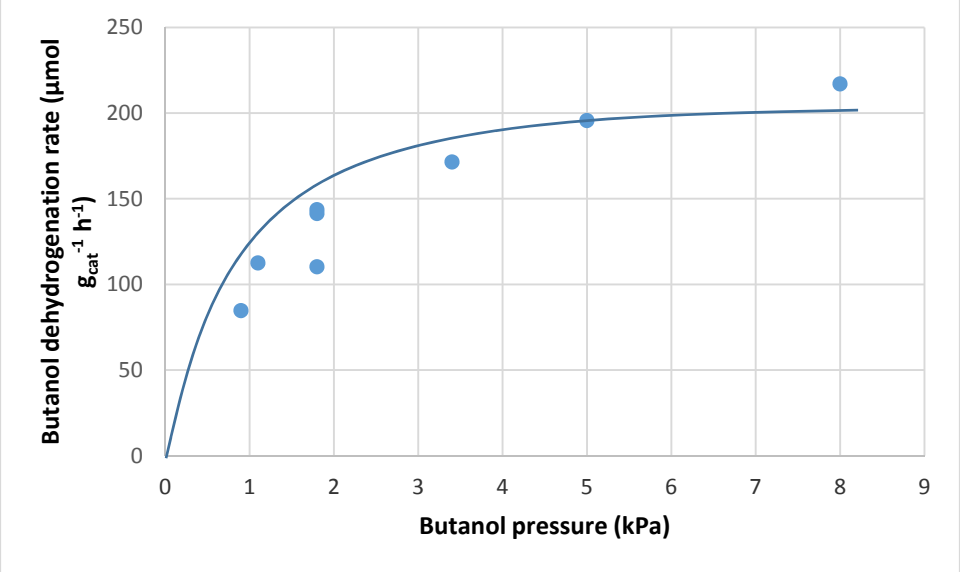

Figure S 9: Dependence of butanol dehydrogenation rate on butanol pressure over a PdHT catalyst

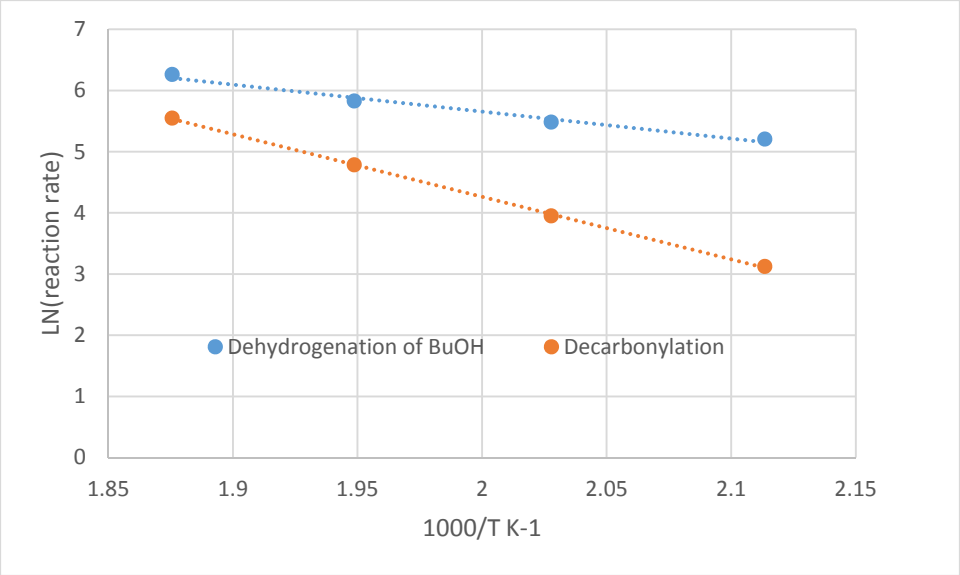

Figure S 10: Arrhenius plot for dehydrogenation and decarbonylation reactions over a PdHT catalyst.

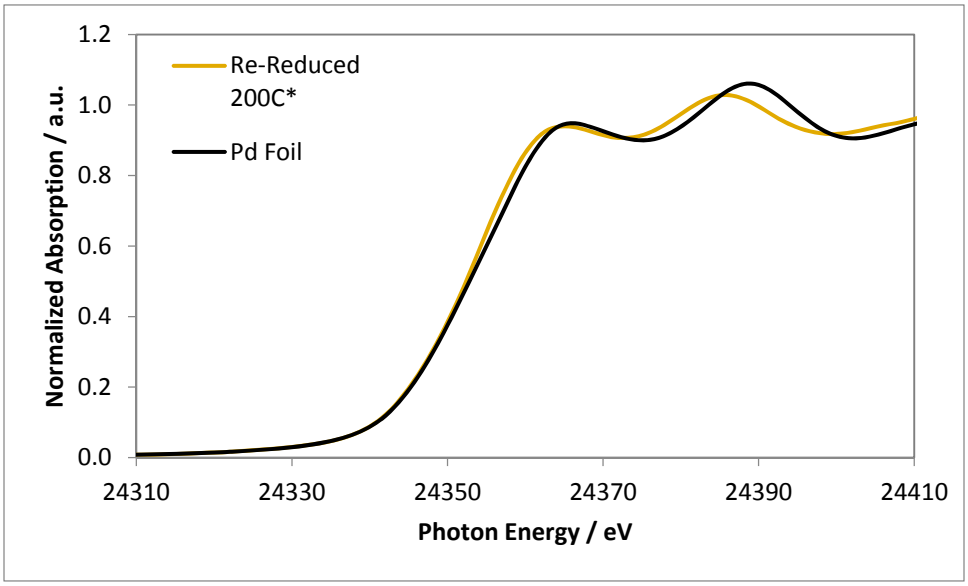

Figure S 11: XANES of the Pd/HT catalyst, calcined at 823 K, reduced at 523 K, air passivated, and then re-reduced at 473 K at the beamline. Note that there are differences in the spectrum above the edge, which are consistent with the formation of a Pd hydride phase. This was caused by cooling the sample to RT and scanning under an H_2/He atmosphere. Neverthless, this phase forms only from metallic Pd, and both the XANES (edge position) and shape of the EXAFS are consistent with the formation of the metallic hydride phase.

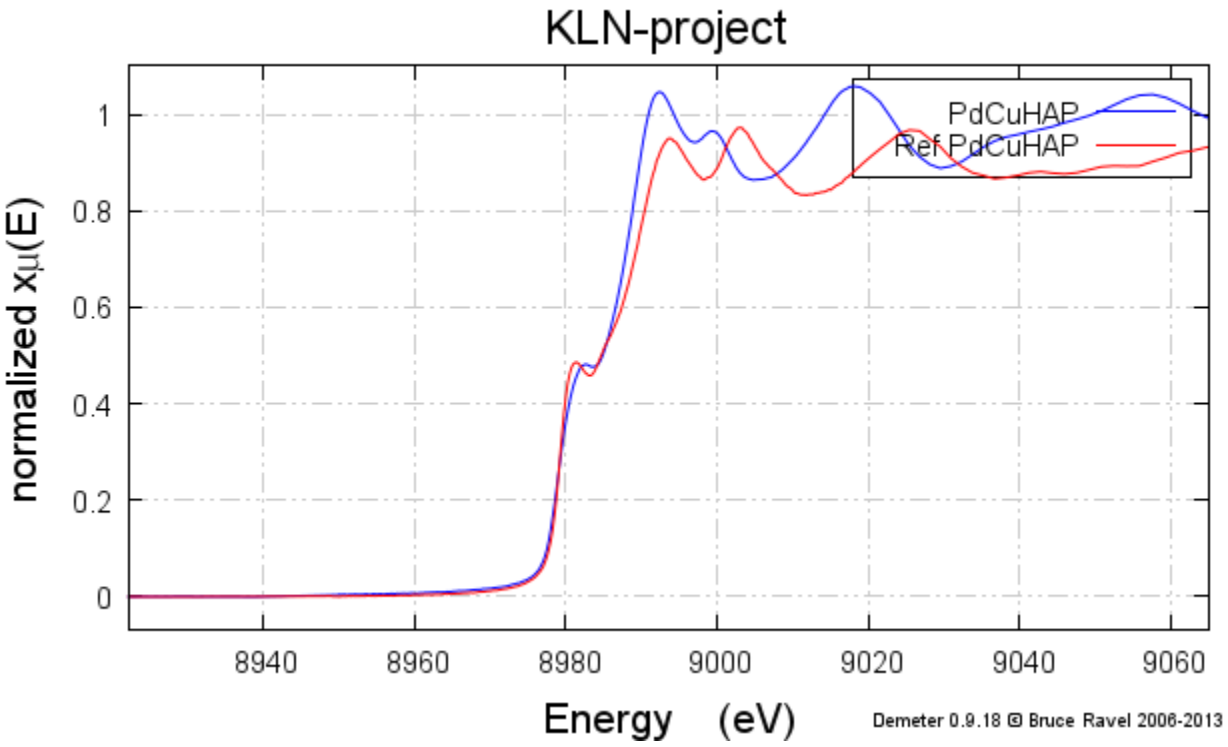

Figure S 12: Cu edge XANES for PdCu/HAP catalyst

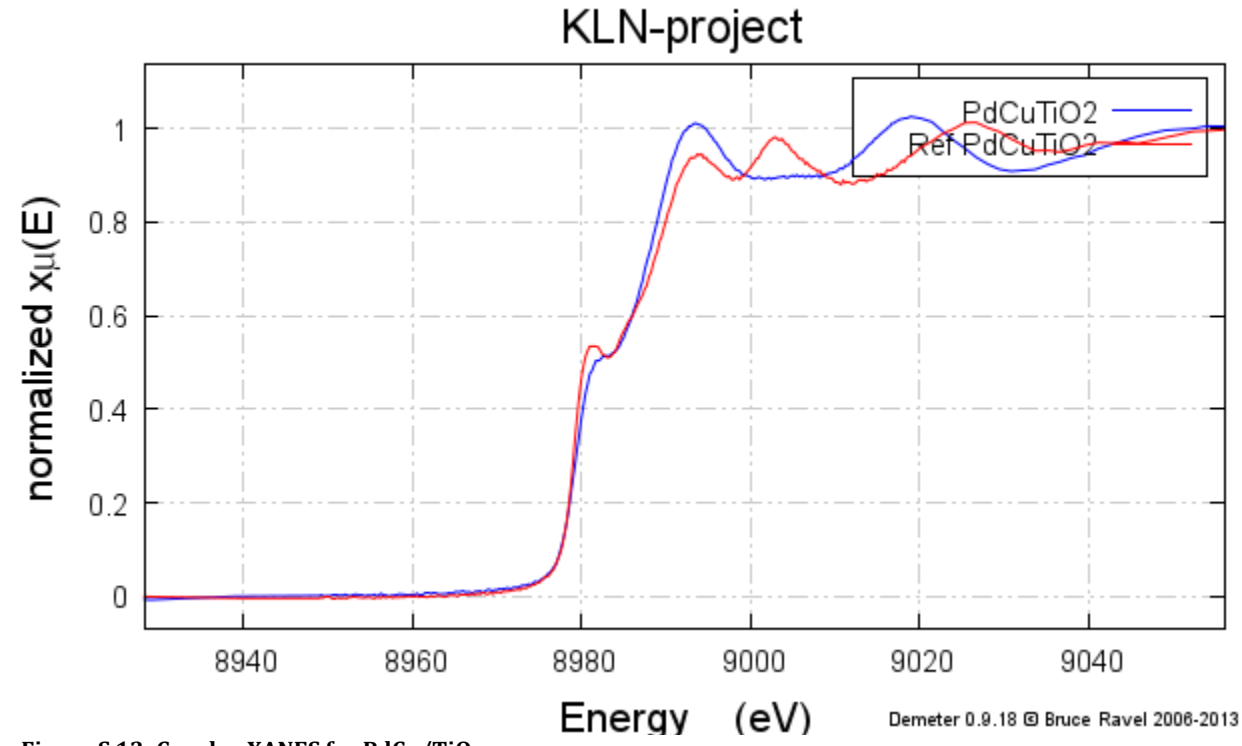

Figure S 13: Cu edge XANES for PdCu/TiO_2

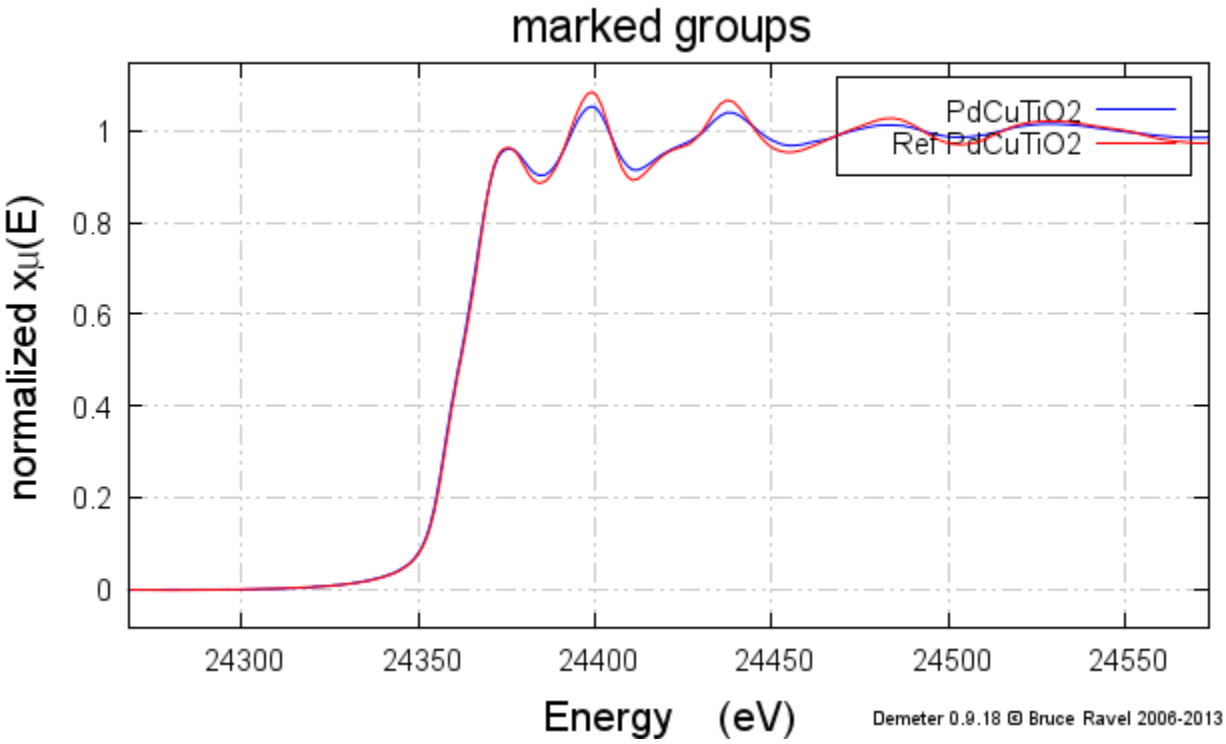

Figure S 14: Pd edge XANES for $PdCu/TiO_2$

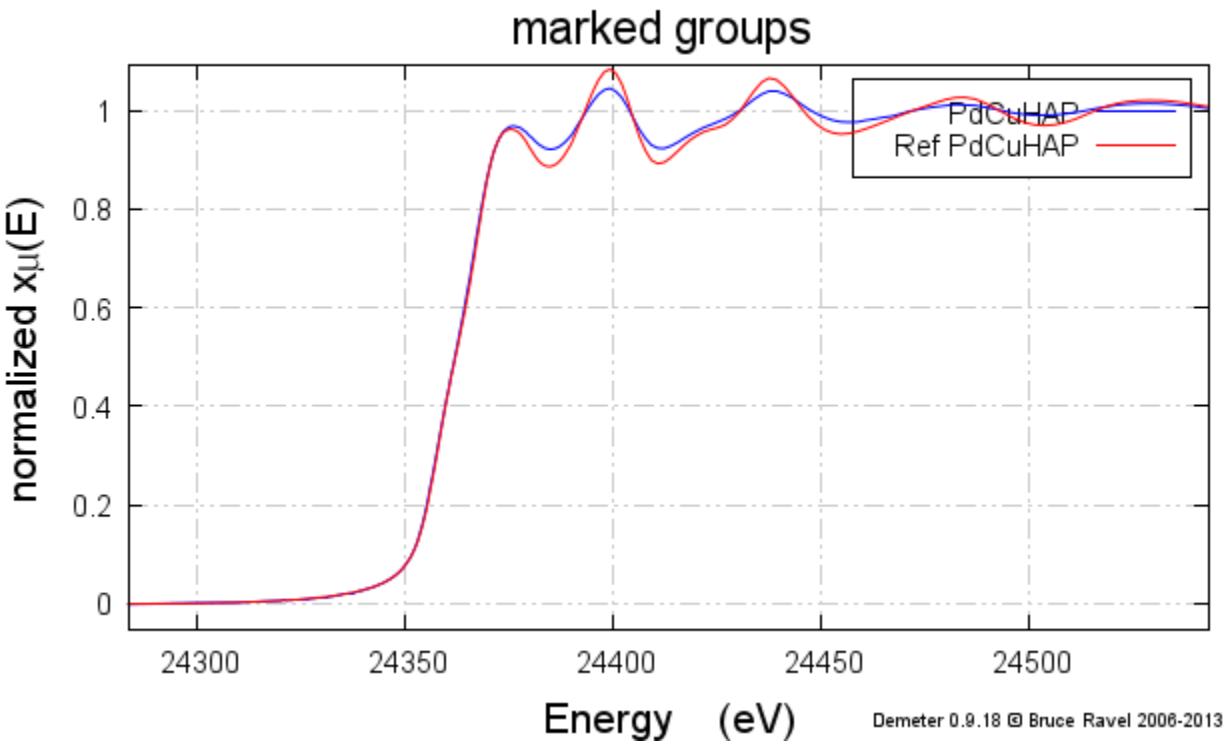

Figure S 15: Pd edge XANES for PdCu/HAP

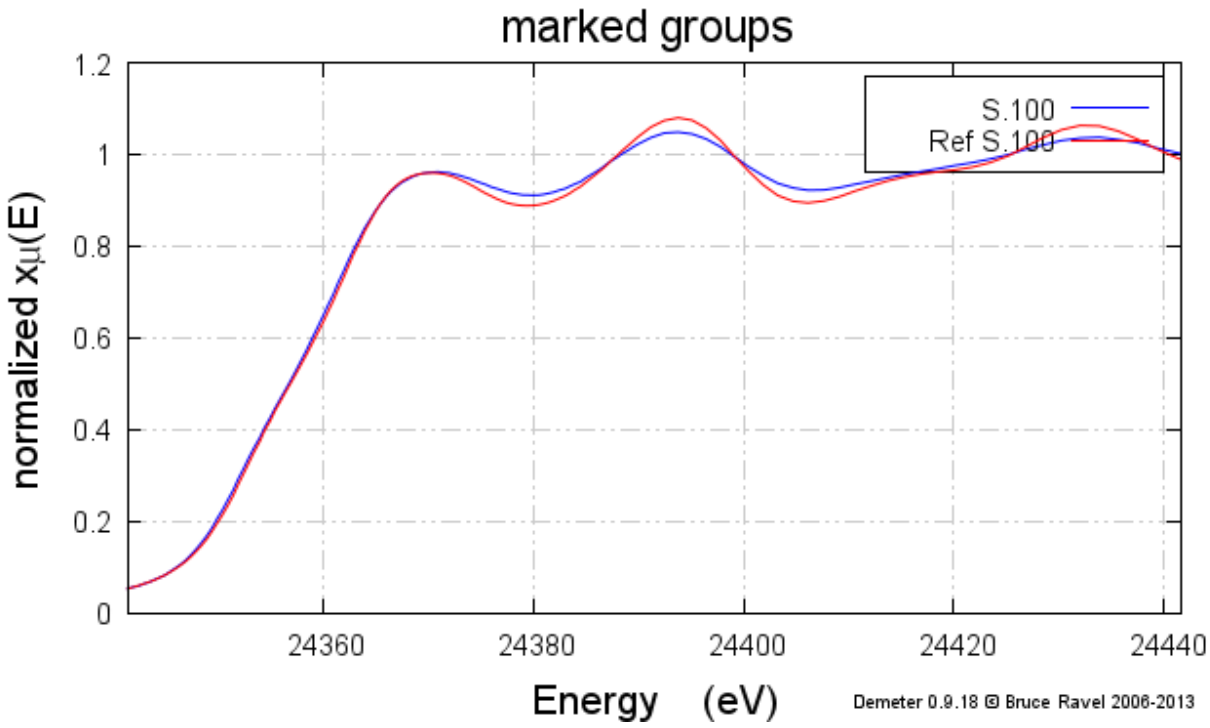

Figure S 16: Pd edge XANES for PdCu/HT-C

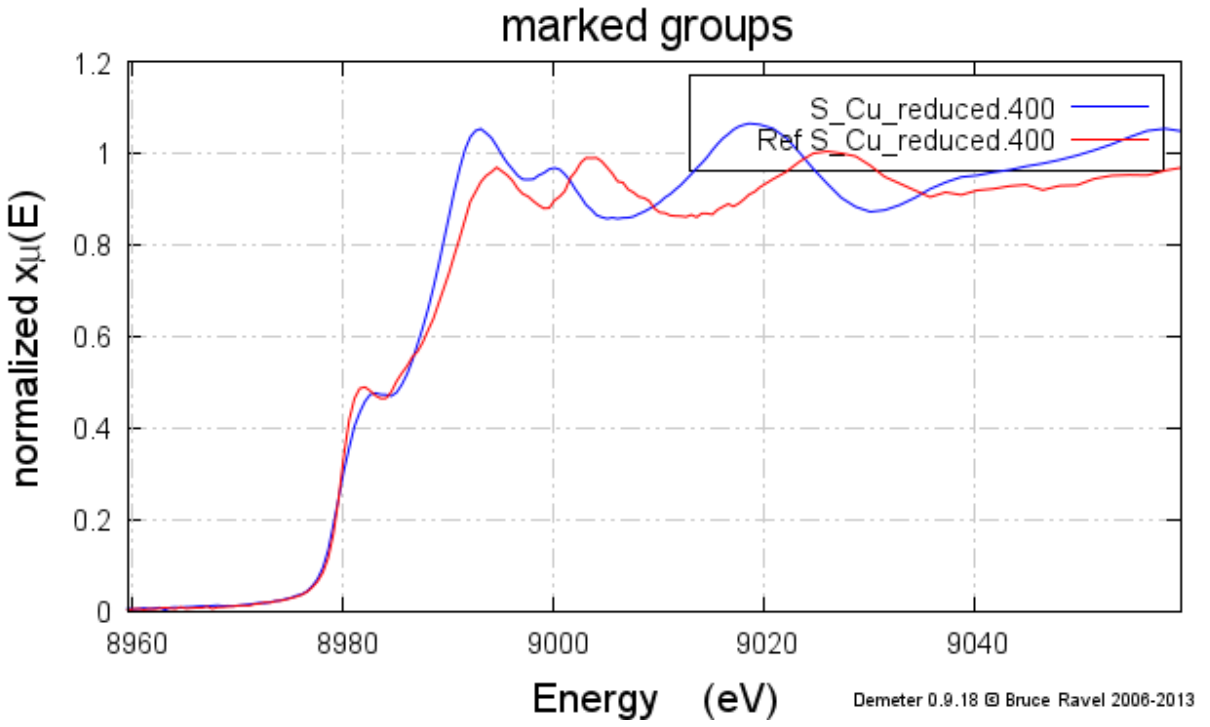

Figure S 17: Cu Edge XANES for PdCu/HT-C

APPENDIX B: SUPPORTING INFORMATION FOR CHAPTER 2

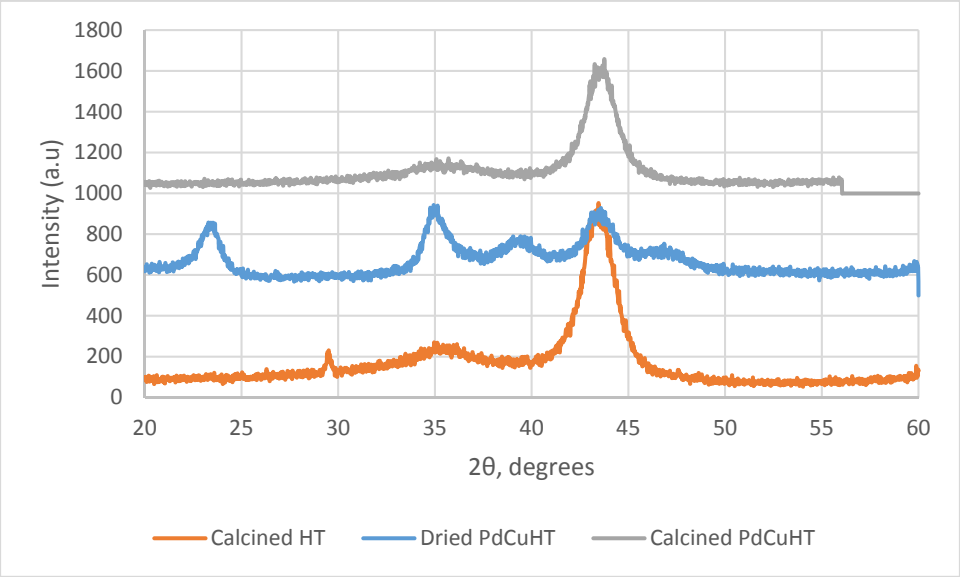

Figure S 1: Effects of preparation on the crystal structure of PdCu/HT catalysts

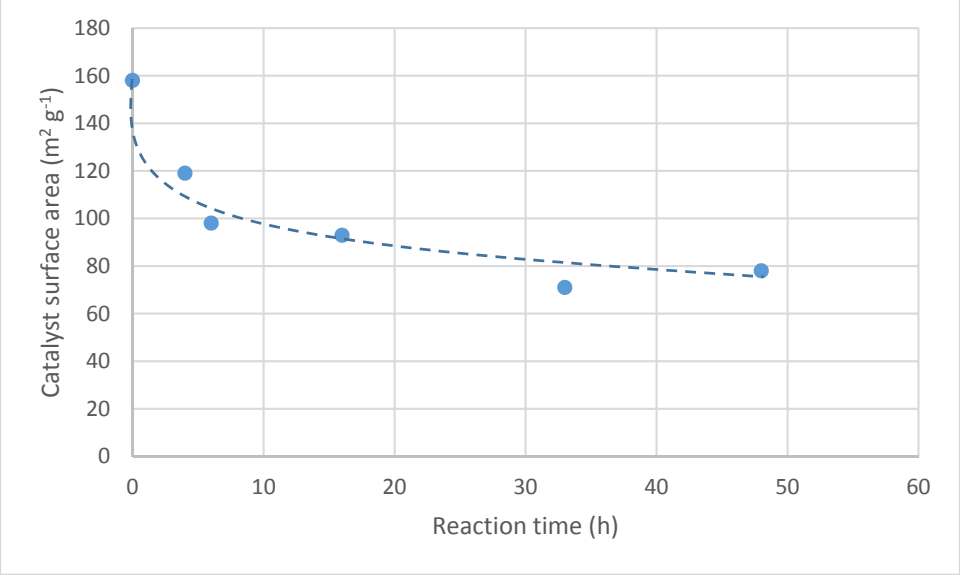

Figure S 2: Effects of batch reaction time on a Pd/HT catalyst.

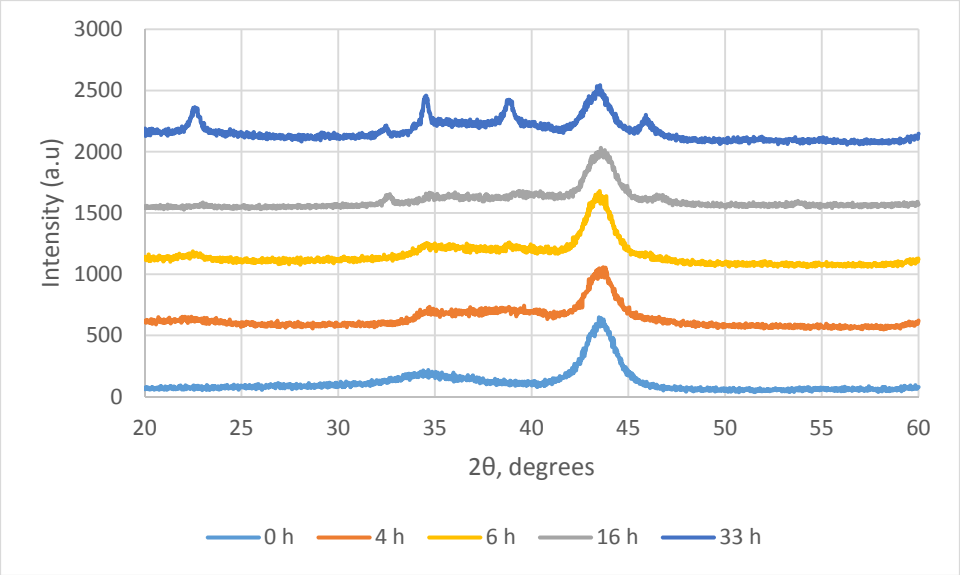

Figure S 3: Effects of reaction time on Pd/HT catalyst structure.

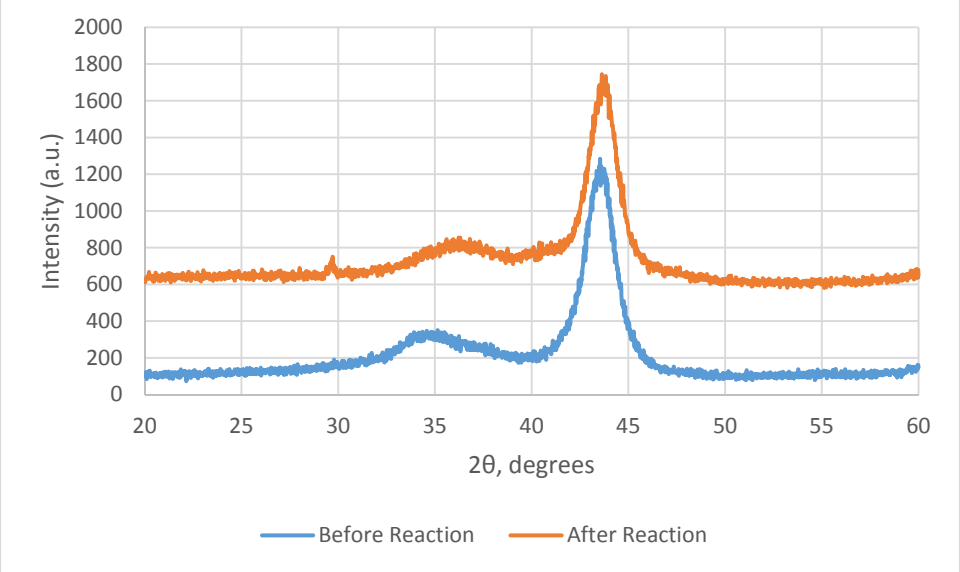

Figure S 4: Effects of the gas-phase flow reaction on the structure of a PdCu/HT catalyst

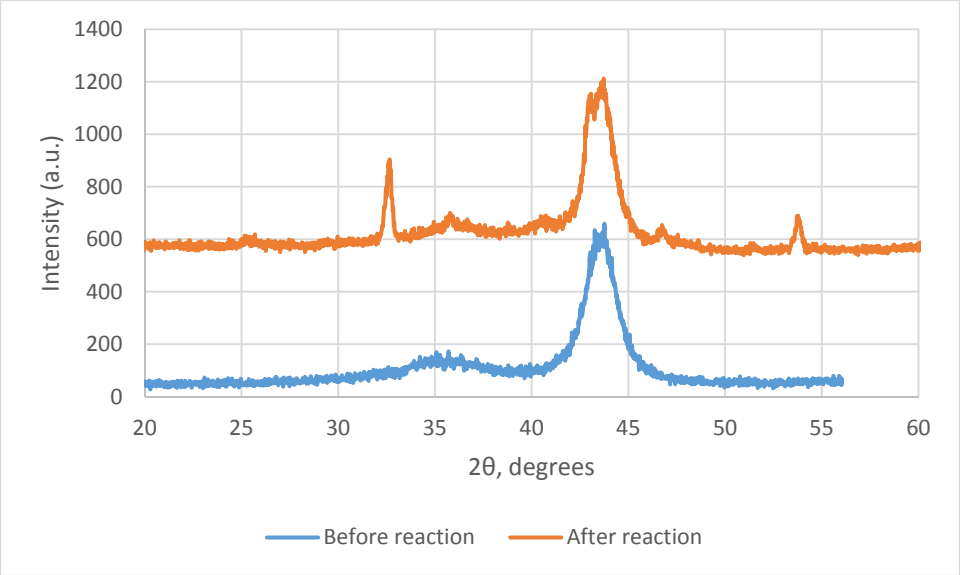

Figure S 5: Effects of the liquid phase reaction on the structure of PdCu/HT catalysts

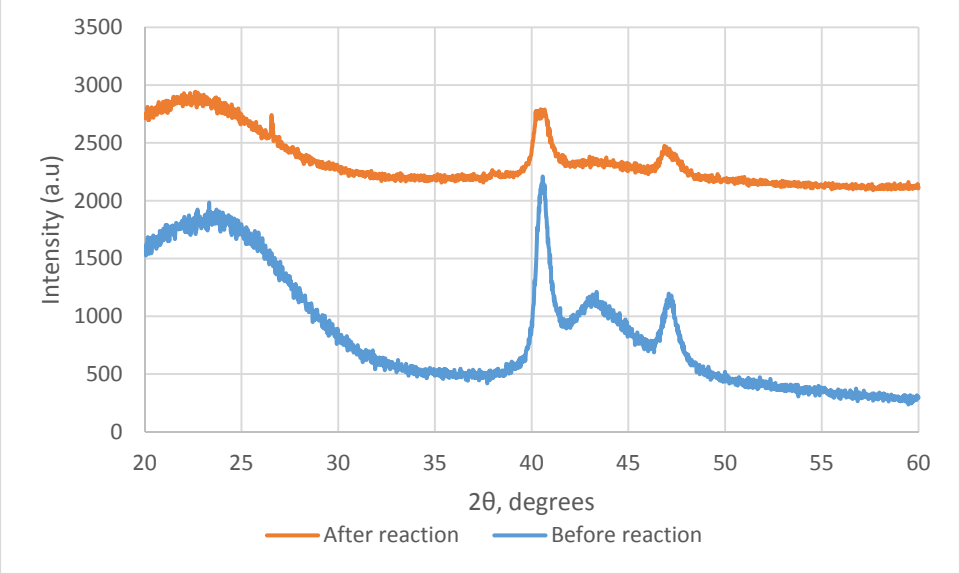

Figure S 6: Effects of liquid-phase reaction on the structure of PdCu/HT-C catalysts

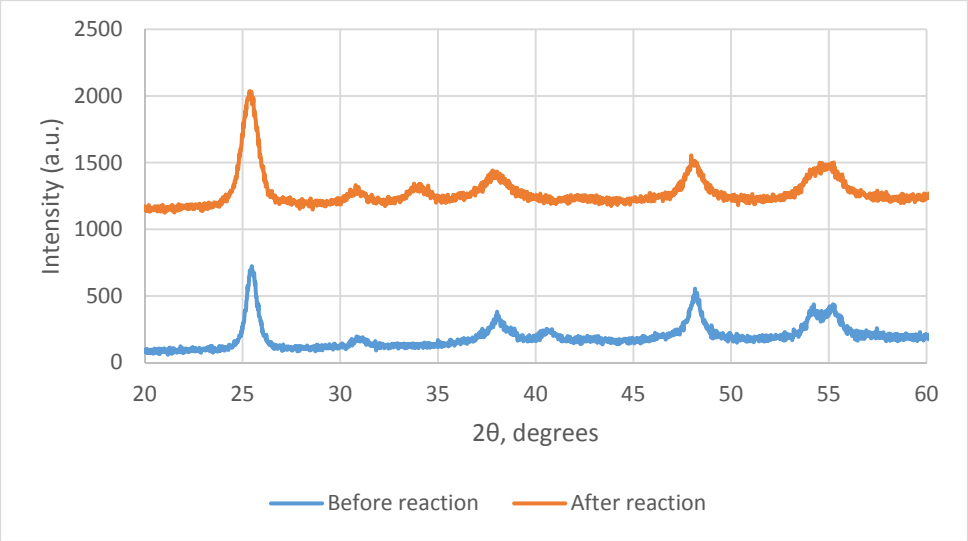

Figure S 7: Changes in the crystal structure of SC-PdCu/TiO_2 in the liquid-phase ABE flow reaction.

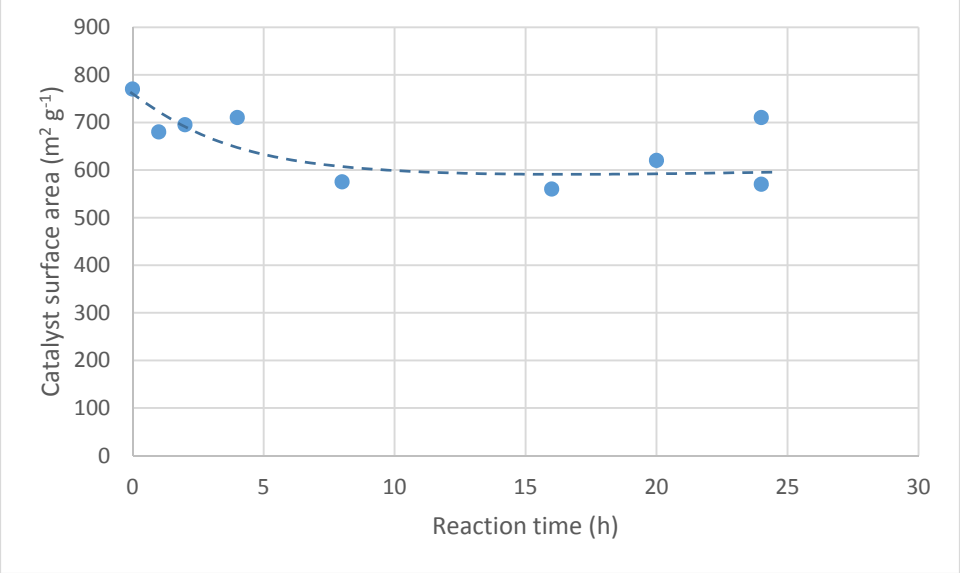

Figure S 8: Effects of batch reaction time on PdCu/HT-C catalysts. Dashed line represents qualitative trend.